



A high power Fabry-Perot resonator for precision Compton polarimetry with the longitudinally polarised lepton beams at HERA

Fabian Zomer

► To cite this version:

Fabian Zomer. A high power Fabry-Perot resonator for precision Compton polarimetry with the longitudinally polarised lepton beams at HERA. Physique des Hautes Energies - Expérience [hep-ex]. Université Paris Sud - Paris XI, 2003. tel-00007045

HAL Id: tel-00007045

<https://theses.hal.science/tel-00007045>

Submitted on 7 Oct 2004

HAL is a multi-disciplinary open access archive for the deposit and dissemination of scientific research documents, whether they are published or not. The documents may come from teaching and research institutions in France or abroad, or from public or private research centers.

L'archive ouverte pluridisciplinaire **HAL**, est destinée au dépôt et à la diffusion de documents scientifiques de niveau recherche, publiés ou non, émanant des établissements d'enseignement et de recherche français ou étrangers, des laboratoires publics ou privés.

Mémoire d'Habilitation à Diriger des Recherches

**A high power Fabry-Perot
resonator for precision Compton
Polarimetry with the
longitudinally polarised
lepton beams at HERA**

Fabian Zomer

Habilitation soutenue le lundi 22 décembre 2003, devant la commission d'examen :

MM.	D. Barber	rapporteur
	A. Blondel	rapporteur
	M. Davier	président
	M. Klein	rapporteur
	C. Pascaud	

Pour Matthieu, mon fils
Pour ma famille
Pour mes amis

“Wenn man sich sein Haus fertig gebaut hat, merkt man, unversehens Etwas dabei gelernt zu haben, das man schlechterdings hätte wissen müssen, bevor man zu bauen-anfieng.”

(“Quand on a construit une maison, on a généralement appris quelque chose qu'on aurait dû savoir avant de commencer à construire.”)

F. Nietzsche (Jenseits von gut und böse)

Contents

1	Polarisation and HERA Upgrade Physics program	9
1.1	Right Handed Charged Current	10
1.1.1	Cross-section ratio: the precision requirement for the polarisation measurement	11
1.1.2	Absolute cross-section: effect of the polarisation rise	14
1.2	Propagation of the polarisation uncertainties to the CC cross-section . . .	25
1.3	The neutral currents case: effect of the polarisation rise	28
1.4	Summary	30
1.5	Appendix	33
1.5.1	Introduction	33
1.5.2	Measurement of NC and CC cross-sections	34
1.5.3	Phenomenological analysis of inclusive measurements at HERA . .	36
2	Electron beam Polarisation and Polarimetry	51
2.1	Electron beam polarisation	51
2.1.1	Polarisation build-up in storage rings	52
2.1.2	Depolarisation effects	53
2.1.3	Spin rotators and longitudinal polarisation at HERA	54
2.1.4	Optimisation of the polarisation at HERA	55
2.1.5	Polarisation operations at HERA	56
2.1.6	Polarisation and physics analysis	58
2.2	Polarisation measurement: Compton scattering	63
2.2.1	Jones and Stokes-Mueller Formalism in optics	63
2.2.2	Laser beam-electron beam interaction	64
2.2.3	Polarisation measurement modes	66
2.2.4	Polarisation measurement in the few photon mode	71
2.2.5	Numerical studies	74
2.3	Appendix	81
2.3.1	Statistical estimators	81
3	A Fabry-Perot Cavity for an upgrade of the HERA longitudinal polarimeter	93
3.1	A Fabry-Perot cavity for polarimetry	93
3.1.1	Principle of Fabry-Perot cavities	93
3.1.2	Choice of the cavity geometry for HERA	95
3.2	Mechanical design of the cavity	96
3.2.1	Constraints	96

3.2.2	Mechanical design	97
3.2.3	Implementation at HERA	101
3.3	Optical scheme	104
3.3.1	The laser	108
3.3.2	Details of the optical scheme	112
3.3.3	Parasitic ellipticity and birefringence sources of the optical setup . .	119
3.3.4	Optical calibration procedure	124
3.4	Feedback system	124
3.5	Electronics and calorimeter readout	126
3.5.1	Slow control	128
3.5.2	Fast Data Acquisition System	130
3.6	Appendix: Laser and cavity modes	134
3.6.1	Laser beam	134
3.6.2	Cavity eigen-modes	134
3.6.3	Cavity mode structure	136
3.6.4	Number of round trips inside a cavity	137
3.7	Appendix: technical aspects of cavities	137
3.7.1	The mirrors	137
3.7.2	Mechanical tolerances for a monolithic cavity	138
3.7.3	Power Losses due to Laser beam Cavity Coupling Imperfections . .	141
3.8	Appendix: some birefringence estimates	144
3.8.1	Introduction	144
3.8.2	Formalism	144
3.8.3	Birefringence induced by the heated cavity entrance mirror	148
3.8.4	Birefringence induced by air pressure on a perfect vacuum window .	150
4	Ellipsometry and coherent light polarisation	159
4.1	Quarter wave plates	159
4.1.1	Jones matrix for an ideal quartz plate	159
4.1.2	Optical properties of quartz	162
4.1.3	Characteristics of our quartz plates	164
4.1.4	Choice of the quartz quarter wave plate	165
4.1.5	Plate surface state and cleaning	166
4.2	Principle of the ellipsometer	169
4.3	Calibration of the quartz plate	173
4.3.1	Experimental set-up	173
4.3.2	Stability and precision of the photodiode readout	177
4.3.3	Fit procedure	179
4.3.4	Results	184
4.4	Shaping of the laser beam polarisation	188
4.5	Summary	191
4.6	Appendix: Misalignments	193
4.6.1	Glan-Thomson/Wollaston prisms misalignment	193
4.6.2	Misalignment of the tilt and azimuthal axes	194
4.6.3	Rotation axis misalignment	197
4.7	Appendix: Electro-optic crystal	199
4.7.1	Null static field	201

4.7.2	Longitudinal static field	201
5	Results of the operation of a test cavity and of the final cavity	207
5.1	Setup of the test cavity	207
5.2	Laser beam/cavity coupling	209
5.3	Feedback operations and cavity gain performance	215
5.3.1	Estimate of the cavity gain	218
A	Model for the propagation of Gaussian beams in anisotropic plates	229
A.1	A 2×2 matrix method for anisotropic parallel plates. I: plane waves	230
A.1.1	Multi-layer anisotropic parallel plates	230
A.1.2	Anisotropic parallel plate	234
A.2	A 2×2 matrix method for anisotropic parallel plates. II: Gaussian beam . .	237
A.2.1	Introduction	237
A.2.2	Vector Fourier optics in the paraxial approximation	237
A.2.3	Application to anisotropic layer	240
A.2.4	Scalar Fourier Approximation	242
A.2.5	Example: uniaxial parallel plate	245
A.2.6	Conclusion	253
A.2.7	Annex I	253
A.2.8	Annex II	255
A.3	Effects of surfaces roughness on the transmission of Gaussian beams by anisotropic parallel plates	256
A.3.1	Introduction	256
A.3.2	Formalism	257
A.3.3	Numerical simulations	264
A.3.4	Conclusion	266

Introduction

This document was written in order to obtain the French Habilitation Diploma. Since considerable freedom is allowed for the substance and the form of such a document, I have taken this opportunity to provide a rather detailed technical report on the new HERA polarimeter.

After approximately eight years of running, the HERA electron-proton Collider of the German DESY Laboratory has undergone major machine upgrades. These modifications – which took place during the years 2001-2002 – have two aims: an increase of the electron-proton luminosity by a factor of four and the supply of longitudinally polarised electrons at the high energy electron-proton interactions points, i.e. within the two detectors H1 and ZEUS.

During the first year of operation, HERA-II had encountered very difficult background conditions at the H1 and ZEUS interaction points. To reach the high luminosity, it was realised that further modifications of the electron-proton interaction point regions were required. This was the purpose of the year 2003 HERA-II shutdown.

In spite of these difficulties, the good news came from the electron beam polarisation. Just before the 2003 shutdown, the H1 and ZEUS spin rotators, used to polarise longitudinally the naturally transversally polarised electrons, were switched on and a polarisation of 50 % was reached.

To cover accurately the physics of high luminosity polarised electron-proton collisions, an upgrade of the longitudinal polarimeter was proposed and accepted at the end of 2000. This new polarimeter, currently installed at HERA and waiting for its commissioning, is the main topic of this document.

In the first chapter, studies of the impact of the polarisation measurement accuracy on three observables, the right-handed and the standard charged current cross-sections and the determination of the light quark couplings to the Z^0 are presented. These topics do not obviously cover all the HERA upgrade programme but they are quite representative of the requirements for the precision on the polarisation measurement. The main point is that, unlike small polarisation asymmetry measurements, absolute cross section measurements are very sensitive to the polarisation uncertainties. Since the electron-proton luminosity is expected to increase by a factor of four, we show that the accuracy of the polarisation measurements must increase as well.

In the second chapter, the beam polarisation built up and the Compton polarimetry are presented. Very briefly, Compton polarimetry consists in measuring and analysing the energy spectrum of photons backscattered after laser-electron interactions. The polarimeter performances then rely, not only but essentially, on the choice of laser. In this context, I complete this chapter by a study of the statistic and systematic uncertainties related to Compton polarimetry. From this study, we conclude that a continuous laser

beam of a few kilo Watts is desirable to fulfil the physics requirements given in chapter 1.

The polarimeter upgrade, proposed to reach the laser power defined in chapter 2, is described in chapter 3. The core of this polarimeter is a high finesse Fabry-Perot cavity filled by a 750 mW ND:YAG laser. This optical resonator, made of two super-mirrors located around the electron beam, provides a few kilo Watts laser beam. The main experimental difficulties related to the operation of such a device are discussed, namely the mechanical implementation at HERA and the conditions to maintain the optical resonance. The experimental setup consists in two separate pieces: an optical bench and a calorimeter located approximately 60 m downstream. Both pieces, together with their related control and readout electronics are also described.

One important point of the optical setup is the control and the measurement of the laser light polarisation, this is the subject of chapter 4. In this chapter, basics of light polarimetry (usually called ellipsometry) are given. We describe the setups used to measure the laser beam polarisation and to create a laser circular polarisation. This is a very important aspect of our polarimeter since the determination of the electron beam polarisation depends directly on the level of the laser circular polarisation. Results of the calibration of a prototype ellipsometer are reported and an estimate of the uncertainty on the laser polarisation measurement is given.

Before reaching the final design of the cavity installed at HERA, a prototype cavity has been built and operated at Orsay. Results of the laser/cavity alignments and performances of the laser power amplification with this prototype are described in chapter 6. I also give the performances of the final cavity that we operated both at Orsay and HERA (without electron beam at the time of writing this document).

An appendix is devoted to electromagnetic calculations related to laser beam propagation in anisotropic plates. This technical work was required in order to reach a high level of accuracy in the determination of the laser polarisation.

Before ending this introduction, I would like to emphasize that this document does not only describe my personal contribution but the work of an entire group. The list of the contributors is: Baroyer, E. Barrelet, W. Beckhusen and his group, C. Berg and his group, R. Bernier, F. Berny, F. Blot, M. Bouchel, V. Brisson, T. Caceres, J. Colin, P. Favre, P. Corona, P. Deck, M. Desmond, H. Hirseman, Y. Holler, M. Jacquet-Lemire, B. Jacquemard, J. Ludwig, F. Marechal, R. Marie, N. Meyners, C. Pascaud, E. Pfuetzenreuter and his group, Y. Queinnec, A. Reboux, D. Richard, P. Rivoirard, C. Ronic, K. Sieber, V. Soskov, T. Szatkowski, S. Trochet, Z. Zhang and the LAL workshop group, the LAL administrative group and myself.

Chapter 1

Polarisation and HERA Upgrade Physics program

With HERA-II, the physics of longitudinally polarised lepton – unpolarised proton scattering at high momentum transfer is opened. Experiments of this kind have been carried out in the past at SLAC [1] and at CERN [2] but on fixed targets and therefore at small transfer momentum. Though their sensitivity to the electroweak parameters was very small, these early precise experiments have confirmed the universality of the Standard Model in lepton-hadron deep inelastic scattering.

With HERA-II, among a large number of physics topics, a high precision electroweak physics program becomes feasible with longitudinally polarised charged lepton-proton deep inelastic scattering. These topics were discussed during a workshop held in 1995-1996 [3] and more recently, new topics related to the Quantum-Chromo-Dynamics were covered in refs. [4, 5]. The experimental advantage of an electron-proton collider experiment, with respect to a fixed target neutrino-nucleus experiment is manifold (see appendix 1.5.1).

Briefly summarising, the use of longitudinally polarised lepton beams allow to pin down chiral couplings, that is the couplings of the quarks to the Z^0 in the Standard Model. In theories going beyond the Standard Model, additional chiral couplings also appear. This is the case for lepto-quarks models or super-symmetry theories with R-parity violation. For these researches, the lepton beam polarisation helps to improve the limits on these couplings and in case of discovery, to discriminate between various theoretical scenarios. Assuming that the Standard Model holds, longitudinally polarised lepton beams also bring new constraints on the parton density functions [4] and on the parton-parton correlation functions [5].

Although the HERA-II physics programme has been extensively discussed in ref. [3], the propagation of the statistical and systematic uncertainties of the polarisation measurement to the physics results were not fully investigated in that document.

This point had to be investigated for the HERA longitudinal polarimeter upgrade proposal [6]. In this context, I have performed a statistical analysis of the effects of the polarisation measurements for three physics topics: determination of the right handed charged current (RH) cross-section, measurement of the charged current (CC) cross-section and determination of the light quark coupling constants to the Z^0 . In addition, I also studied the potential gain obtained by doing the analyses with a polarisation binning. This work is described in detail in the present chapter.

In the following sections, I assume that the reader is familiar with the kinematics and

dynamics of deep inelastic electron-proton scattering. If not, I have included an introduction to this topic in the appendix of this chapter. This appendix describes the unpolarised cross-section measurements and the related structure function physics analyses performed before the HERA-II machine upgrade. For a complete review concerning unpolarised ep deep inelastic scattering, I refer to the Habilitation document of Zhiqing Zhang [7].

1.1 Right Handed Charged Current

The search for right handed charged current (RH CC) in e^-p deep inelastic scattering is one of the most spectacular subjects that one can cover with a longitudinally polarised lepton beam. For a detailed introduction to this search we refer to ref. [8]. Here, it suffices to say that the RH CC is a non standard contribution to the pure V-A coupling of the CC process. In e^-p and e^+p interactions, it is taken into account by writing the observed CC cross-sections in the following way

$$\sigma_{obs,CC}^{e^+}(P) = \frac{1+P}{2}\sigma_{CC}^{e^+} + \frac{1-P}{2}\sigma_{LH}^{e^+} \quad (1.1)$$

$$\sigma_{obs,CC}^{e^-}(P) = \frac{1-P}{2}\sigma_{CC}^{e^-} + \frac{1+P}{2}\sigma_{RH}^{e^-} \quad (1.2)$$

where: $\sigma_{LH}^{e^+}$ and $\sigma_{RH}^{e^-}$ are vanishing in the standard model and represent the RH CC cross-sections; $\sigma_{CC}^{e^+}$ and $\sigma_{CC}^{e^-}$ are the standard CC cross-sections (see eq. 1.24 in appendix 1.5.1) and correspond to the reactions $e_R^+ + p \rightarrow \bar{\nu}_e + X$ and $e_L^- + p \rightarrow \nu_e + X$, respectively.

From eqs. 1.1 and 1.2, one sees that $\sigma_{LH}^{e^+}$ and $\sigma_{RH}^{e^-}$ can be measured by combining e^+ and e^- beam data and/or different polarisation $P > 0$ and $P < 0$. A data sample of beam charge \pm and polarisation $\pm|P|$ will be denoted by $e_{\pm|P|}^{\pm}$ throughout this chapter.

Among the possible cross-section ratios one can build using the four data samples $\{e_{\pm|P|}^{\pm}\}$, the following [8]

$$R_4(|P|) = \frac{\sigma_{obs,CC}^{e^+}(-|P|) + \sigma_{obs,CC}^{e^-}(|P|)}{\sigma_{obs,CC}^{e^+}(|P|) + \sigma_{obs,CC}^{e^-}(-|P|)} \quad (1.3)$$

is sensitive to the RH CC signal. In this expression, the subscript *obs* refers to the measured cross-section at a given value of the lepton beam polarisation P .

Note that, according to the above definition one gets $\sigma_{obs,CC}^{e^+}(P=0) = \sigma_{CC}^{e^+}/2$ in the standard model. Defining further

$$r_4 = \frac{\sigma_{LH}^{e^+} + \sigma_{RH}^{e^-}}{\sigma_{CC}^{e^+} + \sigma_{CC}^{e^-}} \text{ and } \alpha = \frac{1-|P|}{1+|P|} \Rightarrow R_4(|P|) = \frac{\alpha + r_4}{1 + \alpha r_4} \quad (1.4)$$

Notice that in the case where only two data samples $\{e_{\pm|P|}^{\pm}\}$ are available one has [8]

$$R_2(|P|) = \frac{\sigma_{obs,CC}^{e^-}(|P|)}{\sigma_{obs,CC}^{e^-}(-|P|)}, \quad r_2 = \frac{\sigma_{RH}^{e^-}}{\sigma_{CC}^{e^-}} \Rightarrow R_2(|P|) = \frac{\alpha + r_2}{1 + \alpha r_2} \quad (1.5)$$

and an equivalent expression for e^+ .

The value of r

$$r = \frac{R - \alpha}{1 - \alpha R} . \quad (1.6)$$

can then be obtained by measuring R and α .

However, neither the spin nor the charge of the lepton beam will be changed frequently at HERA. A measurement of R_2 (R_4) is then expected to appear after a few years of data taking with all the experimental problems implied by merging such data. With a fast and precise measurement of the lepton beam polarisation it is nevertheless possible to perform another kind of analysis based on a fit to the observed cross-sections themselves as functions of the polarisation P . Writing eq. (1.2) as

$$\sigma_{obs,CC}^{e^-}(P) = \frac{\sigma_{CC}^{e^-} + \sigma_{RH}^{e^-}}{2} - P \frac{\sigma_{CC}^{e^-} - \sigma_{RH}^{e^-}}{2} , \quad (1.7)$$

$\sigma_{RH}^{e^-}$ is determined from a linear fit to the observed cross-section as a function of P . This fit can be performed step by step during data taking if data are acquired during the polarisation rise in order to get a polarisation range from 0 to P_∞ (see chap. 2). The result of this fit is a model independent determination of $\sigma_{RH}^{e^-}$.

In both cases, the accuracy is limited by statistical and systematic errors on the cross-section and on the polarisation measurements. Uncertainties on the CC cross-section measurement, as estimated in H1, are shown in fig. 1.1 as a function of Q^2 and are of the order of a few percent where statistics is large (at high Q^2 , systematics will decrease with an increase of the statistics). As for the polarisation uncertainties, they depend on the polarimeter performance.

The aim of the following studies is to determine what performance is required for the physics analysis. We start by an estimate of the influence of the polarisation's statistical and systematic accuracies on the r measurement (eq. 1.6). Because error propagations to the cross-section measurement (eq. 1.7) are easily handled, the effects of the CC's systematics will be described for this measurement only.

1.1.1 Cross-section ratio: the precision requirement for the polarisation measurement

For the sake of simplicity we shall consider r_2 and R_2 that we shall denote r and R .

Experimentally, the observed cross-sections are derived from the number of events:

$$\sigma_{obs}^{e^-}(P) = \frac{N_{obs,P}^-}{\mathcal{L}_P(e^-)}$$

where $N_{obs,P}^-$ is the number of observed CC events with e^- beam of polarisation P and $\mathcal{L}_P(e^-)$ is the corresponding luminosity.

Statistical uncertainty

The statistical uncertainty of the R 's measurement is therefore given by:

$$\frac{\delta R}{R} = \frac{\delta N_{obs,P}^-}{N_{obs,P}^-} \oplus \frac{\delta N_{obs,-P}^-}{N_{obs,-P}^-} \oplus \frac{\delta \mathcal{L}_P(e^-)}{\mathcal{L}_P(e^-)} \oplus \frac{\delta \mathcal{L}_{-P}(e^-)}{\mathcal{L}_{-P}(e^-)}$$

with $a \oplus b = \sqrt{a^2 + b^2}$. Here the correlations between the polarisation and luminosity measurements are effectively neglected. We therefore already assume that the luminosity monitor and the polarimeter are precise and fast enough to control these correlations (see chap. 2).

Assuming $r = 0$ for the error calculation and the same luminosity for both polarisation samples ($\mathcal{L}_P(e^-) \approx \mathcal{L}_{-P}(e^-)$) one gets

$$\frac{\delta R}{R} = \sqrt{\frac{4}{\sigma_{CC}^2(1-P^2)\mathcal{L}} + 2\left(\frac{\delta\mathcal{L}}{\mathcal{L}}\right)^2}.$$

From eq. 1.6 one further obtains the uncertainty on r :

$$\frac{\delta r}{r} = \frac{[4P\delta R] \oplus [2\sqrt{2}(1-R^2)\delta P]}{(1+P-R(1-P))(P-1+R(1+P))}, \quad (1.8)$$

where the factor $\sqrt{2}$ comes from the fact that there are two independent polarisation measurements having the same uncertainty δP . Substituting the expression of R one further gets:

$$\delta r = \frac{(1+P+r-Pr)^2}{4P}\delta R \oplus \frac{(1-r^2)}{\sqrt{2}P}\delta P,$$

where it is obvious that the larger P , the smaller δr . Fig. 1.2 shows δr as a function of δP for an integrated luminosity of 250 pb^{-1} per data sample and neglecting the statistical uncertainty of the luminosity measurement: in order to be able to neglect the contribution of the polarisation statistical uncertainty one must keep $\delta P < 0.2 \times 10^{-2}$.

In eq. 1.8 the same value $|P|$ has been taken for the positive and the negative beam charge samples. In practice they may differ and eq. 1.8 can easily be modified by defining P_+ for the value of the positive beam charge and P_- for the negative beam charge. In fig. 1.2 δr as a function of δP is shown for $\delta R = 2\%R$ and $P_+ = 0.5$, $P_- = -0.4$ (dashed curve), $P_+ = 0.4$, $P_- = -0.5$ (dotted curve). As expected, δr is very sensitive to P_+ because of the $(1+P)/2$ polarisation weight of eq. 1.2.

The accuracy on the determination of r can be increased, in principle, by considering different values of P . This is possible by measuring the polarisation during the polarisation rise. This possibility will be described in the next section in the context on the cross-section measurement.

Effect of polarisation's systematic uncertainties

Finally, using eq. 1.5 one can also estimate the effect on r of an additive systematic shift $\delta_{add,sys}$ of the polarisation measurement. The simplest case corresponds to $\sigma_{RH} = 0$. In this case $r = 0$ and $R = (1 - |P|)/(1 + |P|)$ where $|P|$ is the polarisation delivered by HERA. However, the “measured” polarisation factor α reads as $\alpha = (1 - |P| + \delta_{add,sys})/(1 + |P| + \delta_{add,sys})$ so that one obtains a fake “measured” value of r :

$$r_{sys} = \frac{\delta_{add,sys}}{2 + \delta_{add,sys}} \approx \frac{\delta_{add,sys}}{2}. \quad (1.9)$$

Therefore, looking at fig. 1.2, it appears to be crucial to keep the systematic uncertainty on the polarisation measurement below $\approx 5 \cdot 10^{-3}$ absolute.

Note that, if instead of an additive systematic shift, one considers a scaling systematic shift $\delta_{sca,sys}(P) \propto P$, then $\alpha = (1 - |P + \delta_{sca,sys}(P)|)/(1 + |P + \delta_{sca,sys}(P)|)$. As a result the systematic shift induced on the determination of r is also given by eq. 1.9 but with an opposite sign.

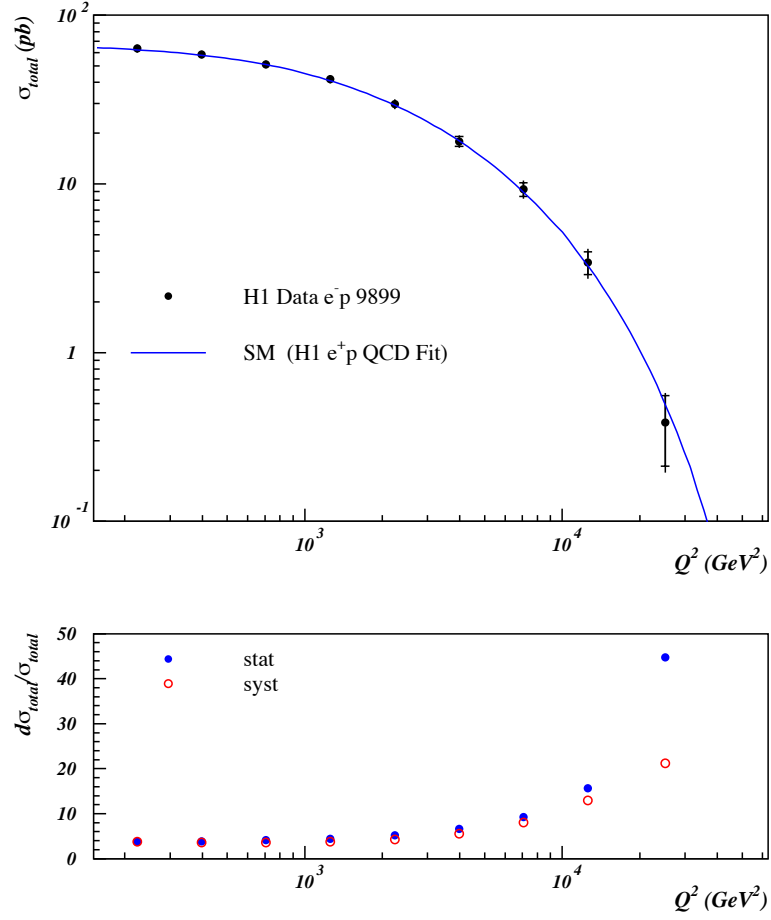


Figure 1.1: Top plot: H1 measurement of $\int_{Q^2}^s (d\sigma^{e^-}/dQ^2) dQ^2$ as a function of Q^2 . Bottom plot: estimates of the statistical and systematic uncertainties. From [23].

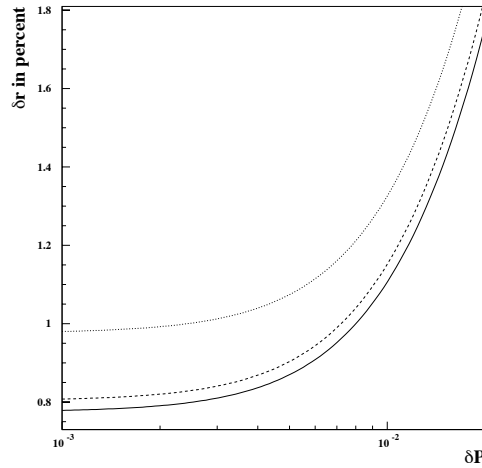


Figure 1.2: *Statistical uncertainty on the determination of r in % (see text) as a function of the statistical uncertainty of P . Full curve: $P_+ = 0.5$ and $P_- = -0.5$; dashed curve: $P_+ = 0.5$ and $P_- = -0.4$; dotted curve $P_+ = 0.4$ and $P_- = -0.5$. Systematics are not taken into account for this figure.*

1.1.2 Absolute cross-section: effect of the polarisation rise

To determine directly the RH CC, a linear fit to $\sigma_{obs,CC}^{e^-}(P)$ can be performed using eq. (1.7). Statistical and systematic uncertainties on the polarisation and $\sigma_{obs,CC}^{e^-}(P)$ measurements can thus be taken simultaneously into account.

Usually one divides the systematic uncertainties in two parts [9, 10]: 1) those which induce correlations between the measurements (usually named “correlated systematics”) 2) those which do not induce correlations between the measurements (“uncorrelated systematics”).

However, in the case of the observed CC cross-section integrated over Q^2 , only one measurement is considered and thus, this distinction doesn’t make sense. Nevertheless two kinds of systematic uncertainties can be distinguished in this case [11]:

- Additive sources, i.e. those which do not depend either implicitly or explicitly on the polarisation: all systematic uncertainties related to the background subtraction (the contamination from the high Q^2 neutral current is in principle polarisation dependent, but this dependence shows up only at very high $Q^2 \approx M_Z^2$). For illustration, effects of an additive systematic shift is shown in the bottom plot of fig 1.3.
- Scaling sources, i.e. those which depend implicitly but not explicitly on the polarisation: all uncertainties which scale with the cross-section measurement, that is all except the additive one in the case of a single measurement (see the top plot of fig 1.3).

In order to perform a quantitative error propagation, we shall consider the situation where $\sigma_{RH}^{e^-} = 0$. This assumption implies that the uncertainty on $\sigma_{RH}^{e^-}$ is related to the

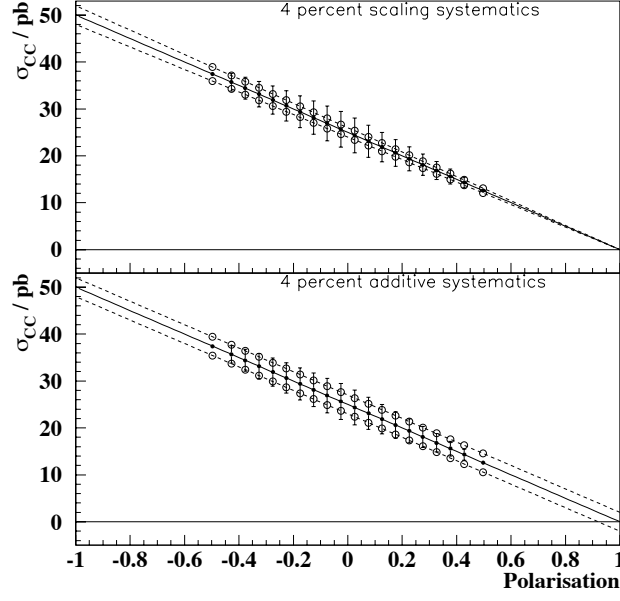


Figure 1.3: Cross-section as a function of polarisation for $\mathcal{L} = 250 \text{ pb}^{-1}$ per beam charge. Full dots show the nominal (unbiased) measurements and error bars are statistical only (see eq. 1.12 together with eq. 1.13 and 1.15). Empty dots show the shifts induced by $\pm 4\%$ scaling (top plot) and $\pm 4\%$ additive (bottom plot) systematic uncertainties. The full lines and the dashed lines are here as guide lines to illustrate how the unbiased and the biased cross-sections behave respectively.

limit of existence of the RH CC. In this case the error propagation is very simple. From eq. 1.7 one can see that the RH CC cross-section is given by extrapolating $\sigma_{obs,CC}^{e^-}(P)$ to $P = +1$ (see fig. 1.3). Therefore, the uncertainty on $\sigma_{RH}^{e^-}$ depends only on the statistical uncertainty and on the additive systematic uncertainties.

In some sense, the search for RH CC is a measurement of the residual background if such a signal doesn't exist. It means that all systematic uncertainty studies related to the CC cross-section measurement must also be performed for all backgrounds. In the case of the CC cross-section these effects are of second order but they are of the first order for the RH CC.

Anticipating section 1.2 one also sees, from eq. 1.7, that the CC cross-section is given by the ordinate intercept at $P = -1$ (see fig. 1.3). Therefore the uncertainty on this quantity depends on statistics and on both, additive and scaling, systematic uncertainty sources (the additive contribution being reduced by constraining the fit to the standard model expectation).

Note that the systematic error propagation is straightforward in these two physics cases. Nevertheless we shall incorporate them in the covariance matrix for sake of completeness.

Fit procedure

The simplest procedure to determine $\sigma_{RH}^{e^-}$ is the χ^2 minimisation. It is defined by

$$\chi^2 = \vec{V} \cdot W \vec{V}, \quad (1.10)$$

with W the inverse of the $n \times n$ (n = number of polarisation bins) covariance matrix and

$$V_i = \sigma_{obs,CC}^{e^-}(\bar{P}_i) - (a\bar{P}_i + b).$$

a and b are the two unknown parameters¹

$$a = -\frac{\sigma_{CC}^{e^-} - \sigma_{RH}^{e^-}}{2}; b = \frac{\sigma_{CC}^{e^-} + \sigma_{RH}^{e^-}}{2}.$$

\bar{P}_i is the averaged polarisation of the i^{th} bin.

a and b are determined by minimising the χ^2 and $\sigma_{RH}^{e^-}$ is finally given by

$$\sigma_{RH}^{e^-} = a + b \quad \text{with} \quad \delta\sigma_{RH}^{e^-} = \sqrt{\vec{\partial}\Sigma \mathcal{M}^{-1} \vec{\partial}\Sigma} \quad (1.11)$$

using standard statistical formula where \mathcal{M} is the 2×2 fit matrix

$$\mathcal{M}_{ij} = \frac{1}{2} \frac{\partial^2 \chi^2}{\partial p_i \partial p_j}; p_1 \equiv a; p_2 \equiv b$$

and $\vec{\partial}\Sigma = (1, 1)$ (i.e. partial derivative of $(a + b)$ by a and b). Note that the χ^2 is a quadratic form of a and b . Hence, since we are only interested in $\delta\sigma_{RH}^{e^-}$, the value of the

¹We shall only perform a model independent analysis, i.e. two parameters are considered. Using further constraints, i.e. fixing $-a = b$ and looking at deviations from the SM predictions leads to a more accurate determination of a limit on the RH CC. This point is described in section 1.2.

χ^2 doesn't enter our calculations. Our estimates of $\delta\sigma_{RH}^{e^-}$ are then also valid for the case $\sigma_{RH}^{e^-} \neq 0$ up to the error treatment which assumes $\sigma_{RH}^{e^-} = 0$.

Instead of $a + b$, $(a + b)/(a - b)$ or $(-b/a)$ could have also been considered. It can be shown that for $\sigma_{RH}^{e^-} = 0$ all error estimates coincide. However, if $\sigma_{RH}^{e^-} \neq 0$, the derivative vector $\vec{\partial}\Sigma$ depends on a and b in the later two cases. Explicit values of a and b (i.e. a model for RH CC) are therefore required to perform the error calculations.

Returning to the calculation of $\delta\sigma_{RH}^{e^-}$, there are two contributions to consider:

- *Statistical uncertainty.* Neglecting for now the systematics, the matrix W is diagonal ($W_{ii} = w_i$) and depends on the luminosity since the statistical precision is estimated from the number of CC events:

$$\delta_{stat}(i) \approx \frac{\sqrt{N_{obs,CC}^{e^-}(\bar{P}_i)}}{\mathcal{L}_i} = \sqrt{\frac{\sigma_{CC}^{e^-}(1 - \bar{P}_i)}{2\mathcal{L}_i}} \quad (1.12)$$

and $w_i = 1/\delta_{stat}^2(i)$. \mathcal{L}_i is the luminosity corresponding to the i^{th} bin, normalised to the total luminosity:

$$\mathcal{L}_i = C \int_{t(P_i)}^{t(P_{i+1})} \mathcal{L}(t) dt, \quad \mathcal{L}(t) = \frac{1}{(1 + 0.42t/5.9)^{1/0.42}}, \quad C = \frac{\mathcal{L}_{TOT}}{\sum_{i=0}^n \mathcal{L}_i}, \quad (1.13)$$

where the following beam (time dependent) life time $\tau_L(t) \approx 0.42 \times t + 5.9$ with t given in hour, has been used as estimated by looking at a typical HERA fill (see fig. 2.5 in chap. 2); $t(P)$ is obtained by inverting the time evolution of the polarisation

$$P(t) = P_\infty [1 - \exp(-t/\tau)] \quad (1.14)$$

with $\tau_P = \tau_{ST}/P_{ST} \times P_\infty$, $\tau_{ST} = 43.2$ min, $P_{ST} = 0.916$ as determined at HERA [12]. It is worth mentioning that the rising curve is not as smooth as eq. 1.14 in reality (see chap. 2). For numerical estimates $\mathcal{L}_{TOT} = 250 \text{ pb}^{-1}$ will be used. This number corresponds to the, optimistic, expected luminosity corresponding to one year of data taking. An average fill duration $t_{max} = 12\text{h}$ will be chosen. In the expression for χ^2 , the value of the polarisation \bar{P}_i is the mean weighted by the luminosity:

$$\bar{P}_i = \frac{\int_{t(P_i)}^{t(P_{i+1})} P(t) \mathcal{L}(t) dt}{\mathcal{L}_i}. \quad (1.15)$$

- *Systematic uncertainties.* For CC, the sources of systematic uncertainties are determined for the whole data sample, so that they do not depend on the polarisation value. Therefore dividing the CC measurements into polarisation bins introduces a correlation between these bins. These effects are taken into account via the covariance matrix [11]:

$$\text{Cov}_{ij} = \delta_{stat}^2(i) \delta_{ij} + \delta_{sca}(i) \times \delta_{sca}(j) + \delta_{add}(i) \times \delta_{add}(j) \quad (1.16)$$

where δ_{ij} stands for the Kronecker symbol, $\delta_{add}(i)$ and $\delta_{sca}(i)$ are the additive and scaling systematic uncertainties respectively. If ϵ_{add} and ϵ_{sca} are the relative additive and relative scaling systematic uncertainties, then

$$\delta_{add}(i) \approx \epsilon_{add} \sigma_{CC}^{e^-}, \quad \delta_{sca}(i) \approx \epsilon_{sca} \frac{1 - \bar{P}_i}{2} \sigma_{CC}^{e^-}.$$

In these expressions the difference between scaling and additive uncertainties is explicit. The additive source is taken to be a fraction ϵ_{add} of a reference data sample of a given beam charge (here $P = -1 \Rightarrow \sigma_{obs} = \sigma_{CC}$): because the “background cross-section” doesn’t depend on polarisation, its contribution is the same in any polarisation bin i . On the contrary, the scaling uncertainty is proportional to the observed CC cross-section (i.e. $\sigma_{CC}^{e^-}(1 - \bar{P}_i)/2$). For numerical estimates ϵ_{add} and ϵ_{sca} will be defined by the quadratic sum of all systematic uncertainties of each type since the measurement is the same in all polarisation bins.

It is worth mentioning that the covariance matrix expression (eq. 1.16) holds only in the case of symmetric systematic uncertainties. Asymmetric systematics require a special treatment [13] which can noticeably modify the results.

In fig. 1.4, $n_{obs,CC}^{e^-}$ is plotted as a function of P_i for two extreme bin widths, 0.5 and 0.01, using the numbers given above and $P_\infty = \pm 0.5$. One first remarks that, because of the polarisation and luminosity time evolution, the bulk of the statistics is located around $\pm|P_\infty|$. The use of the polarisation weighted by the luminosity reduces the maximum polarisation when the bin width is large (0.47 in our simplistic description). Note that because of the low statistics observed in certain bins the χ^2 procedure is not really adequate. The adequate statistical procedure should be the likelihood maximisation which is not considered here.

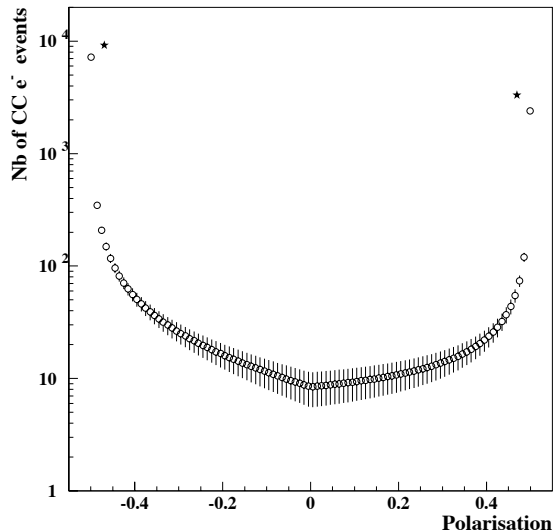


Figure 1.4: Number of events computed using $\sigma_{CC}^{e^-} = 50 \text{ pb}$ as a function of the polarisation for two bin width, $dP = 0.5$ (stars) and $dP = 0.01$ (empty dots). Here two beam polarisation data samples are considered $e_{\pm|P|}^-$ and $|P_\infty| = 0.5$. Each sample represents 250 pb^{-1} . The statistical uncertainties shown in this figures reflect the polarisation build-up curve as specified in the text as well as the luminosity decay during the fill. A luminosity fill duration of 12 h has been considered.

Numerical estimates

To perform numerical estimates of $\delta(\sigma_{RH}^{e^-})$, we choose: $P_\infty = \pm 0.5$ (see eq. 1.14), $\sigma_{CC}^{e^-} = 50$ pb which corresponds to $Q^2 > 10^3$ GeV² (above this threshold the background is below 1%) and an average luminosity fill duration of 12h. As for the systematics we take $\epsilon_{sca} = 0.04$ and $\epsilon_{add} = 0.01$ (the value of ϵ_{add} is not determined in the unpolarised CC analyses, it is estimated from the uncertainty on the background subtraction). These are not exactly the numbers corresponding of the H1 1998-1999 $\sigma_{CC}^{e^-}$ measurement but the systematic error propagation is so simple that any change in the relative additive systematic uncertainty is directly applicable to $\delta(\sigma_{RH}^{e^-})$ (ϵ_{sca} has no effects as we shall see).

Three analyses are performed using:

- $[+/-]$ = two data samples $e_{-|P|}^-$ and $e_{+|P|}^-$;
- $[-]$ = single data sample $e_{-|P|}^-$;
- $[+]$ = single data sample $e_{+|P|}^-$.

For each data sample we take $\mathcal{L}_{TOT} = 250$ pb⁻¹ (there are two times more events in analysis $[+/-]$ than in $[-]$ and $[+]$) and we vary the number of polarisation bins between 1 and 50.

Effect of CC's uncertainties only

The relative uncertainty $\delta(\sigma_{RH}^{e^-})$ has been estimated, for the three analyses, according to the procedure described in the previous sections.

To illustrate such a linear fit, the error band of the $[+/-]$ analysis, when no polarisation bins are used, is shown in fig. 1.5. $\delta(\sigma_{RH}^{e^-})$ is given by the extrapolation of the error band at $P = +1$ and $\delta(\sigma_{CC}^{e^-})$ by the extrapolation at $P = -1$.

Another parameter has been introduced for this study: a timing threshold above which the luminosity and polarisation measurements begin. For now, in the HERMES analyses, only runs with $|P| > 0.4$ are used for physics (below this limit, the polarisation measurement is currently not precise enough). For $|P_\infty| = 0.5$ and using our simplistic polarisation build-up formula, $|P| = 0.4$ is reached at $t = 40$ min. Therefore we show the error estimates as a function of the polarisation bin width for three timing thresholds $t_{cut} = 0, 10$ min (one may not be able to take data at the beginning of the luminosity run) and 40 min.

As a result, $\delta(\sigma_{RH}^{e^-})$ decreases significantly when the polarisation bin width decreases for the $[+]$ and $[-]$ analyses (see fig. 1.6). There is no improvement for the $[+/-]$ analysis as can be seen from fig. 1.7. The reason is that, because of the linearity, no additional information is provided by the polarisation binning when two charge samples are considered.

In order to illustrate the effect of the non-diagonal terms of the covariant matrix (= the correlations), we have repeated the $[+/-]$ analysis by fixing $\text{Cov}_{ij} = 0$ for $i \neq j$. The result is shown in fig. 1.7. Without accounting for these terms, the uncertainty on $\delta(\sigma_{RH}^{e^-})$ is overestimated as well as the influence of the polarisation bin width.

Another study that can be made is the polarisation/depolarisation scenario: once the polarisation growth is finished, the beam is depolarised so that another rise starts again. One can model it by changing the average duration of the run to, say, 2.5 h (it is 12h

for the results given above). The results are shown in fig. 1.6 for the analysis [+]. With this scenario one loses sensitivity for all the analyses since the weight of the largest polarisation value is reduced.

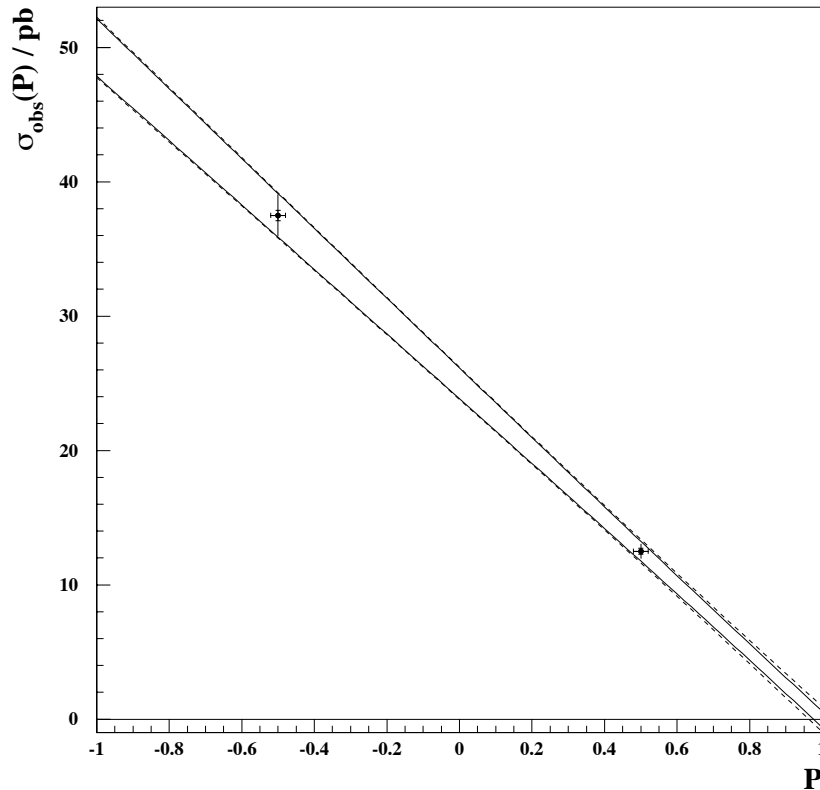


Figure 1.5: *CC cross-section measurement together with the error band computing from the linear fit. Two beam polarisation data samples are considered $e_{\pm|P|}^-$ and $|P_{\infty}| = 0.5$. Each sample represents 250 pb^{-1} . The inner error bar of each data point represents the statistical uncertainty and the outer error bars is obtained by adding quadratically the statistical at the systematic uncertainties. The full curves correspond to the case where the statistical uncertainty on the polarisation measurement is fixed to 0.2% and the dashed curves to 2%.*

Effects of CC's uncertainties and polarisation's statistical uncertainty

The influence of the statistical uncertainty of the polarisation is estimated by adding quadratically $\delta P \times \sigma_{CC}^-/2$ to the diagonal of the covariance matrix (eq. 1.16). The result is shown in fig. 1.8 (see also fig. 1.5). As already stated in section 1.1.1, we also find here that the polarisation's statistical accuracy must be kept at the few per mille level, even when the CC cross section's uncertainties are taken into account. The gain by going from $P_{\infty} = 0.5$ to $P_{\infty} = 0.6$ is also shown. In the same figure another scenario is shown: a sample of $e_{|P_{\infty}|}^-$ corresponding to 250 pb^{-1} and a sample of unpolarised e^- corresponding to the HERA-I data taking are combined. As a result it appears that this

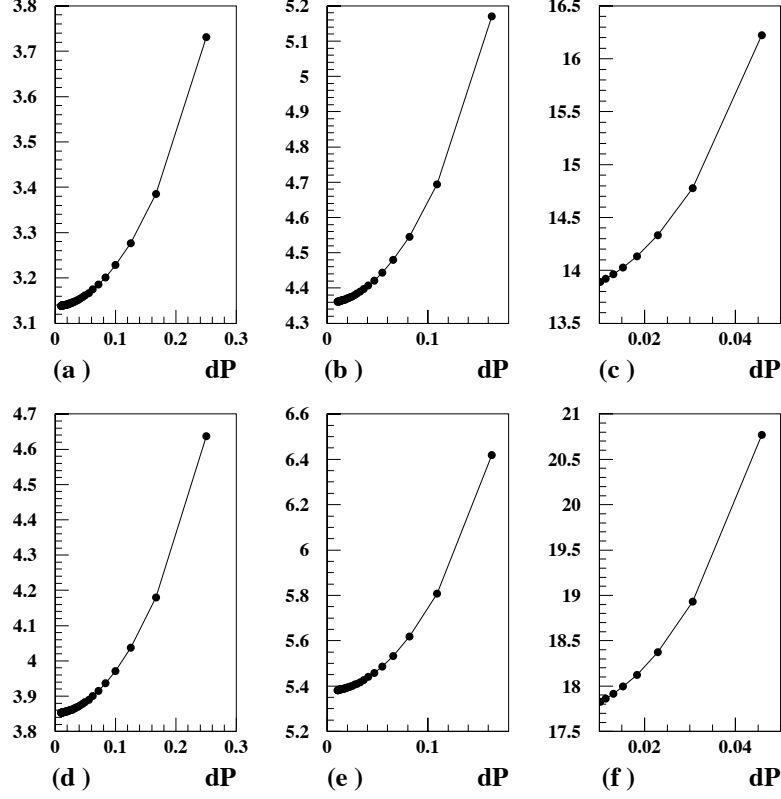


Figure 1.6: All plots show the uncertainty (statistical plus systematics) on $\sigma_{RH}^{e^-}/\sigma_{SM}$ in percent for $Q^2 > 1000 \text{ GeV}^2$ as a function of the polarisation bin width dP . These results are obtained from a χ^2 minimisation for one data sample $e_{\pm|P|}^+$ and $|P_\infty| = 0.5$, corresponding to 250 pb^{-1} . The plots of the first column (a,d) correspond to $t_{cut} = 0$ (see text); the second column (b,e) to $t_{cut} = 10 \text{ min}$; the third column (c,f) to $t_{cut} = 40 \text{ min}$. Plots (a), (b), (c) correspond to an average luminosity fill duration of 12 h and plots (d), (e), (f) to 2.5 h.

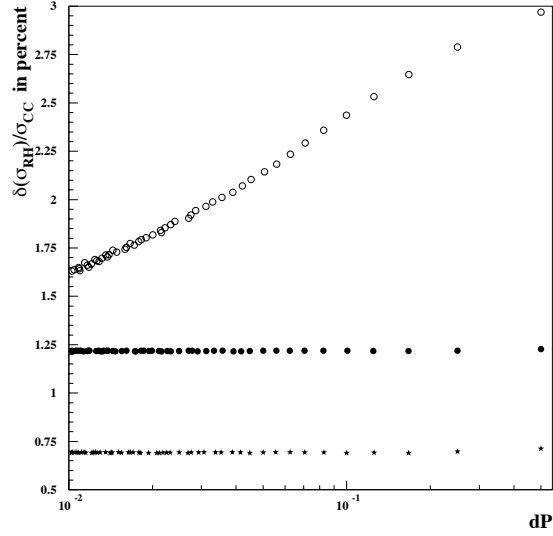


Figure 1.7: Uncertainties on $\sigma_{RH}^{e^-}/\sigma_{SM}$ as a function of the polarisation bin width dP . These results are obtained from a χ^2 minimisation to two data samples $e_{\pm|P|}^-$ with $|P_\infty| = 0.5$, each corresponding to 250 pb^{-1} . The stars show the contribution of the statistical uncertainty; the full dots take into account all systematic uncertainties (see text) and the open circles are the results of the calculations where the non-diagonal terms of the covariance matrix are neglected.

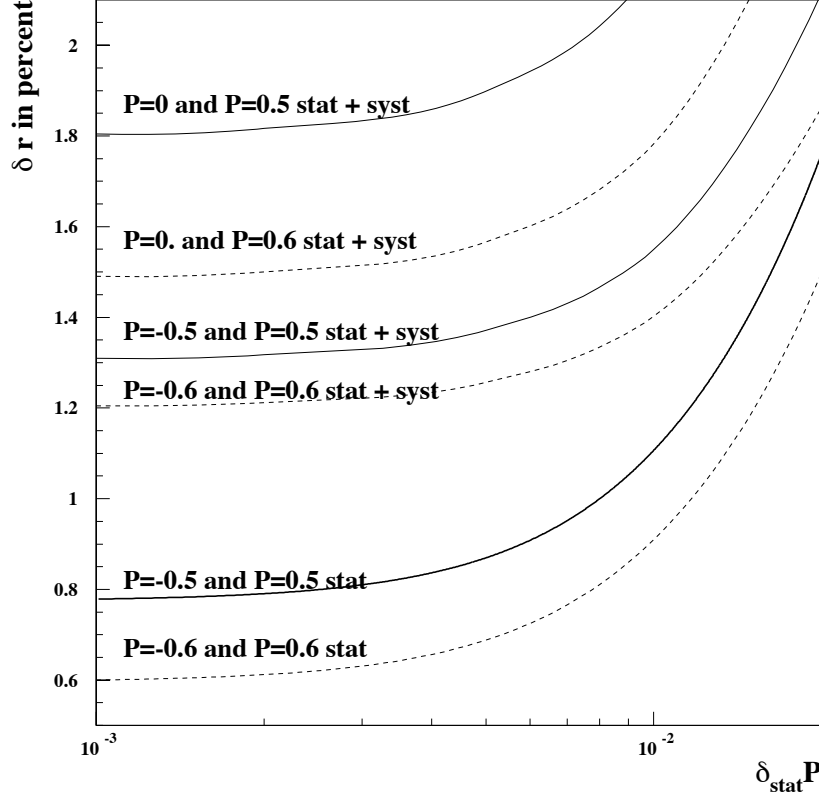


Figure 1.8: Uncertainties on $\sigma_{RH}^{e^-}/\sigma_{SM}$ as a function of the polarisation statistical uncertainty δP . The curves for which the statistical and systematic uncertainties on the CC cross-section are taken into account are obtained from a χ^2 minimisation to the two data samples $e_{\pm|P|}^-$ (for two cases $P = \pm 0.5$ and $P = \pm 0.6$), each corresponding to 250 pb^{-1} . The curves for which only the statistical uncertainty are considered have been determined as explained in section 1.1.1. For comparison, results of the χ^2 fit to the positive polarised and a 100 pb^{-1} unpolarised independent data samples are also shown (=curved denoted by $P = 0$ and $P \neq 0$).

scenario permits a determination of RH CC better than the 2% level. The difference between the analysis $[+/-]$, the optimum case, and this latter scenario decreases as the polarisation $|P_\infty|$ increases.

Effects of CC's uncertainties and polarisation's systematic uncertainties

We finally give an estimate of the effect due to a systematic shift of the polarisation measurement. Minimising the χ^2 (eq. 1.10) by taking the “true” value \bar{P}_i to evaluate $\sigma_{obs,CC}^{e^-}$ and the shifted polarisation $\bar{P}_i + \delta_{add}(P)$ to compute the linear form, it is easy to show that, with $\sigma_{RH}^{e^-} = 0$, one gets the following fake RH CC

$$\delta_{sys}(a+b) = -\delta_{sys}(P)\sigma_{CC}^{e^-}\frac{1}{2}. \quad (1.17)$$

Taking $\delta_{add}(P) = \pm 0.01$, one gets $\delta_{add}(a+b) = \mp 0.25$ pb (i.e. 0.5% relative) using the previous example. This value is very close to the uncertainties estimated above. It is then important to keep the systematic uncertainty on the polarisation below 0.01.

If instead of an additive shift, a scaling shift $\bar{P}_i(1 + \delta_{sca}(P))$ is used, the effect is also given by eq. 1.17.

Model dependent Limit on the RH CC

The present highest limit on the non-standard boson W_R (or W') mass has been determined by the D0 Collaboration from a peak search in the Jacobian distribution [14]. They obtain $M_{W_R} > 720$ GeV at 95 % CL. This is of course a model dependent search since it relies on Monte Carlo distributions where the W width is used for the W_R width. From the expression given in ref. [8] we estimate the limit on M_{W_R} using the measured cross section above a Q^2 threshold Q_{min}^2 by simply integrating the propagators. In order to compare with the D0 result, the left and right couplings are taken to be the same and the mixing angle is neglected (i.e. $g = g'$ and $\zeta = 0$ in the notation of ref. [8]). From the $[+/-]$ analysis discussed above, we obtain:

$$\sigma_{RH}^{e^-} < 2 \times \delta(\sigma_{RH}^{e^-}) \text{ at 95\% CL} \Rightarrow \frac{(M_W^2 + Q_{min}^2)(M_W^2 + s)}{(M_{W_R}^2 + Q_{min}^2)(M_{W_R}^2 + s)} < 2 \times \frac{\delta(\sigma_{RH}^{e^-})}{\sigma_{CC}^{e^-}}. \quad (1.18)$$

Results are shown in fig. 1.9 for $Q_{min}^2 = 1000$ GeV² and various beam polarisation and luminosity values. It will be very hard to reach the D0 limit at HERA. As illustrated in this figure, to approach the D0 limit, a very high luminosity, a very high machine polarisation, a high polarisation accuracy and a complete control of all systematics are required.

However, unlike the Tevatron result, the HERA measurement will provide a model independent cross-section measurement. To illustrate this point, let us take into account the W_R width [15] in eq. 1.18. We obtain

$$\int_{Q_{min}^2}^s \frac{(M_{W_R}^2 + Q^2)^2}{((M_{W_R}^2 + Q^2)^2 + \Gamma_{W_R}^2 M_{W_R}^2)^2} dQ^2 < \frac{2(s - Q_{min}^2)}{(M_W^2 + Q_{min}^2)(M_W^2 + s)} \times \frac{\delta(\sigma_{RH}^{e^-})}{\sigma_{CC}^{e^-}}$$

where the W width has been neglected. Using this expression, limits in the plane (Γ_{W_R}, M_{W_R}) can be computed. They are shown in fig. 1.10 where the uncertainty on the polarisation measurement is neglected.

Values of Γ_{W_R} as large as 200 GeV will not change significantly the limits on M_{W_R} . This is obviously not the case for hadron-hadron colliders.

In addition, it should be mentioned that the W 's are produced in the t channel at HERA while they are produced in the s channel at the Tevatron.

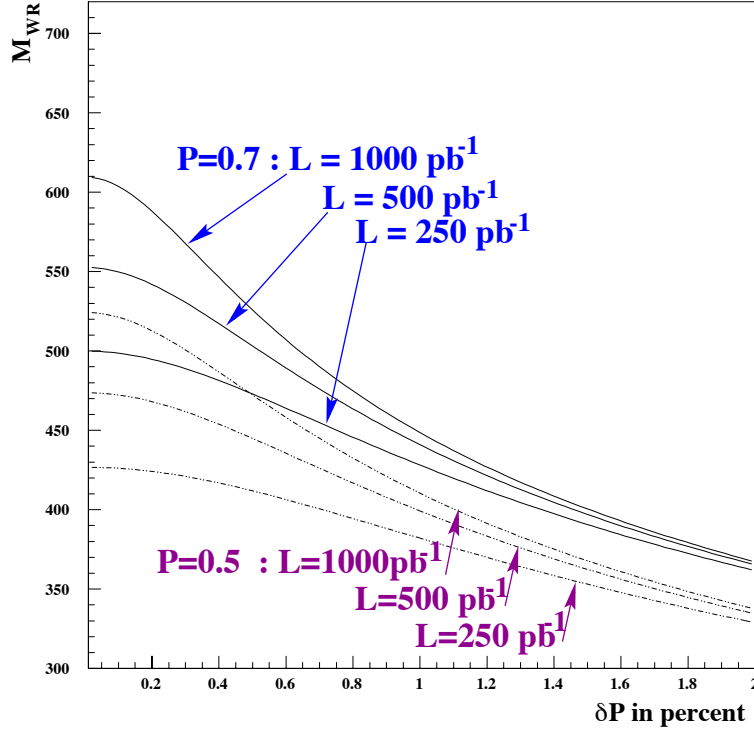


Figure 1.9: 95 % CL limits on M_{W_R} as a function of the statistical precision on the polarisation measurement for: $P = 0.7$ full curves and $P = 0.5$ dashed curves. Uncertainty on $\sigma_{RH}^{e^-}/\sigma_{SM}$ has been computed using eq. 1.8. For each group of curves, the upper one correspond to an integrated luminosity per charge samples of 1000pb^{-1} , the middle one to 500pb^{-1} and the lower one to 250pb^{-1} . Only the statistical accuracy on the CC cross-section measurement has been taken into account.

1.2 Propagation of the polarisation uncertainties to the CC cross-section

The procedure of the previous section can also be used to extract the CC cross-section integrated over Q^2 . In practice one may be more interested in the single or double differential CC cross-section. The qualitative features derived in this section should also apply to these observables.

From a statistical point of view, one can roughly estimate the required precision on the polarisation measurement by considering one data sample and a beam polarisation P :

$$\sigma_{obs}^{e^-} = \sigma_{CC}^{e^-} \frac{1-P}{2} \Rightarrow \frac{\delta\sigma_{CC}^{e^-}}{\sigma_{CC}^{e^-}} = \frac{\delta N_{obs}}{N_{obs}} \oplus \frac{\delta\mathcal{L}}{\mathcal{L}} \oplus \frac{\delta P}{1-P},$$

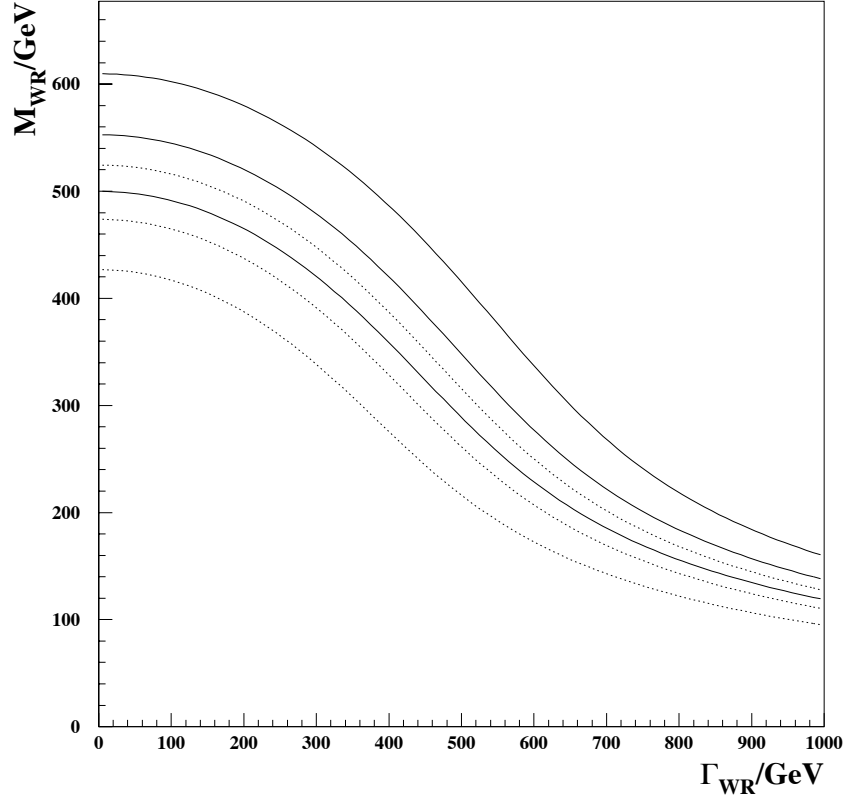


Figure 1.10: 95 CL limits in the plane (Γ_{WR}, M_{WR}) . The six curves correspond to the six experimental conditions of fig. 1.9. Uncertainties on the polarisation measurement are neglected for this plot.

which requires, taking the same numbers as in section 1.1.1, $\delta P < 1\%$.

Concerning the fit procedure, there are two possibilities:

- A two-parameters fit (see fig. 1.5) leading to $\sigma_{CC} = -a + b$. The derivative vector is here $\vec{\partial}\Sigma = (-1, 1)$ (see eq. 1.11).
- A one-parameter fit constraining $b = -a$ leading to $\sigma_{CC} = -2a \equiv 2b$. In this case one has $\delta\sigma_{CC} = 2/\sqrt{\partial^2\chi^2/\partial^2a}$.

Effects of CC's uncertainties only

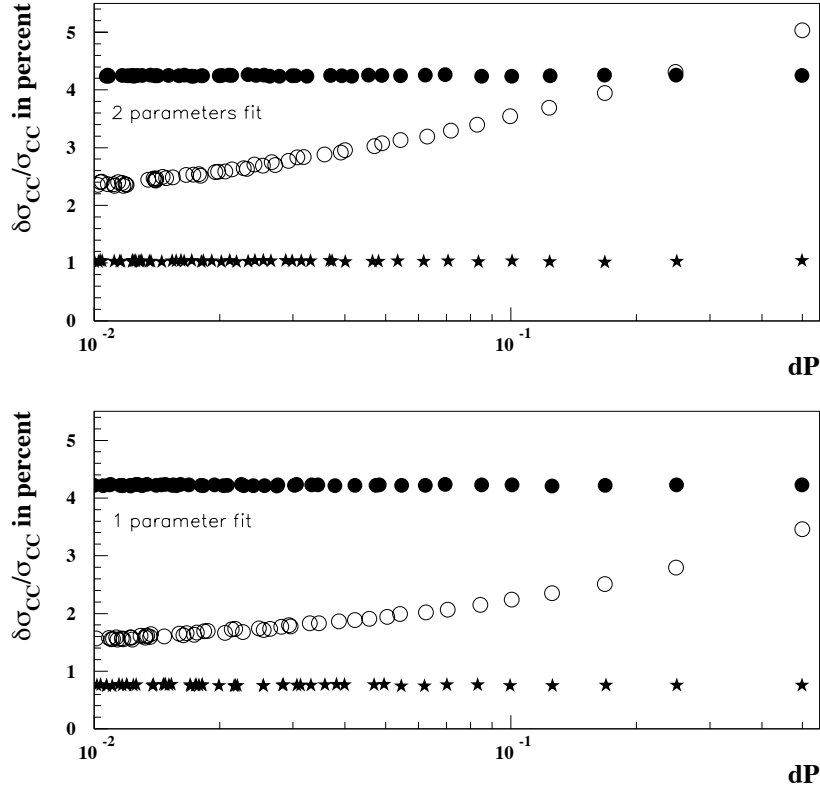


Figure 1.11: Same as fig. 1.7 but for the CC cross-section measurement. The results of the one parameter fit (see text) are shown in the bottom plot and the top plot shows the results of the two parameters fit.

The numerical estimates of the previous section are repeated for these two new fits. Conclusions are the same as in the RH CC case (see section 1.1.2).

The bias obtained by neglecting the non-diagonal terms in the covariance matrix is also shown in fig. 1.11 for the two fits. Here $\delta(\sigma_{CC})$ is underestimated but the polarisation bin width influence is still overestimated. The statistical uncertainty contribution to $\delta(\sigma_{CC})$ is also shown and one can verify that the systematic uncertainty is effectively $\approx 4\% \oplus 1\% = \epsilon_{sca} \oplus \epsilon_{add}$.

As in the previous section, effects due to a systematic shift of the polarisation are estimated. For the two parameters fit one gets the same formula as eq. 1.17 but with an opposite sign. For the one parameter fit one gets

$$\delta_{add}(a) = -\sigma_{CC}^{e^-} \delta_{add}(P) \frac{\sum_{i,j} (1 - \bar{P}_i) W_{ij}}{\sum_{i,j} (1 - \bar{P}_i)(1 - \bar{P}_j) W_{ij}} \quad (1.19)$$

$$\delta_{sca}(a) = -\sigma_{CC}^{e^-} \delta_{sca}(P) \frac{\sum_{i,j} (1 - \bar{P}_i) \bar{P}_j W_{ij}}{\sum_{i,j} (1 - \bar{P}_i)(1 - \bar{P}_j) W_{ij}} \quad (1.20)$$

For a given polarisation shift and for the two analyses $[+/-]$ and $[-]$, the ratios on the right hand side of eq. 1.19 and 1.20 are of the order of $1/2$ (same as in eq. 1.17). For the analysis $[+]$, these factors reach ≈ 2 and ≈ 1 in eq. 1.19 and 1.20 respectively.

It is then also necessary to keep the systematic uncertainties of the polarisation below the percent level to enable a meaningful CC cross-section measurement.

1.3 The neutral currents case: effect of the polarisation rise

Neutral Current (NC) measurements at high Q^2 permit the determination of the quark couplings to the Z^0 [3, 16, 17]:

$$a_q = I_3^q \text{ and } v_q = I_3^q - 2e_q \sin^2 \theta_W$$

where I_3^q is the third component of the weak isospin of the quark flavour q . As usual we shall only distinguish the U ($= u, c$) and down D ($= s, c, b$) type of quarks so that $q = U$ or D in the above equation. Since the u and d contribution dominates at high Q^2 at HERA, the determination of $a_{U,D}$ and $v_{U,D}$ is complementary to the results of LEP heavy flavour measurements.

The NC cross-section $d^2\sigma/dxdQ^2$ depends on the lepton charge and on the polarisation at high Q^2 . Its expression is lengthy and can be found in ref. [18, 19]. We shall follow the work described in this article but in a much more simplified form. The reason is that we are looking at the gain of an analysis performed in bins of polarisation with respect to the same analysis performed with only two polarisation states $\pm|P|$. Our simplified procedure is the following

- the Born cross-section is used to compute $d^2\sigma/dxdQ^2$ (= no Monte Carlo generation is performed) for $Q^2 > 1000 \text{ GeV}^2$
- the x and Q^2 bins of [10] are chosen so that the statistical error is estimated (by mean of the average theorem) to be

$$\delta_{stat}(d^2\sigma) = \sqrt{\frac{d^2\sigma}{\mathcal{L} \Delta_x \Delta_{Q^2}}}$$

where $d^2\sigma$ stands for $d^2\sigma/dxdQ^2$; Δ_x and Δ_{Q^2} are the bin widths and x ($x = 0.02, \dots, 0.65$) and Q^2 ($Q^2 = 1000, \dots, 30000 \text{ GeV}^2$) the bin centres.

- A χ^2 is computed: $\chi^2 = \chi_{e^+}^2 + \chi_{e^-}^2$ with

$$\chi_{e^\pm}^2 = \sum_{i,x,Q^2} \frac{[d^2\sigma^{e^\pm}(\bar{P}_i; \delta a_q, \delta v_q) - d^2\sigma_{SM}^{e^\pm}(\bar{P}_i)]^2}{[\delta_{stat}(d^2\sigma^{e^\pm})]^2} \quad (1.21)$$

and $q = U, D$. In eq. 1.21 the “measurement” is $d^2\sigma_{SM}^{e^\pm}(\bar{P}_i)$ and the “theory” is $d^2\sigma^{e^\pm}(\bar{P}_i; \delta a_q, \delta v_q)$. The unknown parameters δa_U , δa_D , δv_U and δv_D are defined by

$$a_q = a_{q,SM} + \delta a_q \quad , \quad v_q = v_{q,SM} + \delta v_q$$

where the subscript SM stands for Standard Model. Here $d^2\sigma_{SM}$ is the “measurement” (i.e. $\delta a_q = 0$ and $\delta v_q = 0$) so that $\chi^2 = 0$ when the fit parameters vanish since the “measurements” are not smeared (we checked that applying a Gaussian smearing doesn’t change the results).

As in the previous section we define a polarisation binning. We have considered, as in [19] an integrated luminosity of 250 pb^{-1} per type of beam and per polarisation sign. Taking $P = 0.7, 0.5$ and fixing a_U v_U (a_D and v_D fixed) we obtain, using MINUIT, the 1σ contour plot shown in fig. 1.12. It is astonishingly close to the result of ref. [19] which includes electroweak higher order effects and detector simulation. The same kind of agreement is obtained for a_D and v_D (a_U and v_U fixed) and for the fit where the four couplings are free.

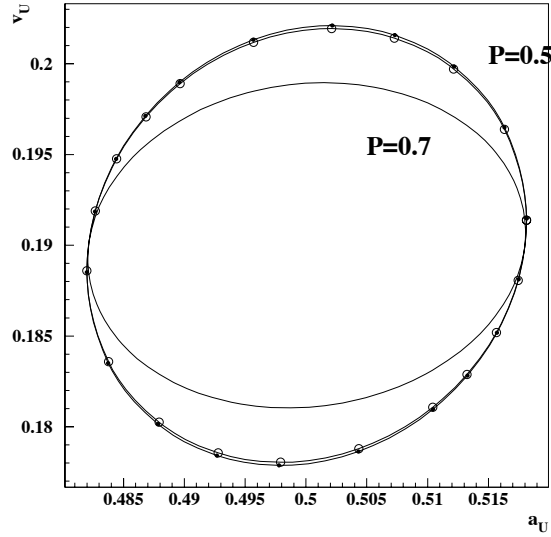


Figure 1.12: 1σ contour plot for v_U , a_U (v_D , a_D fixed) and $P_\infty = 0.7$ (inner curve), $P_\infty = 0.5$ (outer curves). The full dots indicate the result obtained with four data samples $e_{\pm|P|}^\pm$ and the open circles show the results obtained using the same data samples but in bins of polarisation (10 bins of width 0.05). As in ref. [3] (p. 185), we have considered 250 pb^{-1} for each data samples.

As a result, when the four data samples $e_{\pm|P|}^{\pm}$ are included in the fit we find no significant differences between the fit with or without polarisation binning (see fig. 1.12). Even with a fine binning such $dP = 0.01$.

We have finally studied the effect of a systematic uncertainty on the polarisation measurement: in eq. 1.21 the “true” polarisation \bar{P}_i is used to compute $d^2\sigma_{SM}(\bar{P}_i)$ and it is shifted by $\delta_{sys}(P)$ to compute $d^2\sigma$. Then the fit is repeated. The resulting shifts of the couplings are shown in figs. 1.13 and 1.14 for $\delta_{sys}(P) = \pm 0.01$ and ± 0.02 . From these figures we conclude that it is crucial to control any systematic uncertainties at a level below 0.01. This is particularly important for the up quark couplings since the future HERA-II measurement will provide a precision comparable with LEP [20] as shown in fig. 1.15. In addition, the HERA-II and LEP measurements are complementary since the couplings to the heavy quarks c and b are determined at LEP.

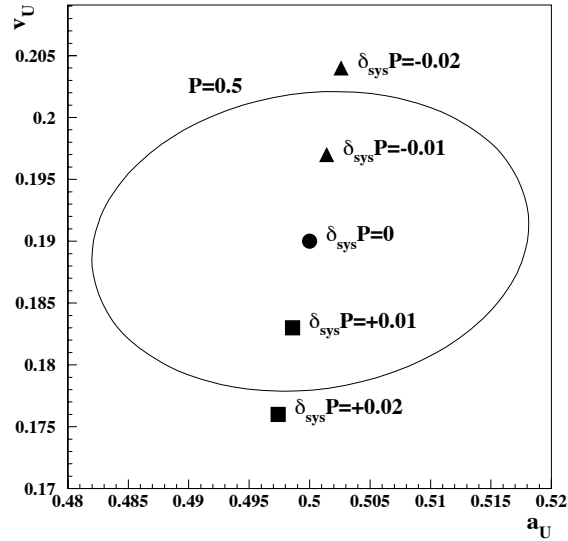


Figure 1.13: The full curve shows the 1σ contour plot for v_U , a_U (v_D , a_D fixed) and $P = 0.5$ assuming a perfect polarisation measurement. The points show the ellipse centre shift observed when the polarisation is shifted by the values indicated on the plot. We have taken 250 pb^{-1} for each of the four data samples $e_{\pm|P|}^{\pm}$. The uncorrelated systematic uncertainties are not taken into account.

1.4 Summary

The precision required for the polarisation measurement at HERA-II has been estimated for three topics, the RH CC, the CC cross-section measurement and the extraction of the quark electroweak couplings. As a result a statistical precision and a systematic precision better than 0.01 (absolute) are needed.

We have shown that with only one beam charge and polarisation data sample, $e_{-|P|}^-$ or $e_{+|P|}^+$, the smaller the polarisation bin width, the better the statistical uncertainty on

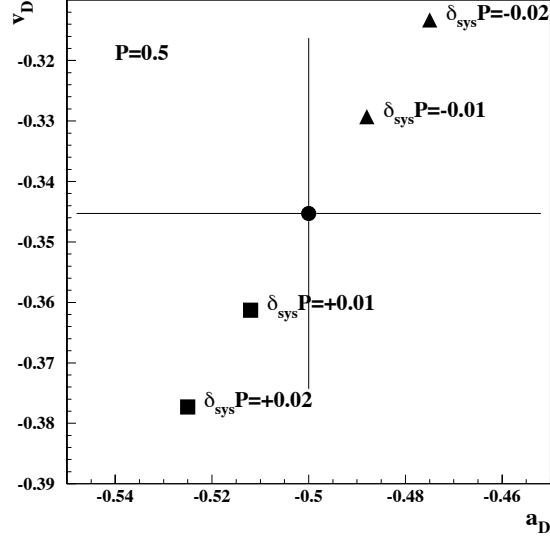


Figure 1.14: The error bars show v_D , a_D (v_U , a_U fixed) obtained by the fit with $P = 0.5$ and a perfect polarisation measurement. The points show the central value shift observed when the polarisation is shifted by the values indicated on the plot. We have taken 250 pb^{-1} for each of the four data samples $e_{\pm|P|}^{\pm}$. The uncorrelated systematic uncertainties are not taken into account.

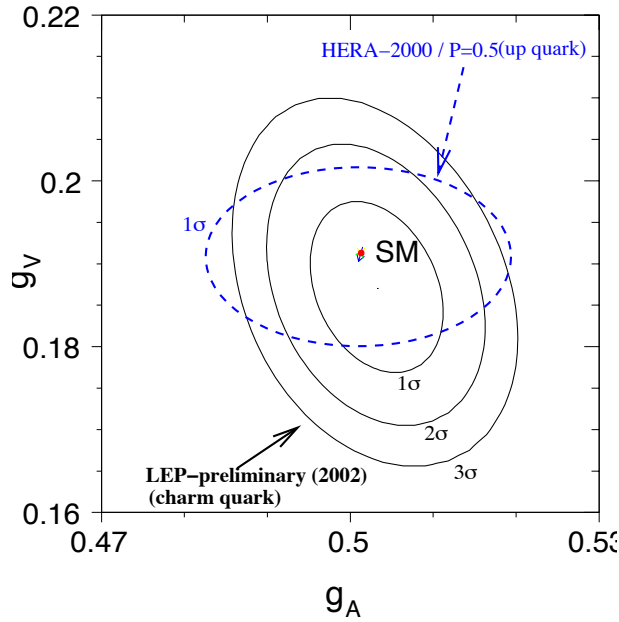


Figure 1.15: Same as fig. 1.12 with the latest LEP results.

the measurements of RH CC and CC cross-sections. To some extent these features also apply for the electroweak coupling determination.

Let us stress that throughout this chapter we have assumed that the luminosity and the polarisation are uncorrelated. As it will be shown in chap. 2, this is only true when the polarisation is measured bunch by bunch within one minute approximately.

1.5 Appendix

In this appendix, an introduction to the deep-inelastic electron-proton scattering is given. This text is an updated and slightly modified version of a long proceeding written for the Ringberg Workshop on the new trends in HERA physics (1999).

1.5.1 Introduction

In the Deep Inelastic Scattering (DIS) processes observed at HERA, a lepton $\ell = e^\pm$ of 27.5 GeV interacts with a proton P of 920 GeV yielding a lepton ℓ' and a set of hadrons X in the final state. Following the nature of ℓ' the interaction proceeds via a neutral ($\ell' = e^\pm$) current (NC) or a charged ($\ell' = \nu_e, \bar{\nu}_e$) current (CC). DIS events are collected in the H1 and ZEUS experiments [21] which are located at the two $e^\pm P$ interaction points of HERA.

The kinematics of the DIS inclusive processes, $\ell(k) + P(p) \rightarrow \ell'(k') + X$, is determined by two independent kinematic variables, besides the energy of the incoming lepton and proton. One usually chooses them among the four Lorentz invariants²

$$Q^2 \equiv -q^2 = -(k - k')^2, \quad x = \frac{Q^2}{2p \cdot q}, \quad y = \frac{p \cdot q}{p \cdot k}, \quad W^2 = (q + p)^2.$$

At HERA energies, one can neglect the lepton and proton masses so that the useful relation $Q^2 = xys$ holds. These kinematic variables are obtained experimentally by measuring the momentum and/or the hadronic energy, the direction of the scattered lepton and/or the hadronic energy flow.

In this Appendix we shall restrict ourselves to the cross-section measurements at HERA in the medium $1.5 \text{ GeV}^2 \leq Q^2 < 150 \text{ GeV}^2$ and high $150 \text{ GeV}^2 \leq Q^2 \leq 30000 \text{ GeV}^2$ domains of the DIS regime. During the past, a large number of precise measurements have been performed in the medium Q^2 region by fixed target experiments [22]. With HERA, three major improvements may be noticed:

- an extension of the Q^2 domain to very high Q^2 (10^4 GeV^2) but also to very small x ($\approx 10^{-6}$) (see fig. 1.16);
- an almost hermetic (4π) detection of the final state leading to the determination of the energy and angle not only of the scattered lepton but also of the produced hadrons;
- an over constrained determination of the kinematic variable;
- from the previous items it follows that the detection of both NC and CC is feasible in the same detector and during the same data taking period;

The somewhat arbitrary distinction between medium and high Q^2 is related to different physics interests. In both regions perturbative Quantum-Chromo-Dynamics (pQCD) describe the HERA data [26, 27]. The pQCD analysis of medium Q^2 data is part of a long

²In the so called 'naive quark' model, x is the proton momentum fraction carried by the struck quark. In the reference frame where the proton is at rest, y is the inelasticity (=fraction of the incident electron energy transferred to the proton). W is the invariant mass of the final state hadronic system X .

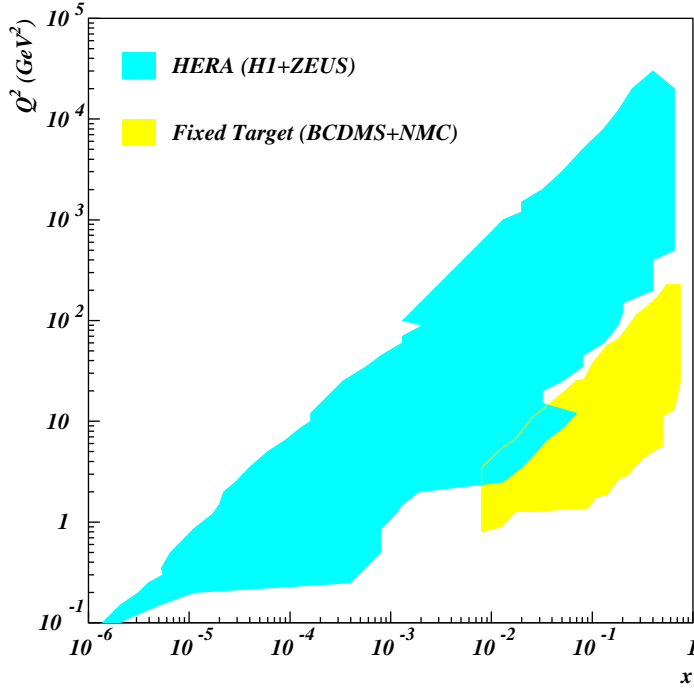


Figure 1.16: Comparison of the HERA and fixed target kinematic domains. From [23]

tradition [30] from which the parton distributions of the nucleon and the strong coupling constant α_s have been extracted. On top of that, very high Q^2 ($\approx M_Z^2$) NC and CC data open a field of research in electroweak physics.

The rest of this appendix is organized as follows. In section 1.5.2 the measurements of NC and CC differential cross-sections are described. Section 1.5.3 is devoted to a phenomenological analysis of these measurements.

1.5.2 Measurement of NC and CC cross-sections

Neutral current events, at medium and high Q^2 , are basically identified by the presence of an electron (or a positron) in the final state. This is done by using tracking and calorimetric devices covering the range $7^\circ < \theta_e < 177^\circ$ and $E'_e > 4$ GeV (at HERA the forward direction $\theta_e = 0^\circ$ corresponds to the direction of the incoming proton).

The differential cross-section measurement is done by counting the number of events within a kinematic interval in, say x and Q^2 . Therefore one of the experimental problems is to achieve a good reconstruction of these kinematic variables from the detector information. Both H1 and ZEUS, can use the outgoing lepton and hadronic final state information, namely polar angles, momenta and deposited energies. It is then possible to define the kinematics of each event by using different (and independent) combinations of experimental information.

In ZEUS the double angle method [24] is used

$$Q_{da}^2 = 4E_e^2 \frac{\sin \gamma_h (1 + \cos \theta_e)}{\sin \gamma_h + \sin \theta_e - \sin(\gamma_h + \theta_e)}, \quad y_{da} = \frac{\sin \theta_e (1 - \cos \gamma_h)}{\sin \gamma_h + \sin \theta_e - \sin(\gamma_h + \theta_e)}$$

$$x_{da} = \frac{E_e \sin \gamma_h + \sin \theta_e + \sin(\gamma_h + \theta_e)}{E_p \sin \gamma_h + \sin \theta_e - \sin(\gamma_h + \theta_e)}.$$

The hadronic polar angle γ_h is defined by $\tan \gamma_h/2 = \sum_i (E_i - p_{z,i})/P_{t,h}$, where E_i and $p_{z,i}$ are the energy and longitudinal momentum of the final state hadron i and where $P_{t,h}$ is the total transverse momentum of the hadronic final state particles.

Since $dx/x = 1/y dE'_e/E'_e$, the electron method is used in H1 to determine Q^2 and x :

$$Q_e^2 = \frac{(E'_e)^2 \sin^2 \theta_e}{1 - y_e}, \quad y_e = 1 - \frac{E'_e}{E_e} \sin^2(\theta_e/2)$$

for $y > 0.15$, while for $y \leq 0.15$ the Σ method [25] is used

$$Q_\Sigma^2 = \frac{(E'_e)^2 \sin^2 \theta_e}{1 - y_\Sigma}, \quad y_\Sigma = \frac{\sum_i (E_i - p_{z,i})}{\sum_i (E_i - p_{z,i}) + E'_e (1 - \cos \theta_e)}.$$

The reason for the differences between the methods used by H1 and ZEUS are related to the calorimeter performances: H1 possesses finely segmented electro-magnetic calorimeters and ZEUS a very good hadronic calorimetry.

The redundancy in the determination of the kinematic variables is a crucial point and presents many advantages: minimization of the migration between the ‘true’ and the measured kinematic variable by choosing one particular method; cross calibration of the various calorimeter devices, and studies of photon radiation from the lepton line by comparing leptonic and hadronic information.

Once the collected events are gathered in x - Q^2 bins, besides the subtraction of photoproduction background, correction factors are applied for: the efficiency of the event selection; detector acceptance; wrong reconstruction of the kinematics due to detector effects, and the contribution of higher order electroweak processes. When possible, these correction factors are determined and/or cross checked from the data themselves. If this is not possible, then they are determined from a full simulation of the DIS and background processes including the detector response.

For the medium Q^2 data we shall describe the results of the high statistics 1996-1997 data analysis [26]. For high Q^2 , e^\pm beam data published in ref. [27] will be presented.

At medium Q^2 and for the H1 measurements, the main systematic uncertainties are: the electron energy scale ($\approx 0.3\%$), the hadronic energy scale ($\approx 2 - 3\%$), the electron polar angle (≈ 0.3 mrad), the photoproduction background at high- y only ($\approx 3\%$ effect on the measurements) and the correction factors (see above) applied to the data (each one is of the order of 1-2%). The overall data normalization (including the luminosity measurement) uncertainty is 1.5 %. The systematic uncertainty is, in total, of the order of 3% and is larger than the statistical uncertainties which are at the level of 1 % for $Q^2 < 100$ GeV².

At high Q^2 the systematic uncertainties are similar. In ZEUS the statistic and systematic uncertainties amount to 3-5% for the kinematic range $400 \text{ GeV}^2 < Q^2 < 30000 \text{ GeV}^2$ considered in the analysis.

In charged current (CC) events, the outgoing neutrino escapes the detection. Such events are then characterized by missing transverse energy $p_{t,miss}$ (the analysis cut is $p_{t,miss} > 12$ GeV).

For the reconstruction of the kinematic variables, one can only use information from the hadronic final state, i.e. the Jacquet-Blondel method [28], giving,

$$y_{JB} = \frac{\sum_i (E_i - p_{z,i})}{2E_e}, \quad Q_{JB}^2 = \frac{p_{t,miss}^2}{1 - y_{JB}}.$$

The CC event statistics is still low, ≈ 900 events for $Q^2 > 400$ GeV² in ZEUS (and similar numbers for H1). However the systematic uncertainty, for both experiments, is dominated by the hadronic energy scale, which induces an effect of the order of 10%, except at very high Q^2 and very high x where the effect is above 20%. Other systematic sources related to the $p_{t,miss}$ cut, acceptance correction and photoproduction background subtraction (in the lowest Q^2 bins) lead to measurement uncertainties between 4% and 8%.

1.5.3 Phenomenological analysis of inclusive measurements at HERA

As mentioned in the introduction, we shall distinguish the phenomenological analysis of the medium Q^2 data from the high Q^2 data. As we are interested in the HERA data, it should be noted that we are considering the region of large $W^2 \gg 10$ GeV². Therefore, we will not be concerned by the non-perturbative effects and the higher twist effects appearing in the small W^2 region so that the symbol pQCD, appearing below, refers to the leading twist of pQCD.

For all the mathematical details which cannot be given here we refer to ref. [29] and references therein.

Analysis of the medium Q^2 NC data

In the one boson exchange approximation, the NC differential cross-section reads

$$\frac{d\sigma^{e^\pm p}}{dx dQ^2} = \frac{2\pi\alpha_{em}Y_+}{xQ^4}\sigma_r, \quad \sigma_r = F_2(x, Q^2) - \frac{y^2}{Y_+}F_L(x, Q^2) \mp \frac{Y_-}{Y_+}xF_3(x, Q^2), \quad (1.22)$$

where $Y_\pm = 1 \pm (1 - y)^2$. The nucleon structure functions are modelled using the quark-parton model and pQCD. In the so called naive parton model one writes

$$F_2(x) = \sum_{i=1}^{n_f} A_i(Q^2)x[q_i(x) + \bar{q}_i(x)], \quad F_3(x) = \sum_{i=1}^{n_f} B_i(Q^2)[q_i(x) - \bar{q}_i(x)]$$

where q_i (\bar{q}_i) is the density function of the quark (anti-quark) of flavor i , n_f is the number of active flavors and $F_L = 0$ in the quark parton model. The functions A_i [18, 30] depend on the electric charge e_i ($A_i = e_i^2$ for $Q^2 \ll M_Z^2$) and embody the effects of the Z exchange and $\gamma - Z$ interference in their Q^2 dependence. The same holds for the functions B_i [30] except that they vanish at $Q^2 \ll M_Z^2$.

Going beyond the simple parton model, higher order contributions in α_s are taken into account. In doing so, mass singularities appear in the initial state of DIS processes

and cannot be regularised without resumming the whole perturbative series. This resummation is done in a restricted kinematic region where $\alpha_s \log Q^2$ is large [29]. This latter region is defined by $Q^2 \gg \Lambda^2 \approx 0.3^2 \text{ GeV}^2$, and the pCDQ calculations are safe for Q^2 above a few GeV^2 . In this domain, the parton density functions (pdf) are given by the solution of the DGLAP equations [29]:

$$\begin{aligned} M_F \frac{\partial q_{i,NS}^\pm(x, M_F^2)}{\partial M_F} &= P_{NS}^\pm \otimes q_{i,NS}^\pm(x, M_F^2) \\ M_F \frac{\partial}{\partial M_F} \begin{pmatrix} \Sigma(x, M_F^2) \\ g(x, M_F^2) \end{pmatrix} &= \begin{pmatrix} P_{qq} & n_f P_{qg} \\ P_{gq} & P_{gg} \end{pmatrix} \otimes \begin{pmatrix} \Sigma(x, M_F^2) \\ g(x, M_F^2) \end{pmatrix} \end{aligned} \quad (1.23)$$

with $A \otimes B \equiv \int_x^1 A(z)B(x/z)dz/z$ and where $\Sigma = \sum_{i=1}^{n_f}(q_i + \bar{q}_i)$ is the singlet quark density, $q_{i,NS}^- = q_i^- \equiv q_i - \bar{q}_i$ and $q_{i,NS}^+ = q_i + \bar{q}_i - \Sigma/n_f$ are the two non singlet densities and g is the gluon density. The splitting functions $P_{i,j} = \alpha_s(M_R^2)P_{i,j}^{(0)} + \alpha_s^2(M_R^2)P_{i,j}^{(1)}$ describe the branching of parton j from parton i , and they can be computed with pQCD up to the second order. In eq. (1.23) M_F is the factorization scale (below which the mass singularity is resummed) and M_R is the renormalisation scale (related to the ultra-violet singularity). As the two scales must be chosen somehow arbitrarily, a natural choice for M_F is $\sqrt{Q^2}$, i.e. the virtual mass of the probe. We shall, as usual, also set $M_R = M_F$ for convenience. It is worth mentioning that the DGLAP equations are universal, i.e. that they are independent of the specific hard process.

Eq. (1.23) embodies the mass singularity resummation and therefore it only describes the so called light parton, i.e. the parton of flavour i and mass m_i such that $m_i^2/Q^2 \ll 1$. In the medium Q^2 range one can take the gluon, the up, down and strange quarks as the light partons. For the heavy quarks (charm and beauty) one needs to specify a particular scheme. We have chosen the fixed-flavor-scheme (FFS) [31] – suitable in the HERA medium Q^2 range – where beauty is neglected, and where the charm contribution is computed from the boson-gluon-fusion process $\gamma g \rightarrow c\bar{c}$ plus the α_s^2 corrections. In this scheme charm is produced ‘outside’ the hadron. The relation between the pdfs and the structure functions depends on the renormalisation scheme. In Next-to-Leading-Log-Approximation (NLLA) and in the $\overline{\text{MS}}$ scheme one obtains:

$$\begin{aligned} F_i(x, Q^2) &= x \sum_{j=1}^{n_f} \left[\left(1 + \frac{\alpha_s(Q^2)}{2\pi} C_{j,q} \right) \otimes e_j^2(q_j(x, Q^2) + \bar{q}_j(x, Q^2)) \right. \\ &\quad \left. + 2 \frac{\alpha_s(Q^2)}{2\pi} C_{j,g} \otimes g \right] + F_i^{c\bar{c}}(x, Q^2) \end{aligned}$$

for $n_f = 3$ and where $i = 1, 2$ (there is a similar expression for F_3 with $F_3^{c\bar{c}} = 0$); $C_{j,q}$ and $C_{j,g}$ are the coefficient functions depending on the hard process; $F_i^{c\bar{c}}$ is the charm contribution [32]. It suffices here to say that it depends on m_c^2 and on a renormalisation scale that we choose to be $\sqrt{m_c^2 + Q^2}$. Note that $F_L = F_2 - 2xF_1 \neq 0$ in the NLLA.

To solve the system of integro-differential equations (1.23), one must provide some initial conditions, i.e. some input functions of x at a given Q^2 for each pdf. Since these functions reflect some unknown non-perturbative mechanism, they must be parameterized with the help of a set of parameters. As we shall see below, these parameters are determined by comparing the calculations to the experimental data.

Concerning the data-theory comparison, from which the input pdfs have to be determined, both H1 and ZEUS use a χ^2 minimization procedure. The main steps of the fitting procedure are summarized below. For each iteration:

1. the pdfs are parameterized at a given value of Q^2 denoted Q_0^2 , chosen to be 7 GeV² in the ZEUS fit and 4 GeV² in the H1 fit,
2. the DGLAP equations are solved numerically in the x -space [33].
3. the evolved pdfs are convoluted with the coefficient functions to obtain the structure functions.
4. Assuming that all experimental uncertainties are normally distributed a χ^2 is computed. A crucial point of the analysis is the χ^2 expression which permits the use of the correlations introduced by some of the systematic uncertainties. Details can be found in ref. [9].

Further details on the fit can be found in the H1 publication of ref. [26]. The result of the H1 fit is shown in fig. 1.17 together with the data. The agreement between data and pQCD is excellent. The gluon density obtained from this fit is shown in fig. 1.18. The error bands of the gluon density include the experimental error propagation as defined in ref. [9] and a theoretical uncertainty which includes the variation of all the fit ingredients (charm mass, Q_0^2 , data rejection cuts, parameterisation forms, α_s , experimental error treatment). The theoretical uncertainties are now dominating the determination of gluon momentum xg , i.e. the third order splitting functions are needed.

Analysis of the high Q^2 NC and CC data

The fits applied to the high Q^2 data differ from the one described in the previous section by a different calculation of the contribution of the heavy quarks to the structure functions. As $m_c \approx 1.5$ GeV, one has $m_c/Q^2 \ll 1$ at high Q^2 . The large term $\alpha_s^n \log^n(Q^2/m_c^2)$ – dominating the calculation of $F_2^{c\bar{c}}$ – must be resummed already at $Q^2 \approx 20$ GeV². The massless scheme is therefore used and only data with $Q^2 \geq 10$ GeV² are included in the fit ³. In the massless scheme, charm and beauty are considered as partonic constituents of the proton and their density functions are obtained by solving the DGLAP equations with the initial conditions $c(x, Q^2 \leq m_c^2) = 0$ and $b(x, Q^2 \leq m_b^2) = 0$. Such fits describe the HERA NC and CC (see figs. 1.19 and 1.21) data above $Q^2 = 10$ GeV².

In fig. 1.19 one can observe the different behavior of e^-p and e^+p cross-sections at very high Q^2 . This is related to the different sign of the contributions of F_3 to σ_r . Fig. 1.20 shows $d\sigma/dx$ together with the results of two pQCD fits including or not the Z exchange and $\gamma - Z$ interference. With the present data, sensitivity to electroweak effects in NC is for the first time observed at HERA.

Up to now we have only described the NC cross-sections and related structure functions. For CC processes, in the one boson exchange approximation, one has

$$\frac{d\sigma_{CC}^{e^\pm p}}{dx dQ^2} = \frac{G_F^2}{2\pi x} \frac{M_W^4}{(M_W^2 + Q^2)^2} \Phi_\pm(x, Q^2), \quad (1.24)$$

³This Q^2 threshold is indicative and it can be lowered

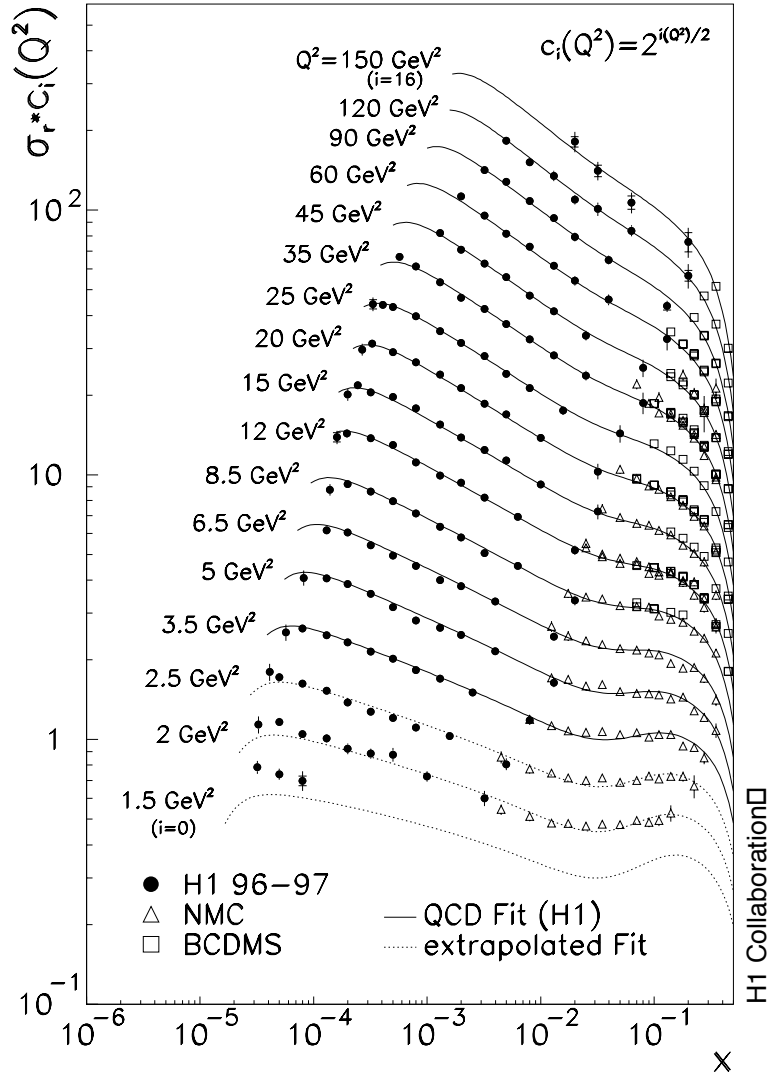


Figure 1.17: *H1* measurements of σ_r together with the result of a pQCD fit (see text). The dotted lines describe the fit result extrapolated in the region where the data are excluded from the fit (i.e. $Q^2 \leq 2.5 \text{ GeV}^2$).

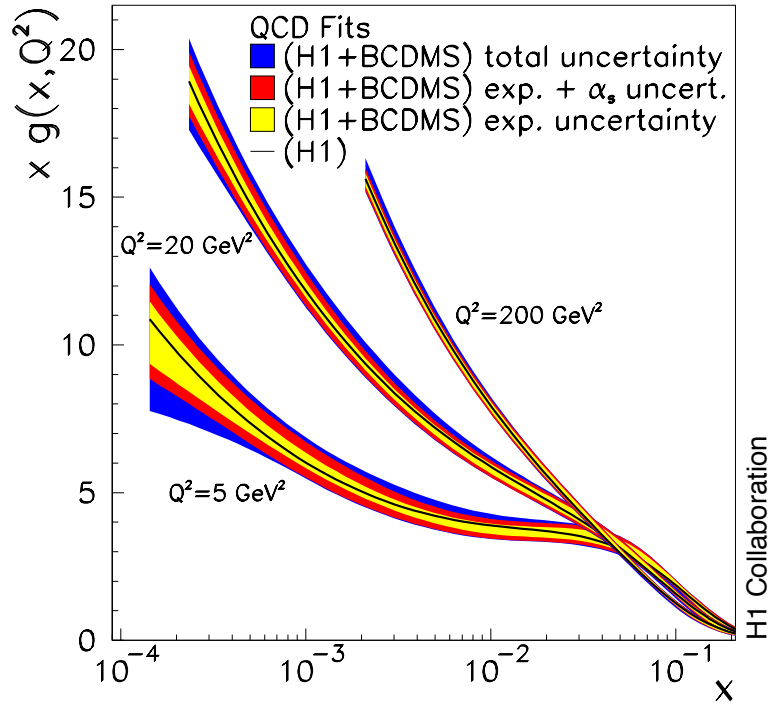


Figure 1.18: xg extracted from the *H1* fits.

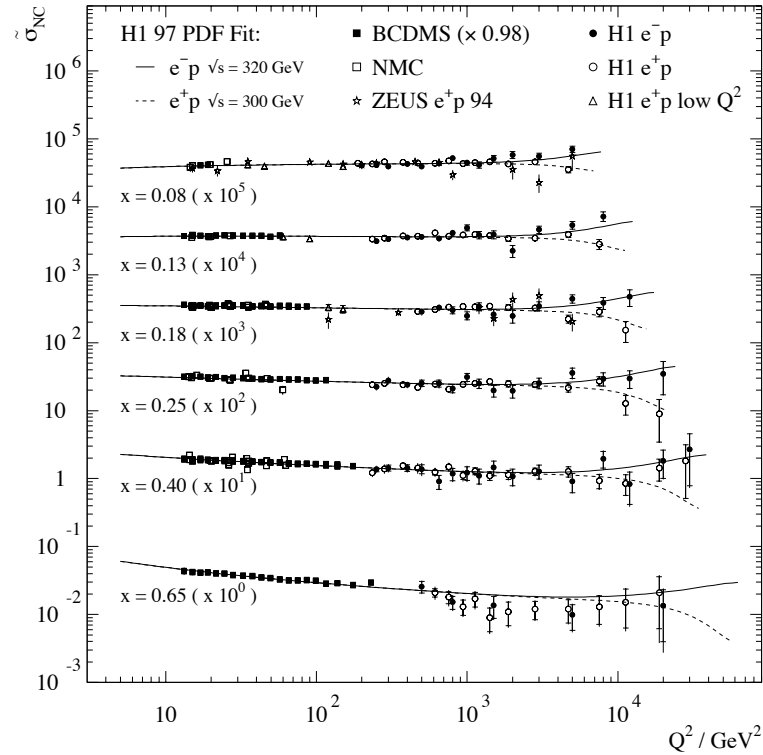


Figure 1.19: High Q^2 *H1* measurements of $\tilde{\sigma} \equiv \sigma_r$ (eq. 1.22) compared with pQCD fit results (see text).

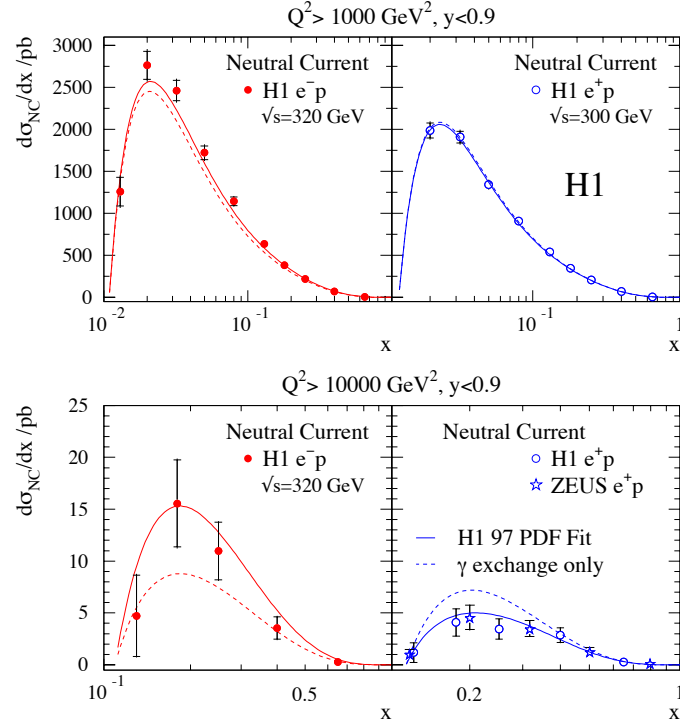


Figure 1.20: *H1* measurements of $d\sigma^{NC}/dx$ together with results from *pQCD* fits and different assumptions on electroweak contributions.

ZEUS CC 1994-97

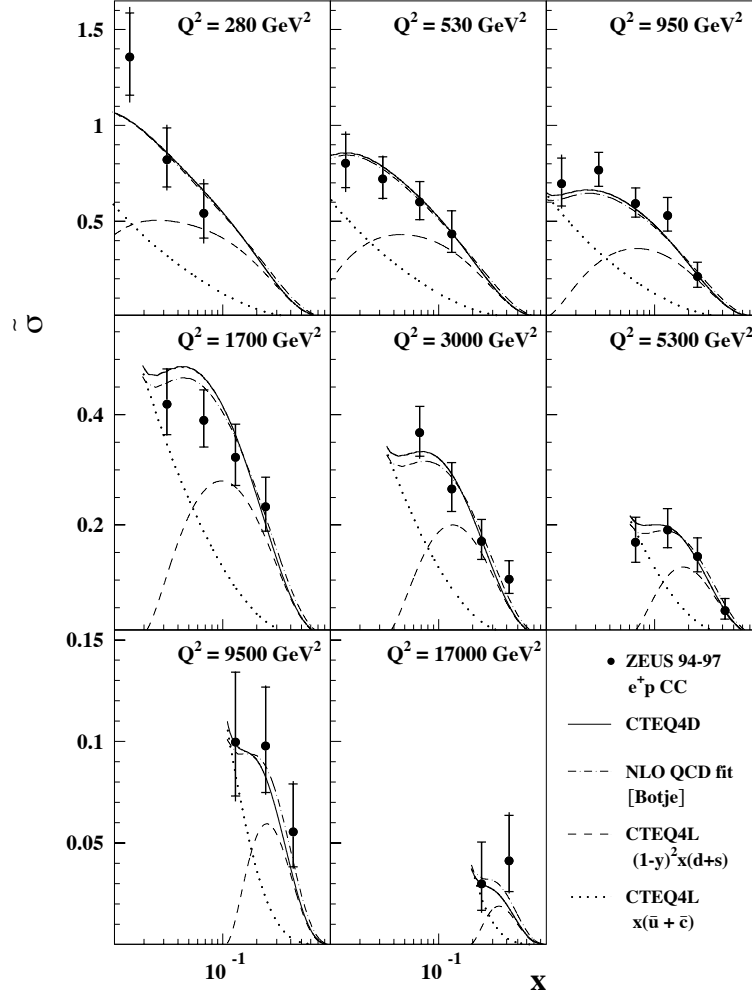


Figure 1.21: *ZEUS* measurements of $\tilde{\sigma} \equiv \Phi_+$ together with various *pQCD* calculations (see text).

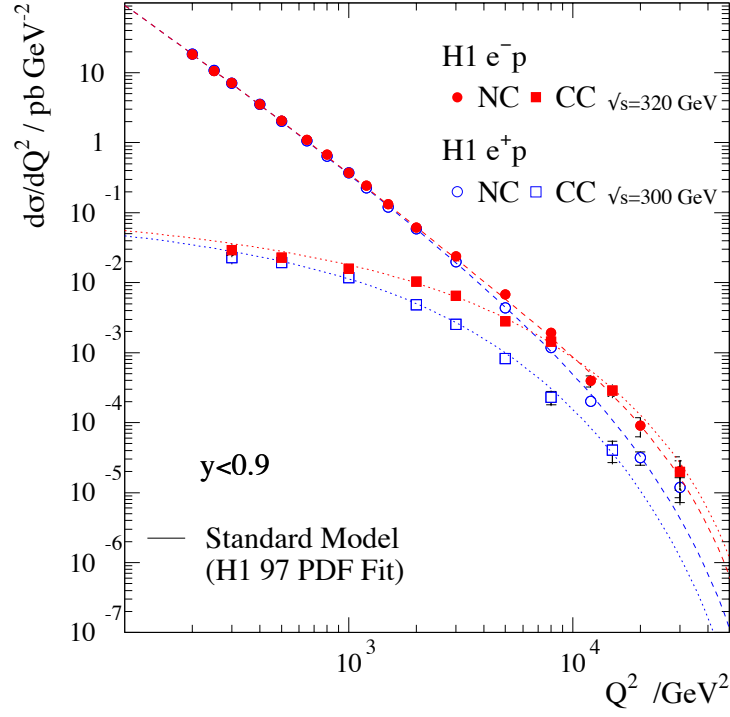


Figure 1.22: *H1* measurements of $d\sigma^{CC}/dQ^2$ and $d\sigma^{NC}/dQ^2$ together with the pQCD fit results.

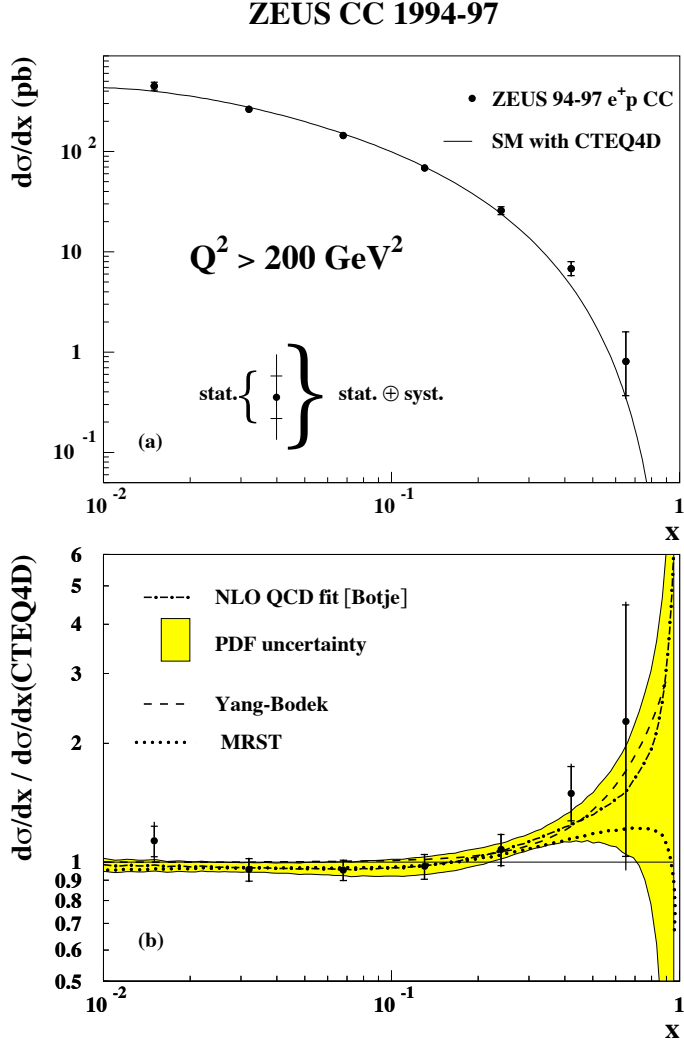


Figure 1.23: ZEUS measurements of $d\sigma^{CC}/dx$ (for e^+p) together with various pQCD results (see text).

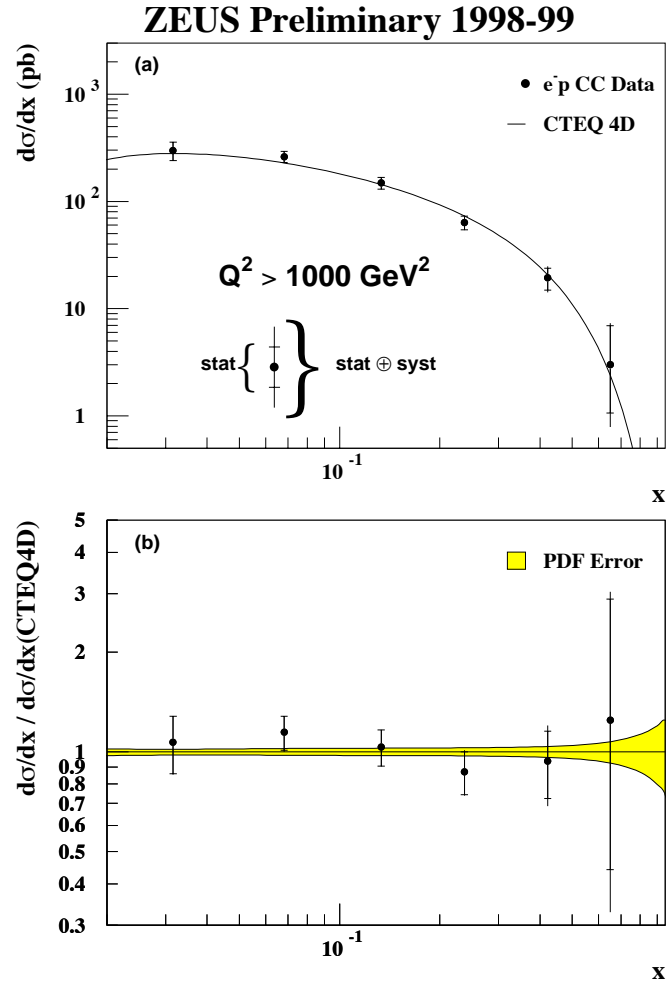


Figure 1.24: *ZEUS* measurements of $d\sigma^{CC}/dx$ (for e^-p) together with the *pQCD* fit result.

where G_F is the Fermi constant, and where the functions Φ_{\pm} depend on CC structure functions (see [30] for example). From eq. (1.24) one can first remark that the Q^2 slope of the CC differential cross-section (see fig. 1.22) permits a determination of M_W , assuming (or not) the precisely measured value for G_F [34]. To extract M_W , H1 and ZEUS have used two different procedures. In H1, M_W is taken as an extra free parameter (G_F is fixed) of the pQCD fit and in ZEUS, the pdfs of CTEQ [35] are used in order to extract M_W and G_F (variations of the pdf choice is taken into account within the errors). The results are

$$\begin{aligned} \text{H1 : } M_W &= 80.9 \pm 3.3(\text{stat.}) \pm 1.7(\text{syst.}) \pm 3.7(\text{theo}) \text{ GeV} \\ \text{ZEUS : } M_W &= 80.4^{+4.9}_{-2.6}(\text{stat.})^{+2.7}_{-2.0}(\text{syst.})^{+3.3}_{-3.0}(\text{pdf}) \text{ GeV} \end{aligned}$$

and treating G_F as free, ZEUS obtain

$$\begin{aligned} M_W &= 80.8^{+4.9}_{-4.5}(\text{stat.})^{+5.0}_{-4.3}(\text{syst.})^{+1.4}_{-1.3}(\text{pdf}) \text{ GeV}, \\ G_F &= [1.171 \pm 0.034(\text{stat.})^{+0.026}_{-0.032}(\text{syst.})^{+0.016}_{-0.015}(\text{pdf})] \times 5 \cdot 10^{-5} \text{ GeV}^{-2}. \end{aligned}$$

Let us point out that, concerning the H1 result, the theoretical uncertainty is dominated by the variation of the results when varying the ratio \bar{d}/\bar{u} in the pQCD fit, and by the choice of the nuclear corrections applied to the deuterium target data entering the fit. These results, in good agreement with the world average values [34], show that the standard model gives a good description of both space-like (CC in DIS) and time-like (W production in $p\bar{p}$ and e^+e^- collisions) processes.

In order to see the sensitivity of the CC cross-section to the pdfs, we write Φ_{\pm} in LO

$$\Phi_+ = x\bar{U} + (1-y)x\bar{D}; \quad \Phi_- = xU + (1-y)x\bar{D}$$

with $U = u + c$ and $D = d + s$. From these expressions and from fig. 1.21 one can remark that: with positron (electron) beams one can determine d^v (u^v) at high x and small- y and $\bar{u} + \bar{c}$ ($\bar{d} + \bar{s}$) at small y . Let us mention that d_v and the sea quarks are basically determined in the global pQCD fits by μ -deuterium and $\nu(\bar{\nu})$ -iron fixed target data, which require some nuclear corrections. Therefore, with the HERA $e^{\pm}p$ CC events one may have, with more statistics, a unique means to determine these quark densities.

In fig. 1.23, $d\sigma/dx$ is shown together with the error band determined by the ZEUS pQCD fit (without the CC and NC data described in this appendix), and with the results of a recent analysis where an ansatz $d/u \neq 0$ as $x \rightarrow 1$ [36] was introduced. Although the statistics is still low, one can notice from fig. 1.23 that this latter hypothesis is not required by the HERA data.

In fig. 1.24, the measurement of $d\sigma^{e^-p}/dx$ is shown. The error band of the pQCD is much smaller than in fig. 1.23, therefore one can expect a better determination of electroweak parameters. The size of the error bands reflect that u^v is much better constrained than d^v in the pQCD fits.

Extraction of F_L

The longitudinal structure function is very hard to determine. It requires to combine data in a given x - Q^2 bin from different beam energies. However, from eq. (1.22), one observes that at high y the cross-section receives a contribution both from F_2 and F_L .

Therefore, taking F_2 from the result of a pQCD fit (see previous section) applied to the low y ($y < 0.35$) data one can determine F_L at high y by subtracting F_2 , extrapolated to high y . To reach lower Q^2 , where pQCD is not reliable, another method is used. Writing

$$\frac{\partial \sigma_r}{\partial \log y} = \frac{\partial F_2}{\partial \log y} - 2y^2 \frac{2-y}{Y_+^2} F_L - \frac{y^2}{Y_+} \frac{\partial F_L}{\partial \log y},$$

neglecting $\partial F_L / \partial \log y$, and assuming that $\partial F_2 / \partial \log y$ is a linear function of $\log y$, one can determine F_L (these assumptions being justified by experimental observations). $\frac{\partial \sigma_r}{\partial \log y}$ is shown in fig. 1.25 and F_L in fig. 1.26. This determination is consistent with the NLO calculation of pQCD. It should be pointed out that because of the high sensitivity of F_L to the gluon density xg , a precise measurement of F_L would provide a complementary determination of xg .

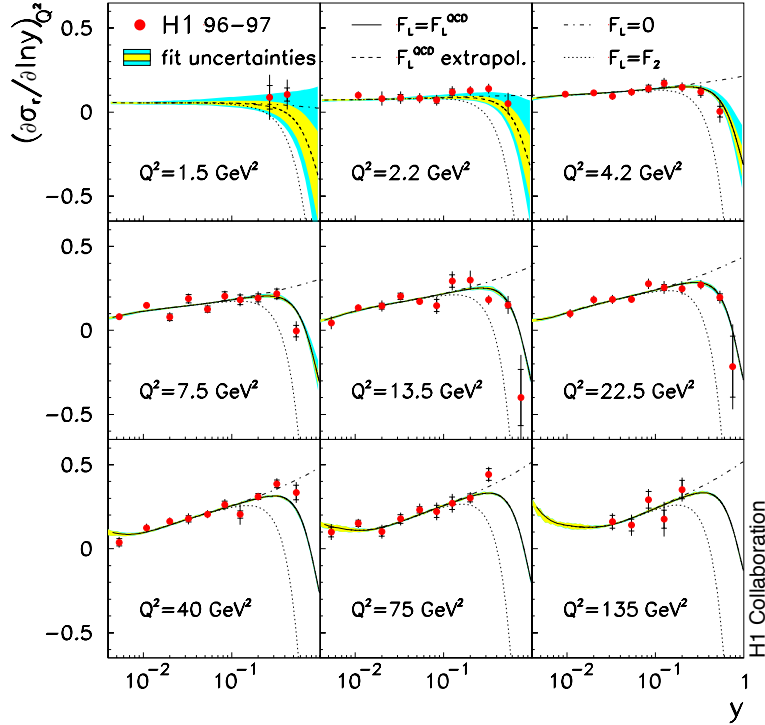


Figure 1.25: *H1* determination of $\frac{\partial \sigma_r}{\partial \log y}$ (see text). The sensitivity of this quantity to F_L is demonstrated by comparing QCD calculation in the two extreme cases $F_L = 0$ and $F_L = F_2$.

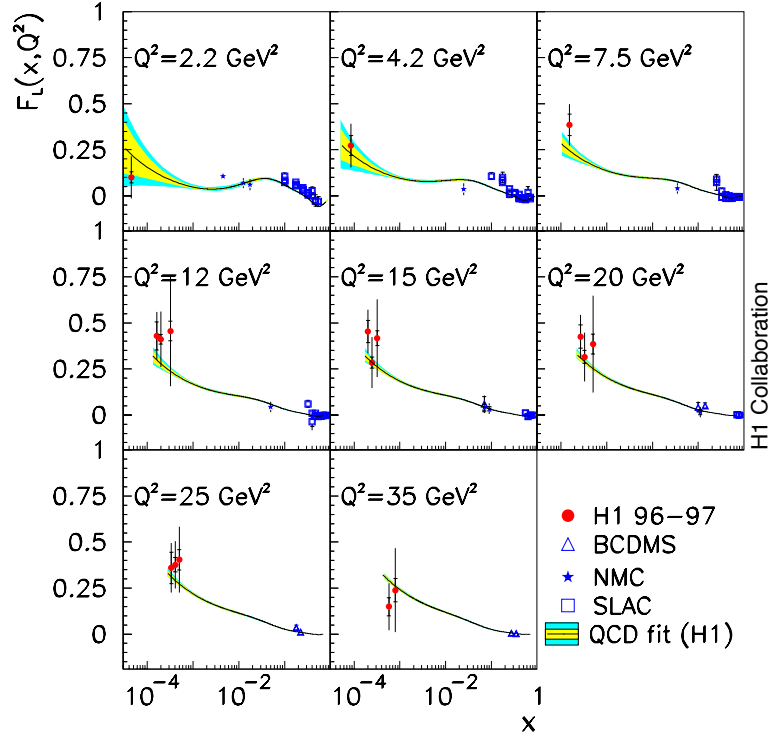


Figure 1.26: *H1 determination of F_L compared to fixed target measurements and to QCD calculations.*

Bibliography

- [1] C.Y. Prescott et al., Phys. Lett. B 77 (1978) 347.
- [2] A. Argento et al., Phys. Lett. B 140 (1984) 142.
- [3] Proceedings of the 1995/1996 Future Physics at HERA Workshop, ed. G. Ingelman, A. De Roeck and R. Klanner (DESY, Hamburg, 1996).
- [4] M. Klein, in 9th International Workshop on Deep Inelastic Scattering (Bologna 2001).
- [5] P. Kroll, M. Schurmann and P.A.M. Guichon, Nucl. Phys. A 598 (1996) 435.; A. Freund and M. Strimann, Phys. Rev. D 60 (1999) 071501.
- [6] E. Barrelet et al., *Proposal to upgrade the leongitudinal polarimeter*, DESY-PRC-00-06, 2000.
- [7] Z. Zhang, *Nouveaux aspects de la structure du proton avec le collisionneur HERA*, Habilitation Thesis, Orsay, France, 2000. LAL report LAL 00-57/2000.
- [8] Cornet and Rückl, P. 771 Vol. 2, in [16].
- [9] C. Pascaud and F. Zomer, LAL 95-05/1995.
- [10] H1 Coll., C. Adloff et al., Eur. Phys. J., C13 (2000) 609.
- [11] G. D’Agostini, CERN Yellow Report 99-03
- [12] D.P. Barber et al., Nucl. Instr. Meth., A338 (1994)166.
- [13] G. D’Agostini and M. Raso, **hep-ex/0002056**.
- [14] D0 Coll., Phys. Rev. Lett.76 (1996) 3271.
- [15] M.A. Doncheski and J.L Hewett, Z. Phys. C (1992) 209.
- [16] Proceedings of the 1987 HERA Physics Workshop, ed. R.D. Peccei (DESY, Hamburg, 1988).
- [17] Proceedings of the 1991 HERA Physics Workshop, ed. W. Buchmuller and G. Ingelman (DESY, Hamburg, 1992).
- [18] M. Klein and T. Reinmann, Z. Phys. C 24 (1984) 151.
- [19] R. J. Cashmore et al. p. 163-207 in [3].

- [20] Results from LEP, available on <http://lepewwg.web.cern.ch/LEPEWWG/> (2002).
- [21] H1 Coll., Nucl. Instr. Meth. A336 (1997) 348; The ZEUS detector, status report DESY-1993.
- [22] BCDMS Coll., Phys. Lett. B223 (1989) 485; Phys. Lett. B237 (1989) 592; NMC Coll., Nucl. Phys. B483 (1997) 3.
- [23] Z. Zhang, private communication.
- [24] S. Bentvelsen et al., p. 23 in [17], K.C. Hoeger, p. 43 *ibid*.
- [25] U. Bassler and G. Bernardi, Nucl. Instrum. Meth. A 361 (1995) 197; Nucl. Instrum. Meth. A 361 (1999) 583.
- [26] H1 Coll., Eur. Phys. J. C13 (2001)33; ZEUS Coll., DESY-01-064 (2001), accepted by Eur. Phys. J. C.
- [27] ZEUS Coll., Eur. Phys. J. C11 (1999) 427; ZEUS Coll., Eur. Phys. J. C12 (2000) 411; see ref. [10]; H1 Coll., Eur. Phys. J. C19 (2001) 269.
- [28] A. Blondel and F. Jacquet, *Proceeding of the study of an ep facility in Europe*, ed. U. Amaldi, DESY 79/48 (1979) 391.
- [29] W. Furmanski and R. Petronzio, Z. Phys. C1 (1982) 293.
- [30] See for a recent review: A.M. Cooper-Sarkar, R.C. Devenish and A. De Roeck, Int. J. Mod. Phys. A13 (1998) 3385.
- [31] M. Gluck, E. Reya and M. Stratmann, Nucl. Phys. B422 (1994) 37.
- [32] E. Laenen et al., Nucl. Phys. B392 (1993) 162 and 229; Phys. Lett. B291 (1992) 325.
- [33] C. Pascaud and F. Zomer, DESY 96-266; J. Blümlein et al., in ref. [3].
- [34] Particle Data Group, Eur. Phys. J. C15 (2000) 1.
- [35] CTEQ4 Coll., Phys. Rev. D55 (1997) 1280; MRS Coll., Phys. Rev. D51 (1995) 4756.
- [36] U.K. Yang and A. Bodek, Phys. Rev. Lett. 82 (1999) 2467.

Chapter 2

Electron beam Polarisation and Polarimetry

In this chapter, the electron beam polarisation rise in storage rings and the polarisation measurement are described. The former topic has been covered by many review articles and text-books in the past ([1, 2, 3, 4]). Another very useful document is a thesis on the HERA polarisation after the HERA-II upgrade [5] where qualitative and quantitative aspects are much developed. Since I didn't contribute in this field, I will only give a very brief account on this very rich topic.

In this chapter I will therefore concentrate on the electron beam polarisation measurement. Moreover, with regard to the HERA machine I will only describe polarimetry experiments in high energy electron storage rings.

2.1 Electron beam polarisation

The definition of the polarisation of an electron bunch is not straightforward. We shall therefore start by the very basic definition in order to define precisely what is the “polarisation” that we do measure in the HERA ring.

As we shall later see in this chapter, the polarisation of an electron bunch can be measured by Compton scattering, i.e. via laser beam - electron beam interactions. The polarisation measurement thus gives access to an average value. In Quantum Mechanics, this measurement corresponds to a statistical system with missing information (i.e. the spin state of all electrons at a given time). To describe such a system the density matrix formalism [6] is the most useful one [3].

Let us first give the definition of the “spin vector” \vec{S}_k attached to a single particle circulating on a given trajectory at a given energy. Giving the quantum state $|\Psi_k\rangle$ describing this system, one gets, in the centre of mass of the electron:

$$\vec{S}_k = \langle \Psi_k | \vec{\mathcal{S}} | \Psi_k \rangle$$

where $\vec{\mathcal{S}} = (\mathcal{S}_X, \mathcal{S}_Y, \mathcal{S}_Z)$ is the spin vectorial operator (in the basis of the eigen-vectors of the third Pauli matrix, $\vec{\mathcal{S}}$ is represented by the three Pauli matrices $\vec{\sigma}$). The direct axis system is chosen such Z coincides with the direction of motion and Y is the vertical axis, see fig. 2.1).

We can now define the spin polarisation of a mono-energetic electron bunch [3]:

$$\vec{P} = \frac{2}{\hbar} \sum_k p_k \langle \Psi_k | \vec{S} | \Psi_k \rangle \equiv \left\langle \frac{2}{\hbar} \vec{S} \right\rangle,$$

where p_k is the probability of a single particle state $|\Psi_k\rangle$ to occur. Hence, the bracket stands here for the average of all possible one particle spin quantum states (i.e. ensemble average).

2.1.1 Polarisation build-up in storage rings

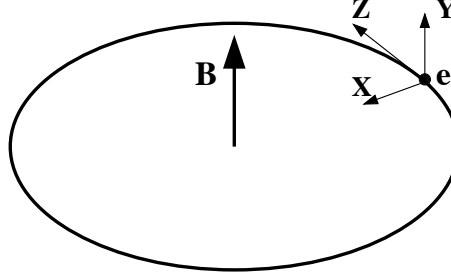


Figure 2.1: Axis system and perfect circular orbit around a magnetic field.

Unlike linear accelerators where polarised electrons are created and kept polarised up to the interaction point [7], in storage rings the polarisation is built up thanks to synchrotron radiation in the bending magnets. This is the so called Sokolov-Ternov effect [8].

Since this effect is the key point of polarisation at HERA, let us give here more details. An electron beam deflected around a magnetic field aligned along the Y axis radiates photons (see fig. 2.1). During this process, a flip of the projection of the electron spin along Y can occur. The spin-flip probabilities per unit of time $w_{\uparrow\downarrow}$ (spin up \rightarrow spin down) and $w_{\downarrow\uparrow}$ (spin down \rightarrow spin up) corresponding to an electron spin aligned and anti-aligned respectively with the magnetic field have been calculated in ref. [8]. Using the notations of ref. [2], one has:

$$w_{\uparrow\downarrow} = \frac{5\sqrt{3}}{16} \left(1 + \frac{8}{5\sqrt{3}} \right) c\lambda_c r_0 \frac{\gamma^5}{\rho^3}, \quad w_{\downarrow\uparrow} = \frac{5\sqrt{3}}{16} \left(1 - \frac{8}{5\sqrt{3}} \right) c\lambda_c r_0 \frac{\gamma^5}{\rho^3}$$

where γ is the electron Lorentz factor, ρ the bending radius of the magnetic field,

$$\lambda_c = \hbar/(m_e c) = 3.8616 \cdot 10^{-13} \text{ m}$$

is the reduced electron Compton wavelength and

$$r_0 = e^2/(4\pi\epsilon_0 m_e c^2) = 2.8179 \cdot 10^{-15} \text{ m}$$

is the classical electron radius.

The fact that $w_{\uparrow\downarrow} \neq w_{\downarrow\uparrow}$ implies that starting from an unpolarised beam, synchrotron radiation induces a transverse polarisation. Asymptotically, this polarisation is given by

$$P_{ST} = \frac{w_{\uparrow\downarrow} - w_{\downarrow\uparrow}}{w_{\uparrow\downarrow} + w_{\downarrow\uparrow}} = \frac{8}{5\sqrt{3}} \sim 92.4\%$$

and the time evolution reads

$$P_Y(t) = -P_{ST} \left(1 - e^{-t/\tau_{ST}} \right)$$

with

$$\tau_{ST} = \frac{1}{w_{\uparrow\downarrow} + w_{\downarrow\uparrow}} = \frac{8\rho^3}{5\sqrt{3}c\lambda_e r_0 \gamma^5},$$

where P_{ST} is often called equilibrium or asymptotic polarisation and the subscript ST refers to the Sokolov-Ternov effect. Note that the asymptotic polarisation is a constant, below 1 and anti-parallel with respect to the magnetic field (it is parallel for positron beams). At HERA for an electron beam energy $E_e \approx 27$ GeV one gets $\tau_{ST} \approx 40$ min. This very long time, reflecting the small spin-flip probability, must be compared to the time interval between two photon emissions $\sim 10^{-8}$ s.

These results are valid under the following assumptions: the magnetic field is homogeneous, after radiation the electron stays on its perfect circular orbit and synchrotron radiation is a random process. Although the latter assumption is justified, this is obviously not the case for the formers. We must now then look at the spin-orbit coupling effects.

2.1.2 Depolarisation effects

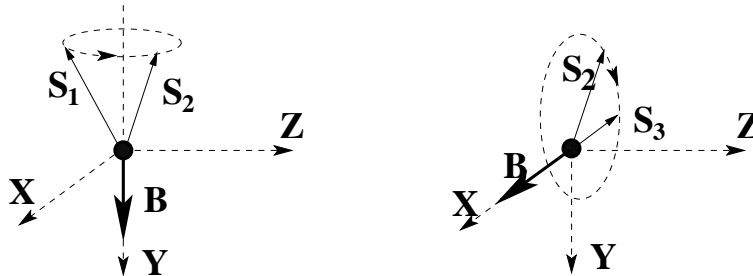


Figure 2.2: Naive illustration of depolarisation effects. Left plot: precession of the spin vector around the magnetic field normal to the plane of motion. Right plot: precession around a magnetic field perpendicular to the beam direction and inside the plane of motion.

The evolution of \vec{S} inside homogeneous and inhomogeneous electromagnetic fields is described by a first order semi-classical differential equation, named the T-BMT equation (see [4] for an overview). One of the key features of the spin motion in magnetic fields is the spin-precession. It is illustrated in fig. 2.2: when the magnetic field experienced by

the electron is perpendicular to the plane of motion, the spin direction changes but its projection along Y remains constant while the precession around a magnetic field inside the plane of motion reduces the spin projection along Y .

Since the T-BMT equation is a linear differential equation containing a cross product between electromagnetic field vectors and the spin vector, electric and magnetic fields change the direction of a spin vector but not its absolute value, i.e. spins precess. We have already seen that synchrotron radiation in dipoles causes a build up of polarisation by the Sokolov–Ternov effect. However, it can also lead to depolarisation. This happens as follows: after a photon of synchrotron radiation is emitted, a particle jumps from its original orbit to another. A spin then “feels” magnetic fields in the quadrupoles which it would not have felt in the absence of photon emission and, by the T-BMT equation, its precession is modified. Then, since photon emission is stochastic, the spins in the bunches “diffuse”. In the presence of depolarisation the asymptotic polarisation is reduced with respect to P_{ST} .

To get an idea of these dynamics one must look at the time scales. The orbit period is $\approx 10^{-5}$ s at HERA and the betatron and synchrotron oscillations periods are $\sim 10^{-6}$ s and $\sim 10^{-4}$ s respectively. Once excited, these oscillations are damped within $\sim 10^{-2}$ s typically. If we now compare these time scales to the time scale for synchrotron emissions $\sim 10^{-8}$ s, we see that an electron bunch corresponds to a superposition of a large number of orbits.

The major effect of transverse perturbing magnetic fields is the resonant depolarisation. In a perfectly flat machine, the number of 2π spin precessions around the vertical direction per turn is given by $\nu_0 = a\gamma$ with $a = (g - 2)/2$ the electron gyro-magnetic anomaly. This is the so called “naive spin tune”[3] ($\nu_0 = 62.5$ at HERA). In a real machine, the spin tune is not given by this simple formula (although in HERA the real “spin tune” is still approximately proportional to the beam energy[3]) but the important point is that, when the spin tune and the frequency of the perturbing magnetic field are the same, then the spin is coherently kicked at each turn. To optimise the beam polarisation, one obviously has to choose a beam energy far from depolarisation resonances.

Another source of depolarisation is the effect of the proton bunch charge on the electron bunch polarisation. This phenomenon, named beam-beam effect, can be viewed as a quadrupole magnet effect on the electron beam. There is no clear statement about the importance of this depolarisation source for HERA-II, though some experience was gained after the 2000 proton focusing upgrade. With the HERA-II upgrade, it is then expected that beam-beam effect will further reduce the polarisation.

An important point for polarimetry must be noted here. Comparing the polarisation build up characteristic time (≈ 40 mn) to the other process time scales, one sees that polarisation is varying very slowly and is therefore the same, in absolute value but not in direction, all over the ring.

2.1.3 Spin rotators and longitudinal polarisation at HERA

From what has been described in the previous sections, one sees that the electron beam is vertically polarised at HERA. To convert this polarisation into a longitudinal polarisation, spin rotators must be supplied.

In principle a spin rotator is a simple device. Making use of the spin precession, a set of transverse magnetic fields can transform a transverse to a longitudinal polarisation.

These spin rotators are located around the electron-proton interaction points (in the arcs of HERA) and longitudinal polarisation must be transformed back to transverse polarisation before the arcs in order not to depolarise the beam. That's why rotators always appear by pairs.

In practice one has to face many problems for the rotator design: the space constraints (e.g. solenoids are space consuming and are weak spin rotators unlike bending magnets), the beam orbit stability, sensitivity of the field design to the beam energy, facility to switch from e^- to e^+ and the optimisation of the beam polarisation.

The mini-rotator solution [9] has been chosen for HERA. It consists in three series of horizontal bending magnets interleaved with vertical bending magnets as shown in fig 2.3.

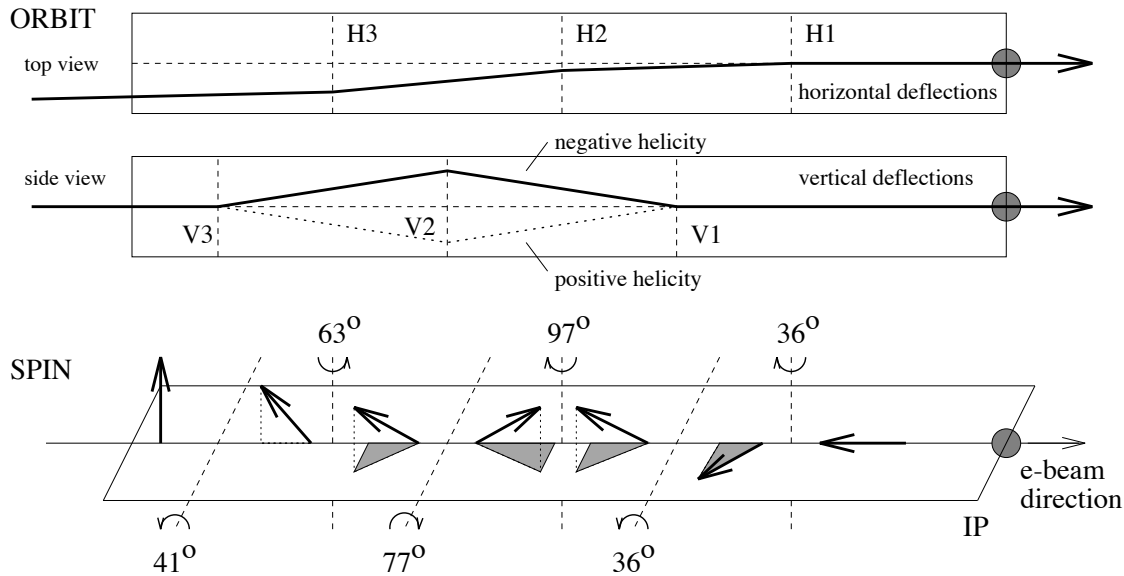


Figure 2.3: Mini rotator at HERA. A schematic view of the orbit motion is shown in the two top plots and changes of the spin direction in the bottom plot. Symbols V and H refer to vertical and horizontal bending magnets respectively. The total length of the spin rotator is 56 m.

2.1.4 Optimisation of the polarisation at HERA

When nothing is done to counteract depolarisation effects, the equilibrium transverse polarisation, written here P_∞ with $P_\infty < P_{ST}$, is very low [10]. A description of the complex techniques used to optimise the polarisation in a ring like HERA is outside the scope of this document.

With regard to the performances of the polarimeter, it is however necessary to mention one of these techniques, the “closed orbit spin matching” [11]: eight ensembles of magnets (named the harmonic bumps) are located in the HERA straight sections in order to minimise the effects of the distortion of the closed orbits on the polarisation. [11]

To optimise the harmonic bumps, an empirical procedure is adopted: an operator varies the kick amplitudes of the beam inside the magnets constituting the harmonic

bumps and then observes the expected asymptotic polarisation. If the polarisation increases then the variation is continued, if not the process is stopped (see also fig. 2.9). Therefore a very fast and accurate polarisation measurement would help to optimise the polarisation at HERA.

2.1.5 Polarisation operations at HERA

Before the year 2000, HERA operated with two spin rotators around the HERMES experiment. After the HERA upgrade, spin rotators have been installed around H1 and ZEUS experiments (see fig. 2.4). Thus the HERA ring now contains three pairs of spin rotators.

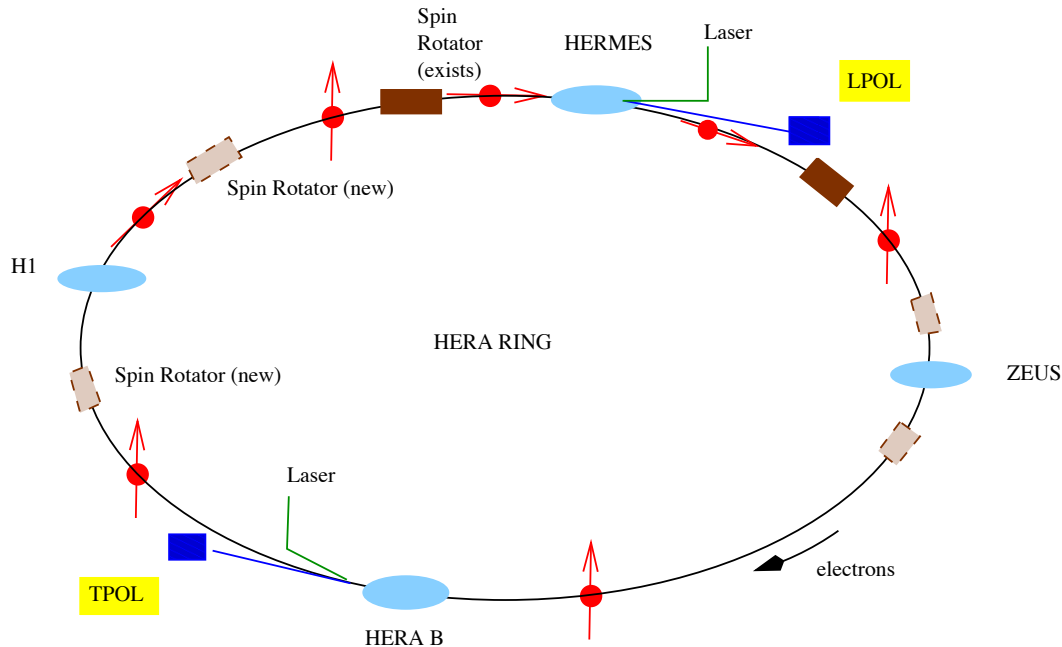


Figure 2.4: Schematic view of the HERA ring. Before 2000, two spin rotators were installed around HERMES. Since the 2000 shutdown, pairs of spin rotators have been installed around the H1 and ZEUS experiments. Positions of the TPOL and LPOL Compton polarimeters are also indicated.

Two polarisation measurements are currently performed at HERA (see section 2.2): the longitudinal polarisation (LPOL) measurement is performed after the HERMES interaction point (IP) and the transverse polarisation (TPOL) is measured in the west hall close to the HERAB experiment¹. Both measurements agree within their measurement uncertainties and their accuracies are indicated in tab. 2.1. The variation of polarisation with time is shown in fig. 2.5 for three different machine fills. These measurements provide an illustration of the behaviour of the polarisation at HERA: rise time of the order of 40 min, non-reproducibility of polarisation variations from a fill to another.

¹The reason why no polarimeter is located after H1 or ZEUS is that not enough space is available around the experiments and that it is not needed.

	Laser beam power	$\Delta P_{stat.}$	$\Delta P_{syst.}$
LPOL	33 MW (pulsed)	1%/min (all bunches) 1%/bunch over 30 min	$\approx 2\%$
TPOL	10 W (continuous)	1%/min (all bunches)	$\approx 2\%$

Table 2.1: *Main characteristics of the existing HERA polarimeters: laser beam power, statistical and systematic uncertainties.*

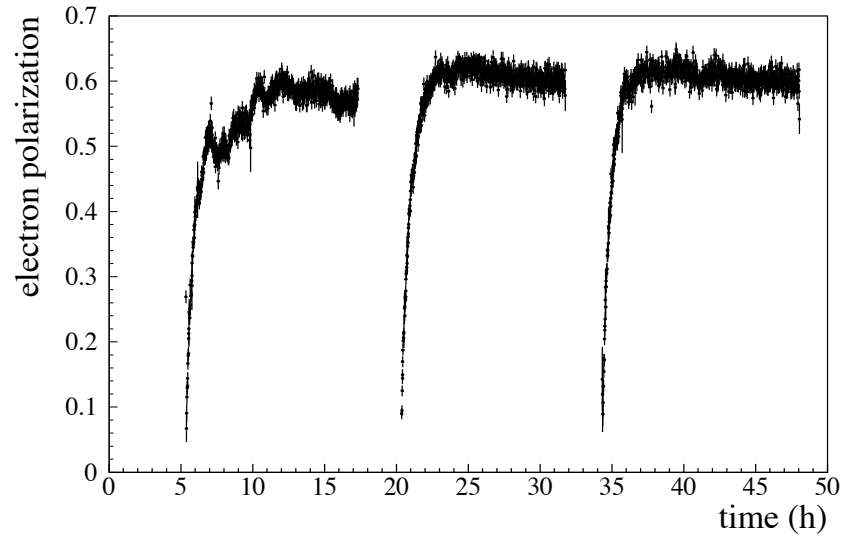


Figure 2.5: *Polarisation rise at HERA for three machine fills. Measurements come from the HERA-LPOL setup [12].*

There are approximately two hundred electron bunches circulating in the HERA ring (the beam current is around 50 mA) and some of them do not collide with protons. Hence, they do not suffer from beam-beam effects and their polarisation is often different from that of the colliding bunches. Typical differences between the polarisation of colliding and non-colliding bunches are shown in fig. 2.6. The two plots of this figure correspond to different machine fills and one can see that relative difference of polarisation between colliding and non-colliding beams varies from fill to fill and can reach 10 – 50%.

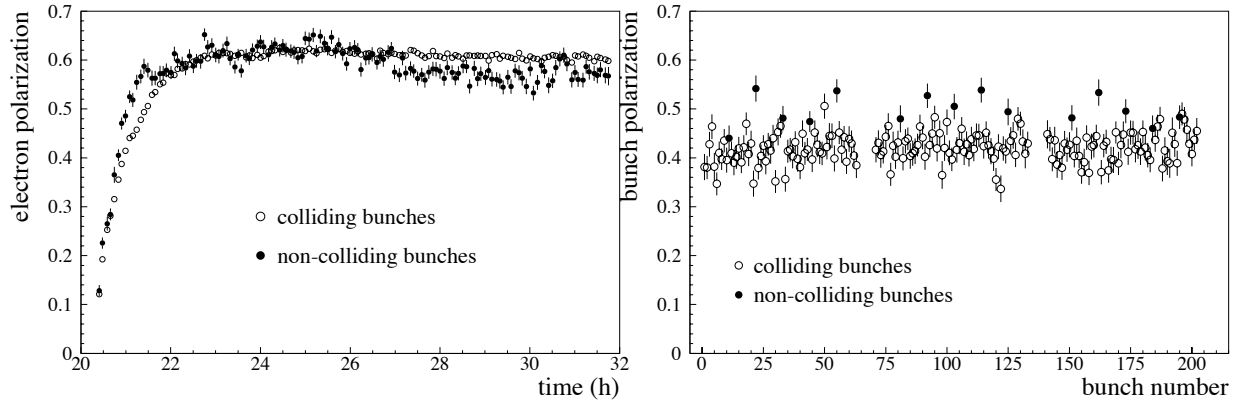


Figure 2.6: *Left plot: polarisation as a function of time measured by the HERA-LPOL [12]. Right plot: polarisation as a function of the bunch number measured by the HERA-LPOL [12]. In both plots, polarisation of the colliding and non-colliding bunches are shown separately.*

To further illustrate the unpredictable aspect of the polarisation behaviour, an online measurement performed after the TPOL data acquisition system upgrade [13] is shown in fig. 2.7. The structure of the three trains of bunches is clearly visible and the bunch to bunch polarisation variation inside one train is attributed to the interaction between the electron beam and its associated wake-field and the RF cavities (which vanishes between two trains of bunches). Variations of the equilibrium polarisation also appears naturally because of the slow drift of the beam orbit² inside the magnetic fields during a run duration (typically 10 h). Fig. 2.8 shows that such variations can be as large as $\sim 10\%$.

Finally, an illustration of the tuning of the harmonic bumps is shown in fig. 2.9. This tuning was performed after a change of the beam optics. The optimisation steps are clearly visible (“bumps” in the polarisation rise-up). As mentioned above, a fast and precise polarimeter would certainly help to avoid the decrease of the equilibrium polarisation.

2.1.6 Polarisation and physics analysis

Two important topics are described here: the value of the longitudinal polarisation at the H1 IP and the systematic uncertainty on physics measurements due to the uncertainty in the knowledge of the polarisation. The results reported below were produced for the LPOL upgrade proposal [14].

As mentioned in the Introduction, the increase of luminosity at HERA is achieved by further squeezing of the electron and proton beams at the IP. This stronger focusing is

²For example, this can happen when the machine group optimises the orbit to increase the luminosity for one of the HERA experiments.

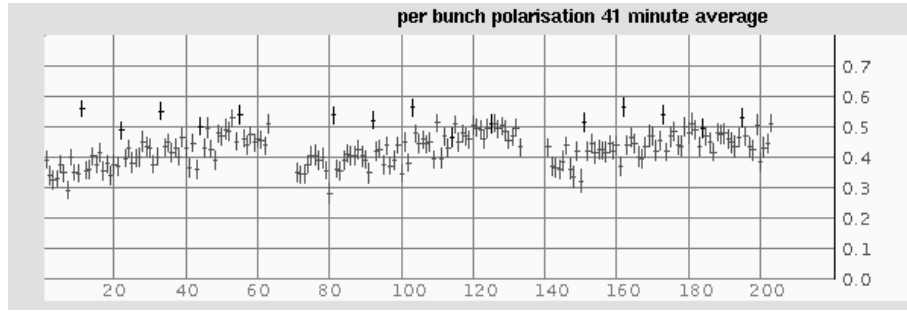


Figure 2.7: *On-line polarisation measurement as a function of the bunch number. Data come from the upgrade TPOL setup. Isolated points above 0.5 correspond to the non-colliding bunches.*

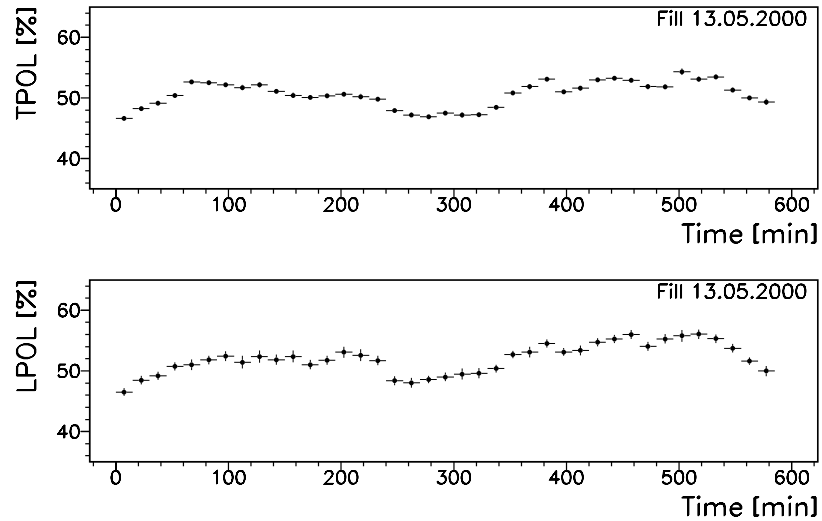


Figure 2.8: *Off-line TPOL and LPOL polarisation measurement as a function of time. Polarisation is averaged over all bunches.*

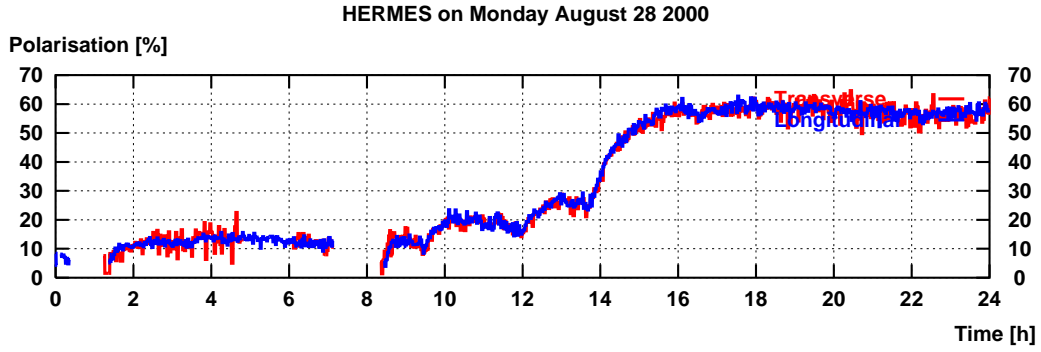


Figure 2.9: Optimisation of the harmonic bumps after a machine modification. The tuning procedure of the bump is clearly visible.

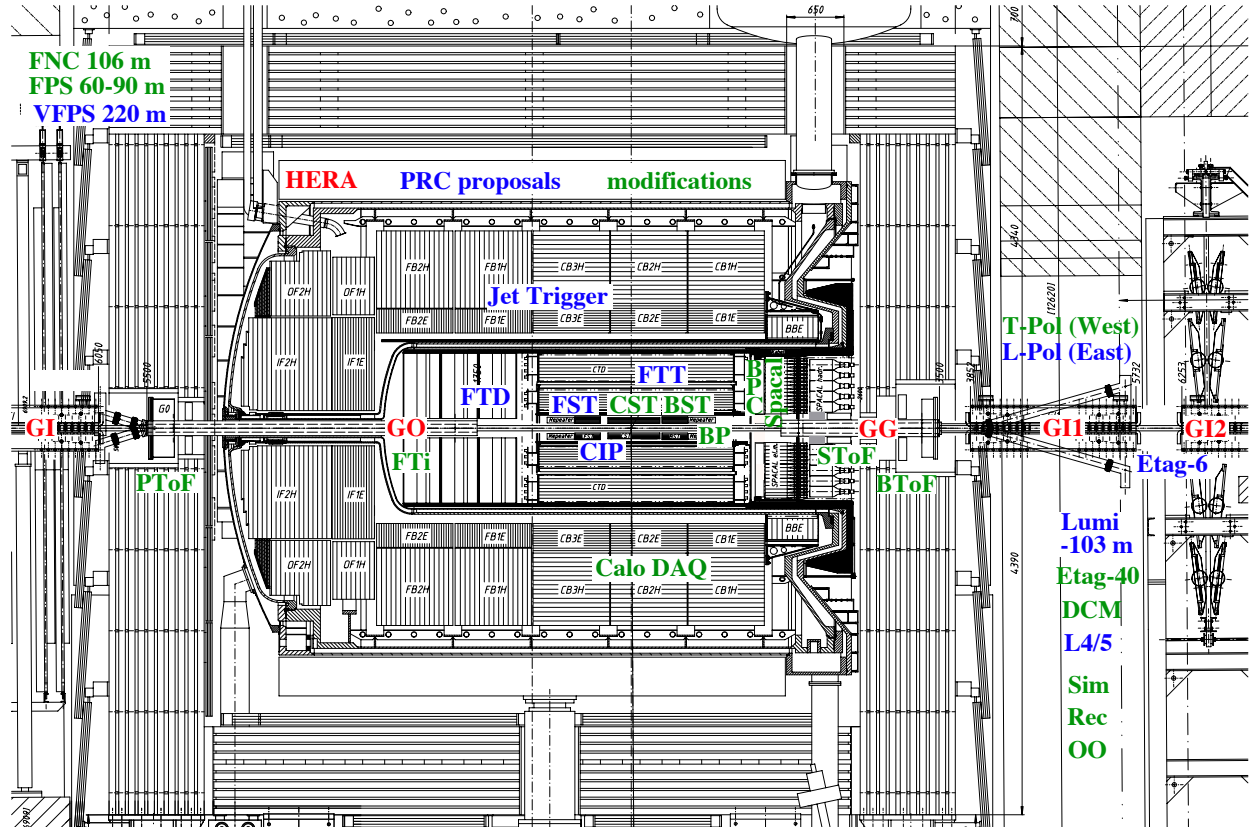


Figure 2.10: Side view of the H1 detector. The various upgrades performed for HERA-II are indicated. The two new elements increasing the luminosity are the combined function super-conducting magnets GG and GO.

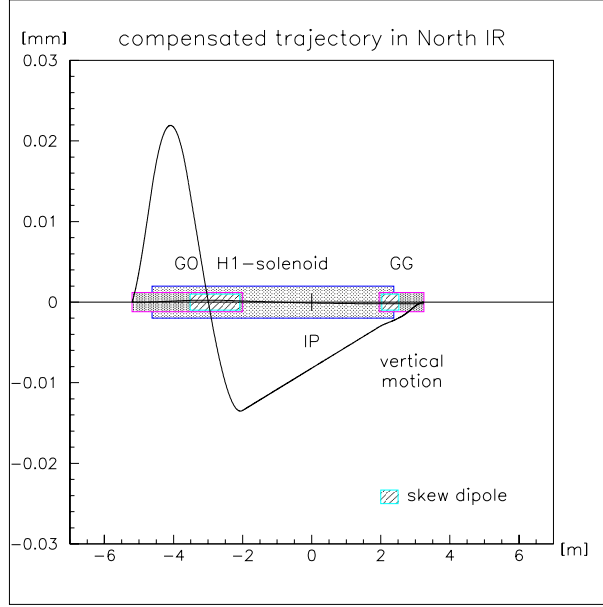


Figure 2.11: *Schematic view of the corrected orbit in the horizontal plane inside the H1 solenoid. GO and GG are the combined function long supra-conducting magnets. From [5]*

obtained by installing, among other optical elements, two long combined function superconducting magnets (for vertical beam focusing and electron-proton beam separation) inside the ZEUS and H1 experiments [15]. While these ~ 2 m long magnets fit well outside the ZEUS solenoid the situation is different in H1 where one of the magnets (on the upstream electron beam side) is located inside the solenoid (see fig. 2.10). Then the direction of polarisation changes between the H1 entrance and the H1 IP (see fig 2.11) so that the rotators must be slightly retuned to ensure that the polarisation axis remains vertical in the arcs and extra depolarisation is avoided [5]. The new layout also precludes the use of compensating solenoids. Thus the resulting effects on the optics have been neutralised with skew quadrupoles. This, together with the new, more complex fields at the ends of the H1 solenoid causes extra depolarisation.

The second topic is related to the question of what polarisation inputs are needed for physics analysis. When N_{run} machine fills are combined, what is indeed needed is not the absolute beam polarisation but the luminosity weighted polarisation:

$$\bar{P} = \frac{\sum_{r=1}^{N_{run}} \int_{t_{min,r}}^{t_{max,r}} \sum_{b=1}^{N_{bunch}} P(r, b; t) \mathcal{L}(r, b; t) dt}{\sum_{r=1}^{N_{run}} \int_{t_{min,r}}^{t_{max,r}} \sum_{b=1}^{N_{bunch}} \mathcal{L}(r, b; t) dt} \quad (2.1)$$

where $(t_{max,r} - t_{min,r})$ is the duration of the r^{th} run, N_{bunch} is the number of colliding bunches and $\mathcal{L}(r, b; t)$ and $P(r, b; t)$ are the instantaneous luminosity and polarisation of the b^{th} bunch of the r^{th} machine fill respectively.

From eq. (2.1) it appears that two systematic sources can propagate to the physics measurements: the space and time correlations between luminosity and polarisation. The time correlation effect is important when data taken at the beginning of the machine

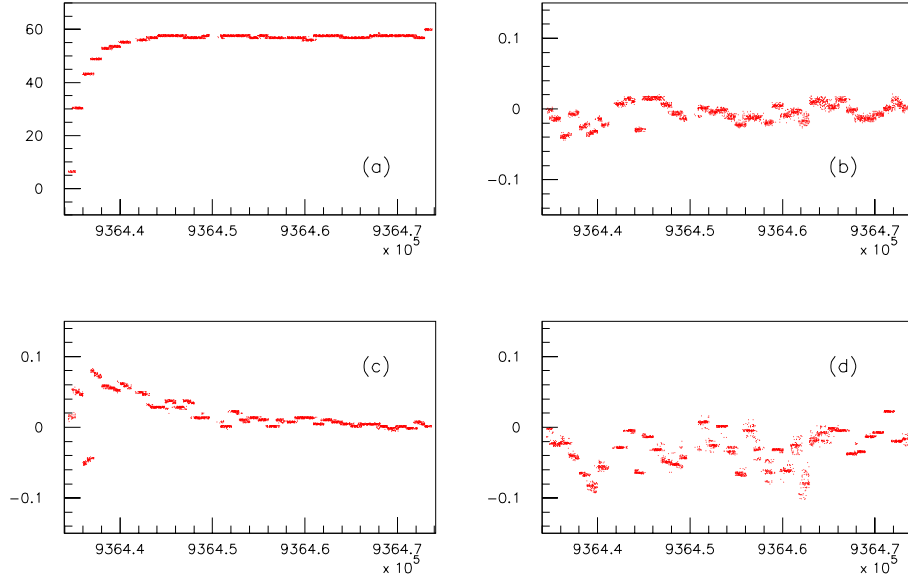


Figure 2.12: Polarisation (a), $C^t(P, L)$ (b), $C^t(P, I_e)$ (c) and $C^t(P, I_p)$ (d) versus the time for one typical fill. From ref. [14].

fills are kept in the analysis. During this period the electron beam current is maximum but luminosity and polarisation are 100% anti-correlated: luminosity decreases with time and polarisation rises up. However, as indicated in section 2.1.5, one cannot correct accurately using a model for the polarisation rise-up. Therefore, to precisely control the correlations between polarisation and luminosity during this period, a fast polarimeter must be operated. A precise estimate of the required time for polarisation measurement depends strongly on the shape of the non-reproducible polarisation rise-up and of the “ t_0 ”, i.e. the H1 and ZEUS Data Acquisition Systems start up.

The second effect is related to a possible bunch to bunch correlations between polarisation and luminosity. That is, for a given run r and at a given time t

$$\frac{1}{N_{bunch}} \sum_{b=1}^{N_{bunch}} P(r, b; t) \mathcal{L}(r, b; t)$$

is not *a priori* the same as

$$\frac{1}{N_{bunch}^2} \sum_{b=1}^{N_{bunch}} P(r, b; t) \sum_{b=1}^{N_{bunch}} \mathcal{L}(r, b; t).$$

To quantify such a correlation, let us introduce the time evolution of the bunch to bunch correlation coefficient $C^t(P, X)$ between the polarisation and a variable X . It is defined by:

$$C^t(P, X) = \frac{\sum_{b=1}^{N_{bunch}} (P_b - \langle P \rangle)(X_b - \langle X \rangle)}{\sqrt{\sum_{b=1}^{N_{bunch}} (P_b - \langle P \rangle)^2 \sum_{b=1}^{N_{bunch}} (X_b - \langle X \rangle)^2}}$$

with $\langle P \rangle = 1/N_{bunch} \times \sum_{b=1}^{N_{bunch}} P_b$ and $\langle X \rangle = 1/N_{bunch} \times \sum_{b=1}^{N_{bunch}} X_b$. Here, X can be e.g. the luminosity \mathcal{L} , the lepton beam intensity I_e or the proton beam intensity I_p .

In fig. 2.12(a) the polarisation as a function of time is shown for a typical HERA fill. For this fill the correlations to the luminosity, the electron and the proton current are shown in fig. 2.12(b), 2.12(c) and 2.12(d) respectively. The luminosity and the current intensity are measured every 10 s and the polarisation corresponds to an average over 10 min. Although correlations seems to exist in the early part of the fill no conclusive statement can be drawn with the current level of accuracy. These studies show anyhow that a fast and precise polarimeter would be useful to measure the luminosity-polarisation correlations, if they exist.

2.2 Polarisation measurement: Compton scattering

Several methods exist for measuring an electron beam polarisation at high energy (see refs. [10, 16] for examples). Among them, the most accurate one at high energy is Compton polarimetry. We therefore concentrate on this method in the following sections. Since interactions between polarised electrons and polarised light are involved, we start with a general and brief introduction to laser light polarisation.

2.2.1 Jones and Stokes-Mueller Formalism in optics

For a detailed introduction to optics and light polarisation we refer to refs. [17, 18]. We summarise here the Jones and Stokes-Mueller formalism.

The electric field vector \mathbf{E} of an electromagnetic wave is obtained by solving the Maxwell equations with the appropriate boundary conditions. For monochromatic and not too divergent waves, the plane wave approximation holds: in isotropic media, \mathbf{E} is located in a plane perpendicular to the wave vector \mathbf{k} , with $|\mathbf{k}| = k = 2\pi/\lambda$ and λ the wavelength.

Introducing a direct system of coordinates $\{x, y, z\}$ and a corresponding unit vector basis $\{\hat{\mathbf{x}}, \hat{\mathbf{y}}, \hat{\mathbf{z}}\}$ such that $\mathbf{k} = k\hat{\mathbf{z}}$, one can write $\mathbf{E} = E_x\hat{\mathbf{x}} + E_y\hat{\mathbf{y}}$ and define the polarisation by the time evolution of (E_x, E_y) . The beam intensity is defined by the Poynting vector. That is, for plane waves in homogeneous and non-absorbing media[19]:

$$I = I_x + I_y = \frac{1}{2}n\epsilon_0 c(|E_x|^2 + |E_y|^2)$$

with n the optical index of the medium, ϵ_0 the vacuum dielectric constant and c the light velocity. This is the energy per unit area per unit time. Since we shall only consider beam intensities in the air, the constant factor in the intensity expression will be skipped so that we shall write $I = I_x + I_y = |E_x|^2 + |E_y|^2$.

Working in the complex space – i.e. $E_x, E_y \in \mathbb{C}$ ³ – and concentrating on the polarisation, the effect of a perfect⁴ optical component can be described by a 2×2 matrix \mathcal{M}_J called Jones matrix [21]

$$\begin{pmatrix} E'_x \\ E'_y \end{pmatrix} = \mathcal{M}_J \begin{pmatrix} E_x \\ E_y \end{pmatrix}$$

³The electric field being given by the real part of the complex field. The use of the complex field to solve the Maxwell equation easier with complex fields (see ref. [20] for example).

⁴By perfect we mean that transmission of plane waves through the optical element does not generate interferences. I.e., multiple internal reflections, if existing, are neglected.

where (E_x, E_y) and (E'_x, E'_y) are the electric field components before and after the optical element respectively. Jones matrices of the commonly used elements (retardation plate, linear and circular polarisers, rotators ...) can be found in textbooks [18, 22, 23].

To describe light polarisation, an alternative approach is the Stokes vector and the Mueller matrix formalism. The Stokes vector is defined by

$$S = \begin{pmatrix} S_0 = |E_x|^2 + |E_y|^2 \\ S_1 = |E_x|^2 - |E_y|^2 \\ S_2 = E_x E_y^* + E_x^* E_y \\ S_3 = i(E_x E_y^* - E_x^* E_y) \end{pmatrix} = \begin{pmatrix} I \\ I_x - I_y \\ I_{+\pi/4} - I_{-\pi/4} \\ I_L - I_R \end{pmatrix} \quad (2.2)$$

where the symbol $*$ refers to the complex conjugate. I is the beam intensity; I_x , I_y , $I_{+\pi/4}$ and $I_{-\pi/4}$ are the intensities measured after a linear polariser oriented along $\hat{\mathbf{x}}$, $\hat{\mathbf{y}}$, $\hat{\mathbf{x}} + \hat{\mathbf{y}}$ and $\hat{\mathbf{x}} - \hat{\mathbf{y}}$ respectively; I_L and I_R are the intensities after circular left and right polarisers respectively. For polarised light, the following relation holds:

$$S_0 = \sqrt{S_1^2 + S_2^2 + S_3^2}.$$

In the forthcoming chapters, we shall often designate S_3 as the degree or level of circular polarisation.

The relation between the Stokes vectors before and after an optical element is also linear and is then described by a 4×4 matrix (called Mueller matrix).

Both formalisms are in principle equivalent and are related by well known mathematical transformations. Essential differences are:

- Partially polarised light is directly described by the Mueller formalism but not in a straightforward way by the Jones formalism.
- When multiple reflections inside anisotropic parallel plates are taken into account together with the Gaussian nature of the laser beam, only the Mueller matrix can be defined (see appendix A).
- As written in ref. [24]: “*The quantum theoretical treatment of electromagnetic radiation fits in very well with the treatment of optics by means of the Stokes parameters. This is quite natural since the Stokes parameters are actually the “observable” quantities in phenomenological optics.*”

This later statement is of prime importance in our case since we are going to collide a high energy electron beam with a laser beam and then observe scattered photons.

In the rest of this document, both formalisms will be used.

2.2.2 Laser beam-electron beam interaction

Interaction between a free photon and a free electron takes place by the well known “Compton scattering” process. However, going from this elementary process to the laser beam – electron interaction is not so simple. To understand this point one has to return to former works (see [24, 25, 26] for ex.). Briefly summarising:

- The two helicity states ± 1 of the photon correspond to circular left and right wave polarisations. In Quantum Field Theory (QFT), the photon field operator can be modified, according to a unitary 2×2 matrix transformation, to describe elliptically polarised radiation (see Zeeman effects in arbitrary oriented magnetic field for ex.).
- The Stokes parameters have the same form in wave optics and in QFT. However the physics interpretation is different: in QFT, $|E_x|^2/\hbar\omega$ and $|E_y|^2/\hbar\omega$, with ω the light wave angular frequency, are the number of photons per unit area unit time observed when the beam passes through linear polarisers (i.e. filters) oriented along $\hat{\mathbf{x}}$ and $\hat{\mathbf{y}}$ respectively. In wave optics $|E_x|^2$ and $|E_y|^2$ are the light intensities as stated above.
- For currently used laser beams one can assume that the photons are independent and all in the same quantum state. The laser beam-electron interaction is then reducible to the photon-electron elementary process.

To simplify our model for the laser beam-electron beam interaction, we shall further assume a mono-energetic and mono-directional electron beam. In this way, and according to the above items, the electron-photon Compton cross-section will be used to describe the interaction of the two mono-energetic beams. The electron beam energy spread (of the order of one per mille of the nominal beam energy at HERA) and the beam angular spread will be taken into account in a future work.

The number of scattered photons per unit of time and solid angle in the electron rest frame (with the Z axis along the direction of motion of the electron) is given by [10]:

$$\begin{aligned} \frac{d^3 n_\gamma}{dt d\Omega} = \mathcal{L}_{\gamma e} C \Big\{ & [1 + \cos^2 \theta + 2(k_i - k_f) \sin^2 \frac{\theta}{2}] \\ & - [S_1 \cos 2\phi + S_2 \sin 2\phi] \sin^2 \theta \\ & - 2 \sin \theta \sin^2 \frac{\theta}{2} S_3 [P_Y \sin \phi - P_X \cos \phi] \\ & - 2 \cos \theta \sin^2 \frac{\theta}{2} (k_f + k_i) S_3 P_Z \Big\}. \end{aligned} \quad (2.3)$$

where $\mathbf{k}_i = k_i \hat{\mathbf{k}}_i$ and $\mathbf{k}_f = k_f \hat{\mathbf{k}}_f$ are the momenta of the incident and scattered photon in the electron rest frame; θ is the angle between \mathbf{k}_i and \mathbf{k}_f in the electron rest frame; ϕ is the azimuthal angle (e.g. orientation of the projection of \mathbf{k}_f in the plane XY) $\vec{P} = P_X \hat{\mathbf{x}} + P_Y \hat{\mathbf{y}} + P_Z \hat{\mathbf{z}}$ is the electron polarisation vector introduced in section 2.1; S_3 is the level of laser light circular polarisation; $\mathcal{L}_{\gamma e}$ is the luminosity for the laser beam-electron beam interaction (see eq. (2.4) in the next section). The global factor C reads

$$C = \frac{1}{2} \left(\frac{e^2}{m_e c^2} \frac{k_f}{k_i} \right)^2$$

where e , m_e and c are the electron electric charge, the electron mass and the light velocity respectively.

Kinematics and angular distribution of the scattered photons are extensively described in refs. [27, 28]. From these studies we see that with a high energy electron beam, the photons are scattered within a cone of a few hundreds of μ rad in the direction of the

electron beam. Therefore the energy distribution can be measured completely within a small calorimeter.

Since Compton scattering is a two body⁵ process, the $\cos \theta$ distribution in the electron rest frame is linearly related to the scattered photon energy distribution in the laboratory frame. Hence, from eq. (2.3) one sees that:

- For best determination of the components of \vec{P} one must maximise the level of laser circular polarisation (i.e. $S_3 \rightarrow \pm 1$) and thus minimise the level of linear polarisation (i.e. $\sqrt{S_1^2 + S_2^2} \rightarrow 0$).
- Knowing the laser beam polarisation, the electron longitudinal polarisation can be determined by a fit to the distribution of the scattered photon energy (after integration over the azimuth angle). To determine the transverse polarisation, one must measure both the energy and the azimuth angle ϕ although it is expected to be very small in the region where the longitudinal polarisation is measured (between a pair of spin rotators).

For obvious reasons, an accurate measurement of the longitudinal polarisation is easier to perform.

2.2.3 Polarisation measurement modes

Assuming a Gaussian shape for the electron beam and the laser beam intensity, expressions for the laser beam-electron beam luminosity $\mathcal{L}_{\gamma e}$ have been calculated in ref. [27]. For a non-vanishing electron-laser beam crossing angle α , they obtained the total luminosity (integrated over the space variables):

$$\mathcal{L}_{\gamma e} \approx \frac{1}{\sqrt{2\pi}} \frac{1 + \cos \alpha}{\sin \alpha} \frac{I_e}{ec} \frac{P_{laser} \lambda}{hc} \frac{1}{\sigma_{ex}^2 + \sigma_{\gamma}^2} \quad (2.4)$$

where σ_{ex} and σ_{γ} are the electron beam radius along the x axis and the laser beam radius (see appendix 3.6.1 of chap. 3) respectively; P_{laser} is the laser beam power; I_e is the electron beam current. Note that eq. 2.4 assumes that the plane of interaction of the electron and laser beams is vertical (along y).

In a storage ring where electron bunches are separated by Δt in time, the number of back-scattered photons per bunch is then given by

$$n_{\gamma}/bunch = \Delta t \iint \frac{d^3 n_{\gamma}}{dt d\Omega} d\Omega.$$

Depending on the value of n_{γ} , one can define three different measurement modes:

- Single photon mode: $n_{\gamma} \ll 1$
- Few photon mode: $n_{\gamma} \approx 1$
- Multi photon mode: $n_{\gamma} \gg 1$.

⁵At HERA the centre of mass energy of the Compton process is below the pair mass threshold (i.e. e^+e^- pair cannot be created).

When $n_\gamma \gg 1$, the statistical uncertainty on the measurement of the longitudinal polarisation is better as well as the ratio of the signal to background. But, in fact, high values of n_γ induce large systematics on the scattered photon energy measurement and therefore the few photon mode appears to be a good compromise between the single and the multi photon modes. In addition, a high energy pulsed laser beam is needed for the multi photon mode and the laser beam transport and diagnostics are not easy for such beams so that additional systematic bias may thus appear.

Mathematical details of the statistical analysis leading to the determination of P_Z in these three modes are given in appendix 2.3. In this section, we briefly discuss the advantages and disadvantages of these three modes. A detailed description of the few-photon mode polarisation measurement is given in section 2.2.4. This mode was not considered by previous experiments, this is our original contribution in this field.

For the three modes of polarisation measurement, one must supply an experimental setup similar to the one shown in fig. 2.13, that is: a photon extraction line and a calorimeter to measure the energy and beam position if the determination of P_X and/or P_Y is foreseen. In such experiments, the two main backgrounds are: beam-gas bremsstrahlung and beam-blackbody radiation Compton scattering (see section 2.2.4 for details).

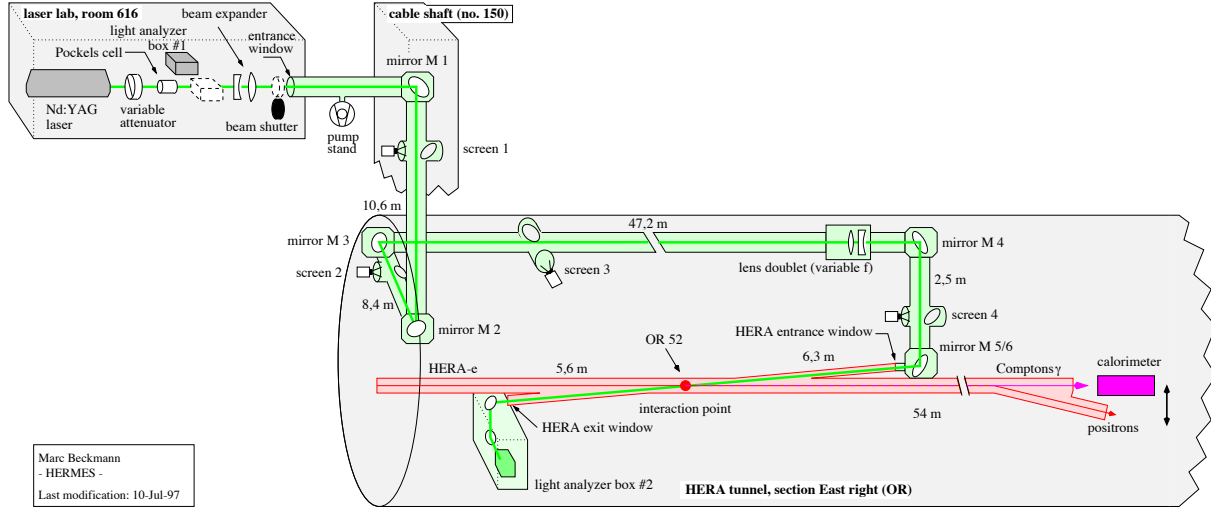


Figure 2.13: *Layout of the present longitudinal polarimeter at HERA. The laser beam is brought inside the electron vacuum beam pipe by an entrance window. Compton photons are scattered in the direction of the electron beam within a very narrow angular cone. Back-scattered photons escape the beam pipe through an exit window located at the end of the right section and enter a calorimeter ≈ 60 m downstream from the laser beam-electron beam interaction point (IP). An optical bench is located on the other side of the IP to stop the laser beam and to measure the light polarisation.*

Single photon mode

In this mode, the probability that two Compton scatterings occur within a single bunch crossing is negligible. Therefore eq. (2.3) can be used to fit the experimental data.

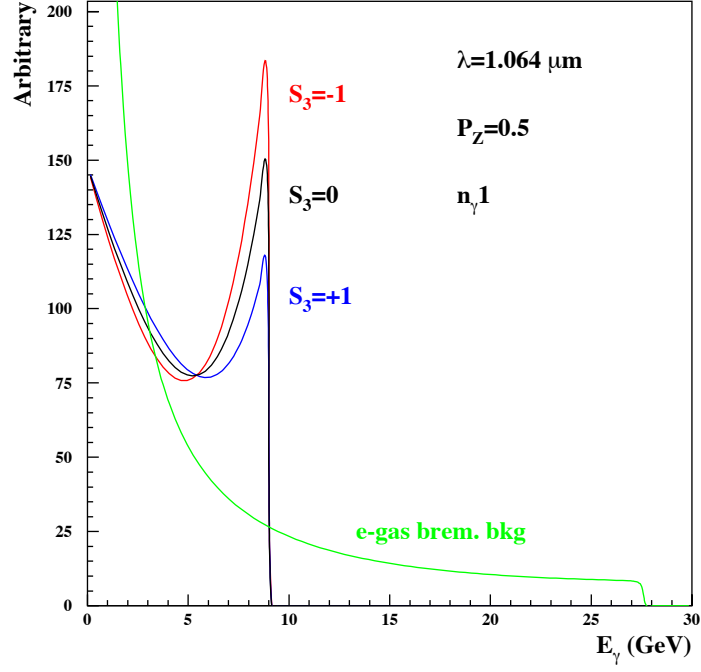


Figure 2.14: *Back-scattered Compton photon energy spectra for three values of the laser degree of circular polarisation $S_3 = 0, \pm 1$. Also shown is the electron beam - gas bremsstrahlung background for an electron beam energy of 27.5 GeV. Relative normalisations between Compton and bremsstrahlung spectra are arbitrary and no detector effect has been taken into account.*

Fig. 2.14 shows the energy distributions calculated with eq. (2.3) for $P_Z = 0.5$ and $S_3 = \pm 1$ using the HERA electron beam energy (27.5 GeV) and the ND:YAG laser beam wavelength $\lambda = 1.064\mu\text{m}$. From this figure one sees that the sensitivity to P_Z is mainly located in the high energy region of the spectrum. Calorimeters operating in the range 1-10 GeV are then required. In fig. 2.14, the edge of the Compton energy distribution comes from the kinematic limit of the Compton scattering.

To discuss the performance of the single photon mode, let us describe the present TPOL measurement setup at HERA [10]. A 10 W laser with green light is used and $n_\gamma \approx 0.01/\text{bunch}$. The calorimeter is segmented in two parts in the vertical direction so that the total photon energy and the vertical position of the photon impact can be reconstructed simultaneously.

A description of the data analysis leading to the measurement of P_Y is outside the scope of this work (see[10]). What is interesting to mention here is that P_Y is measured at a few percent level. This accuracy is limited by: the knowledge of the electron beam shape, the determination of the y position from the energy measurements, the statistics. Currently, the statistical precision of the HERA-TPOL measurement is $\approx 10\%$ per bunch and per minute.

The advantage of the single photon mode is that one can calibrate the calorimeter absolutely using the Compton edge (and the bremsstrahlung edge, see fig. 2.14). With the recent upgrade of the HERA-TPOL data acquisition system, the accuracy on the absolute calibration is below 0.5% and controlled on a 1 min time base. The disadvantage of this mode is the low statistics due to low luminosity. In the case of large background levels, the signal may also be too diluted thereby reducing the polarisation measurement accuracy.

From the performances of the TPOL measurement in the single photon mode, one sees that the accuracy of the longitudinal polarisation measurement would be limited by statistics in this mode.

Few photon mode

To extract the longitudinal polarisation, one proceeds as in the single photon mode except that we must now consider a Poissonian superposition of back-scattered photons. Multi-convolutions of eq. (2.3) must then be calculated and a fit has to be performed to the experimental data. Fig. 2.15 shows the energy distributions in the few photon modes. Comparing with the single photon mode one can remark the presence of the double Compton edge and a high energy tail. This means that one gets three points to perform an absolute calibration of the calorimeter: the two Compton edges (and the bremsstrahlung edge, see fig. 2.14). This allows a survey of the calorimeter linearity.

For longitudinal polarisation, we proved that non-linear fits are numerically stable and reproduce the experimental distributions (within the accuracy of these measurements, see appendix 2.3)

Experimentally one must use a very high continuous laser beam power (typically a few kW) to reach $n_\gamma/\text{bunch} \approx 1$. Nevertheless, special experimental setups are feasible as will be shown in chap. 3.

With respect to the single photon mode, advantages of this method are threefold: first the statistics is large, second the ratio signal to background is better and third single and double Compton edges can be used to calibrate the calorimeter. Very precise longitudinal

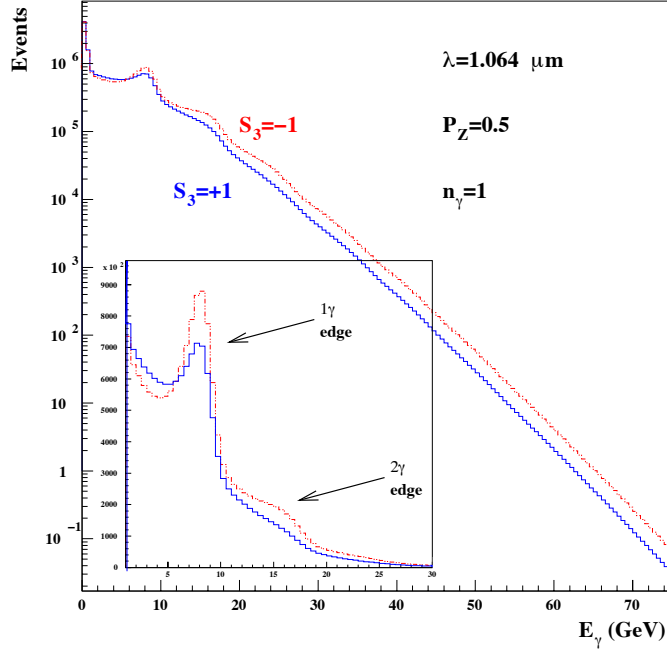


Figure 2.15: Compton energy spectra for $S_3 = \pm 1$ in the few photon mode ($n_\gamma/\text{bunch} = 1$). Distributions are shown on linear and logarithmic scales to exhibit the long energy tail. Gaussian smearing of the photon energy has been applied as indicated in appendix 2.3.

polarisation measurement (below $1\%/bunch/min$) can then be achieved in principle. The disadvantage is that one has to perform a non-linear fit, but it turns out that this is more a numerical difficulty than a disadvantage.

Multi photon mode

When the background is large, or when the polarisation needs to be known after a single bunch crossing (i.e. at linear colliders), high energy pulsed lasers are used. After a bunch-laser beam interaction a large number photons are back-scattered, typically $\approx 1000/bunch$.

One can then apply the limit theorem so that \vec{P} is obtained from the measurement of the average energy and average impact position in the calorimeter. The averages are linear forms of the \vec{P} components. To illustrate the measurement of P_z in this mode, experimental energy distributions taken by the HERA-LPOL are shown in fig. 2.16. The longitudinal polarisation is linearly proportional to the difference between the two distributions obtained with a laser beam polarised circular left and right.

The disadvantage of this mode is that a total energy ~ 10 TeV is seen by the calorimeter. Since the energy calibration of the calorimeter is done using low energy beam electrons (and the single photon Compton edge), the polarisation measurement is affected by a systematic uncertainty of the order of a few percent ⁶. Another difference compared with the

⁶At LEP, the transverse polarisation was measured in the multi-photon mode [29] and an overall systematic uncertainty of 15% was quoted [30] (which was not a limiting factor since the polarimeter was

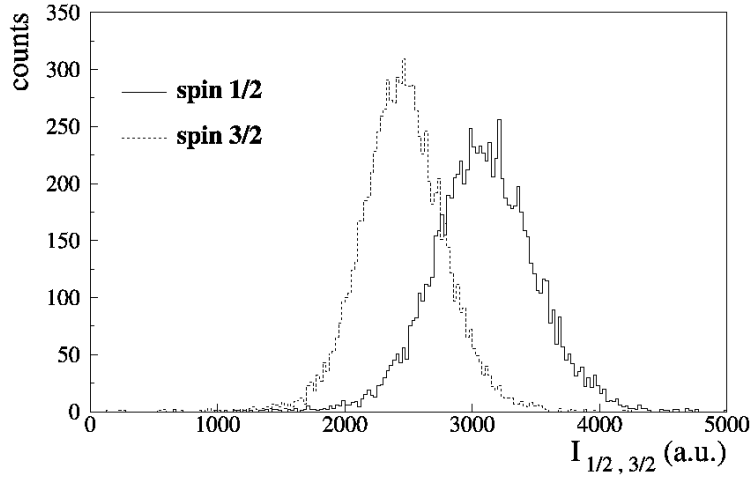


Figure 2.16: *HERA-LPOL experimental photon energy distributions for $S_3 = +1$ (spin 3/2 in the plot) and $S_3 = -1$ (spin 1/2 in the plot). From [12].*

two other modes is that one cannot extract the polarisation without combining the two photon energy spectra corresponding to the laser beam left and right polarisation. The statistics is limited by the laser pulse frequency (100 Hz maximum for the HERA-LPOL) this leads to a statistical precision of the present HERA-LPOL comparable to the one of the HERA-TPOL (see above).

Before ending this section, it should be mentioned that in linear colliders it is possible to detect the scattered electron instead of the scattered photons. The advantage is twofold: the polarisation information is carried by the lower part of the electron energy spectrum and the use of a spectrometer leads to a measurement of both the scattered angle and the energy. This redundancy led to the high precision longitudinal polarisation measurement at SLAC-SLC [7] using a high power pulsed laser.

Since we are detecting the scattered photons at HERA, in order to reach the per mille level on the statistical and systematic accuracies on the longitudinal polarisation measurement, we choose to use the few photon mode. The rest of the chapter is devoted to a more detailed description of the few photon mode.

2.2.4 Polarisation measurement in the few photon mode

In this section we present the basic formula used in our studies. Our “experimental setups” are also described there. Next, a numerical study, describing the performance of the LPOL measurement in the few photon mode is presented. This study was performed for our proposal of the LPOL upgrade.

Signal

For a longitudinally polarised electron beam, the Compton scattering differential cross-section is obtained from eq. (2.3). In the laboratory rest frame and as a function of the

used to measure the beam energy by depolarisation resonances [31]).

back-scattered Compton photon (BCP) energy one gets (see eq. (8) of [10], we won't give here the complete expression which is obtained by elementary algebra from eq. (2.3)):

$$\frac{d\sigma_c}{dE_\gamma} = \frac{d\sigma_0}{dE_\gamma} + S_3 P \frac{d\sigma_z}{dE_\gamma} \quad (2.5)$$

where $S_3 = -1$ for a circular-right polarised laser beam and $S_3 = +1$ for a circular-left laser beam; P is the electron beam LPOL; E_γ is the BCP energy in the lab. frame. $d\sigma_0/dE_\gamma$ and $d\sigma_z/dE_\gamma$ are two functions of E_γ and of the lepton and laser beam energies, E_e E_λ respectively.

In our numerical studies we shall use $E_\lambda = 1.165$ eV (the ND:YAG laser energy) and $E_e = 27.5$ GeV.

Beam Gas bremsstrahlung background

The differential cross-section $d\sigma(e + g \rightarrow e + g + \gamma)/dE_\gamma$ - where g stands for the residual gas in the beam pipe - is described by eq. (1) of ref. [32]:

$$\frac{d\sigma_{eg}}{dE_\gamma} = 4\alpha r_e^2 \frac{E_{e'}}{E_e E_\gamma} \left[\left(\frac{E_e^2 + E_{e'}^2}{E_e E_{e'}} - \frac{2}{3} \right) [Z^2 \ln(184.15 Z^{-1/3}) + Z \ln(1194 Z^{-2/3})] + \frac{1}{9}(Z^2 + Z) \right] \quad (2.6)$$

where $E_{e'} = E_e - E_\gamma$; r_e is the electron classical radius and $\alpha = 1/137$. The mean atomic number of the residual gas nucleus is taken to be $Z = 4.2$ [32].

A more complete formula [33] has also been implemented in our numerical program.

Compton-blackbody scattering background

This background is extensively described in ref. [34] where it has been studied using the TPOL set-up. It consists of blackbody photons radiated by the beam pipe ($T \approx 310$ K). A rate of 0.013/bunch for a current of 0.3mA/bunch has been reported. However, the LPOL interaction point is located after 50m of an HERA straight section (to be compared to 7.3 m for the TPOL where a weak dipole deviates the beam). Therefore, with an electron beam current of 40 mA and 190 bunches, one expects a rate of ≈ 0.06 photons per bunch for LPOL.

To describe this background we shall follow the calculations of ref. [34] to which we refer for more details.

The blackbody energy spectrum (in the lab. frame) is given by:

$$\frac{dn(E_\lambda)}{dE_\lambda} \propto \frac{E_\lambda^2}{e^{E_\lambda/k_B T} - 1}$$

where k_B is the Boltzmann constant. The energy distribution of the blackbody photon scattered by the electron beam (in the lab. frame) is given by

$$\frac{dn(E_\gamma)}{dE_\gamma} \propto \int_{(\cos \theta_\lambda)_{min}}^1 \int_{E_{\lambda,min}}^{E_{\lambda,max}} \frac{dn(E_\lambda)}{dE_\lambda} (1 + \beta \cos \theta_\lambda) \frac{d\sigma_c}{dE_\gamma} dE_\lambda d \cos \theta_\lambda \quad (2.7)$$

where:

- θ_λ is the angle between the incoming blackbody photon and the electron beam direction in the lab. frame;
- $\beta \approx 1$ is the electron beam velocity;
- $E_{\lambda,max}$ is infinite in principle but it suffices – for the numerical computation of the integral – to take $E_{\lambda,max} \approx E_{\lambda,min} + 12 \times k_B T$;
- $d\sigma_0/dE_\gamma$ is the unpolarised Compton differential cross-section (c.f. eq. (2.5)) including both E_λ and θ dependences;
- the lower bound of the integral is given by the kinematic relations:

$$(\cos \theta)_{min} = \frac{m_e k_{i,min}}{\beta \gamma E_{\lambda,max}} - \frac{1}{\beta} ; \quad E_{\lambda,min} = \frac{m_e k_{i,min}}{\gamma(1 + \beta \cos \theta_\lambda)}$$

with $\gamma = 1/\sqrt{1 - \beta^2}$ and $k_{i,min} = E_\lambda/2(E_e - E_\lambda)$.

- the proportionality factor is not important since we normalised the amount of events to the integral over the energy (from 0 to 3 GeV).

The maximum energy reached by the scattered blackbody photon is given by

$$E_{\gamma,max} = \frac{E_e}{1 + \frac{m_e}{2\gamma E_{\lambda,max}(1+\beta)}}$$

and amounts to ≈ 3 GeV for $E_{\lambda,max} = 0.3$ eV.

Synchrotron radiation background

All details concerning the synchrotron radiation around the IP of the LPOL can be found in ref. [35]. Here we just briefly summarise the main features related to this background.

The IP is located inside the HERA 90BH bending magnet. The calorimeter is then illuminated by synchrotron radiation which is made of a large number of low energy photons (the total reaches ≈ 1 TeV). A lead plate is located in front of the calorimeter so that only 100 MeV is seen in the detector. We shall not consider this background in the present study since it appears as an energy pedestal in the calorimeter and can thus be determined experimentally [34]. The effect of the lead plate on the resolution will be studied by varying the energy resolution of the calorimeter.

Measurement set-up

To extract the electron longitudinal polarisation, we shall adopt the usual measurement procedure. The following three measurements are performed successively:

1. Laser off: background energy distribution is measured (eqs. (2.6,2.7)).
2. Laser beam circular left polarised (=Laser left): signal measurement with $S = +1$ (eq. (2.5), pile-up with backgrounds of (eqs. (2.6,2.7)) is included.
3. Laser beam circular right polarised (=Laser right): signal measurement with $S = -1$ (eq. (2.5), pile-up with backgrounds of (eqs. (2.6,2.7)) is included.

With a 10 MHz data acquisition system, one can consider at most $\approx 3 \cdot 10^6$ records per minute for each electron bunch and each of the three experiments. These records contain any kind of background or signal photons and even electronic noise (e.g. electronic pedestals).

Note that, once the backgrounds are understood, only one experiment (laser left or right) is required in principle to determine the polarisation.

2.2.5 Numerical studies

Mathematical expressions of the statistical estimators that can be used to extract the longitudinal polarisation are given in appendix 2.3.

We shall concentrate here on the few photon mode and therefore use the estimator #1 of the appendix 2.3 (= a Likelihood fit to the scattered photon energy spectrum). A fitting programme has been written and tested with experimental data of the HERA-LPOL. These data were taken by “reducing” the power from the HERA-LPOL pulsed laser. However, since the electronics, the laser operation mode (i.e. pulse delay) and the calorimeter are designed for the multi photon mode, the data quality is not optimum for the single and the few photon modes. This feature is illustrated by the top plots of figs. 2.17 and 2.18 where the background fits are compared to the laser off measured energy distributions. The very large Gaussian centred at 0 is the pedestal distribution which extends up to the bremsstrahlung edge. In any case, by fitting these distributions one finds $P \approx -0.55$ and $n_\gamma \approx 1.5, 6$ for figs. 2.17 and 2.18 respectively. Fit results are shown together with experimental data and it is important to note that the high energy tails are well described. Notice that the two laser-on distributions of fig. 2.18 are not Gaussian.

We have performed a series of studies to estimate the accuracy of a longitudinal polarisation measurement in the few photon mode considering a ND:YAG laser (wavelength $\lambda = 1.064\mu\text{m}$). Laser off, left and right energy histograms for one electron bunch are computed varying n_γ and P . The number of entries corresponds to 6 s DAQ period, i.e. $\approx 6 \cdot 10^6$ DAQ events. Next a fit using estimator #1 is performed and both P and its uncertainty are determined.

The absolute statistical accuracy ΔP obtained from this analysis is presented in fig. 2.19 for $P = 0.5$ and two bremsstrahlung background rates describing the range presently observed in the HERA-LPOL region. For $n_\gamma > 0.3$ one sees that a statistical accuracy below 1%/bunch/min is reached. However, using eq. (2.4) one finds that this number corresponds to a ND:YAG laser power of $\approx 20\text{kW}$ for a 1 mA electron beam current (that is $\approx 500\text{W}$ for 40 mA) and a laser-electron crossing angle of 58 mrad.

Using our numerical programme, we can also estimate the main systematic uncertainties. To do so, the calorimeter energy response is modelled by a Gaussian of width $\sigma = 14.4\%\sqrt{E} \oplus 0.435\%E$ corresponding to the new calorimeter. Three Compton rates $n_\gamma/\text{bunch} = 0.1, 1, 2$ and eight values of the electron beam polarisation $P = 0, 0.1, \dots, 0.8$ are chosen. The following effects have been studied:

- Uncertainty on the linear calibration constant: taking a scale uncertainty of 0.5%⁷, the systematic shifts of the polarisation measurements are below 0.1%.
- Uncertainty due to non-linearity: taking a non-linearity of 1% at 20 GeV, the systematic shifts of the polarisation measurements are shown in fig. 2.20. The effect is

⁷This is the present uncertainty quoted by the HERA-TPOL, see section 2.2.3

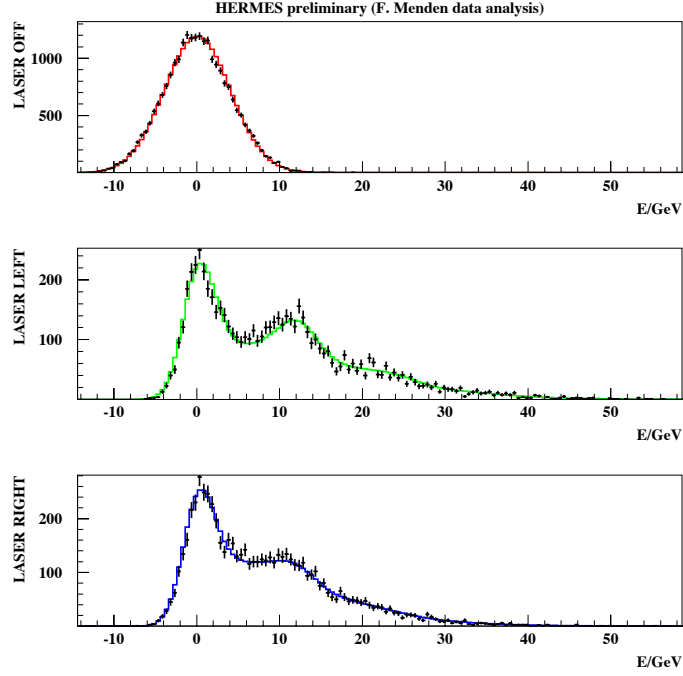


Figure 2.17: Data taken at the HERA-LPOL by the HERMES Collaboration (crosses). Upper plot is the observed laser off energy distribution, lower plots are the laser on experiments. Laser wavelength is $\lambda = 0.5\mu\text{m}$ and electron beam energy $E_e = 27.5\text{GeV}$. Full lines show the results of a fit to the experimental data.

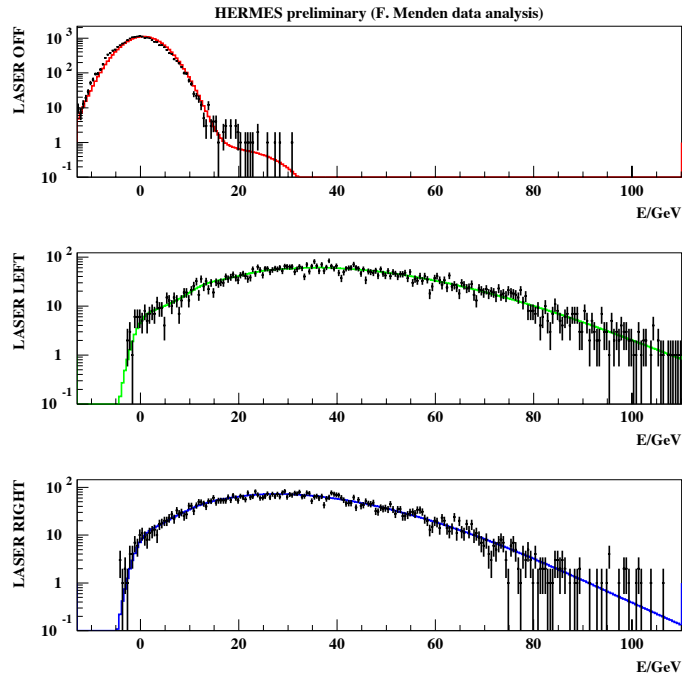


Figure 2.18: As fig. 2.17 but for a higher laser pulse energy and a vertical logarithmic scale.

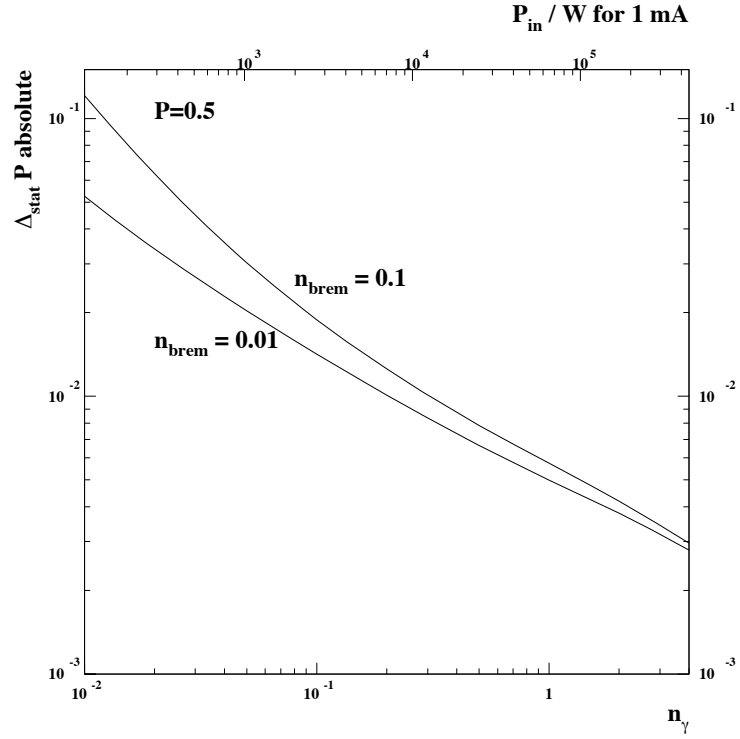


Figure 2.19: Statistical uncertainty of the polarisation per bunch and per minute as a function of the number of back-scattered photons, n_γ . Two curves are shown for two different background levels of 1% and 10%. Also shown is the laser power needed to obtain a given number of back-scattered photons, assuming a crossing angle of 58 mrad.

large, especially for a large event rate. Fig. 2.21 shows the numerical derivatives of the energy distributions with and without 1% non-linearity. Using the three points (1γ , 2γ and bremsstrahlung kinematic edges), such an effect can be controlled at a few per mille level so that the remaining systematic uncertainty on the polarisation measurement can be reduced at a few per mille level as well.

- Uncertainty due to the knowledge of the dead material in front of the calorimeter: to estimate this effect we have generated the energy spectra taking into account 2X0 of lead (model of ref. [36] is used) and perform the fits without it. The systematic shifts obtained for the polarisation measurements are shown in fig. 2.22. This is an important effect. Our example is not realistic but it shows that a precise control and modelling of effects of dead materials is necessary.

From this study we conclude that an accuracy at the few per mille level can be achieved in the few photon mode. A longitudinal polarimeter operating in this mode is then adequate for the HERA-II physics programme. A precise control of the calorimeter response and material is however mandatory.

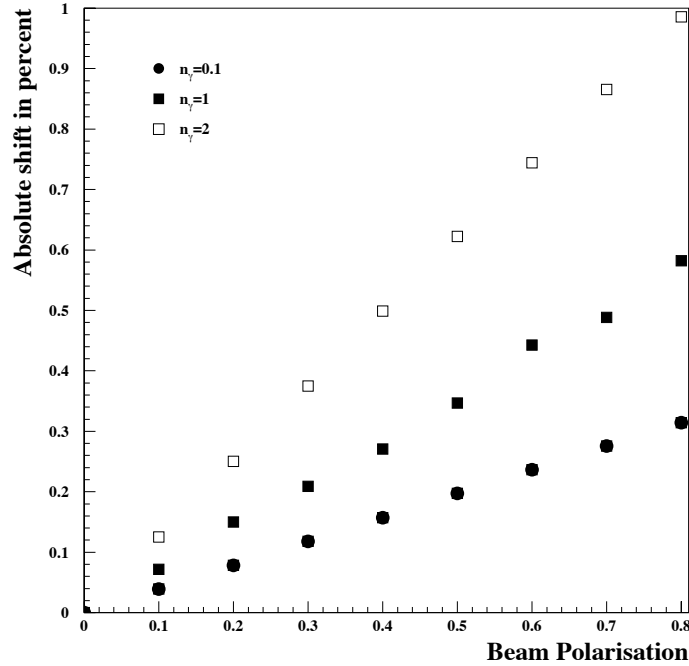


Figure 2.20: *Systematic shift of the polarisation measurement induced by 1% calorimetric non-linearity at 20 GeV.*

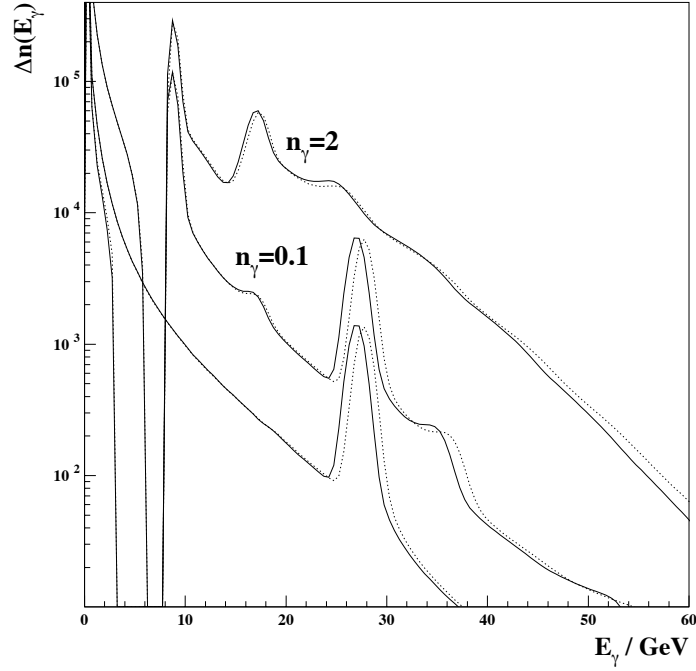


Figure 2.21: Numerical derivatives of the energy distributions for a perfect detector (full curves) and including a 1% non-linear calibration factor (dashed curves). The lower curve is the laser-off distribution. The numerical derivatives shown in this figure are simply obtained by subtracting the contents of all pairs of adjacent bins of the photon energy spectra.

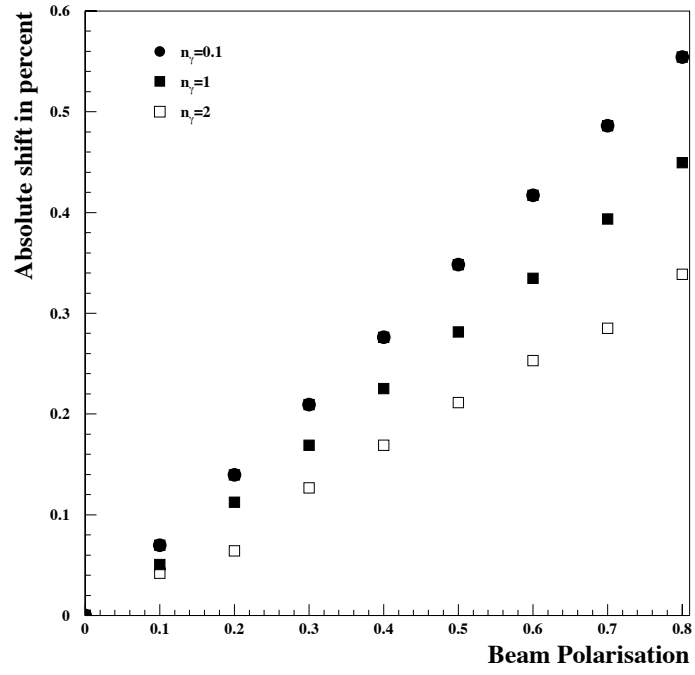


Figure 2.22: *Systematic shift of the polarisation measurement induced by ignoring the two radiation lengths of lead in the fit (see text).*

2.3 Appendix

This appendix is a revised version of an internal note written by C. Pascaud and myself. It describes the statistical analysis of the back-scattered Compton photons (BCP) energy distribution in the three modes defined in section 2.2.3. We thus construct some statistical estimators from a model of the BCP energy spectrum. Since our statistical treatment for the few photon mode cannot be found in the literature, details are given here.

2.3.1 Statistical estimators

Notations

In order to introduce our notations let us first consider the single-photon mode. Let us also consider one of the three experiments defined in the previous section. In this case there is, at most, one photon observed in the calorimeter. Then, after one period T_{DAQ} of Data Acquisition (DAQ), the average number of events of energy between E and $E + \Delta E$ is:

$$n_{1\gamma}(i, n, e, E) = \sum_{k=1}^3 a_k(n, i) \times \epsilon_k^e \times f_k(E) \quad (2.8)$$

where i stands for the bunch number; n is the number of DAQ periods accumulated since the beginning of the luminosity run ($n \times T_{DAQ}$ is the total elapsed time); e is the experiment index ($e = 1, 2, 3$); the constants a_k will be determined by the fit, they are defined by

$$\begin{aligned} a_1(n, i) &= \mathcal{L}_B(n, i) \times T_{DAQ} \\ a_2(n, i) &= \mathcal{L}_c(n, i) \times T_{DAQ} \\ a_3(n, i) &= P(n, i) \times \mathcal{L}_c(n, i) \times T_{DAQ}; \end{aligned} \quad (2.9)$$

$\mathcal{L}_B(n, i)$ and $\mathcal{L}_c(n, i)$ are the background (electron beam - residual gas and electron beam - blackbody photons interactions)⁸ and electron beam-laser beam luminosities respectively, they are defined for each bunch i and are functions of the elapsed time nT_{DAQ} . $f_1(E)$ is the background energy distribution; $f_2(E)$ is the energy distribution for unpolarised electrons; $f_2(E) + f_3(E)$ is the energy distribution for totally polarised electrons and laser beam circular left polarised ($P = +1$); ϵ_k^e characterises the three experiments described in the previous section and has the following values:

- $\epsilon_k^1 = 1, 0, 0$ Laser off;
- $\epsilon_k^2 = 1, 1, 1$ Laser left;
- $\epsilon_k^3 = 1, 1, -1$ Laser right.

f_1 , f_2 and f_3 can be determined by a full simulation of the detector response to the BCP and to the background. To be explicit we give here the expressions of these functions

⁸In fact there is one parameter a per background source. In order to simplify the presentation we choose to gather all these parameters into a single one.

in the case of the single-photon mode. Neglecting for now any detector effects, one has:

$$\begin{aligned} f_1(E) &= \int_E^{E+\Delta E} \frac{d\sigma_B}{dE'} dE' \\ f_2(E) &= \int_E^{E+\Delta E} \frac{d\sigma_0}{dE'} dE' \\ f_3(E) &= \int_E^{E+\Delta E} \frac{d\sigma_Z}{dE'} dE' \end{aligned} \quad (2.10)$$

However, in the general case the number of photons observed in the detector is not fixed. Some complex mixtures are expected: one (or more) BCP can occur together with one (or more) background event. We shall now turn to the description of this general case.

Probability for the number of photons per bunch-crossing

We drop now the bunch and elapsed time indexes. The average number of photons observed in the detector after **one bunch-crossing** for one experiment set-up e is given by

$$M_e = \int_0^\infty \frac{dm_e(E)}{dE} dE \quad (2.11)$$

where $dm_e(E)/dE$ is simply obtained by dropping the integral over the energy in the expressions of f_k (see eq. (2.10)).

The fluctuations of M_e following a Poissonian law, one has:

- $\mathcal{P}_0 = e^{-M_e}$ is the probability to have 0 photons when one expects M_e ;
- $\mathcal{P}_N = e^{-M_e} \frac{M_e^N}{N!}$ is the probability to have N photons when one expects M_e .

In the following we shall drop the experiment index e .

Probability for an energy measurement per bunch-crossing

Once a given photon i is observed, the probability to find it with an energy between E_i and $E_i + \Delta E_i$ is $m(E_i)/M$. Hence, the probability to get N photons of energies between E_i and $E_i + \Delta E_i$, $i = 1, \dots, N$ is :

$$\mathcal{P}_N \prod_{i=1}^N \frac{m(E_i)}{M} = \frac{e^{-M}}{N!} \prod_{i=1}^N m(E_i) \quad (2.12)$$

In our case only the total energy $E = \sum_1^N E_i$ is measured. Using eq. (2.12), we can write the probability to get N photons with total energy between E and $E + \Delta E$ as follows

$$e^{-M} \frac{m_N(E)}{N!}$$

with

$$\begin{aligned}
m_i(E) &= \int_E^{E+\Delta E} \frac{dm_i(E')}{dE'} dE', \\
\frac{dm_i(E)}{dE} &= \int_0^{E_e} \cdots \int_0^{E_e} \delta(E - \sum_{k=1}^i E_k) \prod_{k=1}^i \frac{dm(E_k)}{dE_k} dE_k.
\end{aligned} \tag{2.13}$$

Explicitly, we have

$$\begin{aligned}
m_1(E) &= \int_E^{E+\Delta E} \frac{dm(E')}{dE'} dE' \\
m_2(E) &= \int_E^{E+\Delta E} \int_{\max(0, E'-E_e)}^{\min(E_e, E')} \frac{\partial m(E' - E'')}{\partial E'} \times \frac{dm(E'')}{dE''} dE'' dE' \equiv m \otimes m \\
&\vdots \\
m_N(E) &= \int_E^{E+\Delta E} \int_{\max(0, E'-N \times E_e)}^{\min(E_e, E')} \frac{\partial m_{N-1}(E' - E'')}{\partial E'} \times \frac{dm(E'')}{dE''} dE'' dE' \equiv m \otimes m \dots \otimes m
\end{aligned} \tag{2.14}$$

where we have used $dm(E' - E'')/d(E' - E'') = \partial m(E' - E'')/\partial E'$ and where the symbol \otimes is introduced for convenience.

Finally the probability to receive in the detector an energy between E and $E + \Delta E$ is:

$$\int_E^{E+\Delta E} \frac{d\mathcal{P}(E')}{dE'} dE' = e^{-M} \sum_{i=1}^{\infty} \frac{m_i(E)}{i!}. \tag{2.15}$$

The detector response is modelled by a Gaussian of width $\sigma_E = \alpha\sqrt{E} + \sigma_p$ where σ_p represents the pedestal effect. Possible bias of the energy scale is taken into account by using two real parameters β and γ (see eq. (2.16)). Functions m_i must then be replaced by the smeared functions:

$$\frac{d\tilde{m}_i(E)}{dE} = \int_0^{+\infty} \frac{dm_i(E')}{dE'} \times \frac{e^{-\frac{[E(1+\beta+\gamma E) - E']^2}{2\sigma_{E'}^2}}}{\sqrt{2\pi}\sigma_{E'}} dE'. \tag{2.16}$$

Even when no photon enters the calorimeter, because of pedestal, one may measure a non-vanishing energy. We must then extend the range of the index i down to 0 and introduce

$$\frac{dm_0}{dE} = \delta(E)$$

in eqs. (2.13, 2.14). With this change and extensions, the probability to “measure” in the detector an energy between E and $E + \Delta E$ is:

$$\int_E^{E+\Delta E} \frac{d\mathcal{P}(E')}{dE'} dE' = e^{-M} \sum_{i=0}^{\infty} \frac{m_i(E)}{i!} = \mathcal{P}_0 \times \int_E^{E+\Delta E} \frac{d\Psi(E')}{dE'} dE', \tag{2.17}$$

where the last equality serves as a definition of the function Ψ that we shall use below. Eq. (2.17) is normalised as follows:

$$\int_0^\infty \frac{d\mathcal{P}(E)}{dE} dE = 1. \quad (2.18)$$

Proof:

Integrating eq. (2.13) and using eq.(2.11) one gets

$$\int_0^\infty \frac{dm_i(E)}{dE} dE = \prod_{k=1}^i \int_0^{E_e} \frac{dm(E_k)}{dE_k} dE_k = M^i \quad (2.19)$$

so that

$$\int_0^\infty \frac{d\mathcal{P}(E)}{dE} dE = e^{-M} \sum_{i=0}^\infty \frac{M^i}{i!} = e^{-M} \times e^M = 1. \quad (2.20)$$

Estimator #1: Likelihood of the energy distributions

This first estimator is a likelihood maximisation of the energy distributions. In order to simplify the mathematical expressions, let us consider one of the three experiments described in section 2.2.4. During one DAQ period T_{DAQ} we assume that there is a sampling of S measurements (per electron bunch), S being fixed and known. The Likelihood density δL of such an experiment is given by:

$$\delta L = \prod_{i=1}^S \frac{d\mathcal{P}(E_i)}{dE_i}. \quad (2.21)$$

To show how this likelihood density is normalised we turn to the dimensionless likelihood and reformulate eq. (2.21) as follows:

$$L = \prod_{i=1}^S \left\{ \sum_{k=0}^K \mathcal{P}_k h_i^k \right\}$$

with

$$\mathcal{P}_k = \int_{E_k}^{E_{k+1}} \frac{d\mathcal{P}(E)}{dE} dE,$$

where the E_k are a set of energies increasing with k and ranging from $-\infty$ for $k = 0$ to $+\infty$ for $k = K$.

The integer variable h_i^k characterises the i^{th} event: $h_i^k = 1$ if the measured energy is between E_k and E_{k+1} and 0 otherwise. For an event i there is only one value of k such $h_i^k \neq 0$; this can be expressed by:

$$\sum_{k=0}^K \mathcal{P}_k h_i^k = 1 \quad (2.22)$$

then eq. (2.18) may be rewritten:

$$\sum_{k=0}^K \mathcal{P}_k \mathcal{P}_k = 1$$

We see that L is as a function of the variables h_i^k . Its normalisation is obtained by summing over the h_i^k under the constraint of eq. (2.22):

$$\sum_{h_1^0=0}^1 \sum_{h_1^1=0}^1 \cdots \sum_{h_S^0=0}^1 \sum_{h_S^1=0}^1 \cdots \prod_{i=1}^S \left\{ \sum_{k=0}^K \mathcal{P}_k h_i^k \right\} = 1 \quad (2.23)$$

Proof:

We start by performing all the sums related to a given event j . As only the factor concerning the event j depends on that variable we may rewrite eq. (2.23) as follows:

$$\left\{ \sum_{h_1^0=0}^1 \sum_{h_1^1=0}^1 \cdots \sum_{h_S^0=0}^1 \sum_{h_S^1=0}^1 \cdots \prod_{i \neq j} \left[\sum_{k=0}^K \mathcal{P}_k h_i^k \right] \right\} \left\{ \sum_{h_j^0=0}^1 \sum_{h_j^1=0}^1 \cdots \left[\sum_{k=0}^K \mathcal{P}_k h_j^k \right] \right\} = 1$$

Using $\{ h_j^k = 1 \Rightarrow h_j^l = 0 \text{ for } l \neq k \}$ we obtain

$$\sum_{h_j^0=0}^1 \sum_{h_j^1=0}^1 \cdots \left[\sum_{k=0}^K \mathcal{P}_k h_j^k \right] = \sum_{k=0}^K \mathcal{P}_k \mathcal{P}_k$$

which is equal to 1. Finally, working out all the events we arrive at the expected result of eq. (2.23).

Let us now look at the practical use of eq. (2.21). To be explicit, let us re-introduce the experiment index. Instead of δL we shall consider

$$\delta W \equiv -2 \ln \delta L = 2 \sum_{e=1}^3 \left\{ S_e M_e - \sum_{i=1}^{S_e} \ln \left(\frac{d\Psi_e(E_i)}{dE_i} \right) \right\}.$$

In fact the measured events will not be kept individually by the acquisition system but rather put in an histogram. H bins covering the energy range E_0 to E_H are then defined. With

$$\Psi'_k = \frac{\int_{E_{k-1}}^{E_k} \Psi(E) dE}{E_k - E_{k-1}},$$

we get

$$\boxed{W = 2 \left(SM - \sum_{h=1}^H N_h \ln \Psi'_h \right)}, \quad (2.24)$$

where N_h is the number of events contained in the bin h (this quantity is measured experimentally). Notice that in eq. (2.24) there is an implicit sum over the three experiments.

In eq. (2.24) we have omitted two contributions which do not depend upon the parameters a_k :

- a combinatorial factor $\ln(S! \prod_{h=1}^H N_h!)$, which comes from the fact that one would get the same histogram from two experiments differing only by interchange of events i and j ;
- a sum over the bin widths $\ln(E_h - E_{h-1})$.

The parameters to be determined by minimising eq. (2.24) are – for each bunch and each DAQ period – a_1 , a_2 and a_3 (which are directly related to P , \mathcal{L}_c , \mathcal{L}_{bg}). In order to reach this goal we search for the maximum likelihood. In eq. (2.24) N_h and S are taken from the experimental energy histogram and the variations of W with a_k are all contained in $\Psi(E_h)$ and M .

The maximum of W corresponds to the following set of partial differential equations (obtained by differentiating eq. (2.24):

$$W'(a_k) = \frac{\partial W}{\partial a_k} = 2S \frac{\partial M}{\partial a_k} - 2 \sum_{h=1}^H N_h \frac{1}{\Psi'} \frac{\partial \Psi'}{\partial a_k} = 0. \quad (2.25)$$

In order to solve this system we use a classical iterative scheme similar to a χ^2 minimisation procedure. We define

$$\hat{W}_{ij} = \frac{1}{2} \frac{\partial^2 W}{\partial a_k \partial a_j} = \sum_{h=1}^H N_h \frac{1}{(\Psi')^2} \frac{\partial \Psi'}{\partial a_k} \frac{\partial \Psi'}{\partial a_j} - \sum_{h=1}^H N_h \frac{1}{\Psi'} \frac{\partial^2 \Psi'}{\partial a_k \partial a_j} \quad (2.26)$$

and we write a_k some initial values of the unknown parameters. We then search for a set of parameters $a_k + \delta a_k$ such that all the derivatives vanish. Writing a first order expansion for $W'(a_k)$

$$W'(a_k + \delta a_k) = W'(a_k) + \hat{W}_{ij} \delta a_j \quad (2.27)$$

we obtain

$$\delta a_k = - \sum_{i=1}^3 \hat{W}_{ki}^{-1} \times W'(a_i). \quad (2.28)$$

and we iterate until the solution is reached.

Finally the uncertainty on the determination of a_k is as usual given by:

$$\Delta a_k = \hat{W}_{kk}^{-1/2} \quad (2.29)$$

Note: in the single-photon mode Ψ' being a linear function of the unknown a_k , the second term of eq. (2.26) disappears and \hat{W} is positive definite.

Estimator #2: the average energy

This estimator makes sense for the multi-photon mode, i.e. in the limit $M \rightarrow \infty$ where the energy distribution becomes Gaussian. However, even outside this limit the average energy can always be taken as an estimator to measure the polarisation. In this section we derive the expressions of the average and of the width of the energy distribution.

Let us define the average energy of a photon entering the calorimeter (here again we drop the experiment index):

$$\mathcal{E} = M^{-1} \int_0^\infty \frac{dm(E)}{dE} E dE$$

and its variance

$$(\Delta \mathcal{E})^2 = M^{-1} \int_0^\infty \frac{dm(E)}{dE} E^2 dE - \mathcal{E}^2.$$

For N photons entering the calorimeter after a bunch-crossing, the average energy is given by

$$\langle E \rangle_N = N \mathcal{E}$$

with $E = \sum_{i=1}^N E_i$. Defining $E^2 = \sum_{i=1}^N \sum_{j=1}^N E_i E_j$, one gets

$$\langle E^2 \rangle_N = N(\Delta \mathcal{E})^2 + N^2 \mathcal{E}^2.$$

Finally, introducing the Poissonian law to describe the probability that N photons are produced one obtains:

$$\langle E \rangle = \sum_0^\infty e^{-M} \frac{M^N}{N!} \langle E \rangle_N = M \mathcal{E}.$$

Notice that one could have also derived this expression more directly since

$$\langle E \rangle = \int_0^\infty \frac{d\mathcal{P}(E)}{dE} E dE = M \mathcal{E}.$$

For the variance, writing

$$\langle E^2 \rangle = \sum_0^\infty e^{-M} \frac{M^N}{N!} \langle E^2 \rangle_N = M(\Delta \mathcal{E})^2 + M(M+1)\mathcal{E}^2$$

we get

$$(\Delta E)^2 = M(\Delta \mathcal{E})^2 + M \mathcal{E}^2$$

where one should remark the presence of the often forgotten extra term $M \mathcal{E}^2$.

To build an estimator from the measured average energy we shall consider the limit $M \rightarrow \infty$. In this limit the energy distribution is Gaussian:

$$\frac{d\mathcal{P}(E)}{dE} = \frac{\exp - \frac{(E - M \mathcal{E})^2}{2(\Delta E)^2}}{\sqrt{2\pi} \Delta E},$$

and the Likelihood function is then given by:

$$W \equiv -2 \ln L = \sum_{e=1}^3 \sum_{h=1}^H \frac{(E_h^e - M^e \mathcal{E}^e)^2}{(\Delta E^e)^2} + \ln[(\Delta E^e)^2], \quad (2.30)$$

where the factors containing π have been removed and where E_h^e is the energy measured in the bin h . To simplify eq. (2.30) we use

$$\sum_{h=1}^H \frac{(E_h^e - M^e \mathcal{E}^e)^2}{(\Delta E^e)^2} = \frac{1}{(\Delta E^e)^2} \left(H(M^e \mathcal{E}^e)^2 + \sum_{h=1}^H (E_h^e)^2 - 2M^e \mathcal{E}^e \sum_{h=1}^H E_h^e \right),$$

so that introducing the average and the variance of the measured energy distribution

$$E_m^e = \frac{1}{H} \sum_{h=1}^H E_h^e, \quad (\Delta E_m^e)^2 = \frac{1}{H} \sum_{h=1}^H (E_h^e)^2 - H(E_m^e)^2,$$

one finds the following expression for the estimator

$$W = \sum_{e=1}^3 H^e \left\{ \frac{(E_m^e - M^e \mathcal{E}^e)^2 + (\Delta E_m^e)^2}{(\Delta E^e)^2} + \ln[(\Delta E^e)^2] \right\}. \quad (2.31)$$

The unknown parameters a_k are finally determined by minimising eq. (2.31).

Estimator #3: χ^2 for the average energy

By assuming that, in the previous estimator, $(\Delta E_m^e)^2$ is a good estimator of $(\Delta E)^2$ one may transform the likelihood estimator into a χ^2 estimator:

$$\chi^2 = \sum_{e=1}^3 H^e \frac{(E_m^e - M^e \mathcal{E}^e)^2}{(\Delta E_m^e)^2}. \quad (2.32)$$

This estimator is just a simplified version of the previous one and is usually used experimentally.

Estimator #4: Asymmetry

For a given bin h of the energy distribution, the energy asymmetry is defined by

$$A_h^m = \frac{N_h^2 - N_h^3}{N_h^2 + N_h^3 - 2N_h^1},$$

where the upper-scripts refer to the experiment number. In the single-photon mode this quantity is described by $P \times A_h^T$ with $A_h^T = f_3(E_h)/f_2(E_h)$ (see section 2). Because A_h^m is directly proportional to P , one usually takes it as *the* LPOL estimator. However, this is only true for the single-photon mode since the relation between A_h^m and P is no longer linear in the few-photon mode. In the latter case it is of course possible to describe consistently A_h^m but then the relation becomes complicated because the denominator also depends on P . Therefore we shall define an estimator using the energy asymmetry only for the single-photon mode. A straightforward estimator is then

$$\chi^2 = \sum_{h=1}^H \frac{(A_h^m - P \times A_h^T)^2}{(\Delta A_h^m)^2}$$

where ΔA_h^m is the experimental uncertainty of the measurement of A_h^m . From the condition $\partial\chi^2/\partial P = 0$ we obtain:

$$P = \frac{\sum_{h=1}^H \frac{A_h^m A_h^T}{(\Delta A_h^m)^2}}{\sum_{h=1}^H \frac{(A_h^T)^2}{(\Delta A_h^m)^2}}. \quad (2.33)$$

Bibliography

- [1] J. Buon, in *Advances of accelerator Physics and Technologies*, World Scientific, 1993; LAL report 92-28/1992.
- [2] B.W. Montague, Phys. Rep. 113 (1984)1.
- [3] D.P. Barber, 15th Advanced Beam Dynamics Workshop, Monterey, U.S.A. 1998; DESY report 98-096/1998.
- [4] D.P. Barber and G. Ripken, in the Handbook of Accelerator Physics and Engineering, Eds. A.W. Chao and M. Tigner, World Scientific, 2002.
- [5] G.Z.M. Berglund, *Spin-orbit maps and electron spin dynamics for the luminosity upgrade project at HERA*, Ph.D. Thesis, DESY-THESIS-2001-044.
- [6] C. Cohen-Tannoudji, D. Diu and F. Laloe, *MECANIQUE QUANTIQUE, Tome I* (Hermann, Paris 1977).
- [7] R.C. King, *A precise measurement of the left-right asymmetry of Z boson production at the SLAC linear collider*, Ph.D. Thesis, SLAC-452, 1994.
- [8] A.A. Sokolov and I.M. Ternov, "Synchrotron radiation", Akademie-Verlag, Berlin 1968.
- [9] J. Buon and K. Steffen, Nucl. Instr. and Meth. A245 (1986) 248.
- [10] D.P. Barber et al., Nucl. Instr. and Meth., A329 (1993) 79.
- [11] See D.P. Barber et al., Nucl. Instr. and Meth., A338 (1994) 166 and references therein.
- [12] M. Beckmann, Nucl. Instr. Meth., A479 (2002) 334.
- [13] V. Andreev et al., DESY-PRC 98-07; for an update of the Polarization 2000 project see <http://pia.desy.de:9999/TWDM/fcgi/twdmdoc>.
- [14] E. Barrelet et al., DESY PRC 00-02.
- [15] R. Bacher et al. *The HERA luminosity upgrade*, document available on <http://www.desy.de>.
- [16] B. Wagner et al., Nucl. Instrum. Meth. A294 (1990) 541.
- [17] M. Born and E. Wolf, *Principle of Optics*, third eds. Pergamon press, Oxford, England, 1965.

- [18] S. Huard, *Polarisation de la lumière* (Masson, Paris, 1993).
- [19] J.D. Jackson, *Classical electrodynamics*, third eds. John Wiley and sons, New-York 1999.
- [20] P. Yeh, *Optical waves in layered media* (Wiley, New-York, 1988).
- [21] R. C. Jones, J. Opt. Som. Am. 37 (1947) 107.
- [22] E. Collett, *Polarized light: Fundamentals and applications* (Marcel Decker Inc., 1993).
- [23] R.M.A. Azzam and N.M. Bashara, *Ellipsometry and polarized light*, Amsterdam, North-Holland, 1977.
- [24] U. Fano, J. Opt. Soc. Am., 39 (1949) 859.
- [25] G. Araki, Prog. Theo. Phys., 1 (1946)125; Phys. rev., 74 (1948) 472.
- [26] R.J. Glauber, Phys. Rev. 130 (1963) 2529; Phys. Rev. 131 (1963) 2766.
- [27] G. Bardin et al., *Conceptual design report of a Compton polarimeter for Cebaf Hall A*. Document available on <http://www.cebaf.gov/Compton>.
- [28] N. Falleto, *Etude, conception et réalisation d'une cavité Fabry-Perot pour le polarimètre Compton de TJNAF*, Ph.D. Thesis, Université J. Fourier Grenoble 1, 1999.
- [29] M. Placidi and R. Rossmanith, Nucl. Instr. and Meth. A274 (1989) 79.
- [30] L. Knudsen et al., Phys. Lett. B270 (1991) 97.
- [31] L. Arnaudon et al., Phys. Lett. B284 (1992) 431.
- [32] K. Piotrkowski, hep-ex/9504003.
- [33] Y.S. Tsai, Rev. Mod. Phys. 46 (1974)815.
- [34] M. Lomperski, DESY 93-045.
- [35] HERMES Collaboration; W. Lorenzon et al., *A proposal to DESY for a longitudinal Electron Polarimeter at HERA-EAST Section*, (1995).
- [36] G. Grindhammer in *Proceedings of the workshop on calorimetry for supercolliders*, Tuscaloosa, 1989. G. Grindhammer, private communication.

Chapter 3

A Fabry-Perot Cavity for an upgrade of the HERA longitudinal polarimeter

In chap. 1, it has been shown that a fast and precise polarimeter is necessary to reach a high precision on the physics results produced after the HERA upgrade. In chap. 2, we have shown that a solution for a high accuracy Compton polarimetry is the use of a high power continuous laser.

In this chapter, we describe the experimental solution leading to a high Compton scattering rate, namely the Fabry-Perot¹ optical resonator.

3.1 A Fabry-Perot cavity for polarimetry

The formal aspects of optical resonators are the subjects of numerous monographs and articles. In order not to repeat what has already been described elsewhere I refer to refs. [2, 3]. Only the main features concerning laser Gaussian beams and cavity modes are summarised in appendix 3.6.

Details on the use of a Fabry-Perot cavity for polarimetry are given in the very complete ref. [4] (see also [5]) and in CEA-Saclay technical notes [6].

3.1.1 Principle of Fabry-Perot cavities

In its simplest version, a Fabry-Perot cavity consists in two spherical mirrors located opposite to each other. When an incident plane wave arrives in the cavity in phase with the plane waves circulating inside the cavity, the interference is constructive and the power inside the cavity increases. This is a resonance phenomena and since the phase shift of a plane wave after a round trip between two mirrors is $k \times 2L$, with L the distance between the two mirrors and k the wave vector, the resonance condition simply reads

$$\lambda = \frac{2L}{q} \iff \nu = q \frac{c}{2L} \quad (3.1)$$

¹According to the French administration, there is no accent on the letter e of Perot [1].

for $q \in \mathbb{N}^*$ and where $\lambda = 2\pi/k$ and $\nu = kc/2\pi$ are the laser wavelength and frequency respectively.

In practice one has to deal with laser beams which are not plane waves but usually almost Gaussian beams. Fortunately, the eigen-modes of a spherical resonator are also not plane waves. They are determined by the solutions of the paraxial Maxwell equations with the proper boundary conditions. The fundamental mode of these solutions is Gaussian so that, in order for a Gaussian laser beam to propagate inside a cavity, one must add to the frequency matching condition of eq. 3.1 the spatial mode matching conditions (i.e. one must match the cavity/laser waist in size and position).

If the laser beam axis of propagation coincides with the cavity optical axis (see appendix 3.7) and if the laser beam is perfectly Gaussian and mode matched, then there exists only one resonance frequency (modulo 2π) and the full power of the laser beam is efficient. If the mode matching is not perfect (laser beam ellipticity for example) or/and if the laser/cavity alignment is not perfect, then the cylindrical symmetry is broken and, depending on the new geometrical configuration, higher order modes can propagate (see appendix 3.6). The resonance frequencies for these excited modes are all different for stable cavities so that the net effect of such faults is a loss of power in the fundamental mode of the cavity.

Applying the continuity conditions for the electromagnetic field on the cavity mirrors one gets the expression of the field inside the cavity and therefore the corresponding power:

$$P_{in} = P_0 \times G, \quad G = \frac{T}{(1-R)^2} \times \frac{1}{1 + \frac{4R}{(1-R)^2} \sin^2 \frac{2\pi\Delta\nu L}{c}},$$

where P_0 is the incident power, G is the cavity gain, $\Delta\nu$ is the difference between the laser and cavity resonance frequencies, R and T are the reflection and transmission coefficients (for intensity) of the mirror coatings (see appendix 3.7.1). G is shown in fig. 3.1 for a 2 m long cavity with R and T given in table 3.2 of appendix 3.7.1.

From this figure and from the above expression, one defines the following useful quantities:

- the Free Spectral Range $FSR = c/(2L)$ (frequency distance between two longitudinal modes of the cavity);
- the Full Width at Half Maximum $FWHM$ (width of the resonance peak).
- the Finesse $F = FSR/FWHM \approx \pi\sqrt{R}/(1-R)$ (the number of round trips of a plane wave inside the cavity is given by $F/2\pi$, see appendix 3.6.4);
- the characteristic time or filling time of the cavity. For a high finesse, it reads as [4]

$$\tau \approx \frac{LF}{\pi c}.$$

For a 2 m long cavity and for a Nd:YAG laser ($\lambda = 1064$ nm) one gets

$$\frac{FWHM}{\nu} \approx 10^{-11}$$

with the above formula and using the numbers given in table 3.2 of appendix 3.7.1. One also gets the following cavity filling time $\tau \approx 60\mu s$.

In other words, if one wants to keep such a cavity at the resonance, one must match the cavity length and the laser beam frequency at 10^{-11} level. Clearly, a fast feedback system is required in order to ensure this condition.

A feedback loop can act on the cavity length (piezo-electric transducer moving the mirrors) or on the laser beam frequency (frequency continuously tunable laser). For practical reasons, explained in the next section, we have chosen the second solution.

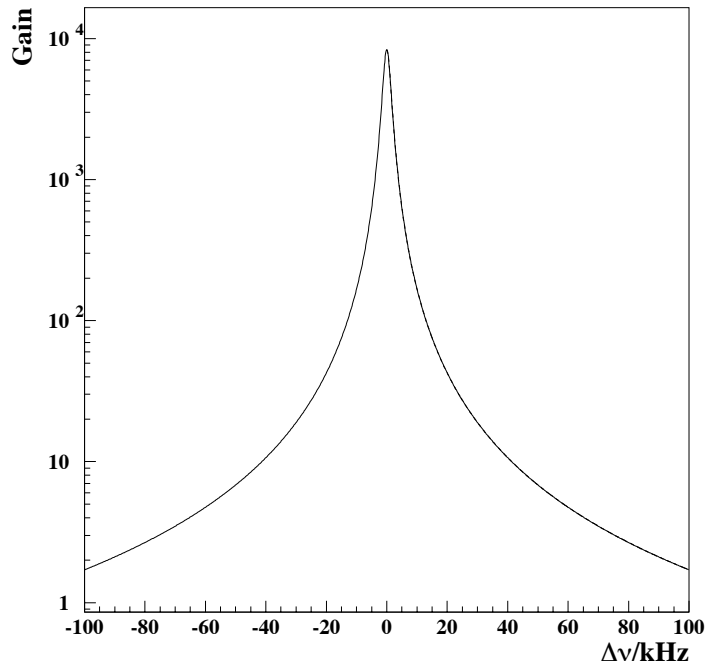


Figure 3.1: *Gain of a 2 m long cavity as a function of the difference between the laser and cavity resonance frequencies. Values of the cavity mirror reflection and transmission coefficients are those given in appendix 3.7.1.*

3.1.2 Choice of the cavity geometry for HERA

The principle of the implementation of a cavity around an electron beam pipe is described in fig. 3.2. The cavity mirrors are introduced inside the cavity, near the electron beam pipe and the laser and all the other optical components are located on the optical table close to the cavity. Since the mirrors are located inside an ultra high vacuum region ($\approx 10^{-9}$ Tor), it is not convenient to use actuators for the feedback. The solution of a monolithic cavity has therefore been chosen. This experimental set-up has been operated successfully at Jefferson Laboratory on the CEBAF accelerator [4, 7, 8] and we have taken advantage of the experience accumulated there.

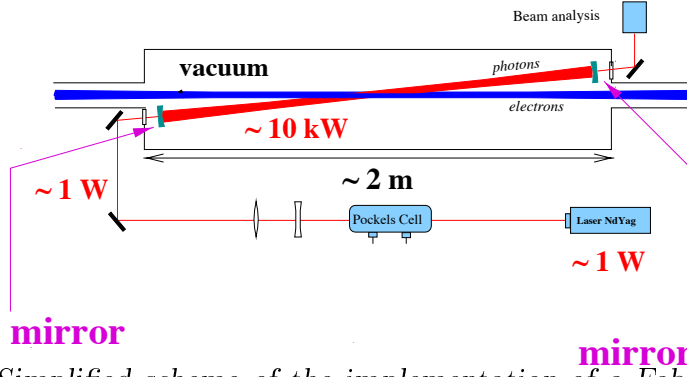


Figure 3.2: *Simplified scheme of the implementation of a Fabry-Perot cavity inside the electron beam pipe. The optical elements and the laser are located close to the beam pipe. From [4].*

The exact layout of the cavity is determined by the total distance between the two mirrors, the radius of curvature of the mirrors and the crossing angle between the laser beam and the lepton beams. This angle is given by $\alpha \approx 2d + \Phi/L$, where L is the cavity length, d is the distance between the electron beam axis and the edge of the mirror and Φ is the mirror diameter. To avoid synchrotron radiation, the laser beam must cross the electron beam in the vertical plane, i.e. along the y axis (see fig. 2.1 of chap. 2). The minimum value for d is then fixed by the machine requirements, that is 2 cm. One must also add 2.5 cm for mechanical purposes. The cavity waist (see appendix 3.6.1 for a definition), i.e the laser beam waist, depends on the mirror radius of curvature R_c . In section 3.7.2 we show that, for confocal cavities $R_c = L$, the mechanical stability is optimum. Considering a confocal cavity with $d = 4.5$ cm and $\Phi = 25.6$ mm and using eq. 2.4 of chap. 2 for the laser beam/electron beam luminosity, one can determine the Compton event rate as a function of the remaining free parameters, the cavity length and the light power inside the cavity. This rate is shown in fig. 3.3 for a 1 mA electron beam intensity and various values of the light power inside the cavity. The grey hatched area corresponds to the scattered photon rate of 1 to 2 photons per interaction for an electron current of 40 mA (typical value for the HERA running). In chap. 2 we have shown that with this event rate the polarisation measurement accuracy is much below 1 per mille per bunch and per minute. Therefore, from this figure it can be seen that a 2 m long cavity intersecting the lepton beam at 3.3 degrees (58 mrad) will deliver the needed luminosity provided a laser beam power of the order of a few kW is supplied, that is 3 kW to fix a number.

In summary, a 2 m long confocal cavity has been chosen for HERA on the basis of mechanical and luminosity constraints. This is twice longer than the CEBAF cavity.

3.2 Mechanical design of the cavity

3.2.1 Constraints

One of the main considerations when designing the cavity is that wake fields from the passing electron beam should not disturb the cavity operation, and that the cavity should

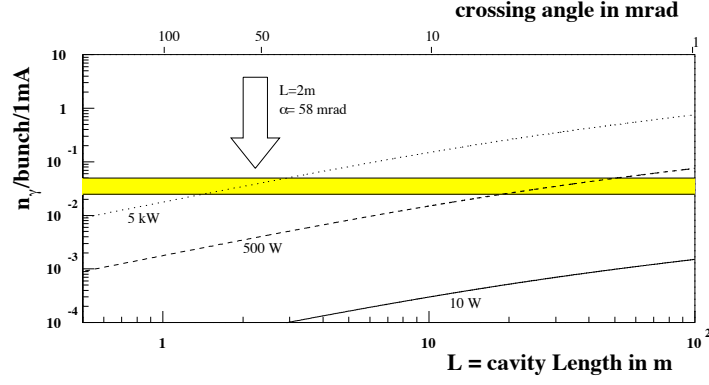


Figure 3.3: Event rate per bunch normalised to a total electron current of 1 mA as a function of the cavity length (bottom scale) and the crossing angle (top scale). For the plot it is assumed that the separation between the beam axis and the mirror centre is kept constant at 5.75 cm.

not perturb the electron beam. The mutual perturbation is minimised by the introduction of a 15 mm diameter tube, which is used to suppress the propagation into the cavity of high frequency modes from the passing beam. Numerical calculations indicate that this tube should extend ± 80 cm from either side of the hole in the beam pipe (see figs. 3.4 and 3.5). By making the hole for the laser beam in the beam pipe as small as possible the power loss through electromagnetic heating is also reduced to an almost negligible level (18 W during injection, less than 0.1 W during normal beam operation [9]).

Another constraint comes from the presence of the small tube around the laser beam inside the cavity. The laser beam must pass ‘far away’ from the tube surface in order not to lose intensity by diffraction. In appendix 3.7, the determination of the mechanical tolerances is described. The laser beam tube size defines in fact the maximum tolerable angular and axial relative misalignment between the two cavity mirrors. For 15 mm diameter, it is safe to require angular and position tolerances of 1 mrad and 1 mm. Under these conditions, the cavity optical axis crosses the mirrors within 3 mm, at most, from their centres. Of course, once the mirrors are mechanically aligned, one has to align and mode match the laser. But with these tight tolerances, we ensure that losses induced by diffraction are negligible.

Another constraint comes from the laser itself. Once turned on, one should not change its frequency by more than ≈ 70 GHz. Above this threshold, the longitudinal mode of the laser changes and this may induce some perturbation on the feedback operations. This frequency threshold induces a constraint on the maximum variation of the distance between the two mirrors. This distance must not exceed $70 \mu\text{m}$ once the cavity has been locked.

3.2.2 Mechanical design

From the constraints given above, the cavity must consist in a cylindrical vacuum vessel surrounding a beam pipe section on which two small tubes are soldered. The mirrors also have to lay in the vacuum and therefore inside the vessel but, because of heat effects

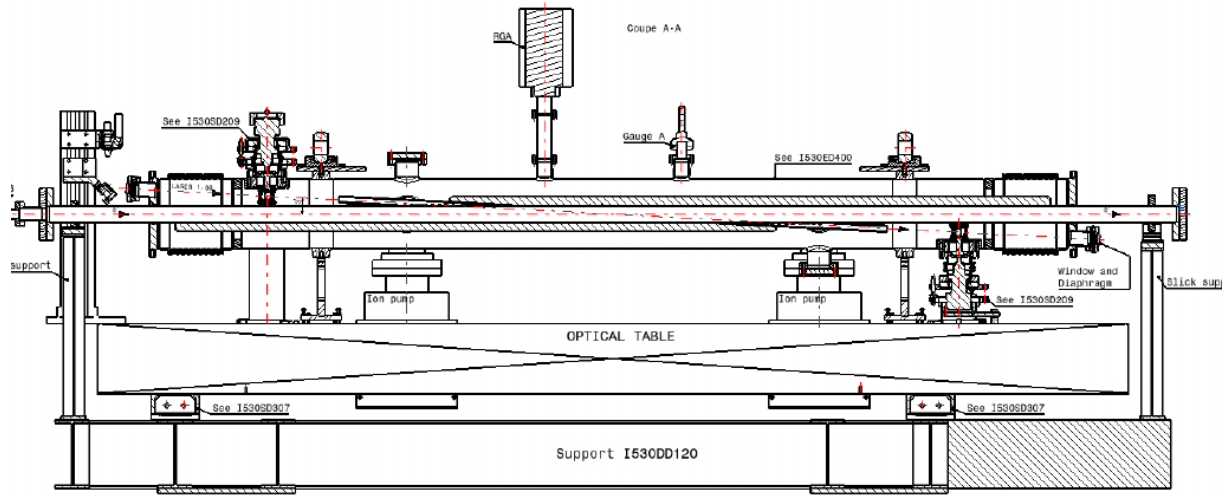


Figure 3.4: *Technical drawing (longitudinal view) of the cavity. See text for comments. From [10].*



Figure 3.5: *Picture of beam pipe inside the cavity (half is shown). Above the elliptic electron beam-pipe, a circular tube is soldered to reduce the wakefield excitations.*

and possible vibrations propagating along the beam pipe, they cannot be mounted rigidly on the vessel. The solution adopted is to mount the mirrors in a post holder fixed to a plate resting on two big cylindrical legs clipped on the optical table (see fig. 3.10). The post holders are linked to the vessel through metal bellows thus filtering the remaining vibrations. In this way, the cavity mirrors are completely part of the optic table which supports all the optics.

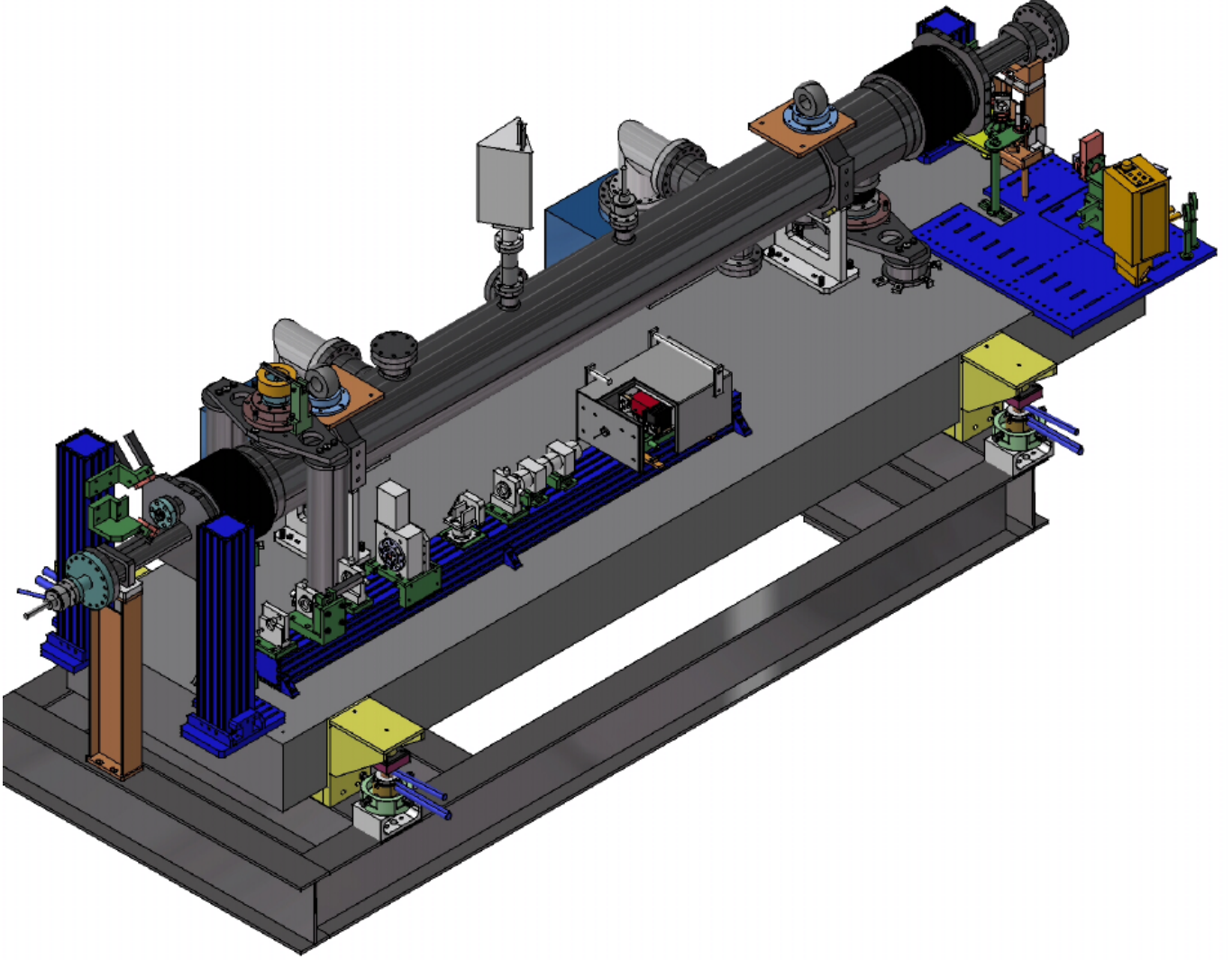


Figure 3.6: *Three dimension technical drawing of the cavity and of the optical scheme. See text for comments. From [10].*

The mechanical scheme is shown in figs. 3.4 and 3.6 and a picture taken during the installation is given in fig. 3.7. All components are made of stainless-steel. To reduce the vibrations coming from the beam pipe, the beam pipe inside the cavity is isolated from the rest of the HERA beam pipe by two standard HERA bellows (not visible on figs 3.4 and 3.6). The cavity vessel is isolated from the beam pipe inside the cavity by two other bellows. The vessel is finally mounted on the table via two pairs of passive absorbers (see

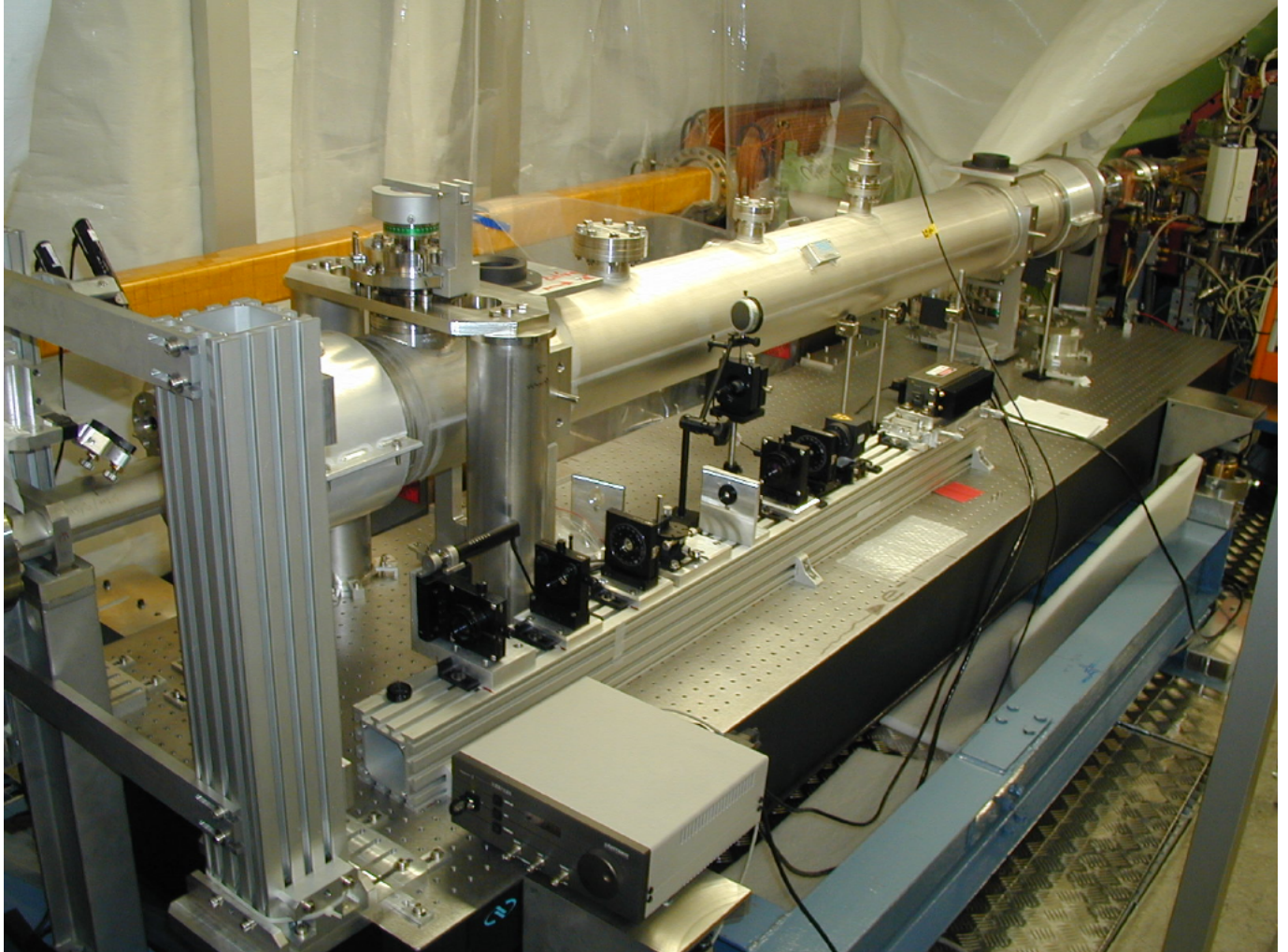


Figure 3.7: *Picture of the cavity taken during the installation. The laser and the optical elements before the cavity entrance are located on the rail parallel to the cavity vessel. The red laser diode, used to aligned the cavity mirrors, enters the cavity by the opposite entrance. It is visible on the picture: between the rail and the cavity vessel and mounted on a post holder at a height higher than the rail.*

fig. 3.8). The optical table is therefore isolated from the beam pipe by a three stage filter: two pairs of bellows and two pairs of absorbers.

The inner part of the cavity is shown in fig. 3.5 (see also fig. 3.4). To increase the gas conductance between the beam pipe and the vessel, holes have been implemented during the soldering of the laser beam tubes. To reduce heat effects induced by synchrotron radiations, the size of the beam pipe inside the cavity has been increased. The tubes are supported by rectangular plates, they have been assembled with respect to the tolerances given in the above section.

The cavity vacuum windows are 3 mm thick and 30 mm diameter silica plates. To avoid birefringence, the windows have been anti-reflection coated and soldered to the stainless steel flanges according to a special procedure (glass-metal soldering). Since the laser beam inclination is 58 mrad with respect to the electron beam, the vacuum windows have been also inclined by 58 mrad.

The optical table must be kept in the machine plane ('HERA is tilted' by 8 mrad and 3 mrad around the horizontal axes x and z respectively, see fig. 2.1 for the axes) and isolated from ground vibrations. Because of large temperature variations inside the HERA tunnel (more than 10 K between open and running conditions), active isolators would have induced movements of the table, therefore only passive absorbers could be used to isolate the table from the ground. A special mechanical interface has been designed to align the table/cavity onto the HERA plane.

Inside the cavity, the vacuum is maintained by two ion pumps visible on fig. 3.6 and pressure is measured by a vacuum gauge (on the top of the cavity vessel, see fig. 3.4). The heavy ion pumps are isolated from the optical table by passive absorbers (see fig. 3.9).

The mirror mounts are shown in fig. 3.10. It is important to be able to align the two mirrors within the accuracies given in the above section. To do so, the rotation around the normal of the optical table is done using a lockable air-vacuum rotator. The orientations of the mirrors in the other directions are performed using a standard optical technique (named 'gimbal mount'): the mirror is attached to a plate which is moved via three micrometric screws acting on a plane, a line and a point. With this technique, the mirror centre stays at the same height during the alignment operations.

The cavity mirrors are aligned with respect to each other using the auto collimation technique and a red laser diode (see chap. 5 for details). The laser diode – visible on fig. 3.6 – is injected inside the cavity by two mirrors (see fig. 3.11) rigidly mounted on a movable rail.

3.2.3 Implementation at HERA

To control the thermal expansions of the cavity and of the optical table, the whole system is surrounded by an isotherm house (see the picture of fig. 3.13). Inside this house, the temperature is controlled and kept constant within $\pm 1^\circ$. This is enough with regard to the laser longitudinal modes since all mechanical components, including the optical table, are made of stainless-steel² (thermal dilatation = 36 μm per degree).

Another purpose of the cavity housing is the radiation protection. The optical elements located on the optic table are made of glass, quartz, calcite, KD*P, TGG and YAG doped

²Only the plates on which the cavity mirror post holders are mounted are in Aluminium.

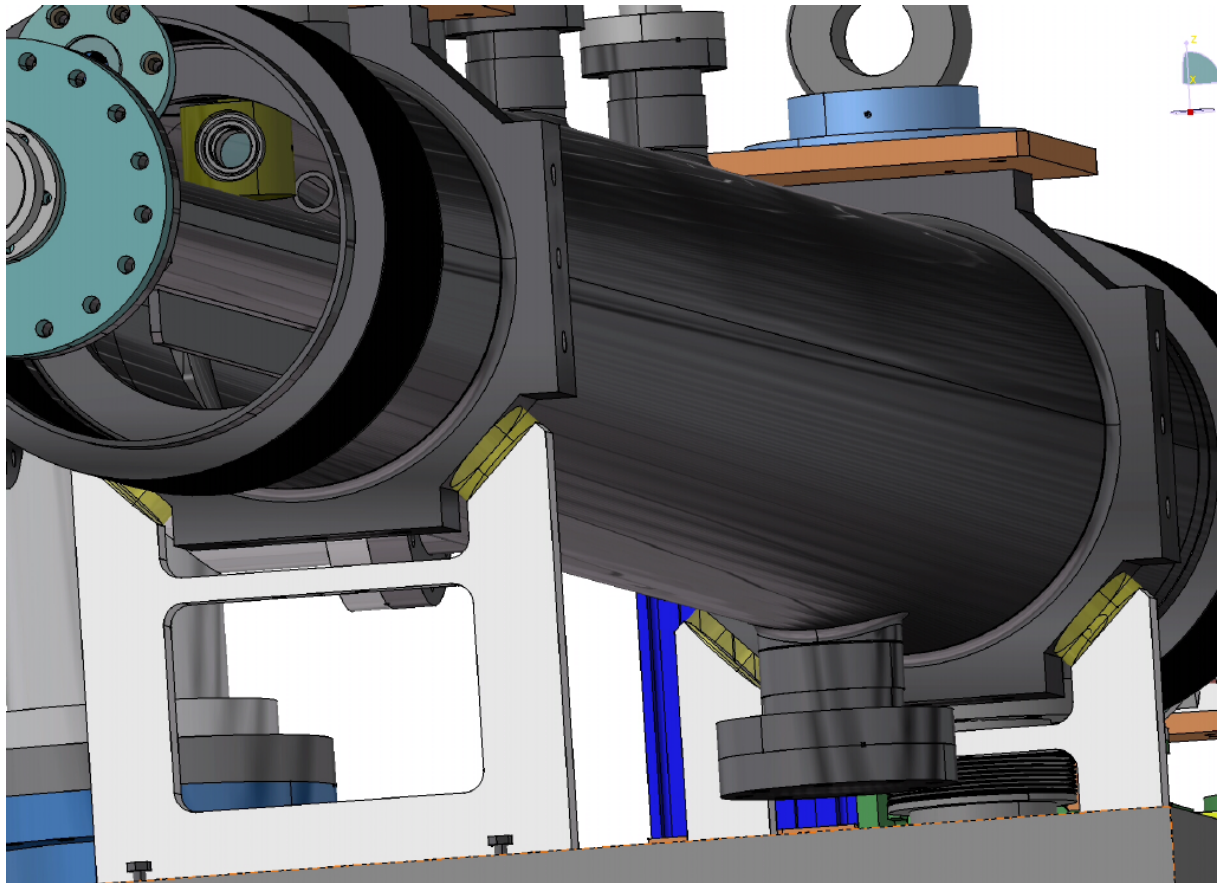


Figure 3.8: *Technical drawing of cavity vessel mount. From [10].*

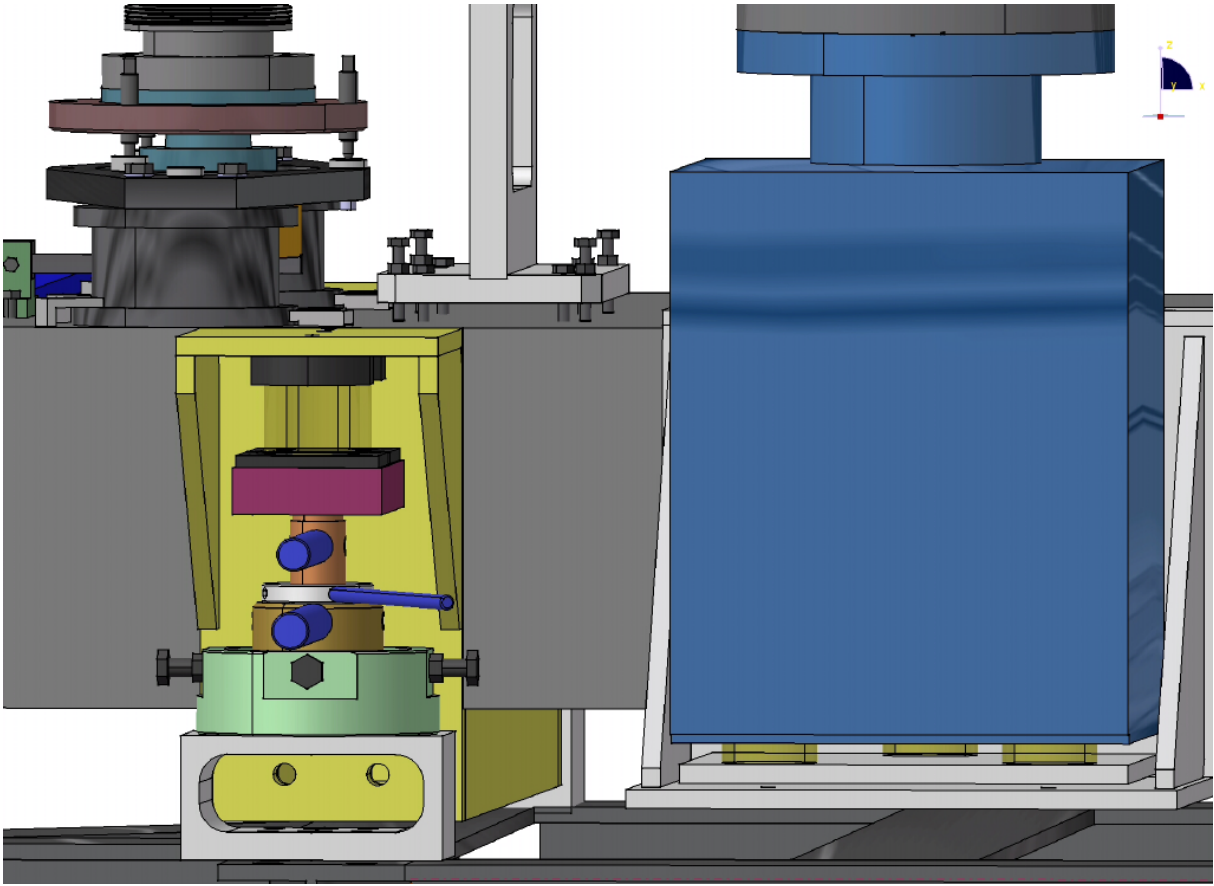


Figure 3.9: *Technical drawing of the ion pump (blue cube on the right of the figure) and of the optical table mount. From [10].*

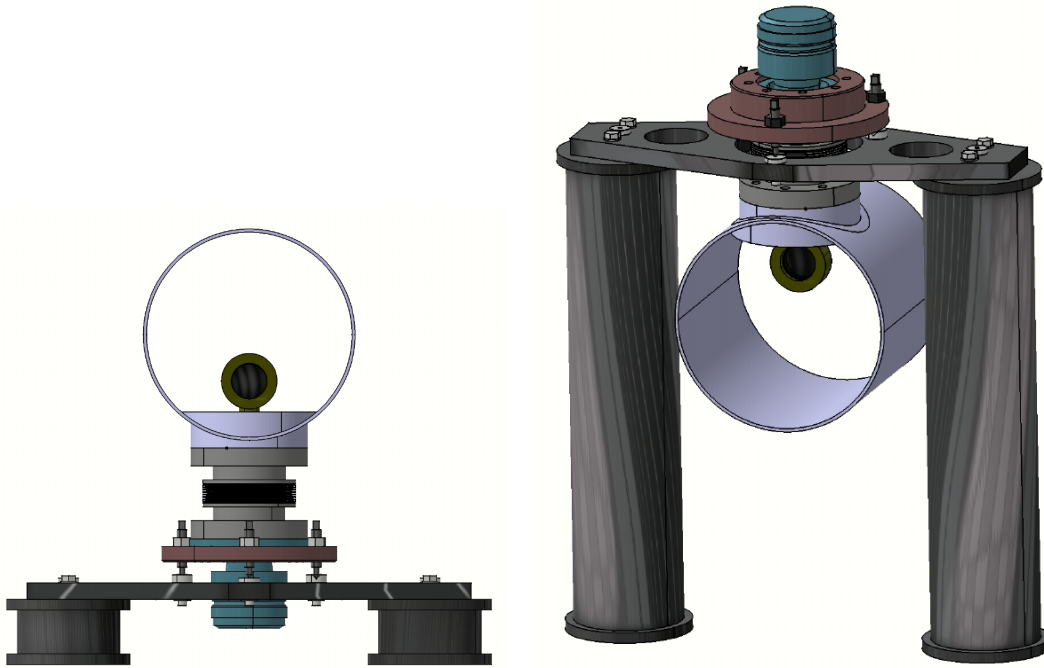


Figure 3.10: *Technical drawing of the cavity mirror mounts (lower and upper mirrors on the left and right sketches respectively). The cylinder around the mirror is the cavity vessel. The bellows, used to isolate the mirror mount from the cavity vessel is visible on the left sketch (below the vessel). From [10].*

crystal. They are all sensitive to deep UV, X-rays and gamma-rays. For example, natural quartz (SiO_2 crystalline) always contain a small amount of crystal site defaults: Al, Na, Li atoms and OH^- molecules [11, 12]. These defaults do not modify noticeably the optical properties of quartz except when it has been irradiated. In this case the quartz is solarised: contaminating atoms are ionised and this leads to absorption of light in the near infrared and visible domain [13].

To avoid radiations, a 3 mm lead shielding is located all around the cavity house. During the summer 2000, we have let a couple of cavity mirrors (junk items) directly on the beam pipe at the future cavity location and we observed no alteration of their optical properties.

3.3 Optical scheme

One needs to provide a set of optical elements in order to inject adequately the laser beam inside the cavity and to control the light polarisation. In this section a brief description of these optical elements is given.

We start by a description of the laser, focusing on the informations necessary to understand our experimental results described in chap. 5. Next all optical elements used in our set-up are described. This section is closed by a discussion on the expected level of parasitic birefringence induced in our set-up.

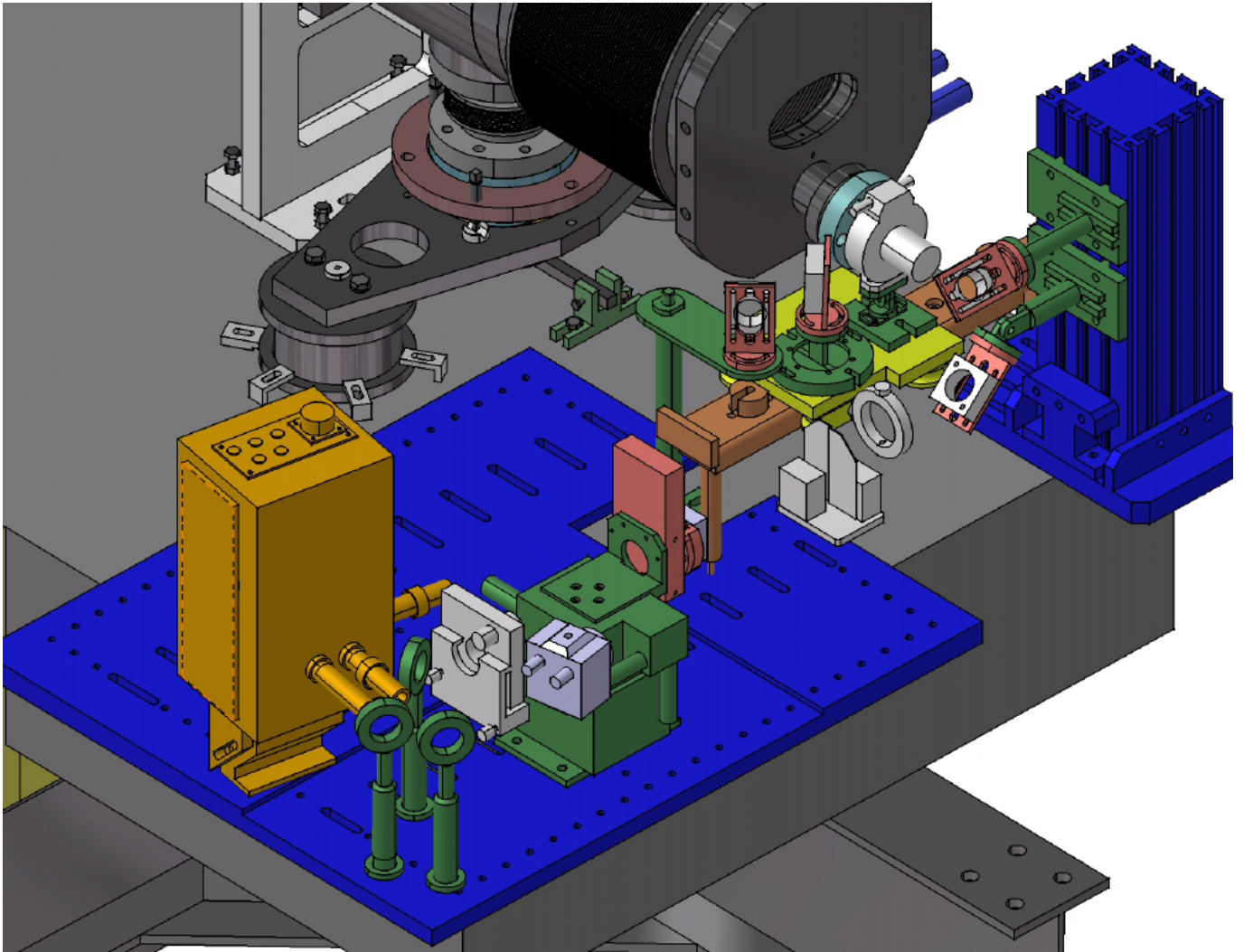


Figure 3.11: *Technical drawing of the ellipsometer. Also visible are the two mirrors used for the cavity mirror alignment. These mirrors, mounted on a rigid rail located ≈ 24.7 cm above the table, are used to inject the red laser diode inside the cavity. The Glan-Thomson prism, also mounted on this rail, used for birefringence calibrations is also shown in this picture. For the sake of clarity, the electron beam pipe has been removed from the drawing. From [10].*

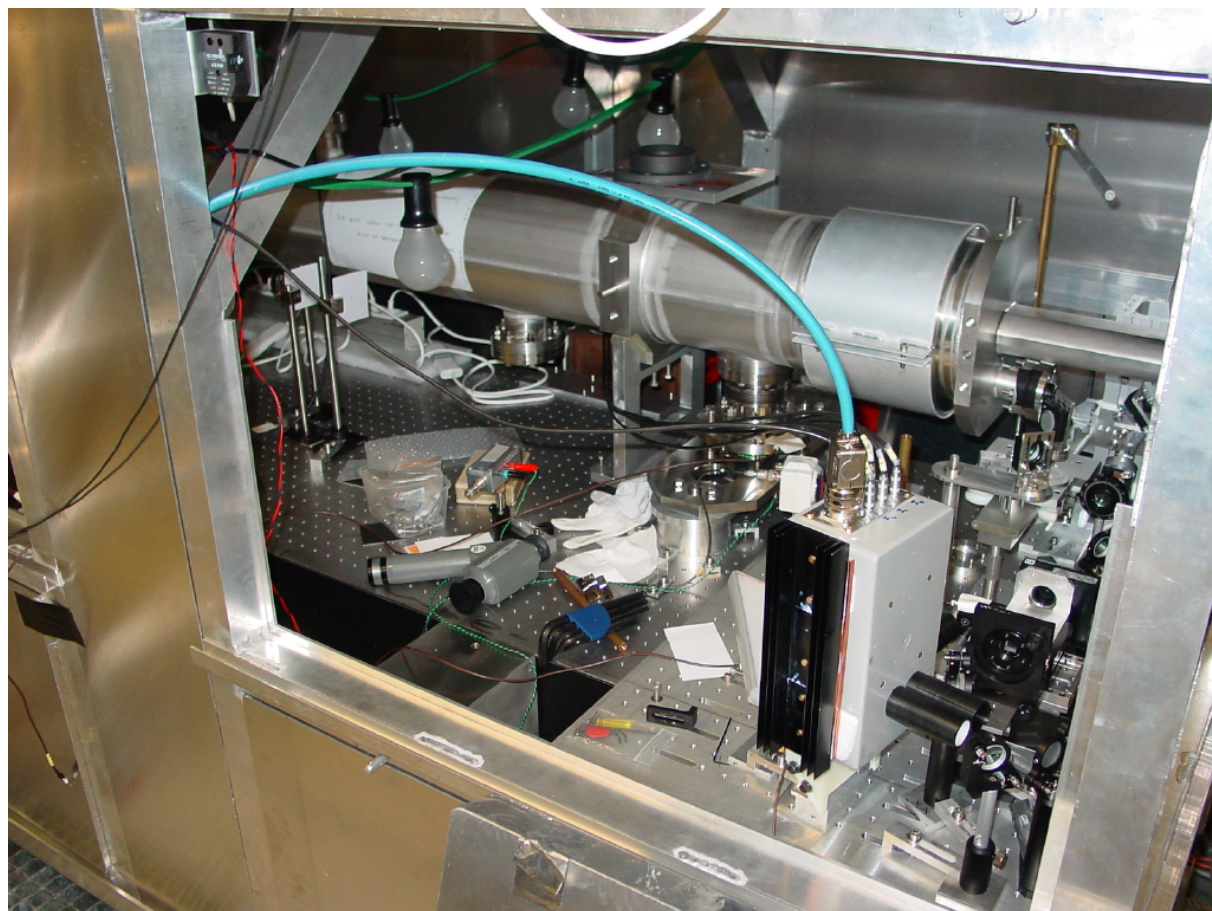


Figure 3.12: *Picture of the cavity output. Visible on this photograph is the cavity housing (thermal isolation plates and aluminium structure), the temperature controlled photodiode box (in front) and the optical elements of the ellipsometer. The lamps were used to heat up the cavity and the optical table.*

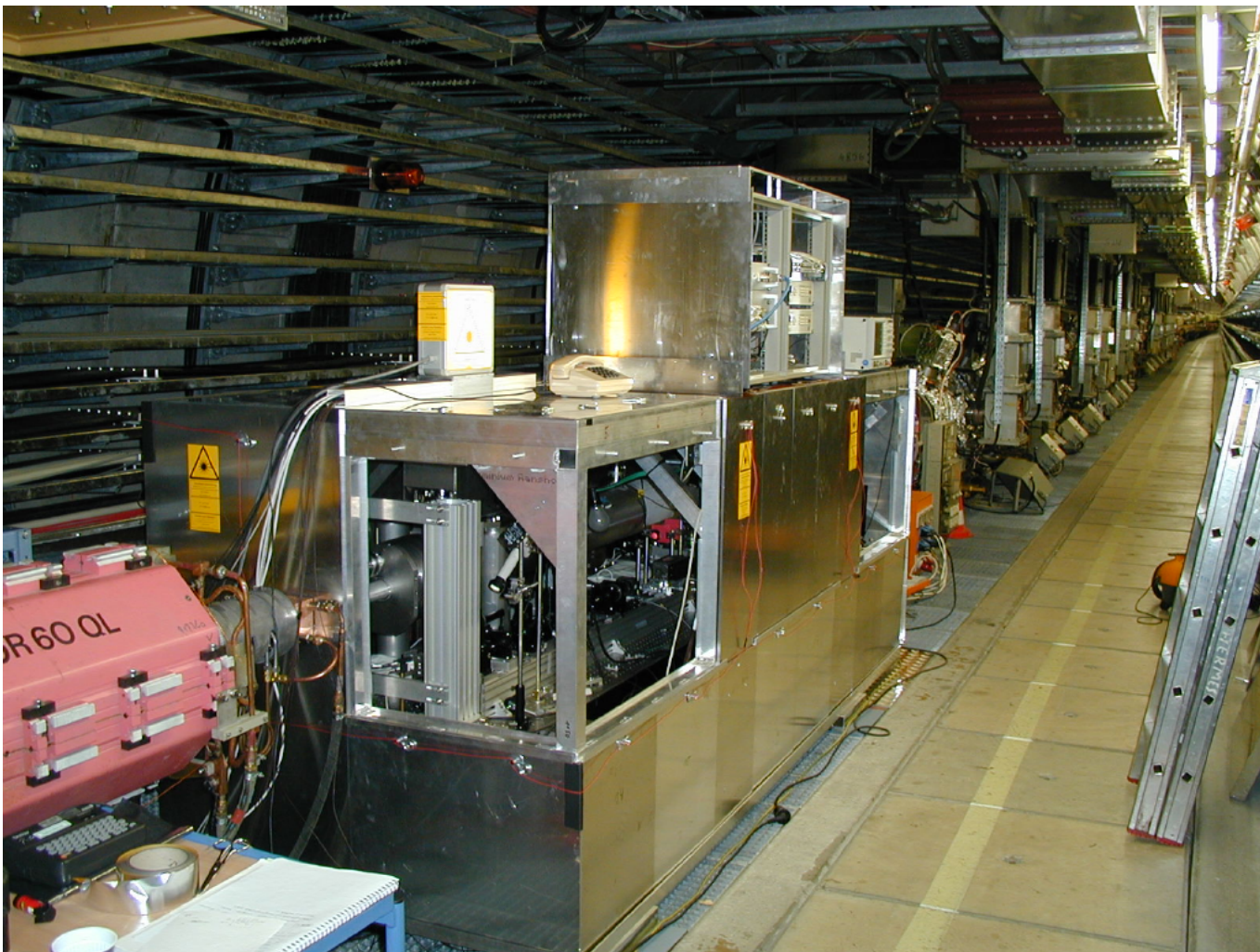


Figure 3.13: *Picture of the cavity house. The electronics is located on the top of the cavity house.*

3.3.1 The laser

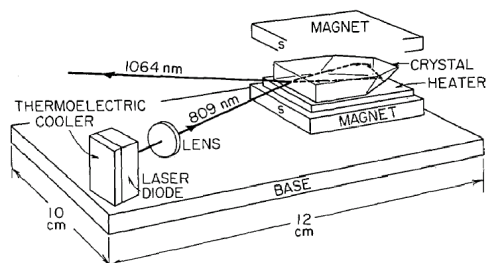


Figure 3.14: *Schematic view of the NPRO laser (see text). From Ref. [15].*

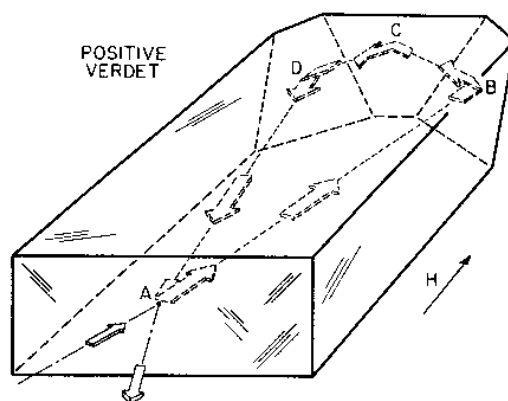


Figure 3.15: *Nd:YAG crystal of a non-planar ring laser (see text for details). The tilts of the light path at points B, C and D fix the polarisation state of the stimulated emitted light. From [14].*

The only laser available from industry, finely tunable in frequency is a non-planar ring Nd:YAG³ laser (Lightwave⁴, model 126). To operate at $\lambda = 1064$ nm, the Nd:YAG rod is pumped by a GaAlAs laser diode cooled in order to emit at 808.5 nm (see fig. 3.14, reasons why a laser is used to pump another laser are given in ref. [16]).

The principle of non-planar-ring oscillator [14, 17] (NPRO) is shown in fig. 3.15. The light emitted by the laser diode enters the rod at point A. The rod surfaces are finely

³It is a solid state Neodymium doped Yttrium-Aluminium-Garnet laser.

⁴Recently, the company Innolight has provided a cheaper similar laser. This new laser is, in addition, less noisy and has a smaller linewidth. But it was unfortunately not yet available when we ordered our Lightwave laser ...

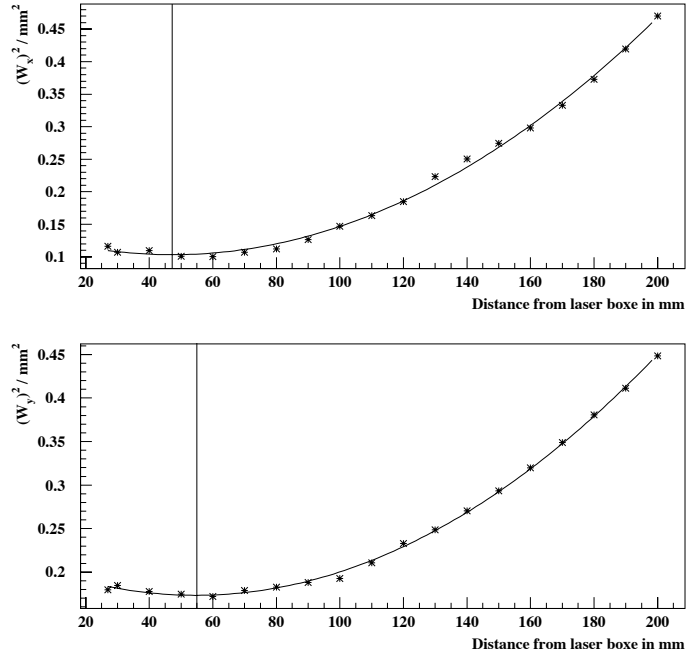


Figure 3.16: *Square of the laser beam radius as a function of the distance from the laser box. Measurement is performed with a beam-scan from Photonics.*

	Given/constructor	measured
Initial Power	760 mW	600-700 mW
Noise amplitude (bandwidth 5 Hz to 10 MHz)	0.019% rms	
Coherence length	>1000 m	
Polarisation	300:1, vertical	
Linewidth	5 kHz over 1 ms	
Frequency jitter	<200 kHz/s	
Frequency drift	<50 MHz/hour	
Thermal tuning range	30 GHz @ 1 GHz/s	
Piezo tuning range	30 MHz @ 4.6 MHz/V (30 kHz bandwidth)	
Waist position	5 cm vertical -	4.7 cm vertical 5.5 cm horizontal
Waist size	0.35 mm vertical 0.46 mm horizontal	0.32 0.42
Beam divergence, full angle	3.9 mrad vertical 3.0 mrad horizontal	

Table 3.1: *Main characteristics of the Lightwave 126-1064-700 laser. We measure the laser beam radius with a beam scan and determine the waist and waist position from a quadratic fit to these measurements.*

polished and coated in such way that total inner reflection occur at points B, C, and D (at point A the transmission is partial and the surface is curve and coated). The crystal is surrounded by a magnetic field H (see fig. 3.14) to match the polarisation state of the resonant mode (garnet is a magneto-optic crystal). The main advantage of such a ring laser, with respect to the standard linear laser cavity, is the reduction of heat inside the crystal (for Nd:YAG laser, heat variation is the main phenomenon broadening the spectral width).

The laser output spatial mode depends strongly on the rod/laser diode alignment [14] and of the entrance surface radius of curvature. We indeed observe a small ‘triangular’ halo when measuring our beam shape with a CCD camera as shown in ref. [14] (this effect is however very small).

The laser beam is also elliptic as shown by our waist measurements reported in fig. 3.16 (the waist in vertical and horizontal direction are different). An intensity measurement performed at 25 cm from the laser box is shown in fig. 3.17. A characteristic diffractive pattern is clearly visible and, as also shown in this figure, Gaussian fits performed on two projections are very bad. This pattern, depending on the distance between the laser box and the beam-scan device (the intensity shape gets more Gaussian as this distance increases, as expected [3]), induces a bias in the determination of the laser beam waist and therefore on the laser/cavity coupling (the propagation of such beam is more complicated than the one of a pure Gaussian beam). It is difficult to estimate the coupling of such beam to our Fabry-Perot cavity but, in any case, we expect a power reduction inside the cavity.

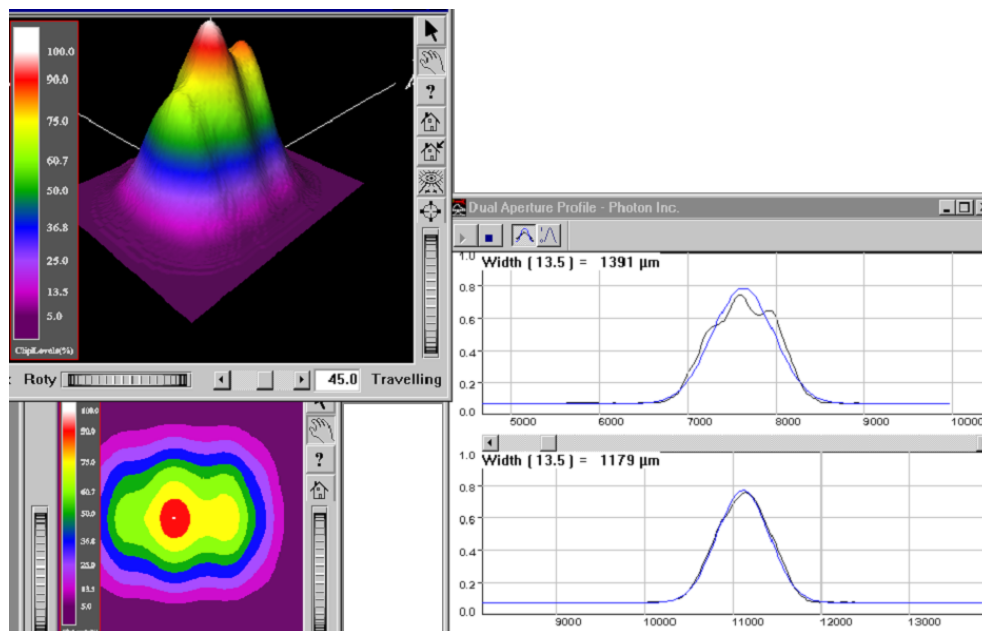


Figure 3.17: *Measurement of the laser beam intensity at 25 cm from the laser box. A 3D view (top left), a 2D contour (bottom left) and two projections (right) are shown. In the latter plot, results of Gaussian fits are also shown.*

There are two ways to modify the laser beam frequency:

- a piezo-electric transducer is located on the rod, thereby modifying the rod geometry and therefore the laser beam frequency (in other words, the transducer changes the laser cavity length). This is a fast and fine tuning: the laser beam frequency changes by 3.4 MHz for per Volt applied on the actuator (**fast channel**, bandwidth ≈ 30 kHz).
- The rod temperature can be varied thanks to a Peletier module (controlled by a DC voltage). This temperature variation induces a change of the laser beam frequency of 5GHz per Volt applied on the Peletier module. This is a slow frequency variation (**slow channel**, bandwidth ~ 1 Hz).

In fig. 3.18, a schematic picture of the noise intensity is shown. The noise is reduced by feedback control on the laser diode temperature. This laser is a low noise laser and is therefore adequate for our purpose.

The main characteristics of the Lightwave laser are given in table 3.1. In chap. 5 we shall advocate the ‘large’ value of the linewidth to explain why not all the laser beam power could be coupled to the cavity. It is then useful to define the laser linewidth here.

The linewidth is the width of the laser lineshape. The lineshape is defined by the Fourier transform (from time to frequency space) of the electric field autocorrelation function $E^*(t)E(t + \tau)$. The physical origin of a non-vanishing linewidth is related to the random emission phase inside the laser medium. For a solid state laser like the ND:YAG, for example, mechanical strain and temperature variations induce some changes of the optical indices and then of the emission phase [18] (many mechanisms contribute to the lineshape [19], an account for this rich physics topic is obviously beyond the scope of the present work). It can be shown [18] that such phase fluctuations lead to a Lorentzian lineshape. The linewidth thus depends on the mechanical and thermal quality of the laser. Even with a perfect device, the irreducible contribution of the spontaneous emission to the stimulated laser light gives a lower limit on the linewidth (the so called Townes limit [16]). This limit is two orders of magnitudes below the number given by the manufacturer.

The coherence length is a parameter related to the laser linewidth and random emission phase. It can be determined by a Mach-Zehnder like interferometer [24]: if the optical path between the two arms of the interferometer is greater than the coherence length, then no interference pattern is observed. Let us get an idea of the impact of a 1000 m coherence length on the cavity resonance conditions. Taking a finesse around 30000, as the one of our cavity, one gets a number of round trips of $\approx 10^4$, that is a total optical path inside the cavity of 40000 m. Comparing the two numbers one sees that the coherent length is smaller than the optical path (and the laser linewidth greater than the cavity FWHM which is around 3 kHz, though it is given at a different time scale) so that we may not be able to ‘fill the cavity completely’.

3.3.2 Details of the optical scheme

One needs to provide a set of optical elements to fulfil the following functions:

- creation of a circular polarisation laser beam and switching between left and right polarisation;
- laser/cavity mode matching;

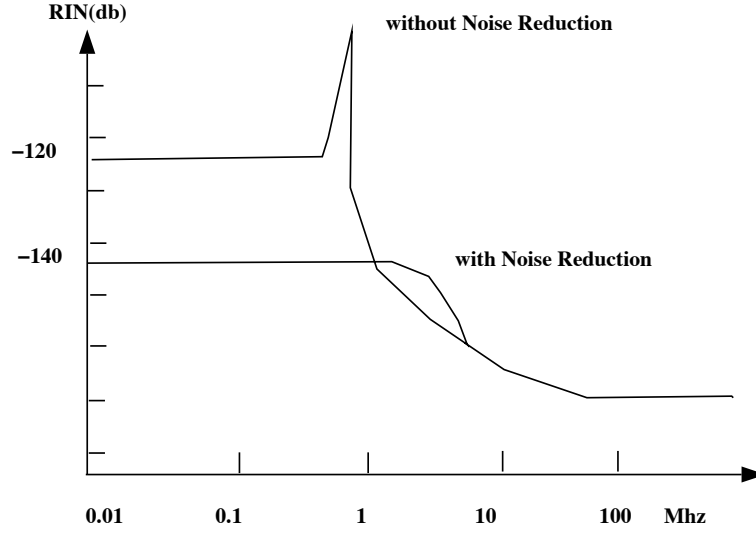


Figure 3.18: Approximate distribution of the residual noise intensity (as a function of the laser beam frequency variation). From [7].

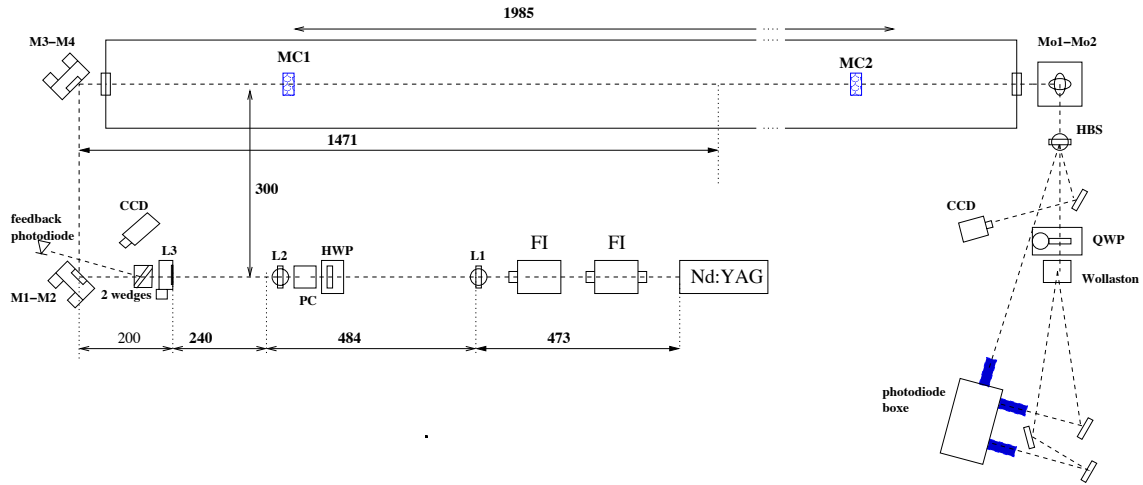


Figure 3.19: Schematic view of the optical scheme together with main distances. From [22].

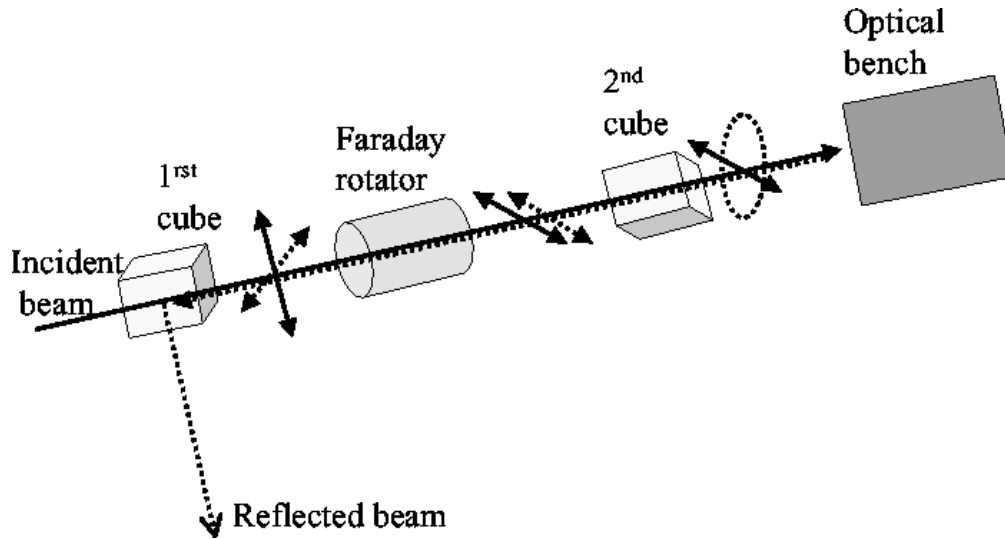


Figure 3.20: Principle of the Faraday isolator used to protect the laser from the light reflected by an ensemble of optical elements (named optical bench on the figure). The first polarisation cube delivers linear polarised light. Then the polarisation is rotated by 45° by the Faraday rotator. This component is made of a terbium gallium garnet crystal located inside a permanent magnet. After the second cube, the polarisation of the beam reflected by an optical bench (dashed ellipse and dashed arrow in the figure) will be rotated by another 45° by the Faraday rotator so that it will be deflected by the first polarisation cube. The second polarisation cube is then used to match the orientation of the polarisation vector after the Faraday rotator and the polarisation of the reflected beam. This scheme leads to a 40 db laser isolation.

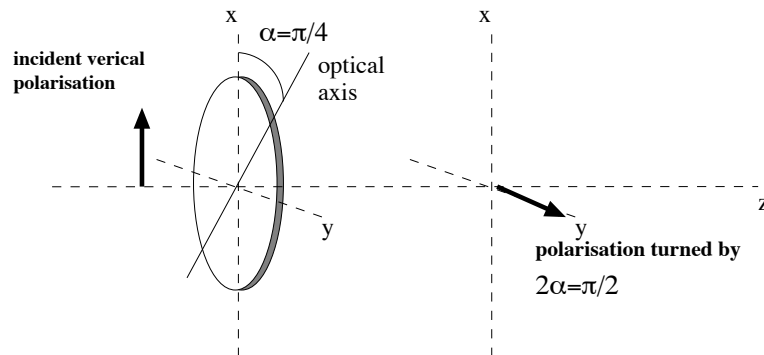


Figure 3.21: Effect of a half wave plate on linear polarisation. See chap. 4 and appendix A for details.

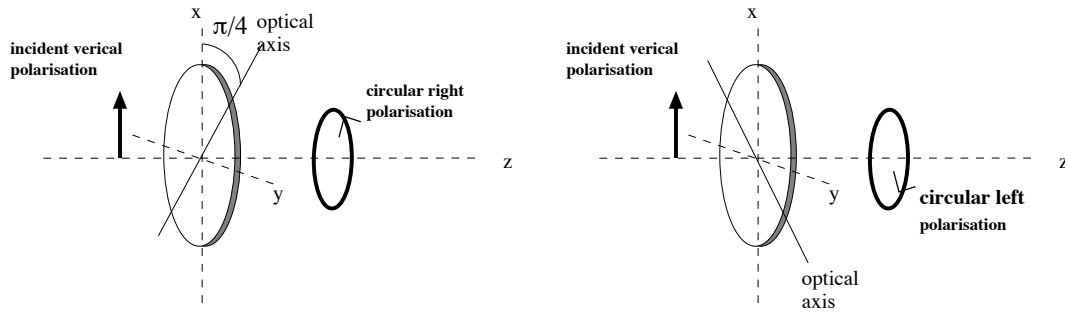


Figure 3.22: *Effect of a quarter wave plate on linear polarisation. See chap. 4 and appendix A for details.*

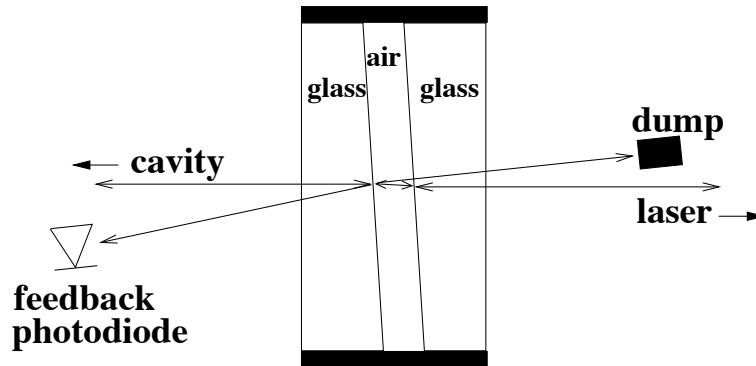


Figure 3.23: *Schematic view of the assembly of the two 6° wedges used to pick-up the beam reflected by the cavity.*

- laser/cavity geometrical alignment;
- extraction of the signal reflected by the cavity for the feedback;
- measurement of the laser beam polarisation.

In addition, because the optical table is close to the HERA beam pipe, all operations on the optical components must be done remotely.

Our Saclay colleagues met the same constraints for the CEBAF cavity project[4, 8]. They provided a very well suited optical scheme that we also used with small modifications. Our optical scheme is shown in fig. 3.19 (see also fig. 3.6). Starting from the laser box we find:

1. A Faraday isolator which insures that no reflected beam enters the laser (this would perturbate the NPRO and then the cavity feedback). This element is made of a gyromagnetic crystal surrounded by a permanent magnet and located between two polarisation separation cubes (see fig. 3.20).
2. A second Faraday isolator used to increase the laser isolation (80 db in all). At the time of writing this document this component is not yet installed.
3. A lens ($f_1 = 400$ mm) to provide a small laser beam inside the Pockels cell and for the laser/cavity mode matching.
4. A quartz half wave plate (thickness $\approx 180\mu\text{m}$) to turn the linear polarisation before the Pockels cell (see fig. 3.21).
5. A Pockels cell: electro-optic KD*P crystal (see appendix 4.7 of chap. 4). For a certain value of the power supply on the crystal the cell acts as a quarter wave plate (i.e. the linearly polarised beam is transformed into a circularly polarised beam, see fig. 3.22). The polarisation is switched from left to right by changing the polarity of the Pockels cell high voltage.
6. Two lenses ($f_2 = -100$ mm and $f_3 = 250$ mm) for laser/cavity mode matching.
7. Two 6° wedge glass plates (see fig. 3.23) to pick-up the beam reflected by the cavity (see fig. 3.24). This signal is used for the cavity feedback (see section 3.4)⁵. Let us mention that the scheme used at CEBAF (see chap. 5) is not usable since the switching of the Pockels cell power supply unlocks the cavity. The two wedge scheme is independent on the beam polarisation and therefore avoids the locking breakdown.
8. Four flat 45° dielectric mirrors M1, M2, M3 and M4: they have been coated in the same run. Two of them are motorised using four Micro-Control stepper motors.
9. The cavity: a vacuum window, the two cavity mirrors and another vacuum window.

⁵In order not to increase the number of optical elements, we first installed the feedback photodiode behind the mirror M4 [23]. But, once installed at DESY, for an unknown reason, we lost a factor twenty on the feedback signal. Due to a lack of time, we used two available wedges, it would have been simpler to use a one face anti-reflection coated parallel plate.

10. Two flat 45° dielectric coated mirrors – Mo1 and Mo2 – to bring the beam emitted from the cavity down to the ellipsometer (see also fig. 3.11).
11. An holographic beam sampler. This is a coated glass plate inducing forward diffraction. The two lateral first order beams are emitted at 10° from the main beam and contain 1% of the power. We use them to control the cavity power and the cavity mode (see also fig. 3.11).
12. The ellipsometer: it consists in a quartz quarter wave plate (QWP), a Wollaston prism (see fig. 3.25) and three InGaAs photodiodes (see chap. 4): two of them read the light intensities of the two beams emerging from the Wollaston prism and the third one reads the laser beam power before the QWP (see previous item). These elements are also visible on the cavity output drawing of fig. 3.11 and on the photograph of fig. 3.12. This is a standard ellipsometer, by rotating the QWP in its plane and then fitting the two intensities measured after the Wollaston prism to an appropriate theoretical expression, one determines the polarisation state of the incident light.
13. Two infrared CCD cameras: one for the alignment (looking at the diffusion on the mirror M1) and one to visualise the mode after the cavity (directly in the beam).

For precise details concerning the optical principles related to the above elements we refer to [20, 21]. We shall briefly describe here the function of some of these elements.

The half wave plate (HWP) works in conjunction with the Pockels cell. For a given value of the DC voltage supplied on the Pockels cell, it serves to rotate the incident vertical polarisation and therefore contributes to define the polarisation state after the Pockels cell (see chap. 4 for details). This component is added with respect to the Cebaf's optical scheme.

The three lenses f_1 , f_2 and f_3 provide the spatial mode matching of the laser beam to the cavity. There is a matrix algebra (named ABCD algebra, see refs. [2, 3]) determining the effects of a convex (concave) surface on the spatial and phase properties of a Gaussian beam⁶. Taking into account the fact that the cavity entrance mirror is spherical we have determined the position and the focal of the three lenses (in fact two would have been enough but we also have to provide a small beam inside the Pockels cell). Since our laser beam is elliptical (i.e. waists are different in x and y directions) and since it is not that easy to determine the exact position of each object on an optical table, the second lens has been mounted on a remotely controlled linear translation stage.

The four mirror M1-M4 system are used to align the laser beam onto the cavity optical axis. Two mirrors would have been sufficient for this purpose but we use four mirrors to reduce the birefringence effect (see section 3.3.3).

All our optical components are anti-reflection coated for 1064 nm. The support is an aluminium rail and the interface elements between this rail and the optical mounts have been designed and built in the LAL workshop.

We have spent much effort on the light polarisation measurement, i.e. operation and calibration of the ellipsometer. This is the subject of chap. 4.

⁶It can be easily shown, in the paraxial approximation, that a Gaussian beam is equivalent to a spherical wave with a complex radius of curvature. The ABCD algebra is then derived from the paraxial geometrical optical rules.

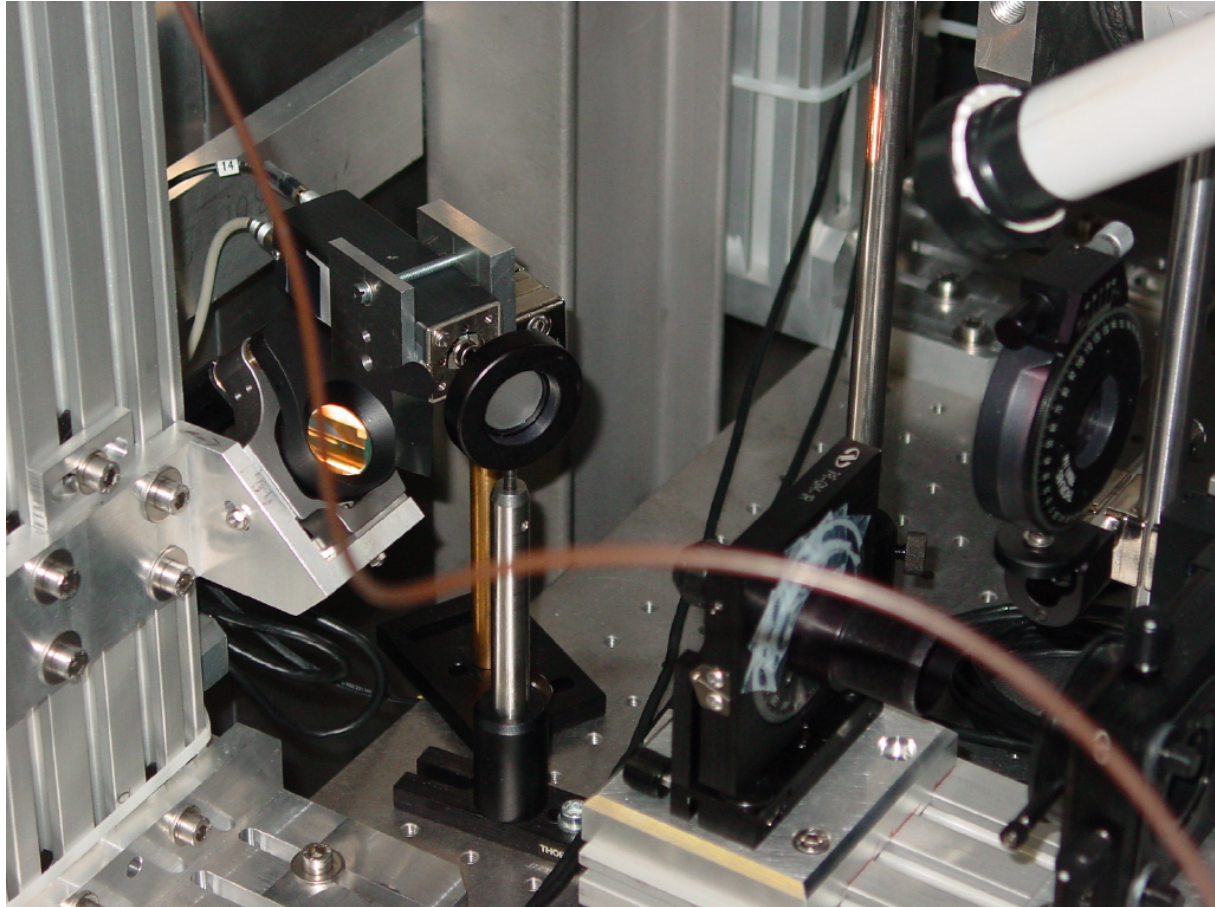


Figure 3.24: *Picture of the mirror M1, the two wedges system (located inside a black tube) and the feedback photodiode and its readout electronic box (with a diffuser in front). Also visible are the CCD used for the laser/cavity alignment (white tube, right upper corner) and the third lens (right bottom corner).*

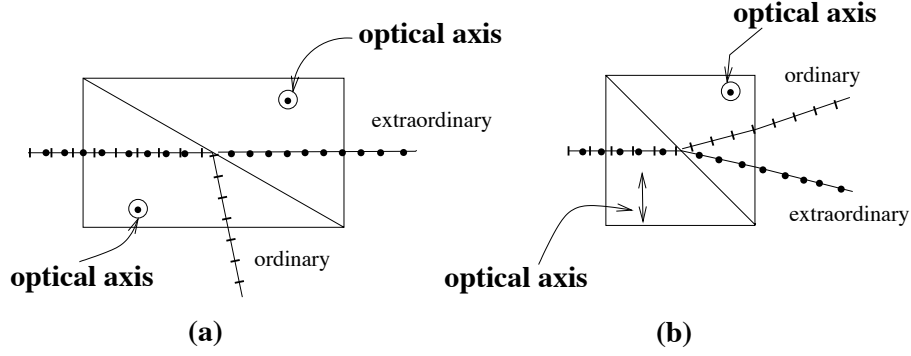


Figure 3.25: Principle of (a) Glan-Thomson prism and (b) Wollaston prism. Both components are made of calcite (uniaxial crystal, see chap. 4 and appendix A) with optical axes as indicated in the figures. They consist in two prism optically glued. Inside the Glan-Thomson prism, at the interface between the two prisms, total internal reflection occurs for the ordinary ray so that the transmitted light is linearly polarised along the extraordinary electric vector (the second half only serves to align the transmitted ray with the incident one). For the Wollaston prism, the optical axes are oriented differently in the two halves. This leads to an angular separation of the ordinary and extraordinary waves.

3.3.3 Parasitic ellipticity and birefringence sources of the optical setup

One of the main constraints for the optical scheme design is the necessity to provide the highest degree of circular polarisation at the centre of the cavity (for Compton scattering with the electron beam, see chap. 2). And to measure it accurately afterwards.

The light polarisation state is controlled by a half wave plate and a Pockels cell. However, all the optical elements located between the Pockels cell and the cavity centre can modify the laser beam polarisation. Non-absorbing elements can in fact induce a parasitic phase shift between the vertical and horizontal components of the electric vector E_x and E_y . This phenomenon will be called here birefringence (although this word refers to the phase shift). In addition to birefringence, an ellipticity can be induced. The main contributors for this effect are the 45° mirrors and the two wedge system.

Two ‘regions’ must be considered: before the cavity centre and after the cavity centre. In the former region, the parasitic birefringence reduces the effective degree of circular polarisation at the laser-electron IP. In the latter region, the birefringence introduces a systematic bias on the laser beam polarisation state measurements.

Let us give here a brief introduction on birefringence using the Jones formalism (for anisotropic crystals, see chap. 4 and for axis-symmetric induced birefringence see appendix 3.8). The Jones matrix of an ideal non-birefringent optical element is simply the 2×2 identity matrix. To take into account a small birefringence one can first assume that the effect is homogeneous within the size of the laser beam spot. Considering the normal incidence and neglecting any internal multiple reflections, the Jones matrix describing

small birefringences of a non-absorbing element is simply the one of a retardation plate:

$$M = \begin{pmatrix} 1 & 0 \\ 0 & e^{i\varphi} \end{pmatrix} \quad (3.2)$$

where φ is called the birefringence and where this matrix expression is given in the so called neutral or eigen-basis. If the incident polarisation is not aligned along the eigenvectors of M , then a relative phase shift is induced between the two components of the electric field. To determine the birefringence of an optical element, a robust method is then to turn this element between two crossed polariser and then to measure the variation of the transmitted intensity. This method leads both to the birefringence and the neutral axis directions.

To control the birefringence/ellipticity of each of our optical elements, one possibility would then be to calibrate all of them accurately. But this task is impossible with regard to the complexity of the phenomenon. Birefringence effects are inhomogeneous, they strongly depend on the beam characteristics, ambient temperature, mechanical stress induced by the mounting and therefore on the laser beam impact point.

The first thing to do is therefore to reduce, when possible, the parasitic ellipticity/birefringence. The dominant source of parasitic ellipticity/birefringence is the 45° dielectric mirrors since they have different reflection coefficients for Transverse Electric (TE) and Transverse Magnetic (TM) waves⁷. No information is provided by the manufacturer, but looking at various manufacturer catalogues one can estimate that reflection coefficients for TM and TE waves may differ by $\approx 0.5\%$.

To reduce this effect, we have adopted a well known mirror scheme⁸: four identical 45° dielectric mirrors M1, M2, M3 and M4 are oriented in such a way that M1 (M2) and M3 (M4) have their normals perpendicular to each other. In this way, the TE and TM waves for M1 (M2) become TM and TE for M3 (M4) respectively so that the ellipticity is, in principle, cancelled out after M4. Since the beam must be inclined by 58 mrad inside the cavity, to keep the orthogonality between M2 and M4, M4 has been turned by 58 mrad around the x axis.

It is difficult to estimate the residual ellipticity/birefringence for this four mirrors scheme. Some studies were performed on a two mirrors scheme (like the one use after the cavity) for the Cebaf cavity project and the result was that the degree of circular polarisation is only modified by one per mille (and roughly one per mille per degree of angular mismatch between the orientation of the two mirrors)[27]. This is satisfactory.

Because it is located after the four mirrors, the cavity entrance window may induce a noticeable birefringence. Although constituted of fused silica, mechanical constraints appear because of air/vacuum pressure (this is mentioned in [25]) and the manufacturing process [28, 29, 30]. In appendix 3.8 we estimate numerically the birefringence induced by the air/vacuum pressure. We find that this effect is negligible. The birefringence induced by manufacturing process (glass-metal soldering from Vermetal) was measured by M. Lintz [31] using the crossed polariser method described above (plus a ‘fine tuning’ rotation/translation of the sample between the polarisers). The result is shown in fig.

⁷These are the two directions of the electric vector: in the plane of incidence (TE) and perpendicular to plane of incidence (TM). Here the plane of incidence is defined by the normal of the mirror and the laser beam propagation axis. See [24] and chap. 4 for more details.

⁸For example, this scheme is used at SLAC/SLC[25] and JLAB/CEBAF [26]

3.27. Within a few millimetre from the window centre, the birefringence can reach at most 5 mrad.

As for the cavity entrance window, one can try to compensate, at least partially, this parasitic birefringence by adjusting the orientation of the HWP and the Pockels cell power supply. In addition, depending on the orientation of the neutral axes within the laser beam spot size, the parasitic polarisation may not be totally spatially Gaussian (see appendix 3.8) so that it may be filtered out when the cavity is locked on the fundamental mode.

However, a second vacuum window is located between the cavity centre and the ellipsometer. To estimate the bias on the determination of the degree of circular polarisation – i.e. the value of the the fourth component S_3 of the Stokes vector (see section 2.2.1) – induced by the 5 mrad window birefringence, let us start from eq. 3.2. S_3 is extracted from the intensity measurements done after the Wollaston prism. The two orthogonal linear polarisation directions transmitted by the Wollaston prism define the absolute basis denoted by $\{\hat{\mathbf{x}}, \hat{\mathbf{y}}\}$. In this basis, the Jones matrix of the birefringent component reads [21]

$$M' = R(-\alpha)MR(\alpha)$$

with α the orientation the neutral axes basis in the absolute basis (we restrict ourselves to the normal incidence) and where $R(\alpha)$ is the 2×2 rotation matrix. If we assume that the laser beam is perfectly circular inside the cavity, then the polarisation state after the window is given by $\mathbf{E}_o = M'\mathbf{E}_i$ with $\mathbf{E}_i^T = (1, i)/\sqrt{2}$. The degree of circular polarisation is further given by (see eq. 2.2 in chap. 2)

$$S_3 = i[\mathbf{E}_o \cdot \hat{\mathbf{x}} (\mathbf{E}_o \cdot \hat{\mathbf{y}})^* - \mathbf{E}_o \cdot \hat{\mathbf{y}} (\mathbf{E}_o \cdot \hat{\mathbf{x}})^*].$$

To second order in φ , one can write $S_3 = 1 + \Delta S_3$ with $\Delta S_3 = -\varphi^2/2$, i.e. the bias is quadratic in φ . It means that degree of circular polarisation of the laser beam is a priori measured with a systematic uncertainty of $\approx 25 \cdot 10^{-6}$ which is much smaller than our requirements. Let us mention that such small birefringence is compatible with some transmission measurements performed within the VIRGO Collaboration on the same kind of window [32].

The cavity mirrors may introduce a birefringence because of the thermoelastic deformation due to the high power circulating inside the cavity [33]. In appendix 3.8 we estimate this effect numerically and we conclude that it is negligible.

A birefringence can also be induced by the multi-layer coating of the cavity mirrors [34, 35, 36, 37, 38]. In refs. [38], precise measurements of the birefringence (and of the orientation of the neutral axis) induced by multi-layer coatings similar to those used in our experiment are described. The order of magnitude of the observed birefringence is $\varphi \approx 10^{-6}$. To estimate the effect of this small birefringence on the polarisation of the beam circulating inside the cavity, we conservatively take $\varphi = 2.5 \cdot 10^{-6}$ [38]. If we assume that the two cavity mirrors are similar, we must just multiply this phase shift by the number of round trips $N = F/2\pi$ (see appendix 3.6.4) and, conservatively, by a factor of two (since there is two reflections per round trips and since the birefringences of each mirror add-up only for the worse relative orientation of the neutral axes[36, 38]⁹). With

⁹Note that the birefringences of the two mirror coatings may also be of different signs and therefore compensate partially.

our cavity finesse $F \approx 30000$ (see chapter 5), we obtain $2N\varphi \approx 2.5 \cdot 10^{-2}$ and thus an effect on the degree of circular polarisation of the order of $(2N\varphi)^2/2 \approx 3 \cdot 10^{-4}$, that is a negligible level for our experiment.

The last source of birefringence for the cavity mirror is the mounting system. This system is shown in fig. 3.26 and it essentially consists in a spring pushing a ring in contact with the cavity mirror. The order of magnitude of the birefringence induced by mechanical stress can be estimated using a simplified version of the calculation presented in appendix 3.8 [39]. Following [40], we introduce an effective parameter $C \approx 10^{-12} \text{ Pa}^{-1}$ for glass such that the induced birefringence reads $2\pi e C p / \lambda$ where p is the pressure supplied on the mirror and e the mirror thickness. The force supplied by the spring on the mirror has been measured [39] (by supplying weights on the system) and is estimated to be at most 2 N, that is a pressure on the mirror $\approx 10^{-4} \text{ Pa}$ and then a birefringence of the order of 10^{-11} for $e = 6\text{mm}$. We can therefore avoid a more quantitative estimate and conclude that this source of birefringence is negligible.

Finally, the two mirrors and the HBS located after the cavity can also induce a birefringence. The HBS birefringence was also measured by M. Lintz [31] but, for this component, it was found to be below the measurement sensitivity ($\approx 0.3 \text{ mrad}$) and therefore negligible with regard to our precision requirement. However, the HBS was mounted in a mirror mount for this measurement and we observed a noticeable birefringence when the locking screw was too tight. We then fixed the HBS in its mount using a stress-free glue. As for the two mirrors system, an in situ calibration procedure has been foreseen (see section 3.3.4) though, as described above, they are not expected to modify significantly the light polarisation.

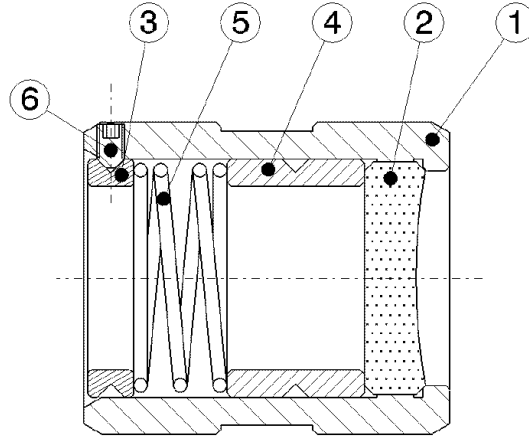


Figure 3.26: *Technical drawing of the cavity mirror mount system. ①: mirror holder; ②: mirror; ③: spacer; ④: spacer; ⑤: spring; ⑥: stop screw. From [10].*

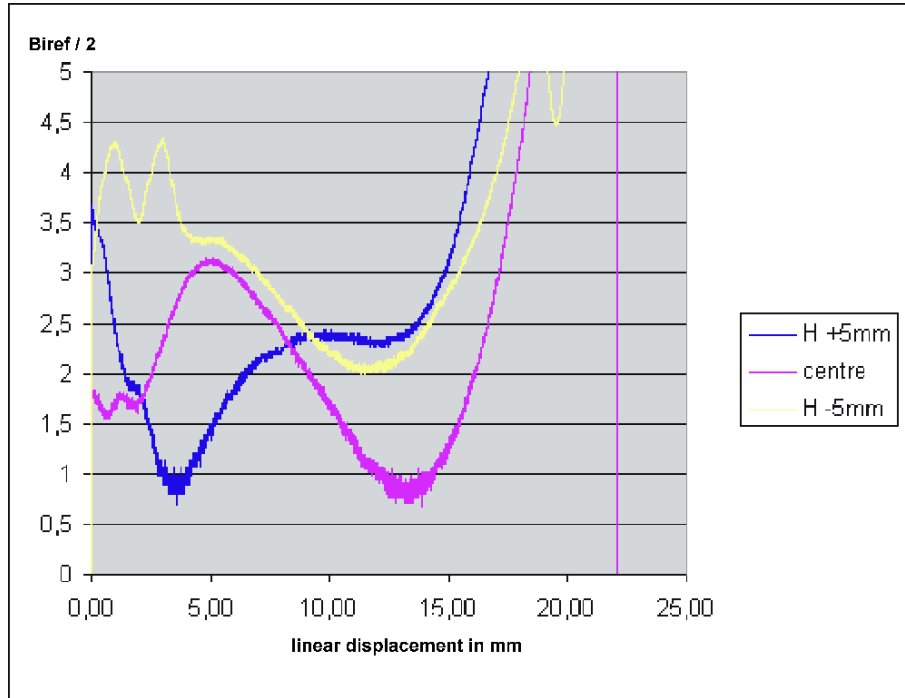


Figure 3.27: Result of the vacuum window birefringence measurement. Different curves correspond to different linear position scans (at the centre and ± 5 mm apart). The window's centre corresponds to 11 mm on the abscissa axis and half the birefringence is plotted on the vertical axis. Measurements are from [31].

3.3.4 Optical calibration procedure

As mentioned in the previous sections, the laser beam polarisation is not measured before the inner part of the cavity and ellipticity/birefringence can be induced by certain of our optical elements. To optimise the degree of circular polarisation at the laser/electron IP, we follow the method of ref. [25]: since the Compton total cross section is an increasing function of the level of circular polarisation, we vary the Pockels cell's voltage and the optical axis orientation of the associated HWP in order to maximise the total number of backscattered photons. Since at the time of writing this document no electron beam has run in HERA yet, we cannot give any result on this procedure.

In order to control the parasitic ellipticity/birefringence induced by our optical elements, we have foreseen to insert a high quality linear polariser (i.e. a Glan-Thomson prism) at various places in our optical scheme: before the four mirror system, before the cavity, after the cavity, before the QWP of the ellipsometer. Rotating the QWP for all these configurations leads, step by step, to an estimate of the optical response of the main pieces of our setup. Again, but here because of a lack of time, we didn't perform this study at the time of writing this document. We postponed these series of measurements for the HERA shutdown of winter 2003.

3.4 Feedback system

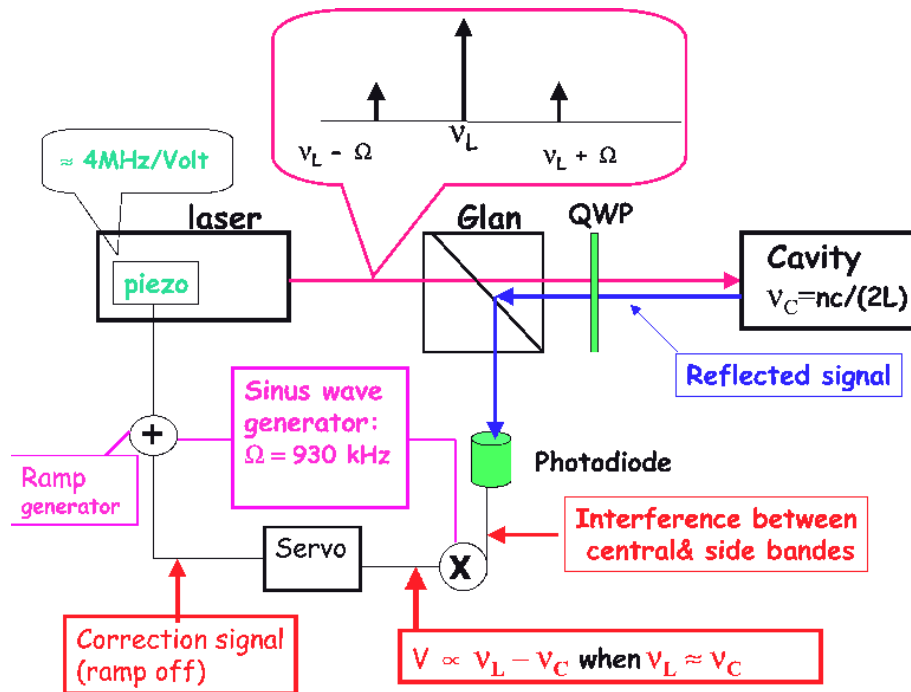


Figure 3.28: Simplified view of the feedback system (see text).

The ‘Pound-Drever’ technique [41, 42] is used for the laser-cavity feedback. This method is illustrated in fig. 3.28. The laser beam frequency is modulated by applying a periodic signal of 50 mV amplitude and $\Omega = 930\text{ kHz}$ frequency on the piezo transducer

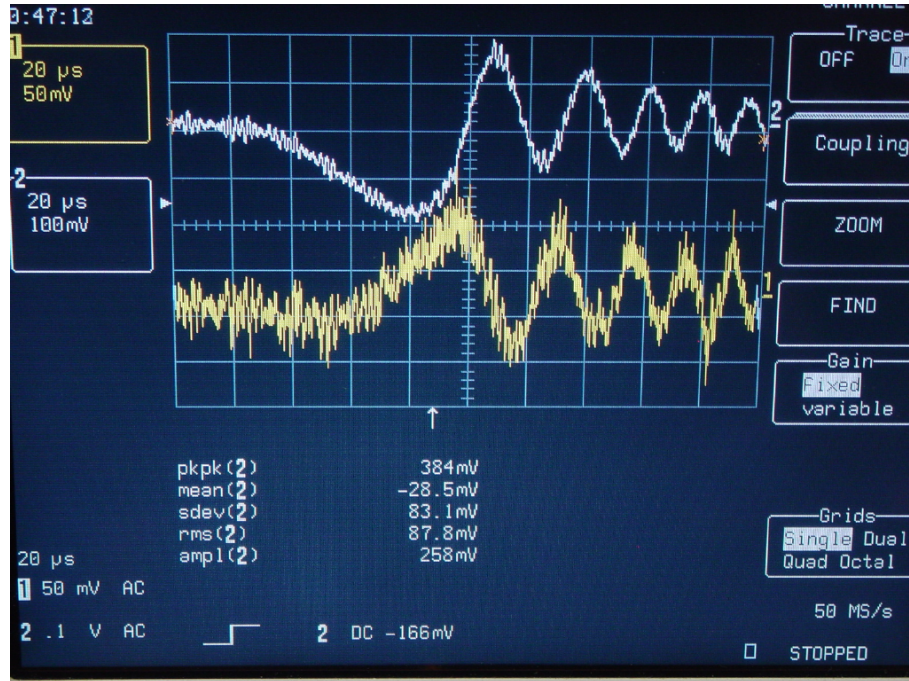


Figure 3.29: Oscilloscope view of the signal reflected by the cavity close to a resonance (upper curve) and the error signal (lower curve). Close to the resonance frequency (minimum of the upper curve), the error signal is linear. These results were obtained in the open-loop feedback mode (see text) during the installation at HERA (i.e. 100 m from the cavity).

(via the laser fast channel, see section 3.3.1). Beside the laser beam frequency ν_L , two side bands of frequencies $\nu_L \pm \Omega$ are generated by this modulation [43]. The electric field has thus three frequency components and the reflected signal measured by the photodiode results from the interference between the central and the side bands. It can be shown (details can be found in ref. [4]) that a demodulation of this signal at the frequency Ω leads to an error signal usable for a feedback loop: close to a cavity resonance frequency ν_c , the error signal is linearly proportional to the difference $\nu_L - \nu_c$ (see fig. 3.29).

To lock the cavity, an electronic feedback system has been designed and built by the SIG group of Saclay. It is a copy of the system used for the CEBAF cavity (itself inspired by the PVLAS experiment system [44]).

This system is depicted in fig. 3.30. A 10 V peak-to-peak ramp, together with the 930 kHz modulation, is supplied on the laser piezo transducer (via the fast channel). The reflected signal is preamplified and next sent to a first module where the error signal is produced. The error signal is then used to build the correction signals supplied on the fast and slow channels. There is a common series of shaping amplification stages and then two different filters in order to distinguish between the low and high frequency components of the correction (bandwidths of ≈ 0.16 Hz and ≈ 30 kHz for the slow and fast channels).

Of course, these correction signals must be applied only when the laser beam frequency is close to a cavity resonance frequency. To decide when the corrections must be applied, the reflected signal is also sent to another module where, according to its amplitude, the system is switched between the ‘closed loop’ and the ‘open loop’ modes. In the ‘open loop’ mode, the corrections to the laser beam frequency are not sent to the piezo transducer whereas in the ‘closed loop’ mode, these slow and fast correction signals are sent to the laser and the ramp is switched off (see fig. 3.31).

As indicated in fig. 3.30, a band pass filter is applied on the reflected signal before the demodulation. This filter, centred on Ω , eliminates all harmonics of the modulation frequency Ω except the fundamental one. The value of Ω is determined by minimising the laser Residual Amplitude Modulation [43, 4, 45] (RAM). When the piezo transducer is modulated, not only the phase is modulated but also the amplitude. This parasitic effect can induce a bias in the error signal.

A spectral density measurement of the reflected signal as a function of the frequency modulation has been performed and results similar to those of ref. [45] were observed. From these results, $\Omega = 930$ kHz has been chosen. However, one should note that the RAM depends on the laser temperature [45]. This temperature is varied during the feedback operations (slow channel) and even during the open loop step where the cavity fundamental mode ‘is brought’ within the frequency range of the ramp (10 V corresponds approximately to $FSR/2 \approx 45$ MHz) by changing the temperature ‘by hand’. A fine tuning of Ω is then not crucial and it is more important to check the feedback stability against temperature variations for a given value of Ω . We performed this study by also varying Ω within the band pass filter range. No modifications of the feedback/locking performance were observed.

3.5 Electronics and calorimeter readout

Our electronics is divided into two parts: a slow control ($\simeq 1$ Hz) system to operate the optical/laser elements and a fast Data Acquisition System (DAQ) to record the calorimeter

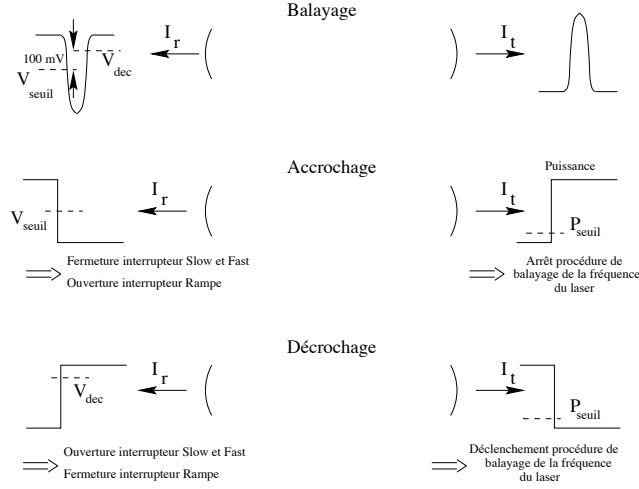


Figure 3.31: *Schematic illustration of the automatic locking procedure. From [4]*

signal at each bunch crossing ($=10$ MHz). Both systems are connected to a master personal computer (PC) which controls the DAQ and the optical processes. PVSS [46] software is used on this PC which is also connected to the DESY database.

3.5.1 Slow control

There is only a small number of electronic components related to the optical tables components (see fig. 3.32): two motor controllers for the two motorised mirrors and the two rotation mounts (turning the HWP before the Pockels cell and the QWP after the cavity); the laser controller, used to change the laser temperature and to switch on/off the laser beam; the double polarity power supply of the Pockels cell that we vary between -4 kV and $+4$ kV; temperature sensors; CCD cameras; the laser beam shutter; the photodiodes readout and the Peletier feedback system.

All these components are located in the HERA tunnel, ≈ 100 m away from the electronics trailer. To transport the photodiode signals used to monitor the laser beam polarisation and the laser beam power (those located after the cavity), individual shielded twisted pair cables are used to reduce the electromagnetic pickup background. The DAC signal sent to the Pockels cell's power supply is also transmitted by this kind of cable (a long term stability better than one per mille if reached).

LabView software [47] is used for the optics slow control. The calculator is a Pentium III 1.25 GHz PC (platform: Windows 2000) located inside a PXI crate [47]. The following PXI modules are read out:

- A multifunction card (NI/PXI-6025E) containing 16 single analogue inputs (or 8 differential), two 12 bit DAC output channels and 24 I/O lines ($=5$ V/TTL signals).

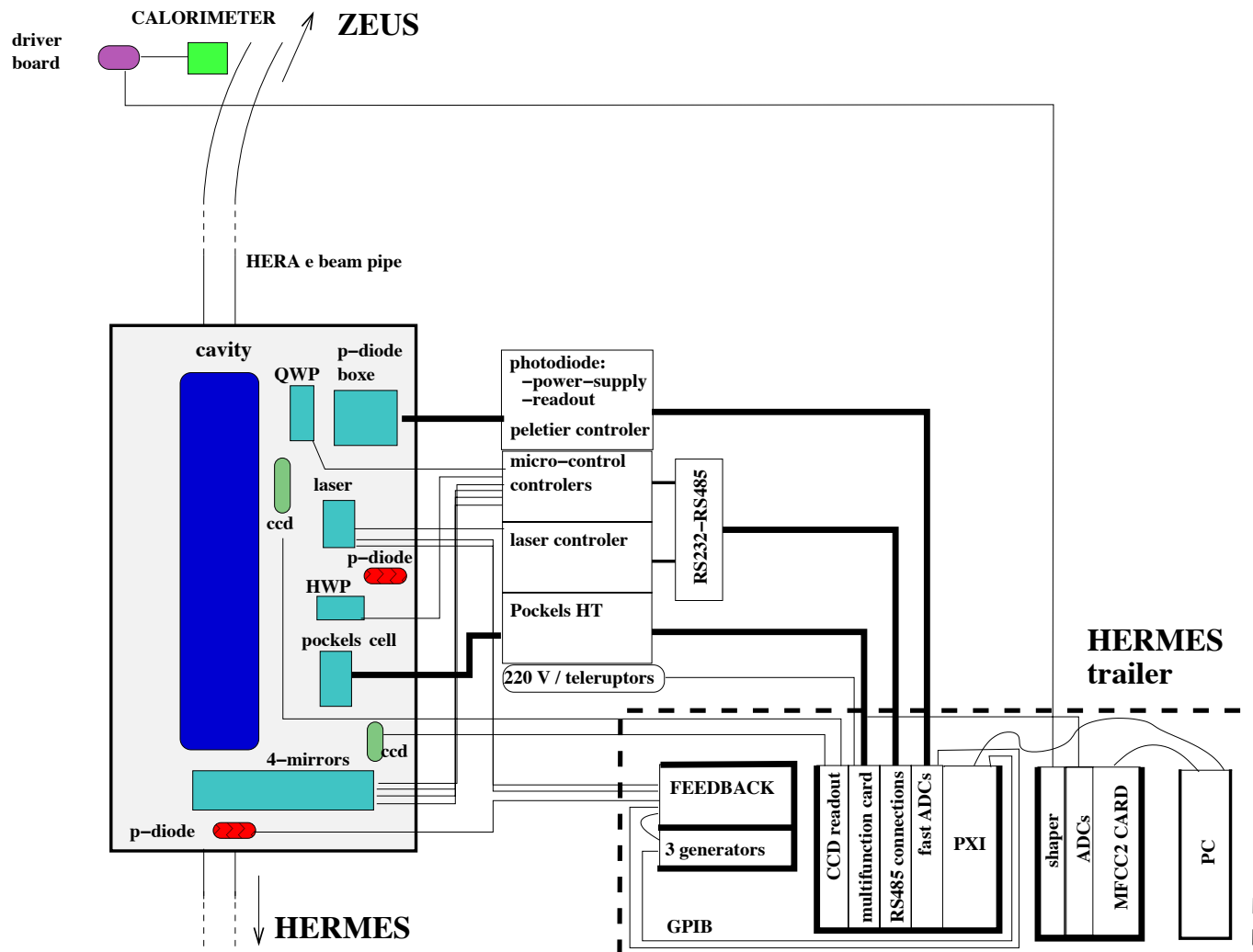


Figure 3.32: Schematic view of the main electronics devices and connections. The temperature sensors are not shown.

Analogue inputs are sequentially digitised by a single 200 kHz 12 bit ADC (there is no low pass filter and no sample and hold). We essentially use these channels to read out the temperature sensors¹⁰ (Analogue Device AD580), some signals from the feedback module and the Pockels cell power supply monitoring. The DAC channels are used to set the Pockels cell's High Voltage. The I/O are used to switch the controller's power supply on/off and to operate the beam shutter.

- Two multichannel ADC cards (NuDAQ/PXI-2010). Each card consists of four independent 14 bit 2 MHz ADCs. They are used for the differential read out of the the photodiodes used by the laser beam polarisation measurement system, the feedback error signal and the signals reflected and transmitted by the cavity. We have chosen this device in order to increase our sensitivity for the polarisation measurement and to avoid the use of a low pass filter. Two 12 bit DAC output channels are also available, they are used to control the feedback module via the PXI.
- A serial RS485 connection module (NI/PXI-8421), used to access the laser controller, the two micro-control stepper motor controllers and the vacuum gauge located in the cavity vessel. Connections are done through RS485/RS232 interface hardware since all our electronic devices only have RS232 ports.
- A monochrome four channel video board (NI/PXI-1409) to readout our CCD cameras.

Finally, the PXI is accessed from everywhere thanks to the Remote-Anything software [48], based on a client-server architecture.

3.5.2 Fast Data Acquisition System

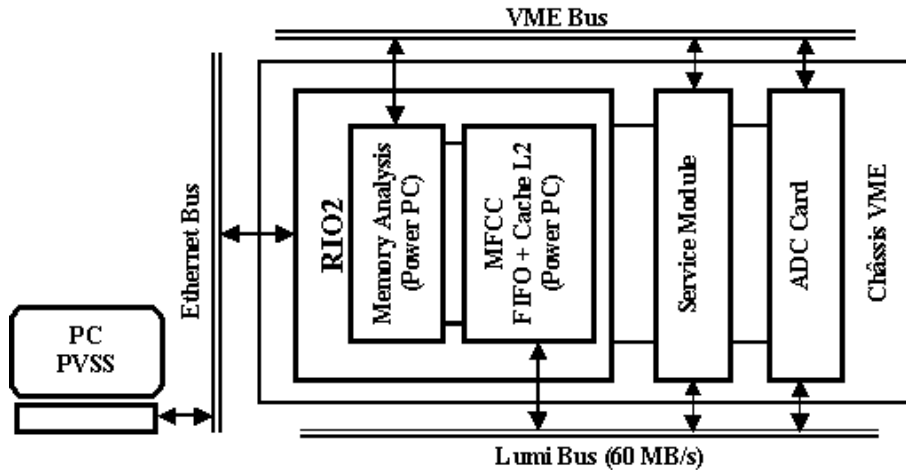


Figure 3.33: *Global architecture of the DAQ system. From [49].*

¹⁰These are integrated circuits which provide a current proportional to the temperature. They drift slightly in time (0.2 K typically within hundreds of hours).

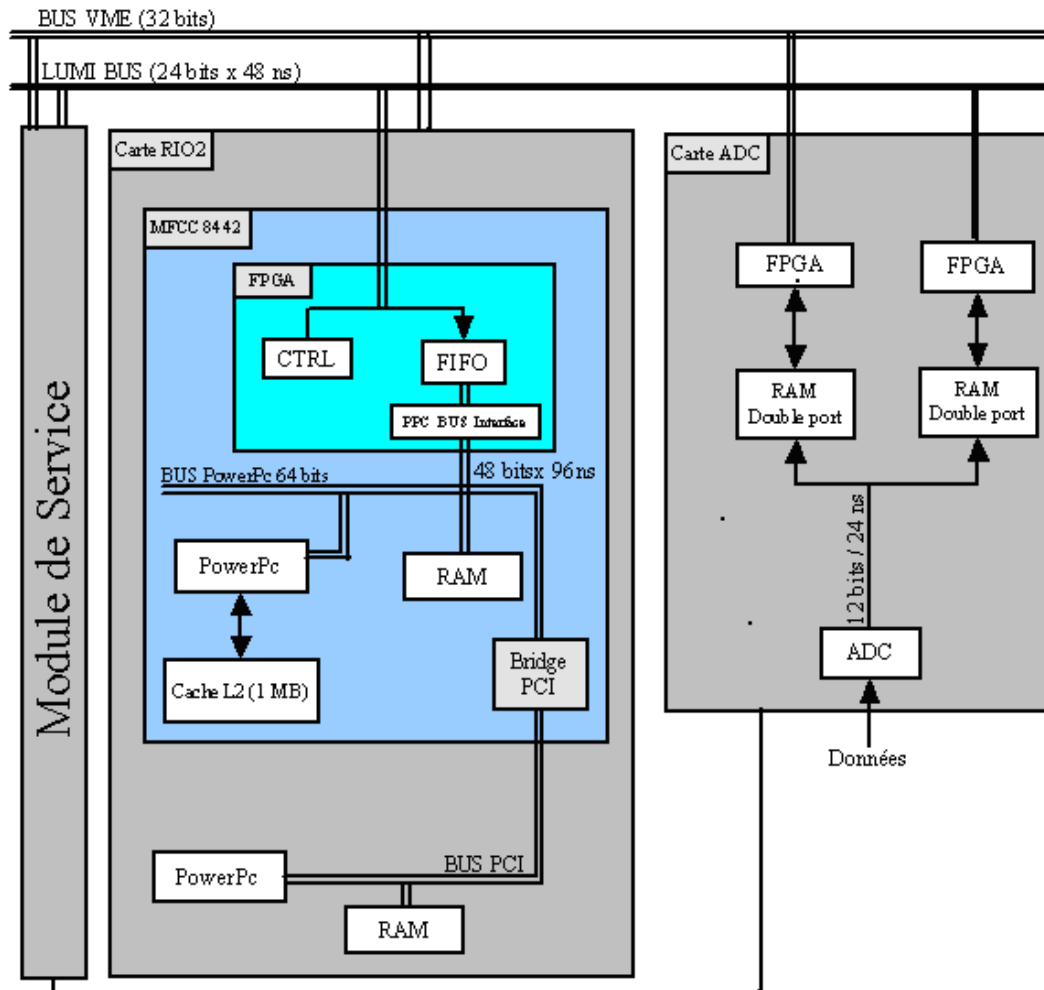


Figure 3.34: Schematic view of the RIO2/MFCC2 board. From [49].

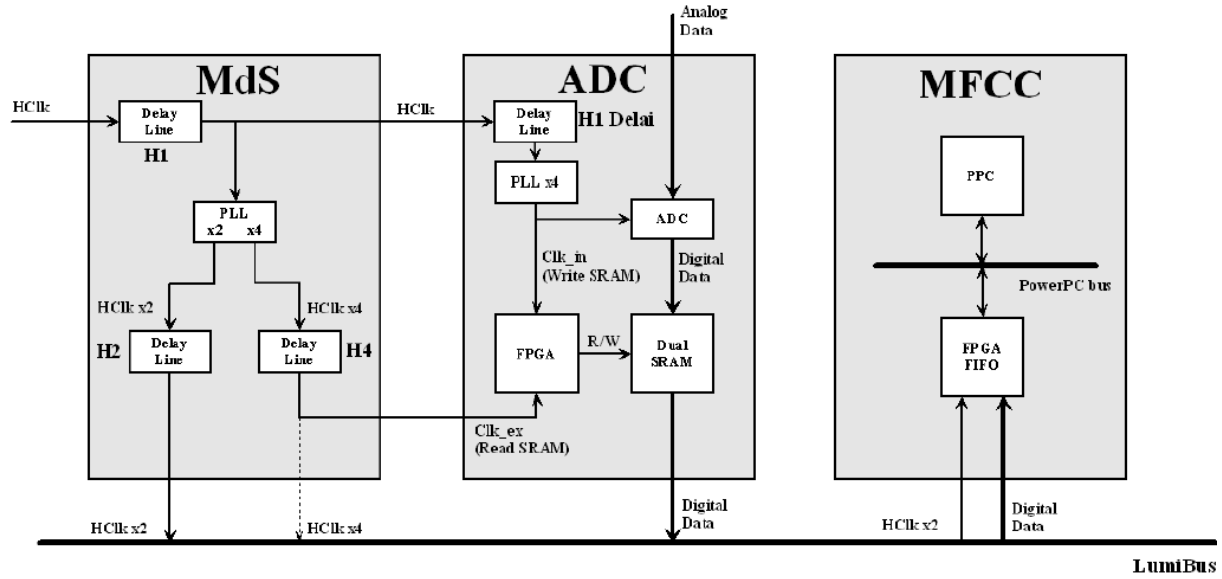


Figure 3.35: Description of the HERA clock distribution. From [51].

The DAQ system is similar to the one used for the electronic upgrade of the HERA transverse polarimeter and for the new H1-Luminosity monitor. In our case, the essential difference is the high DAQ rate requirement of 10 MHz which involves a real-time system.

A radiation hard calorimeter will be installed during the winter shutdown of 2003. To start with, we shall use a sampling (tungsten/scintillator sandwiches) calorimeter readout by a single photo-multiplier.

Starting from the calorimeter (see fig. 3.32) we find: a driver board amplifying the Photo-multiplier signal (gain=10); two 100 m long 50Ω coaxial cables, one for the signal and one without signal to subtract the electromagnetic pickup (= the base line); a shaper board (shaping time lower than 96 ns), used to compensate for the skin effect due to the cable length and to adapt the analogue signal level to the ADC range (0-2 V); a 12 bit 40 MHz ADC board (8 channels); the RIO2/MFCC2 [50] card used for the DAQ.

The DAQ architecture is shown in fig. 3.33 and the core of the system, the RIO2/MFCC2 board, is described in fig. 3.34. The DAQ is synchronised to the first electron bunch by the module named ‘service module’ (see fig. 3.35) and a dedicated bus, the Lumi bus, is used for the data flow (it was developed for the upgrade of the H1 luminosity monitor).

Each calorimeter signal is sampled four times by the ADC between two successive bunch crossings (=96 ns). The samples are written in a buffer memory of the ADC board and continuously added to the FiFo of the FPGA of the MFCC2 board. To get a signal proportional to the energy deposited in the calorimeter, one must sample the analogue signal at its maximum. A tunable delay between the HERA clock and the ADC is used to operate the second sampling at this maximum. The baseline is thus measured by the first sampling and it is subtracted from the second sample by the Power-PC (i.e. by software, two of the four samples being discarded after the timing calibration). The corrected signal is next transferred to the Power PC L2 cache memory. This 1 Mbyte SRAM is configured in order to store the energy histograms of the 220 electron bunches. The memory is refreshed and the histograms transferred to the Power-PC of the RIO2 board (platform:

Lynx/Os) via a PCI bus at each change of the laser beam polarisation. The decay time of the cavity is roughly $60\mu\text{s}$ so that it takes a few milliseconds before reaching a pure polarisation state at the laser/electron IP (and another $60\mu\text{s}$ to reach the full power). We use this physical ‘dead time’ to transfer the histograms.

The synchronisation between the laser beam polarisation switching (each 6 s) and the histogram filling is done with the Pockels cell’s power supply monitoring signal. We send this signal to the ADC in order to trigger the calorimeter readout.

3.6 Appendix: Laser and cavity modes

3.6.1 Laser beam

The electric field of a perfect Gaussian laser beam (= solution of the Maxwell equations in the paraxial approximation [3]) is

$$\mathbf{E} = \mathbf{E}_0 \frac{w_0}{w(z)} e^{i\psi(z)} e^{ik\rho^2/2R(z)} e^{-\rho^2/w^2(z)} e^{i(\omega t - kz)}$$

where: $|E_0|^2$ is the laser beam power; z is the laser beam axis; $\rho^2 = x^2 + y^2$; $\psi(z) = \tan^{-1}(z/z_0)$ is the Guoy phase; $R(z) = z + z_0^2/z$ is the real part of the wave radius of curvature; $w(z)$ is the transverse size of the laser beam:

$$w(z) = w_0 \left[1 + \frac{z^2}{z_0^2} \right]^{1/2}; \quad z_0 = \frac{\pi w_0^2}{\lambda}$$

where z_0 is the Rayleigh range and where $w(0) \equiv w_0$ is the laser beam waist.

Note that one standard deviation of the laser beam intensity distribution is given by $\sigma_\gamma(z) = w(z)/2$. In a cavity where the two mirrors are similar the waist is at the centre of the cavity.

The Gaussian beam is the fundamental mode of a complete basis of solutions of the paraxial Maxwell equations (these modes can be identified by the number of maxima of the beam intensity, the fundamental mode has only one maximum). Two basis are frequently utilised: the Hermite-Gauss functions

$$\mathbf{E} \propto \mathbf{E}_0 H_n \left(\frac{\sqrt{2}x}{w(z)} \right) H_m \left(\frac{\sqrt{2}y}{w(z)} \right) e^{i(n+m+1)\psi(z)} e^{ik\rho^2/2R(z)} e^{-\rho^2/w^2(z)} e^{i(\omega t - kz)}$$

with H_n the Hermite polynomial of order n ; and the Laguerre-Gauss functions

$$\mathbf{E} \propto \mathbf{E}_0 L_p^l \left(\frac{\sqrt{2}\rho^2}{(w(z))^2} \right) e^{i(2p+l+1)\psi(z)} e^{i\phi} e^{ik\rho^2/2R(z)} e^{-\rho^2/w^2(z)} e^{i(\omega t - kz)}$$

where L_p^l is the Laguerre polynomial and ϕ is the azimuth angle in cylindrical coordinates.

The Hermite-Gauss and Laguerre-Gauss modes are usually denoted with TEM_{nm} and TEM_{lp} respectively. Some of them are shown in fig. 3.36.

3.6.2 Cavity eigen-modes

In a cavity made of two spherical mirrors, it can be shown that Hermite-Gauss and Laguerre-Gauss modes are also solutions of the Maxwell equations. But the waist is now constrained by the boundary conditions. For a cavity made of two identical spherical mirrors located at a distance L from each other, the beam radius of curvature on the mirror R and the mirror radius of curvature R_c must be the same. Taking $z = 0$ at the cavity centre this condition reads

$$R(L/2) = R_c.$$

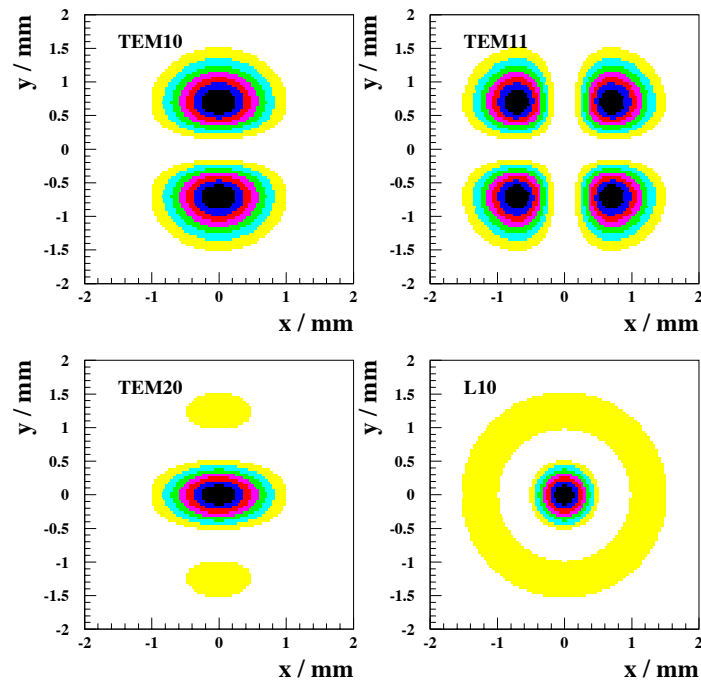


Figure 3.36: *Excited transverse mode appearing when the axial symmetry is broken. TEM10, TEM11 and TEM20 refer to the Hermite polynomials and L10 refers to the Laguerre first order polynomial.*

Hence, one has

$$w_0 = \sqrt{\frac{\lambda}{2\pi}}(L(2R_c - L))^{1/4}$$

where λ is the laser beam wavelength. Here the two mirrors are assumed to be similar so that the waist position is at the centre of the cavity. Notice that for a confocal cavity the waist is simply given by $w_0 = \sqrt{\lambda L/(2\pi)}$.

3.6.3 Cavity mode structure

$TEMnm$ modes resonate at different frequencies inside the cavity. It can be shown [2] that the resonance frequency of an Hermite-Gauss mode of order n, m is given by

$$\nu_{nm}^q = \nu_0 \left[q + \frac{1+n+m}{\pi} \text{acos} \left(1 - \frac{L}{R_c} \right) \right] \quad (3.3)$$

where q is the longitudinal mode, ν_0 the $FSR = c/2d = 75.6$ MHz (see table 3.2), R_c the radius of curvature of the cavity mirror and L the cavity length.

Since our cavity is quasi confocal $R_C \approx L$, one gets

$$\text{acos} \left(1 - \frac{L}{R_c} \right) \approx \frac{\pi}{2}(1 + \delta)$$

with $\delta = -0.0048$. Writing $N = n + m$, eq. 3.3 becomes

$$\nu_N^q = \nu_0 \left[q + (1 + N) \frac{1 + \delta}{2} \right].$$

The mode structure is defined by the position of the cavity modes in the frequency space. From the laser beam frequency $\nu_L = c/\lambda = 3 \cdot 10^{14}$ Hz one sees that $\nu_L/\nu_0 \approx 4 \cdot 10^6$ so that $q \simeq 10^6$. This large number means that various longitudinal modes can be excited inside the cavity by our laser beam. For each longitudinal mode q , the complete set of transverse modes N can appear. For a given transverse mode N and longitudinal mode q one must find the position of all modes located between ν_N^q and $\nu_N^q + \nu_0$. That is the set of integer numbers $\{q', N'\}$ such

$$\nu_N^q < \nu_{N'}^{q'} < \nu_N^q + \nu_0 \Leftrightarrow (1 + N) \frac{(1 + \delta)}{2} < \Delta q + (1 + N') \frac{(1 + \delta)}{2} < 1 + (1 + N) \frac{(1 + \delta)}{2}$$

with $\Delta q = q' - q$. Defining $\Delta N = N - N'$, one further obtains

$$\Delta N(1 + \delta) < 2\Delta q < 2 + \Delta N(1 + \delta)$$

Restricting ourself to the case $\delta\Delta N < 1$ (i.e. $\Delta N \leq 208$ which is a huge number) this equation admits two sets of solutions:

$$\begin{cases} \Delta N \text{ odd} \Rightarrow \Delta q = (\Delta N + 1)/2 \Rightarrow \nu_{N'}^{q'} = \nu_N^q - \frac{\nu_0}{2}(1 + \delta\Delta N) \\ \Delta N \text{ even} \Rightarrow \Delta q = (\Delta N + 2)/2 \Rightarrow \nu_{N'}^{q'} = \nu_N^q - \frac{\nu_0}{2}\delta\Delta N \end{cases}.$$

The mode structure is clearly defined by these two equations. Considering the fundamental transverse mode $N = 0$ and a given longitudinal mode with $q \simeq 10^6$ one

observes that: even modes ($N' = 2, 4, \dots$) are located in the vicinity of ν_0^q at a distance $\pm\Delta\nu = \pm N'\nu_0\delta/2 = \pm N'/2 \times 363$ kHz, and odd modes ($N' = 1, 3, \dots$) are located close to $\nu_0^q \pm \nu_0/2$ (i.e. at half distance between two consecutive *TEM00* longitudinal modes) distant by $\Delta\nu$ from each other.

This mode structure was observed experimentally at the oscilloscope and the distance between the even and odd mode was used to determine the laser piezo coefficient (see section 3.4). Finally, let us mention that we obtain the same results considering Laguerre-Gauss modes by changing $m \rightarrow 2p$ and $n \rightarrow l$ [2].

3.6.4 Number of round trips inside a cavity

In the core of this chapter, the number of round trip inside a cavity is used to estimate the maximum birefringence induced by the reflexions on the multilayer coatings of the cavity mirrors. Since I did not find any definition but just a formula (e.g., see Ref. [38]) I give here a short definition, by the way very simple, for the sake of clarity.

We first have to define the probability for a plane wave to be reflected by one of the cavity mirror. This is given by the ratio between the intensity of the reflected wave and the intensity of the incident wave, that is $R = |r|^2$ where r is the reflection coefficient for the electric field vector (here the mirror coating is assumed to be not birefringent). Avoiding a global transmission factor (which is cancelled by the normalisation), the unnormalised probability of a plane wave to ‘survive’ inside the cavity after n round trips is then given by R^{2n-1} . The ‘number of round trips’ is then defined by the average number of round trips:

$$N \propto \sum_{n=1}^{\infty} n R^{2n-1} = R \sum_{n=1}^{\infty} n (R^2)^{n-1} = R \frac{d}{dR^2} \sum_{n=1}^{\infty} (R^2)^n = \frac{R}{(1-R^2)^2}$$

where we have used $\sum_{n=0}^{\infty} x^n = 1/(1-x)$.

The normalised number of round trip is finally obtained by deviding the previous equation by the sum of the unnormalised probabilities: $\sum_{n=1}^{\infty} R^{2n-1} = R/(1-R^2)$. We obtain:

$$N = \frac{1}{1-R^2} \approx \frac{1}{2(1-R)} = \frac{F}{2\pi}$$

where we have assumed that $R \approx 1$ and where F is the cavity finesse.

3.7 Appendix: technical aspects of cavities

3.7.1 The mirrors

A sketch of the mirrors is given in fig. 3.37.

The spherical mirrors of the cavity have been coated at the SMA/IN2P3 Laboratory of Lyon. They are characterised by the following quantities:

- the substrate is made of silica SiO_2 , its thickness is $e = 6$ mm, its diameter is $\Phi = 1$ inch ≈ 2.5 cm, its radius of curvature is $R_c = 2$ m, and its absorption coefficient is $A_s \approx 1$ ppm/cm;

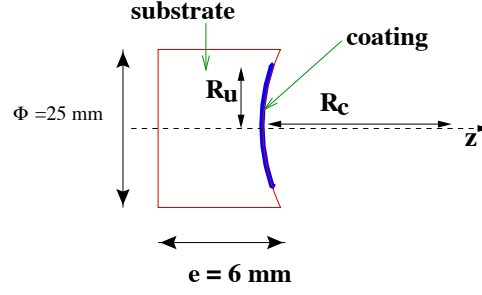


Figure 3.37: *Simplified scheme of the mirror (see text).*

- the coating is made of dielectric quarter wave stacks [54] SiO_2 ($n = 1.47$) / Ta_2O_5 ($n = 2.1$), the size of the coating on the substrate is $R_u \approx 10$ mm. The absorption A , diffusion D , reflection R and transmission T coefficients are given in table 3.2. They are related by $P + R + T = 1$ where $P = A + D$ is the loss.

mirror number	A in centre (ppm)	D over 16 mm diameter (ppm)	T (ppm)
01046/11	1.04	30	105
01046/12	1.9	40	94
01046/13	1.3	38	100
01046/14	1.1	38	92
01046/21	1.04	40	138

Table 3.2: Average characteristics of the mirrors. These parameters vary from point to point on the mirror surface.

Because of the non-vanishing absorption of the coating (inducing heating), there is a maximum laser beam intensity that the mirrors can tolerate. For a Gaussian laser beam, the maximum intensity on the mirrors is localised at $\rho = 0$:

$$I_{max} = \frac{2P_{in}}{\pi w^2(z = L/2)}.$$

For our mirror coating, the intensity damage threshold has been determined with a red laser light [55] $I_{max} < 4\text{MW}/\text{cm}^2$. This number is used in section 3.1.2 where the luminosity is optimised.

3.7.2 Mechanical tolerances for a monolithic cavity

In addition to the length variation – taken into account by the feedback procedure – one has also to consider the effects of mechanical defects. In evaluating these effects we shall assume a perfect alignment of the laser beam axis to the cavity optical axis. Power loss due to such a misalignment will be studied in the next section. Two kinds of defects are to be considered: an angular tilt θ and a mirror optical axis shift ρ (see fig. 3.38). In order to understand the effects of such defects on the cavity one can draw a very simple

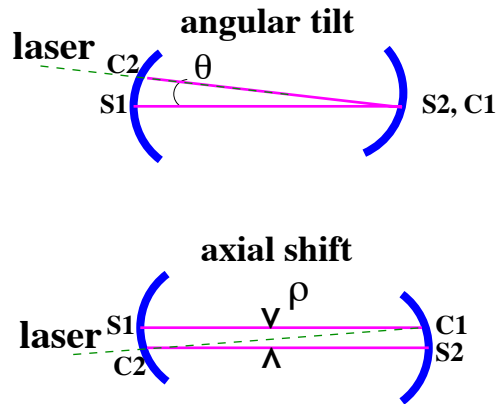


Figure 3.38: Mechanical defects can be decomposed into two independent effects: angular tilt and axial shift. $S1$ and $S2$ are the mechanical mirror centres and $C1$ and $C2$ are the mirror optical centres. The laser beam is aligned on the optical axis.

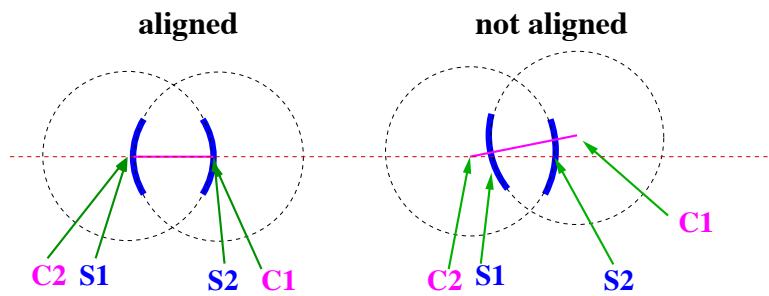


Figure 3.39: Simple drawing to show the effect of a misalignment of two spherical mirrors.

picture (see fig. 3.39). When the mirrors are aligned the optical centres C1 and C2 coincide with the mirror centres S1 and S2. When the mirrors are misaligned, the mechanical axis S1-S2 doesn't coincide anymore with the optical axis C1-C2 of the mirrors. But, since the mirrors are spherical, such misalignments have no effect on the resonance inside the cavity provided the laser beam is aligned with the optical axis. The losses only become significant if the defect is large enough to induce diffraction effects at the mirror edges.

It is very difficult to model the power lost by diffraction inside a Fabry-Perot cavity [3]. However one can estimate it geometrically and thus provide an over estimation of the effect [5, 4, 6]. In ref. [6] the distance D between the optical centre C1 and the mirror centre S2 is calculated. At first order (= assuming that all defects are small compared to the cavity length) one gets:

$$D \leq \frac{R_c^2}{2R_c - L} \left(\frac{\rho}{R_c} + \theta \right)$$

for the maximum distance induced by an angular tilt of θ radians and an axial shift δ . From this expression one can easily verify that $R_c = L$ (= confocal cavity) minimises the factor in front of the brackets. Taking $R_c = L = 2$ m, one gets

$$D[mm] = \rho[mm] + 2\theta[mrad].$$

With a 2 m long cavity the order of magnitude of the mechanical tolerances are $O(1mm)$ for the axis shifts and $O(1mrad)$ for the angle tilts.

The usable radius of the mirror is limited on the one hand by the coating (see 3.7.1), and on the other hand by the aperture of the laser beam tube (see 3.2). If R_u is the usable radius of the mirror, the situation is illustrated in figure 3.40.

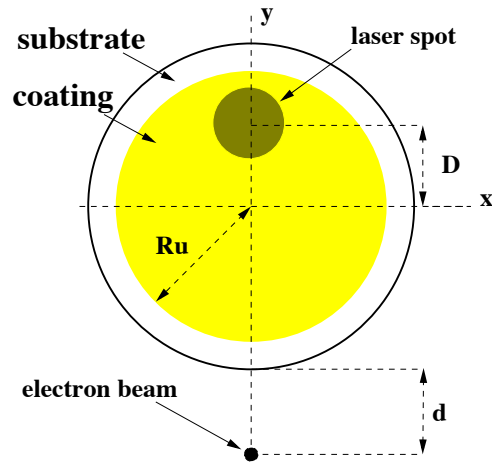


Figure 3.40: *Transverse view of the mirror coating. In this view, d stands for the distance between the electron beam and the lower edge of the mirror.*

Due to mechanical defects, the optical axis can be shifted on the mirror surface by a distance D from the centre. The laser beam width is $\sigma_{spot} \equiv w(z = \pm L/2)/2 = \sqrt{\lambda L/(2\pi)}$. It amounts to ≈ 0.42 mm for $L = 2$ m and for an infrared laser beam. The

fractional power loss is calculated according to the following formula:

$$\delta P = \frac{1}{2\pi\sigma_{spot}^2} \int \int_{x^2+y^2 > R_u^2} \exp\left(-\frac{(x)^2 + (y-D)^2}{2\sigma_{spot}^2}\right) dx dy$$

where the x and y axes are indicated on the above figure. The results are shown in fig. 3.41 for $L = 2$ m as a function of R_u and for various values of the mechanical tolerance D .

Since the coating radius is ≈ 12 mm, the aperture from the laser beam tube, which is 7.5 mm, defines the usable area of the mirror. The possible range of offset for the laser beam spot is then around 5 mm if we safely require $\delta P < 10^{-10}$.

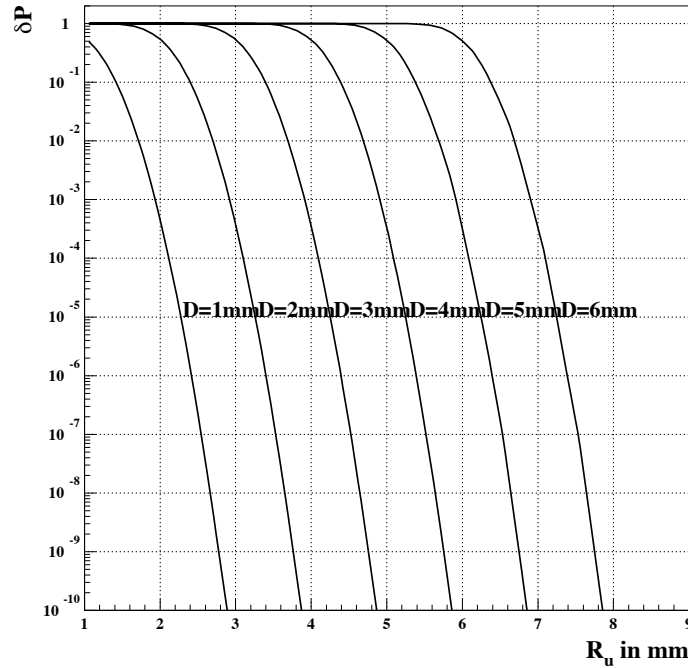


Figure 3.41: *Relative power loss as a function of the usable coating radius for different mechanical defects (see text), for infrared light.*

3.7.3 Power Losses due to Laser beam Cavity Coupling Imperfections

As in the above section, there are two independent geometrical misalignments: a shift Δ between the cavity optical axis and the laser beam axis, an angular α tilt between the laser beam axis and the cavity axis (see fig. 3.42). The effect of such defects is to break the axial symmetry inside the cavity. Higher modes (essentially the TEM₁₀ mode for small defects) are excited and the fundamental Gaussian mode is therefore attenuated. So the power inside the cavity is reduced.

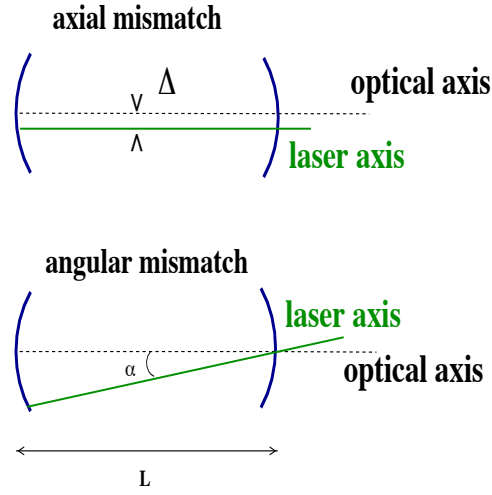


Figure 3.42: Any laser beam-cavity coupling geometrical defects can be described by two independent effects: axial mismatch and angular mismatch.

To first order in the geometrical defects, the power losses $\Delta P_{in} = P_{0,in} - P_{in}$ ($P_{0,in}$ is the power inside the cavity without any laser beam-cavity coupling defects) can be expressed as [52, 53]:

- $\Delta P_{in}/P_{in} = [\alpha\pi w_0/\lambda]^2$ for an angular tilt: if $\alpha \approx 60 \mu\text{rad}$, $\approx 1\%$ of the power is lost.
- $\Delta P_{in}/P_{in} = [\Delta/w_0]^2$ for an axial shift: if $\Delta = 58\mu\text{m}$, 1% of the power is lost,

where we have considered a confocal cavity of 2 m length ($w_0 = 582\mu\text{m}$).

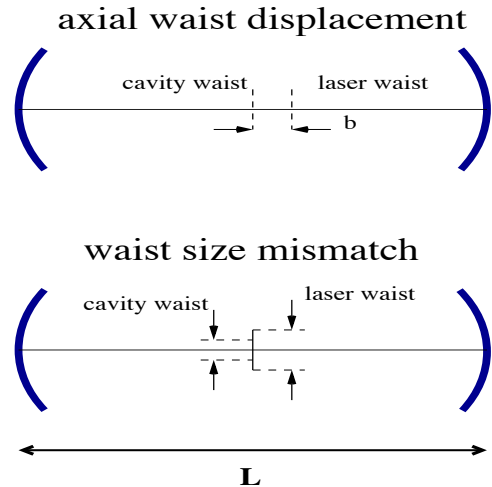


Figure 3.43: Waist position and size mismatches.

As mentioned above, resonance is achieved when the laser beam waist and the cavity waist coincide and are matched. Therefore one must also consider the power losses due

to these mismatches, too. These defects are shown in fig. 3.43 (when these defects are present the mode L10 is excited, see 3.7.1). In first order one gets

- $\Delta P_{in}/P_{in} = [\Delta w/w_0]^2$ for a waist size difference of Δw .
- $\Delta P_{in}/P_{in} = [\lambda b/(2\pi w_0^2)]^2$ for a shift of the waist position by a distance b .

A direct effect of the above is the power loss due to the laser beam ellipticity (the waists in x and y are different for our laser beam). Since the optical devices are optimised for one waist value, this means that the axial symmetry is broken in one direction and, again, that higher modes are excited (here the mode TEM20, see 3.7.1). This effect has been evaluated in [6]. Defining $w_y = \beta w_x$ where w_x and w_y are the laser beam waists in the two orthogonal directions, the relative power loss is

$$\delta P = \frac{\beta}{1 + \beta^2} \left(\frac{\beta^2 - 1}{\beta^2 + 1} \right)$$

which amounts to 5% with our laser beam. In principle, this loss can be avoided by using cylindrical lenses. But, since it is small, we choose to ignore it.

3.8 Appendix: some birefringence estimates

3.8.1 Introduction

The polarisation state of a laser beam transmitted by a birefringent plate is, in general, not trivial. If the birefringence is homogeneous over the laser beam spot size then a phase difference between the two components of the electric field is induced. If this is not the case, the phase difference varies within the laser beam spot. An average polarisation can be computed but one cannot compensate for the change of polarisation since the laser beam polarisation state is not homogeneously distributed in the transverse plane. If a laser beam enters a Fabry-Perot cavity with such a polarisation state the situation is even more complicated since two orthogonal polarisation states (circular left and circular right for example) may be distributed differently in the transverse plane and therefore propagate differently.

From these general considerations, an estimation of possible birefringence effects induced by the optical elements located after the cavity and before the ellipsometer is important. In the present Appendix we shall estimate the birefringence induced by (see fig. 3.44):

- the thermoelastic deformation of the Fabry-Perot mirror substrate due to the fraction of the high circulating power absorbed by the coating.
- pressure difference acting on the vacuum window of the cavity.

In both case, the problem is axis symmetric. Therefore we shall restrict ourselves to this simple symmetry configuration.

An estimate of the birefringence induced by thermoelastic deformation of the mirror substrate is given in ref. [56], we will describe here a more precise model.

It is important to specify that we do not and indeed cannot, estimate what appears to be the dominant source of birefringence: that is the mechanical stress induced by the glass-metal soldering of the vacuum window. This effect was studied experimentally.

This Appendix is organised as follows, in section 3.8.2 the birefringence formalism for Gaussian beams is introduced. Some details are given since the formulation of the problem in cylindrical coordinates is not given in the text books (some details can be found in a French PhD thesis [57]). In section 3.8.3 the birefringence induced by heat effects in the cavity mirror is presented and the effect of the vacuum window is presented in section 3.8.4.

3.8.2 Formalism

Let us start with basic considerations. The optical index matrix of a given optical medium B is defined by

$$B = \begin{pmatrix} 1/n_{xx}^2 & 1/n_{xy}^2 & 1/n_{xz}^2 \\ 1/n_{xy}^2 & 1/n_{yy}^2 & 1/n_{yz}^2 \\ 1/n_{xz}^2 & 1/n_{yz}^2 & 1/n_{zz}^2 \end{pmatrix}$$

where n_{ij} are the generalised refraction indices [21]. When the medium is submitted to mechanical constraints, to first order in the perturbation the index matrix becomes

$$B \rightarrow B + \Delta B \text{ with } \Delta B = \Pi \Theta \quad (3.4)$$

where Π is the piezo-optic tensor of rank four and Θ the rank two stress tensor. The former tensor depends only on the optical medium under consideration and the later tensor depends on the mechanical constraints applied to the medium. In the steady state equilibrium, for an axial symmetric problem, the components of the stress tensor Θ are given by [58]

$$\begin{aligned}\frac{\partial\Theta_{rr}}{\partial r} + \frac{\partial\Theta_{rz}}{\partial z} + \frac{\Theta_{rr} - \Theta_{\phi\phi}}{r} &= 0 \\ \frac{\partial\Theta_{rz}}{\partial r} + \frac{\partial\Theta_{zz}}{\partial z} + \frac{\Theta_{rz}}{r} &= 0\end{aligned}\tag{3.5}$$

in cylindrical coordinates (r, ϕ, z) . For heat effects inside the cavity mirror, the boundary conditions are

- the mirror is isolated and is located in vacuum¹¹.
- the thermoelastic deformation is due to the circulating power (inside the cavity) transmitted by the coating (see fig. 3.45).
- the laser beam propagation axis is the z axis (see fig. 3.45).

This problem has been solved analytically in ref. [59].

For the vacuum window, different boundary conditions will be considered. The determination of the stress tensor is made using to a commercial finite element software [60].

Let us now turn to the relation between the index tensor and the effect on the polarisation of a light wave propagating inside the optical medium. Since all tensors appearing in the present calculations are symmetric, eq. 3.4 is more conveniently explained in a vector form and usually in the Cartesian coordinates [61]:

$$\Delta\mathbf{B} = \Pi\Theta\tag{3.6}$$

where Π contains the piezo tensor components. For silica one gets

$$\begin{pmatrix} \Delta B_{xx} \\ \Delta B_{yy} \\ \Delta B_{zz} \\ \Delta B_{yz} \\ \Delta B_{xz} \\ \Delta B_{xy} \end{pmatrix} = \begin{pmatrix} \pi_{11} & \pi_{12} & \pi_{12} & 0 & 0 & 0 \\ \pi_{12} & \pi_{11} & \pi_{12} & 0 & 0 & 0 \\ \pi_{12} & \pi_{12} & \pi_{11} & 0 & 0 & 0 \\ 0 & 0 & 0 & \pi_{11} - \pi_{12} & 0 & 0 \\ 0 & 0 & 0 & 0 & \pi_{11} - \pi_{12} & 0 \\ 0 & 0 & 0 & 0 & 0 & \pi_{11} - \pi_{12} \end{pmatrix} \begin{pmatrix} \Theta_{xx} \\ \Theta_{yy} \\ \Theta_{zz} \\ \Theta_{yz} \\ \Theta_{xz} \\ \Theta_{xy} \end{pmatrix}\tag{3.7}$$

Because silica is an isotropic medium, the piezo matrix in the above equation is invariant under rotations, i.e. a similar relation holds in cylindrical coordinates. More generally, one can define a rotation operator in the six dimensional space. For example, the cylindrical components of a rank two tensor are derived from the Cartesian components by a rotation of an angle ϕ around the z axis:

$$T_{cyl} = R_z(-\phi)T_{cart}R_z(\phi)\tag{3.8}$$

¹¹This assumption is good when the heat propagation is considered since 1) silica is a bad conductor; 2) the laser beam spot size is much smaller than the mirror diameter.

where T is a rank two tensor (T_{cyl} and T_{cart} being the matrix representations in the cylindric base and Cartesian base respectively) and R_z the rotation operator in \mathbb{R}^3 . Writing explicitly the matrix representation of this equation one obtains the following rotation matrix in the six dimensional space¹²:

$$\tilde{R}_z(\phi) = \begin{pmatrix} \cos^2 \phi & \sin^2 \phi & 0 & 0 & 0 & -\sin 2\phi \\ \sin^2 \phi & \cos^2 \phi & 0 & 0 & 0 & \sin 2\phi \\ 0 & 0 & 1 & 0 & 0 & 0 \\ 0 & 0 & 0 & \cos \phi & -\sin \phi & 0 \\ 0 & 0 & 0 & \sin \phi & \cos \phi & 0 \\ \frac{1}{2} \sin 2\phi & -\frac{1}{2} \sin 2\phi & 0 & 0 & 0 & \cos 2\phi \end{pmatrix} \quad (3.9)$$

with the convention $\mathbf{T}_{cyl} = \tilde{R}_z(-\phi)\mathbf{T}_{cart}$, as in the \mathbb{R}^3 space, with

$$\mathbf{T}_{cyl} = \{T_{rr}, T_{\phi\phi}, T_{zz}, T_{z\phi}, T_{rz}, T_{r\phi}\}.$$

From eq. 3.9 and 3.7 one can effectively verify the rotational invariance property of the tensor Π representation in the six dimensional space

$$\Pi = \tilde{R}_z(-\phi)\Pi\tilde{R}_z(\phi) \Rightarrow \left\{ \Delta\mathbf{B}_{cart} = \Pi\Theta_{cart} \Leftrightarrow \Delta\mathbf{B}_{cyl} = \Pi\Theta_{cyl} \right\}.$$

The cylindrical symmetry of our problems implies $\Delta B_{r\phi} = 0$ and $\Delta B_{z\phi} = 0$. Therefore one has

$$B = \begin{pmatrix} B_{rr} & 0 & B_{rz} \\ 0 & B_{\phi\phi} & 0 \\ B_{rz} & 0 & B_{zz} \end{pmatrix} = \begin{pmatrix} 1/n_0^2 + \Delta B_{rr} & 0 & \Delta B_{rz} \\ 0 & 1/n_0^2 + \Delta B_{\phi\phi} & 0 \\ \Delta B_{rz} & 0 & 1/n_0^2 + \Delta B_{zz} \end{pmatrix} \quad (3.10)$$

where n_0 is the unperturbed silica optical index and where the variations of the tensor index are given, to first order by eq. 3.6. From eq. 3.10 one can write the new index ellipsoid equation. For normal incidence, using the cylindrical coordinates, one finds an ellipse equation with principal axes along \mathbf{u}_ϕ and \mathbf{u}_r with lengths $1/\sqrt{B_{\phi\phi}}$ and $1/\sqrt{B_{rr}}$ respectively. For laser beam aligned along the Oz axis, the Jones matrix describing the effect of the deformed silica substrate on an incident wave plane is then given by

$$M = \exp \left(i \frac{2\pi}{\lambda} \int_{-h/2}^{h/2} \tilde{B}^{-1/2} dz \right)$$

with

$$\tilde{B}^{-1/2} = \begin{pmatrix} n_0 - \frac{n_0^3}{2} \Delta B_{rr} & 0 \\ 0 & n_0 - \frac{n_0^3}{2} \Delta B_{\phi\phi} \end{pmatrix}. \quad (3.11)$$

Finally, ignoring a global phase factor, one gets

$$M = \begin{pmatrix} e^{-i\frac{\Phi(r)}{2}} & 0 \\ 0 & e^{i\frac{\Phi(r)}{2}} \end{pmatrix}. \quad (3.12)$$

¹²It is also useful to define the rotation matrix around the y axis and x axis in order to account for oblique incidence.

with

$$\Phi(r) = \frac{2\pi n_0^3}{\lambda} \frac{1}{2} (\pi_{12} - \pi_{11}) (I_{rr}(r) - I_{\phi\phi}(r)) \quad (3.13)$$

and

$$I_{rr}(r) = \int_{-h/2}^{h/2} \Theta_{rr} dz, \quad I_{\phi\phi}(r) = \int_{-h/2}^{h/2} \Theta_{\phi\phi} dz. \quad (3.14)$$

The matrix of eq. 3.12 is in fact given in the eigen-axes of the medium. To determine the effect on a polarised ray entering the medium at a distance r and angle ϕ from the mirror centre, one must apply a rotation of angle ϕ since the slow and fast axis are defined by \mathbf{u}_r and \mathbf{u}_ϕ :

$$M_{lab} = R^T(\phi) M R(\phi) = \begin{pmatrix} \cos^2(\phi) e^{-i\frac{\Phi(r)}{2}} + \sin^2(\phi) e^{i\frac{\Phi(r)}{2}} & -i \sin(2\phi) \sin\left(\frac{\Phi(r)}{2}\right) \\ -i \sin(2\phi) \sin\left(\frac{\Phi(r)}{2}\right) & \sin^2(\phi) e^{-i\frac{\Phi(r)}{2}} + \cos^2(\phi) e^{i\frac{\Phi(r)}{2}} \end{pmatrix}.$$

Or equivalently:

$$M_{lab} = R^T(\phi) M R(\phi) = \cos \frac{\Phi(r)}{2} \begin{pmatrix} 1 & 0 \\ 0 & 1 \end{pmatrix} - i \sin \frac{\Phi(r)}{2} \begin{pmatrix} \cos(2\phi) & \sin(2\phi) \\ \sin(2\phi) & -\cos(2\phi) \end{pmatrix}.$$

From this expression one can first determine the polarisation state modification of a Gaussian beam entering the optical element under normal incidence along the symmetry axis ($r=0$). If the incident beam polarisation is along the Ox reference axis ($\phi = 0$)

$$\mathbf{E}_{in} = \Psi_{0,0}(r) \mathbf{X},$$

where we choose to use as a basis the Laguerre-Gauss polynomials

$$\Psi_{n,l}(r, \phi) = \sqrt{\frac{2n!}{w(1 + \delta_{0l})\pi(l+p)!}} \left(\frac{\sqrt{2}r}{w}\right)^l L_n^l\left(\frac{2r^2}{w^2}\right) e^{-\frac{r^2}{w^2}} e^{il\phi} \Rightarrow \Psi_{0,0}(r) = \sqrt{\frac{2}{\pi w^2}} e^{-r^2/w^2}.$$

Then, the polarisation state after the optical element is given by

$$\mathbf{E}_{out} = \Psi_{0,0}(r) \left[\left(\cos\left(\frac{\Phi(r)}{2}\right) - i \sin\left(\frac{\Phi(r)}{2}\right) \cos(2\phi) \right) \mathbf{X} - i \sin \frac{\Phi(r)}{2} \sin(2\phi) \mathbf{Y} \right]. \quad (3.15)$$

In the same way, if the incoming polarisation is circular left,

$$\mathbf{E}_{in} = \Psi_{0,0}(r) \mathbf{L} \Rightarrow \mathbf{E}_{out} = \Psi_{0,0}(r) \left[\cos\left(\frac{\Phi(r)}{2}\right) \mathbf{L} + \sin\left(\frac{\Phi(r)}{2}\right) \left(\sin(2\phi) - i \cos(2\phi) \right) \mathbf{R} \right]. \quad (3.16)$$

If this beam penetrates inside a Fabry-Perot cavity, then the two orthogonal polarisation states \mathbf{X} (\mathbf{L}) and \mathbf{Y} (\mathbf{R}) will not propagate following the same spatial mode of the cavity: the $\cos(2\phi)$ and $\sin(2\phi)$ terms can only be coupled to the $\Psi_{n,\pm 2}$ modes. If the cavity is locked on the fundamental mode, then only the incident polarisation state (\mathbf{X} or

\mathbf{L} in the above example) will propagate inside the cavity so that no birefringence effects will be induced. The only effect of birefringence is to reduce the power inside the cavity.

When the beam does not enter along the symmetry axis, if this axis is also the Fabry-Perot cavity axis, then the polarisation will be affected. To see it, one can take the axis Oz along the cavity axis and write the incident electric field

$$\mathbf{E}_{in} = \tilde{\Psi}_{0,0}(r, \phi) \mathbf{X} , \quad \tilde{\Psi}_{0,0}(r, \phi) = \sqrt{\frac{2}{\pi w^2}} e^{-(r^2 - r_0^2/w^2 + 2rr_0 \cos(\phi - \phi_0)/w^2)} ,$$

where r_0 and ϕ_0 define the point of entrance of the beam. From this expression one can see that the projection on the Laguerre modes will not be as straightforward as in the previous case. To further see what happens in this case, one can consider a small transverse beam displacement $r_0 \ll w$ and perform a second order expansion

$$\tilde{\Psi}_{0,0}(r, \phi) \approx \Psi_{0,0}(r) \left(1 + 2r_0 \frac{r}{w^2} \cos(\phi - \phi_0) + r_0^2 \frac{-w^2 + 2r^2 \cos^2(\phi - \phi_0)}{w^4} \right)$$

Inserting this expression in eq. 3.16, for example, one obtains:

$$\mathbf{E}_{out} = \Psi_{0,0}(r) \left[\cos\left(\frac{\Phi(r)}{2}\right) \mathbf{L} + i \frac{r_0^2}{4w^2} \sin\left(\frac{\Phi(r)}{2}\right) e^{2i\phi_0} \mathbf{R} \right] + \left(\sum_{n,l/n \text{ and } l \neq 0} c_{n,l} \Psi_{n,l}(r, \phi) \right) \mathbf{R} .$$

where $c_{n,l}$ are the couplings to higher transverse modes.

Hence, the coupling of the \mathbf{R} component to the fundamental mode occurs only at second order in (r_0/w) (thanks to the $\cos^2(\phi - \phi_0)$ term). Furthermore, since the term in $\sin(\Phi(r)/2)$ must also be taken into account, this coupling will be further reduced for small birefringence.

In conclusion, as far as axis-symmetric birefringence effects are concerned, the cavity acts also as a polarisation state filter.

So far we only considered an incident wave propagating along Oz . As indicated above, for an incident angle α with respect to Oz , one must rotate the stress tensor of an angle α around Oy . Because of the cylindrical symmetry, the result is a modification of eq. 3.14 such that Θ_{rr} is replaced by [57]

$$\Theta'_{rr} = \Theta_{rr} \cos^2 \alpha + \Theta_{zz} \sin^2 \alpha - \Theta_{zr} \sin 2\alpha .$$

The slow and fast axis are obtained by rotating \mathbf{u}_r and \mathbf{u}_ϕ : one finds $\cos \phi \mathbf{u}_r - \sin \phi \mathbf{u}_z$ and \mathbf{u}_ϕ .

Finally, since the birefringence effects are small for high quality optical components, it is convenient to perform a first order expansion for further calculations:

$$M_{lab} \approx \begin{pmatrix} 1 & 0 \\ 0 & 1 \end{pmatrix} - i \frac{\Phi(r)}{2} \begin{pmatrix} \cos(2\phi) & \sin(2\phi) \\ \sin(2\phi) & -\cos(2\phi) \end{pmatrix} .$$

3.8.3 Birefringence induced by the heated cavity entrance mirror

Using the relation between the components of the stress tensor and the strain tensor (see [58]) one can write $\Phi(r)$ as a function of the displacement u_r along Or . Eq. 3.13 becomes

$$\Phi(r) = \frac{2\pi}{\lambda} \frac{n_0^3}{2} (\pi_{12} - \pi_{11}) \int_{-h/2}^{h/2} \left(\frac{\partial u_r(r, z)}{\partial r} - \frac{u_r(r, z)}{r} \right) dz .$$

Using eq. (3.15) of ref. [59] for $u_r(r, z)$ one obtains, after some algebra

$$\Phi(r) = \frac{2\pi}{\lambda} \frac{n_0^3}{2} (\pi_{12} - \pi_{11}) \frac{2\mu\nu}{\mu + L} \sum_{m=1}^N J_2\left(\frac{\zeta_m r}{a}\right) \frac{a}{\zeta_m} (B_m - A_m) \operatorname{sh}\left(\frac{\zeta_m h}{2a}\right), \quad (3.17)$$

with A_m and B_m given by eq. (3.11-3.12) of ref. [59]. From the properties of Bessel function one can see that $\Phi(r=0) = 0$ as expected by symmetry considerations.

In eq. 3.17,

- J_2 is the Bessel function of second order and ζ_m are the solutions of $xJ_1(x) - \tau J_0(x) = 0$ (see [62]) with $\tau = 4\sigma' T_{ext}^3 a / K$; $\sigma' = 0.9 \times 5.67 \cdot 10^{-8}$ is the Stefan-Boltzmann constant corrected for emissivity; $T_{ext} = 300\text{K}$ is the external temperature and $K = 1.38\text{W/mK}$ is the thermal conductivity of the silica. Note that the series is rapidly convergent (i.e. $N=50$ is enough even though one can go up to a few hundred numerically).
- $L = 1.56 \cdot 10^{10} \text{Jm}^{-3}$ is the first Lamé coefficient, $\mu = 3.13 \cdot 10^{10} \text{Jm}^{-3}$ is the second Lamé coefficient and $\nu = 5.91 \cdot 10^4 \text{Jm}^{-3}\text{K}^{-1}$ is the stress temperature modulus of the silica.

For a numerical estimate we consider a confocal Fabry-Perot cavity of 2m length, a laser wavelength $\lambda = 1.064\mu\text{m}$ (i.e. a beam spot diameter of $\approx 1.5 \text{ mm}$ on the cavity mirrors), a circulating power of 10 kW and a coating transmission coefficient of $\approx 10^{-6}$. We use $n_0^3(\pi_{12} - \pi_{11})/2 = 3.46 \cdot 10^{-12} \text{ Pa}^{-1}$. Fig. 3.46 shows the phase Φ as a function of the radial distance r . The effect on the laser beam polarisation state is negligible (Φ is below 1 mrad). In fig. 3.46 the elastic deformation of the coating is also shown.

To get a more quantitative estimate one must project eq. 3.16 on the Laguerre-Gauss eigen-modes of the cavity. To first order in the birefringence one has

$$\mathbf{E}_{out} = \sum_{n,l} \left(\delta_{l0} \delta_{n0} \mathbf{L} + c_{n,l} \mathbf{R} \right) \Psi_{n,l}(r, \phi),$$

with

$$c_{n,l} = \int_0^\infty \int_0^{2\pi} \frac{\Phi(r)}{2} \left(\sin(2\phi) - i \cos(2\phi) \right) \Psi_{0,0}(r, \phi) \Psi_{n,l}(r, \phi) r d\phi dr$$

that is

$$c_{n,l} = \frac{2\pi}{\lambda} \frac{n_0^3}{2} (\pi_{12} - \pi_{11}) \frac{2\mu\nu}{\mu + L} \sum_{m=1}^N f_{m,n,l} \frac{a}{\zeta_m} (B_m - A_m) \operatorname{sh}\left(\frac{\zeta_m h}{2a}\right)$$

and

$$f_{m,n,l} = \frac{\delta_{l2}}{2} \sqrt{\frac{2}{\pi w^2}} \int_0^a \int_0^{2\pi} \left(\sin(2\phi) - i \cos(2\phi) \right) J_2\left(\frac{\zeta_m r}{a}\right) e^{-r^2/w^2} \Psi_{n,l}(r, \phi) r dr d\phi.$$

Because the integrand decreased rapidly one can integrate over r up to infinity. Couplings to the first three Laguerre-Gauss modes are thus:

$$f_{m,0,2} = \frac{1}{16} \left(\frac{w\zeta_m}{a} \right)^2 e^{-\frac{\zeta_m^2 w^2}{8a^2}} e^{-i\frac{\pi}{4}} \quad (3.18)$$

$$f_{m,1,2} = \frac{\sqrt{3}}{384} \left(\frac{w\zeta_m}{a} \right)^4 e^{-\frac{\zeta_m^2 w^2}{8a^2}} e^{-i\frac{\pi}{4}} \quad (3.19)$$

$$f_{m,2,2} = \frac{\sqrt{5}}{245760\sqrt{2}} \left(\frac{w\zeta_m}{a} \right)^8 e^{-\frac{\zeta_m^2 w^2}{8a^2}} e^{-i\frac{\pi}{4}}. \quad (3.20)$$

Using the numerical values given above we found

$$c_{0,2} = -1.610^{-4}, \quad c_{1,2} = -4.710^{-5}, \quad c_{2,2} = -1.710^{-5}$$

to a global phase factor. Taking the squares one sees that the power loss is negligible.

3.8.4 Birefringence induced by air pressure on a perfect vacuum window

Stress tensor components have been computed numerically using finite element software. Results are shown in fig. 3.47 for a 2 cm window diameter and 2 mm width. Two curves are shown, one corresponding to a normal incident ray and one corresponding to an incident angle of 0.1 rad (in this latter case only the phase shifts have been considered). In all cases the birefringent effects are found to be negligible.

A semi analytic calculation has confirmed the results obtained using the finite element method [63].

If such effects were to be present, as stated in the SLAC polarimeter measurement reports [25], they would be due to additional stress effects appearing when building the vacuum windows but not due to the 1 bar pressure.

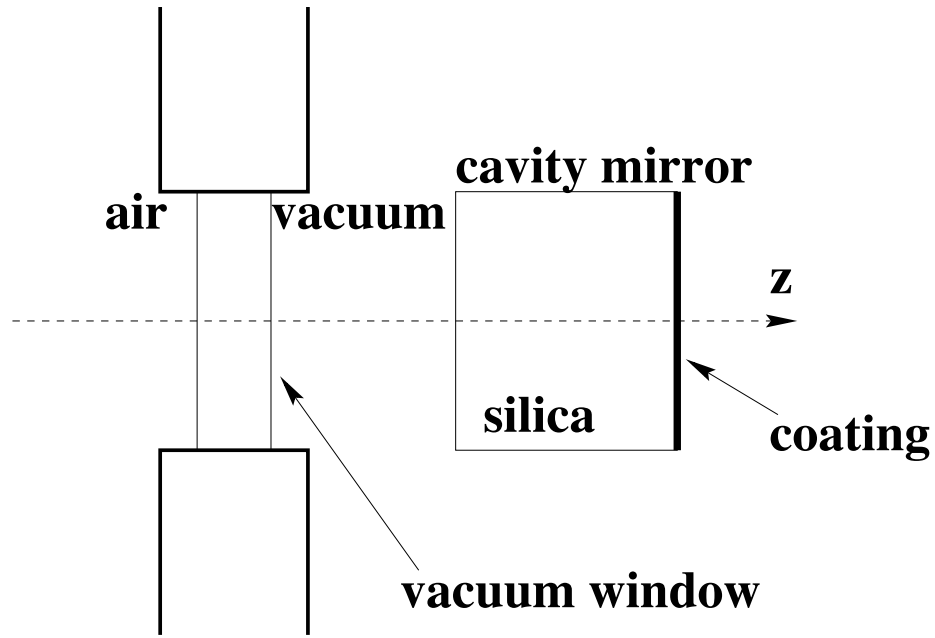


Figure 3.44: Simplified drawing of the Fabry-Perot vacuum window and entrance mirror.

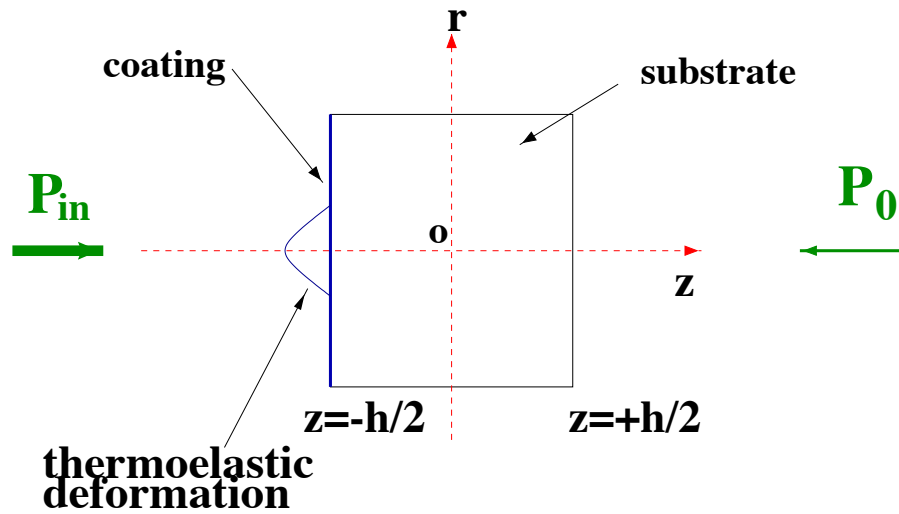


Figure 3.45: Definition of the coordinate system used in the calculations. P_0 is the incoming laser beam power (≈ 1 W) and P_{in} is the power circulating inside the Fabry-Perot cavity.

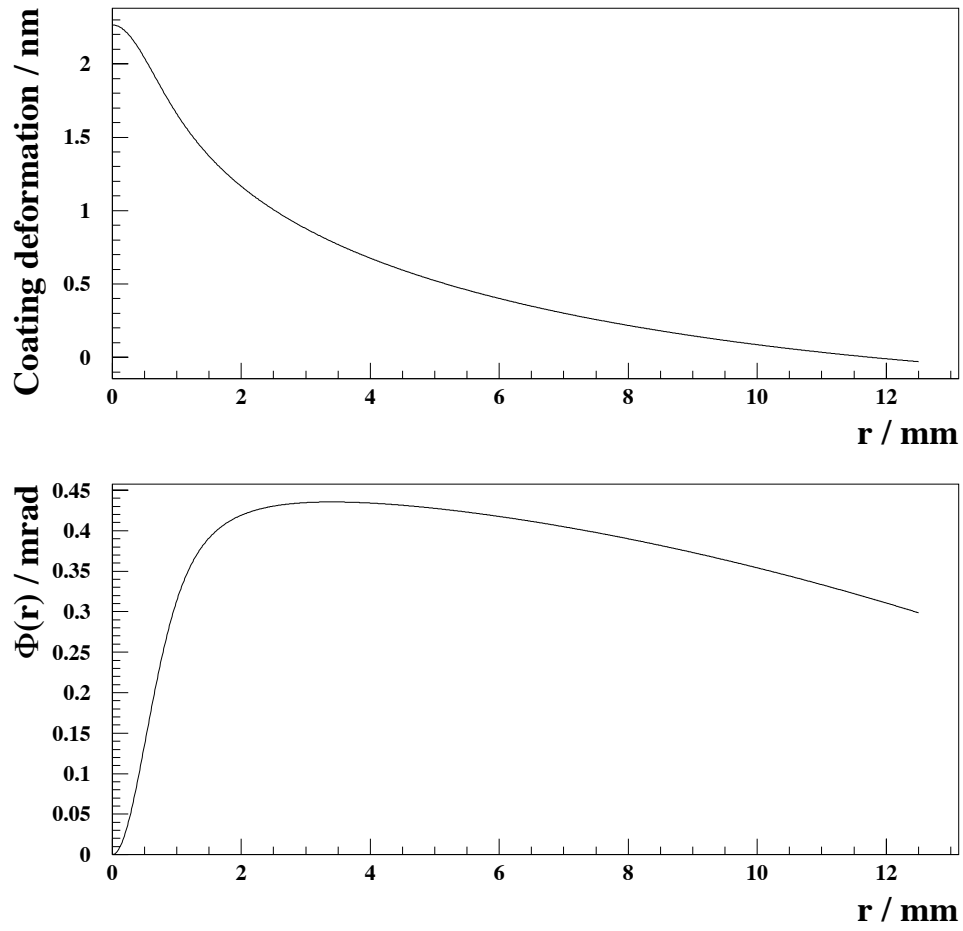


Figure 3.46: Top plot: coating elastic deformation induced by heat effect in the silica substrate. Bottom plot: phase shift induced by the thermoelastic deformation.

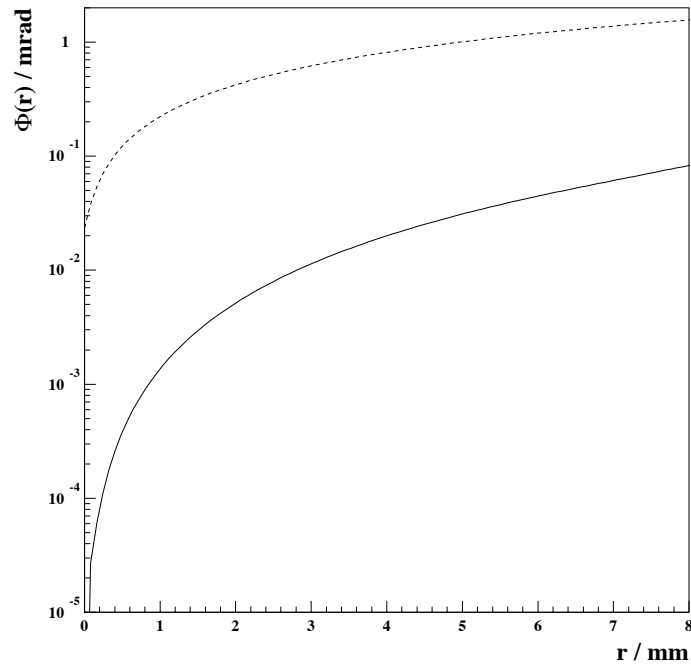


Figure 3.47: Birefringence induced by a vacuum window of 2 cm diameter and 2 mm width. The full curve corresponds to a normal incident angle; the dashed curve corresponds to an incident angle of 0.1 rad.

Bibliography

- [1] F. Cavalier and N. Arnault, private communication.
- [2] H. Kogelnik and T. Li, “Laser beams and resonators”, Proc. of the IEEE 54 (1966) 1312.
- [3] A.E. Siegman, *Lasers* (University Science books, 1986).
- [4] N. Falletto, *Etude, conception et réalisation d’une cavité Fabry-Perot pour le polarimètre Compton de TJNAF*, Université Joseph Fourier-Grenoble 1, 1999. DAPNIA/SPhN-99-03T.
- [5] J.P. Jorda, *Mise au point d’une cavité Fabry-Perot pour la polarimétrie Compton*, PhD. Thesis, Université Paris 6
- [6] P. Rebougeard, “Note de synthèse sur l’optique de la cavité Fabry-Perot du polarimètre Compton”, Internal note 6112N2000002.
P. Rebougeard, “Tolérance mécanique pour la cavité Fabry-Perot du polarimètre Compton”, Internal note 6112N2000003.
- [7] G. Bardin et al., “Conceptual design report of a Compton polarimeter for Cebaf Hall A” (1996). Document available on www.cebaf.gov/Compton.
- [8] N. Falletto et al., “Compton scattering off polarized electrons with a high finesse Fabry-Perot cavity at JLAB”, Nucl. Instrum. Meth. A459 (2001) 412.
- [9] Estimate done by S. Wipf from the DESY accelerator group.
- [10] R. Marie and A. Reboux from the LAL mechanical workshop.
- [11] H. Bahadur, “Low-temperature irradiation in natural crystalline quartz”, J. Appl. Phys. 75 (1994) 1420.
- [12] H. Bahadur, “Infrared characterization of natural and cultured quartz: the effect of electrodiffusion and irradiation”, J. Appl. Phys. 66 (1989) 4973.
- [13] L. Escoubas et al., “Solarization of glass substrates during thin-film deposition”, Appl. Opt. 37 (1998) 1883.
- [14] T.J. Kane and R.L. Bayer, “Monolithic, unidirectional single-mode Nd:YAG ring laser”, Opt. Lett. 10 (1985) 65.

- [15] T.J. Kane, A.C. Nilsson and R.L. Bayer, “Frequency stability and offset locking of a laser-diode-pumped Nd:YAG monolithic nonplanar ring oscillator”, Opt. Lett. 12 (1987) 175.
- [16] R.L. Byer, “Diode Laser-pumped solid-state lasers”, Science, Vol. 239 (1988) 742.
- [17] A.C. Nilsson, E.K. Gustafson and R.L. Bayer, “Eigenpolarisation theory of monolithic nonplanar ring oscillators”, IEEE Jour. Quant. Elec. 25 (1989) 767.
- [18] W. Koechner, *Solide-state laser engineering* (Berlin, Springer-Verlag, 3rd Edt. 1992).
- [19] A. Yariv, *Quantum Electronics*, (J. Wiley and sons, Inc., New-York, 2nd edt. 1998).
- [20] *Handbook Of Optics II* (Mc Graw-Hill, New-York, 2nd edt. 1995).
- [21] See, for example, Huard, *Polarisation*, Masson, Paris (1991).
- [22] V. Soskov from the Lebedev Institute of Moscow.
- [23] Suggestion of A. Delbart from CEA-SACLAY.
- [24] M. Born and E. Wolf, *Principles of Optics* (Pergamon Press, third edt. 1965).
- [25] A. Lath, M. Woods, “Compton laser analysis: determination of polarisization and systematic errors”, SLD Note 236 (1994); M. Woods et al., “Compton laser analysis for the 94/95 SLD run”, SLD Note 246 (1996).
- [26] A. Delbart, “Mini-Compton: spécifications de l’optique, description de l’implantation prévue a TJNAF”, CEA-Saclay note 6-6112R0000025 (1997).
- [27] A. Delbart, “Polarisation du faisceau de photons au CIP: Modélisation des manip en labo, Application à la cavité du polarimètre”, Saclay internal Note 6-6112R2000020 (1999).
- [28] A.A. Studna et al., “Low-retardance fused-quartz window for real-time optical applications in ultrahigh vacuum”, J. Vac. Sci. Technol. A7 (1989) 3291.
- [29] J.E. Logan, N.A. Robertson and J. Hough, “Measurements of birefringence in a suspend sample of fused silica”, Opt. Comm. 107 (1994) 342.
- [30] G.E. Jellison, “Windows in ellipsometry measurements”, Appl. Opt. 38 (1999) 4784.
- [31] Measurement and tutorial/suggestions made by M. Lintz from the Atomic Parity Violation group of the Laboratoire de l’Ecole Normale Supérieure, Paris.
- [32] F. Cleva, “Tests de hublots VERMETAL”, VIRGO internal Note (1996).
- [33] P. Hello, “Optical aspects of interferometric gravitational-wave detectors”, Prog. Opt. 38 (1998) 85.
- [34] S. Carusotto et al., “The ellipticity introduced by interferential mirrors on a linearly polarised light beam orthogonally reflected”, Appl. Phys. B48 (1989) 231.

- [35] P. Micossi et al., “Measurement of the birefringence properties of the reflecting surface of an interferential mirror”, Appl. Phys. B57 (1993) 95.
- [36] D. Jacob et al., “Supermirror phase anisotropy measurement”, Opt. Lett. 20 (1995) 671.
- [37] S. Moriwaki et al., “Measurement of the residual birefringence of interferential mirrors using a Fabry-Perot cavity”, Appl. Phys. B65 (1997) 347.
- [38] J.Y. Lee et al., “Measurement of ultralow supermirror birefringence by use of the polarimetric differential cavity ringdown technic”, Appl. Opt. 39 (2000) 1941.
- [39] A. Reboux, private communication.
- [40] See, for example, J.P. Pérez, *OPTIQUE Fondements et Applications* (Dunod, 6th edt., 2000, Paris) page 455.
- [41] R.V. Pound, Rev. Sci. Instrum 17 (1946) 490.
- [42] R.W Drever et al., Appl. Phys. B31 (1983) 97.
- [43] G. Cantatore et al., ‘Frequency locking of a Nd:YAG laser using itself as the optical phase modulator’, Rev. Sci. Instrum. 66 (1995)2785-2787.
- [44] A.M. De Riva, ‘Very high Q frequency-locked Fabry-Perot cavity’, Rev. Sci. Instrum. 67 (1995)2680-2684.
- [45] J.P. Jorda and N. Falletto, ‘Etude de la modulation laser à haute fréquence: choix de la fréquence de modulation’, CEA internal report 3-6112R2000012.
- [46] See pvss.web.cern.ch/pvss.
- [47] National Instrument products, see www.ni.com.
- [48] Remote Anywhere, see www.remote-anything.com.
- [49] From M. Ait-Mohan, ‘Mise en oeuvre d’un polarimètre pour HERA: système d’acquisition et application de contrôle à l’aide de PVSS’, (2003). Document available on www.lal.recherche/h1/hardware/poll.html.
- [50] See www.ces.ch.
- [51] R. Chiche, LAL electronic group.
- [52] D.Z. Anderson, “Alignment of resonant cavities”, Appl. Opt. 23 (1984) 2944.
- [53] E. Morrison, B.J. Meers, D.I. Robertson and H. Ward, “Automatic alignment of optical interferometers”, Appl. Opt. 33 (1994) 5041.
- [54] Sh.A. Furman and A.V. Tikhonravov, *Optics of multilayer systems* (Frontieres, Gif-sur-Yvette, 1992).
- [55] J.M. Mackowski from SMA/IN2P3-Lyon, private communications.

- [56] W. Winkler et al., “Birefringence-induced losses in interferometers”, Opt. Comm. 112 (1994) 245.
- [57] O. Lubin, *Etude de l'influence des contraintes mécaniques sur des composants optiques de grandes dimensions. Application aux composants du laser Mégajoule*, PhD Thesis, Université Paris 11 Orsay (1998).
- [58] S. Timoshenko and J.N Goodier, *Theory of elasticity*, Mac Graw Hill, New York (1951).
- [59] P. Hello and J.Y. Vinet, “Analytical models of transient thermoelastic deformations of mirrors heated by high cw laser beams”, J. Phys. France 51 (1990)2243.
- [60] Work performed by Julien Bonis from the LAL-Mechanic ingenering group.
- [61] J.F. Nye, *Physical properties of Crystals*, Clarendon Press, Oxford (1985).
- [62] M. Abramovitz and R.C. Stegun, *Hanbook of mathematical functions*, National Bureau of Standards, Appl. Math Ser. 55 (1970).
- [63] Charles Schmit from IPN-Orsay, private communication.

Chapter 4

Ellipsometry and coherent light polarisation

As mentioned in chap. 3, our aim is to provide circular polarisation at the laser beam-electron interaction point and to precisely measure the laser beam polarisation after the cavity. In this chapter, details on the ellipsometer and the circular polariser are given.

Our ellipsometer has been roughly described in chap. 3 (see fig. 3.11). Although this is a simple and classical optical set-up [1, 2], it appeared that much effort, both experimentally and theoretically, had to be spent to reach the per mille accuracy.

The key elements are the quarter wave plate (QWP) and the laser beam intensity readout which are the two main topics of this chapter.

Optical calculations had to be done to model the light polarisation after a QWP. They involve light propagation inside anisotropic parallel plates and Fourier optics. In order not to complicate this chapter, they are reported in appendix A. In the present chapter, only an “ideal” description of the wave propagation in a quartz plate is given.

For the reader not familiar with electromagnetic wave propagation in anisotropic media, I have detailed the solutions of Maxwell equation for the particular case of electro-optic crystals in appendix 4.7.

4.1 Quarter wave plates

4.1.1 Jones matrix for an ideal quartz plate

Commonly used QWPs consist in uniaxial parallel sided quartz plates. A uniaxial medium is first characterised by two optical indices n_o and n_e , named *ordinary* and *extraordinary* respectively ¹. The dielectric tensor is then no longer fully degenerate as for isotropic media, but partially degenerate: the eigenvalue n_o^2 is doubly degenerate and n_e^2 is not degenerate. The eigenvector corresponding to the latter eigenvalue defines the so called *optical axis*. Given n_o and n_e and a plate thickness, the plate is completely characterised by the orientation of the optical axis with respect to the plane of interface. For standard quartz QWP, the optical axis is usually located in the plan of interface. We shall only consider such a QWP.

¹This comes from the behaviour of the refracted rays at an isotropic-uniaxial interface: the phase velocity of the ordinary wave vector is the same as for a dielectric medium of optical index n_o (independent of the optical axis orientation and direction of propagation) but not for the extraordinary ray.

Let us now consider an electromagnetic wave incident on a QWP. We write \mathbf{E}_{in} and \mathbf{E}_{out} the electric vector before and after the QWP respectively. Under normal incidence and for plane waves, the QWP induces a phase shift between the two projections of \mathbf{E}_{in} onto the optical axis and its perpendicular (= neutral axes). From the plane wave expression $\mathbf{E} = \mathbf{E} \exp(i(\omega t - kz))$, one obtains the phase difference:

$$\varphi = (k_e - k_o)e \equiv \frac{2\pi}{\lambda}(n_e - n_o)e \quad (4.1)$$

where k_o and k_e are the ordinary and extraordinary wave vectors respectively, λ is the laser beam wavelength and e is the plate thickness. The Jones matrix (see chap. 2) describing an ideal QWP is then given by (to a global phase factor):

$$M = \begin{pmatrix} 1 & 0 \\ 0 & e^{i\varphi} \end{pmatrix} \quad (4.2)$$

in the neutral axis base. Defining a reference base $\{\hat{\mathbf{x}}, \hat{\mathbf{y}}, \hat{\mathbf{z}}\}$ attached to the optical table with $\hat{\mathbf{z}}$ parallel to the wave vector, one obtains

$$\mathbf{E}_{\text{out}} = R(-\phi)MR(\phi)\mathbf{E}_{\text{in}} \quad (4.3)$$

where ϕ is the angle between the optical axis and $\hat{\mathbf{x}}$ (= the azimuthal angle) and $R(\phi)$ is a 2×2 matrix representing the rotation around $\hat{\mathbf{z}}$ (see appendix 3.8 of chap. 3). It is easy to see that if $\varphi = \pi/2 + 2k\pi$ ($k = 0, 1/2, 1, 3/2, \dots$), taking $\mathbf{E}_{\text{in}}^{\text{T}} = (1, 0)$, then $\mathbf{E}_{\text{out}}^{\text{T}} = (1, -i)/\sqrt{2}$ for $\phi = \pi/4$ and $\mathbf{E}_{\text{out}}^{\text{T}} = (1, i)/\sqrt{2}$ for $\phi = 3\pi/4$. This means that linear polarised light becomes circular right or circular left polarised when $\phi = \pi/4$ and $\phi = 3\pi/4$ respectively. In this case, the quartz plate is called a QWP (when $\varphi = \pi + 2k\pi$ it is called half wave plate). For a QWP, the thickness is then given by

$$e = \lambda \frac{4k + 1}{4(n_e - n_o)}. \quad (4.4)$$

The above description is the one of the elementary textbooks. However, even for an ideal quartz plate, optical properties of crystals are indeed much more complex. A brief description is necessary here in order to estimate the limit of the model that we shall use to describe our quartz plates.

It has been shown by Jones [3] that one can define eight “independent types of crystalline behaviour”. Among the eight types, two describe a global phase shift and a global absorption (by global we mean independent of the incoming light polarisation state). The following six relevant independent types remain:

- Linear birefringence: different phase velocity between the extraordinary and ordinary rays. This effect is in fact described above and leads to the Jones matrix of eq. 4.2. The order of magnitude is $n_e - n_o \approx 10^{-2}$ (see table 4.1).
- Linear dichroism: this is a difference between the absorption coefficients of the extraordinary and ordinary rays. This effect is taken into account by introducing an imaginary part in the expression of the optical indices n_e and n_o . It has been measured in the infrared $\lambda > 2 \mu\text{m}$ region [4] ($|\Im(n_e - n_o)| \approx 3 \cdot 10^{-4}$ for $\lambda = 2.7 \mu\text{m}$) but in the optical domain $\lambda \approx 0.6 \mu\text{m}$ it was found to be beyond the measurement accuracy of the most accurate ellipsometry experiments [5], that is $\lesssim 10^{-5}$.

- Circular birefringence (also called “optical activity”[6] or ‘rotary power’ [7]): when a plane wave propagates along the quartz optical axis, it can be easily shown that the linear birefringence vanishes (see appendix 4.7). However, one experimentally observes a birefringence between the circular left and circular right component of the polarisation vector. This effect is taken into account by introducing the circular optical indices n_R and n_L . For quartz, when the optical axis is roughly perpendicular to the plane wave propagation axis, one has $|n_R - n_L| \lesssim 10^{-4}$ [6].
- Circular dichroism: absorption difference related to the eigen polarisation modes of the circular birefringence. There is no measurement of this effect for quartz.
- Lorentz linear birefringence[8]: historically, a small linear birefringence has been measured in some isotropic crystals. This phenomenon is some orders of magnitude smaller than the linear birefringence introduced above and was not expected for isotropic crystals. This is very difficult to measure, especially in anisotropic crystals where it adds up to the other birefringences (there is no measurement of this effect for quartz for instance). However a measurement with silicon single crystal gives $\Delta n_{Lorentz} \approx 5 \cdot 10^{-6}$ [9].
- Lorentz linear dichroism: absorption difference related to the eigen polarisation modes of the Lorentz linear birefringence. There is no measurement of this effect for quartz.

A physical origin of the linear, circular and Lorentz birefringences has been proposed in a recent series of articles [10]. It is well known[11] that linear birefringence is due to the electric dipole response of the crystal cells to an electromagnetic field. Solving the Maxwell equations by taking into account the electric and magnetic multipole response of the medium, the authors of ref.[10] have shown that the optical activity (= circular birefringence) is due to the electric-quadrupole and magnetic-dipole response and that Lorentz birefringence comes from the electric-octopole and magnetic-quadrupole response.

Since we aim at a per mille accuracy, from the order of magnitudes given above, we obviously neglect the Lorentz birefringence. We included the circular birefringence and circular dichroism in our numerical programme described in appendix A, both according to ref. [10, 12] and to the somehow empirical classical way [6]. We find approximately the same results in both cases: for our quartz plate, the optical activity contributes to our intensity measurements at the level of $\lesssim 10^{-4}$ for an incident laser beam polarised linearly. Surprisingly, when the incident laser beam is polarised circularly, as it will be the case at HERA, the effects induced by the optical activity increase by a factor 10 – 100 (this is in agreement with a measurement reported in ref. [13]). We shall therefore neglect these effects for the calibration procedure described in this chapter (the incident laser beam is polarised linearly) but we shall take the contribution of the optical activity to determine the level of circular polarisation in the future HERA optical setup.

In conclusion we only take into account the linear birefringence. In doing so, accuracy of the model for a $\approx 100 \mu\text{m}$ thickness quartz plate is of the order of 10^{-4} .

In practice, if high precision is foreseen, an account for realistic quartz plates and laser beam is needed. This means that one must take into account the following effects:

- multiple reflections inside the plate.

- Internal faults: this topic is treated in the next section.
- The plate surface state: roughness and contamination. In section 4.1.5 we shall justify that these effects are indeed negligible with regard to our measurement accuracy. A model for the effect of surface roughness is described in section A.3 of appendix A.
- Parallelism fault between the plate interfaces. Using first order perturbation theory, it can be easily verified that for isotropic-isotropic interfaces [14] a small inclination of the interface with respect to the light direction is equivalent to a first order Taylor expansion of the Fresnel coefficients. With a parallelism fault of the order of $10\mu\text{rad}$, the changes of the Fresnel coefficients [11] are negligible but this fault induces another effect: when the QWP rotates around an axis normal to its interface, if the laser beam does not enter exactly at the centre of rotation, then the plate thickness varies during the rotation. This effect is the dominant source of systematics of our measurements.
- Gaussian nature and thus the angular distribution of laser beams (see appendix A);

An account for multiple reflection of a Gaussian beam inside the plate leads to lengthy calculations and formula. They are described in appendix A and further used for our experimental analyses described in section 4.3.4.

4.1.2 Optical properties of quartz

We use plates of natural quartz. Among the huge variety of natural quartz, the ‘optical grade’ are the most transparent crystals. Since crystal colouration is due to a large amount of internal contamination [15] (for ex. the presence of chromium leads to a red colour), transparent quartz is then the most pure form of crystalline SiO_2 . The main effect of the small remaining contamination is only important if the crystal is irradiated (see section 3.2.3). In this section, we briefly review the optical properties of quartz in order to justify that we can effectively control the behaviour of optical quartz plates at the per mille level.

$\lambda(\mu\text{m})$	Ref. [16] $\in [1.0417, 1.0973]$	Ref. [17] $\in [1.01406, 1.08304]$	Ref. [18] $\in [1.05, 1.1]$	Ref. [7] 1.064
$T(^{\circ}\text{C})$	18	18	22	18
n_o	$\in [1.53366, 1.53442]$	$\in [1.533900, 1.534857]$		1.53434
n_e	$\in [1.54238, 1.54317]$			1.54308
$\Delta n \times 10^3$	$\in [8.72, 8.75]$		$\in [8.718, 8.746]$	8.74

Table 4.1: *The measurements of ref. [16] were reported in 1896 and those of ref. [17] in 1911. They are still the best values and they appear (in a limited wavelength range) in the main handbooks [19, 20]. Our plate manufacturer uses $\Delta n = 0.00874$ to determine the plate thickness. The value of ref. [7] is the ‘most probable value’.*

Most of the optical properties of quartz can be found in the very complete book of Sosman [7] (all experimental data are reported and described). We didn’t find a published

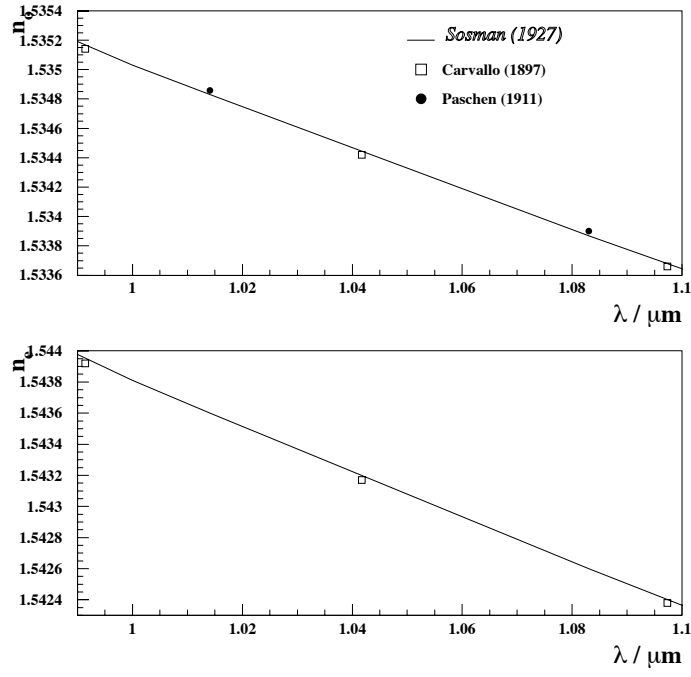


Figure 4.1: quartz optical indices as a function of the wavelength: empty squares are the data from ref. [16] and stars are taken from ref. [17]. The full lines show the ‘most probable’ values of ref. [7].

absolute measurement of the quartz optical indices for $\lambda = 1064$ nm. In table 4.1 we indicate the most precise (up to five digits) experimental values from refs. [16, 17] and the ‘most probable’ value for $\lambda = 1064$ nm [7] (we interpolated between the numbers given in [7]). In fig. 4.1 we show these measurements in the vicinity of $\lambda = 1\mu\text{m}$. From this figure it appears that n_o and n_e are known up to the fifth digit for $\lambda = 1064$ nm.

In ref. [7], a review is made of the variations of the optical indices measured with various samples of transparent quartz or even different parts of the same sample. As a conclusion, the following statement, related to quartz optical indices measurements is given: ‘...difference between two extreme specimens of clear optically acceptable quartz may possibly reach 200×10^{-6} , but if it exceeds this value either the apparatus or the method is subject to suspicion’.

In some sense, this limit also takes into account variations of the internal contamination of transparent quartz. In any case, in ref. [7] measurements of the indices of coloured quartz are also reported: the maximum observed variation is of the order of $5 \cdot 10^{-4}$. Since coloured quartz is an extreme case of contaminated quartz, we conclude that the effect induced by the bulk contamination on the optical properties of transparent quartz is negligible.

From the numbers given above, we conclude that n_o and n_e are known up to the fourth digit for $\lambda = 1064$ nm. Since we aim to control our polarisation measurements at the per mille level, this precision is enough. However, an in situ determination of these parameters would provide, as suggested by Sosman, an estimate of the robustness and effective precision of our measurements.

The variation of the optical indices with temperature has been measured much more recently for $\lambda \approx 1064$ nm [21]: $dn_o/dT = (-7.7 \pm 0.3) \cdot 10^{-6}\text{K}^{-1}$ and $dn_e/dT = (-9.3 \pm 0.3) \cdot 10^{-6}\text{K}^{-1}$ (we have extracted these values from the published curves of ref. [21])².

For the sake of completeness, we also take into account the quartz thermal dilatation: $1/e(de/dT) = 12.38 \cdot 10^{-6}\text{K}^{-1}$ in the direction perpendicular to the optical axis[23].

4.1.3 Characteristics of our quartz plates

According to the plate manufacturer [24], available QWP have the following characteristics:

- an optical axis inclination smaller than 3 mrad with respect to the plane of interface;
- A parallelism between the two plate interfaces better than $10 \mu\text{rad}$;
- A $\lambda/10$ surface quality for $\lambda \approx 500$ nm.
- A thickness at least greater than $\approx 60 \mu\text{m}$.

It is instructive to compute the quartz QWP thickness for $k = 0$, one finds $e_0 \approx 30 \mu\text{m}$. Therefore, the thickest QWP plates, offered by our manufacturer, are half order ($k = 1/2$, $e_{1/2} \approx 90 \mu\text{m}$) and first order ($k = 1$, $e_1 \approx 150 \mu\text{m}$) plates. Such plates are called *few order* plates and they are known to be very sensitive to temperature variations because of their thickness. In order to reduce the thermal sensitivity, a so called *zero order* QWP is

²The values of ref.[21] that are used in the present work are in good agreement with some unpublished values of the National Institute of Standards and Technology shown in ref. [22].

usually used [25]. It consist in two quartz plates in optical contact. With respect to the first plate, the second one has its optical axis rotated by $\pi/2$ and a thickness difference of e_0 (total thickness being ~ 1 mm). The net phase shift is thus given by eq. 4.4 with $k = 0$ so that the quartz thermal effects are minimised. We shall study both types of plate: a first order one and a zero order one.

4.1.4 Choice of the quartz quarter wave plate

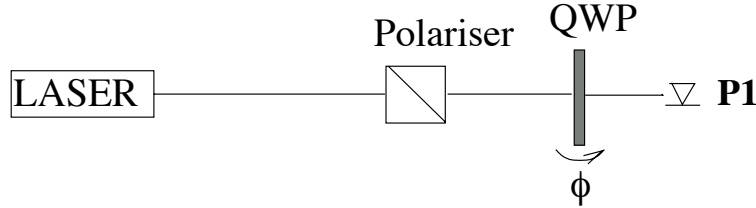


Figure 4.2: *Simple optical scheme set-up to qualify a QWP.*

To test the performance of a quartz plate, the simple setup described in fig. 4.2 has been used. A quartz plate is rotated in its plane under normal incidence and the intensity is measured for each azimuthal angle. This setup is indeed simpler than the one described in the next section but anyhow enough for the present application. For an ideal QWP, the measured intensity is independent of the azimuthal angle (see eq. 4.3) and any modulation of the intensity is to be attributed to the effect of internal multi-reflections (the plate is cleaned-up and sufficiently well aligned). Hence, the modulation amplitude is related to the anti-reflection coating quality.

In principle, when a zero order anti-reflection coated plate is used, both temperature and internal multi-reflection effects are avoided. Such a component was thus ordered and tested. The intensity modulation that we have observed is shown in fig. 4.3. On this figure, a modulation of period π and amplitude of $\approx 1\%$ is visible. This is characteristic of the interferences induced by the internal multi-reflections (=bad quality of the AR coating...). Another modulation, localised in a restricted azimuthal angle range, of amplitude $\approx 7\%$ is visible. This effect is attributed to faults in the two quartz plate assembly.

Since we aim at a per mille accuracy ellipsometer, we didn't further investigate the causes of these effects but rather oriented our choice towards a first order anti-reflection coated QWP (thickness $\approx 150 \mu\text{m}$). Results for the amplitude modulation as a function of the azimuthal angle are shown in fig. 4.4. A residual modulation of 2.5% is visible. Let us mention that this effect was seen for all orientations of the quartz plate and for various modifications of the laser beam shape and laser/plate rotation axis alignment (a minimum of 2% has been reached during this investigation). To understand this effect, we computed the reflection coefficient of the AR coating QWP. Under normal incidence and for an optical axis located inside the plane of interface, calculations are simple³. Using the manufacturer's information for the thickness and for the optical indices of the two

³The plane wave treatment is equivalent to the Gaussian beam treatment in the scalar Fourier approximation defined in appendix A) and dynamic interface matrices are diagonal (see again appendix A).

layers constituting the AR coating, we show the reflection coefficient as a function of the layer thicknesses in fig. 4.5. One can see that a thickness fault of $\sim 10\text{nm}$ can increase the reflection coefficient by a factor ten. This figure also tells us that to model an AR-coated quartz plate at the per mille level, not only the quartz characteristics must be taken into account but also the AR layer thicknesses.

Finally, the decision was taken to use an uncoated few order QWP. In doing so, we had to develop a model, including internal multiple reflections, to describe the transmission of a Gaussian beam by a quartz plate. This is the topic of appendix A.

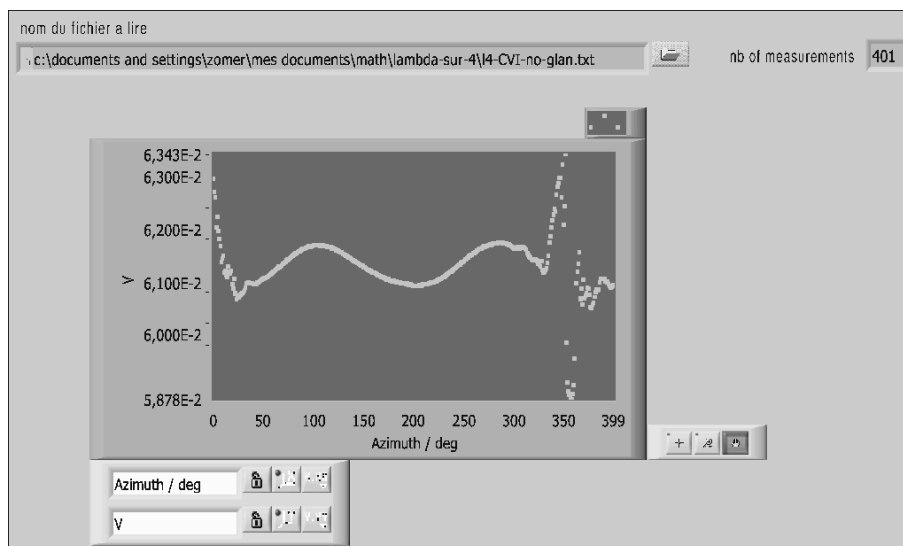


Figure 4.3: *Intensity modulation as a function of the azimuthal angle (see text) for a zero order QWP. This is a online plot obtained with our LabView slow-control frame-work.*

4.1.5 Plate surface state and cleaning

To model the propagation of a Gaussian beam in the quartz plate, we assume that surfaces are perfectly flat. This assumption is justified in this section.

Two different characteristics of the quartz plate surface must be considered: roughness and contamination [26].

To clean the quartz surface we operate under a class 10 air flow and proceed as follows: we start by blowing it with a dry air flow to remove the main dust contamination; next the plate is put inside an ultrasonic bath containing pure alcohol; finally the plate is exposed to a deuterium lamp [27] emitting in the UVC spectral range 180nm-250nm for few hours. Before the final step, surface contamination usually consists in organic compounds which are tightly bound to the surface via Van der Waals forces [28, 29]. During the later stage of the cleaning procedure, the organic compounds are broken into volatile elements like H_2O and CO_2 [30].

To estimate the effect of the surface contamination, we compared a series of optical measurements made with the clean plate under a class 10 air flow and the same measure-

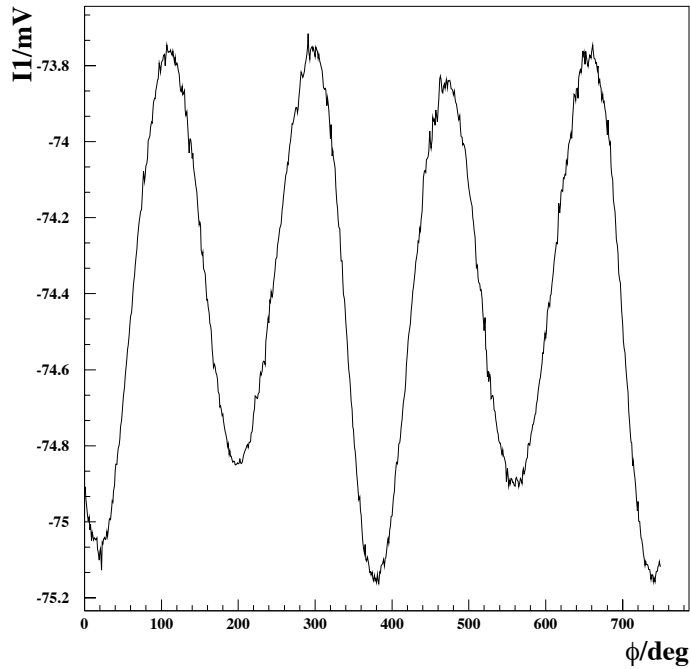


Figure 4.4: As in fig. 4.3 but for an AR coated first order QWP.

ments a few days after the air flow was removed. We find no noticeable effects and this can be understood according to the following argument. Almost all the literature concerning the contribution of surface state are related to ellipsometers working in reflection (around 45° incidence usually). Those instruments are obviously very sensitive to the surface state since the detected light does not propagate deep inside the medium but only ‘sees’ a region close to the surface (for ex., experiments about humidity effects [31] and identification of the surface contamination [32] have been carried out). This is obviously not our case since we measure the light intensity in transmission. The contribution of the surface state is thus much reduced provided the surface is reasonably clean.

Another external parameter which modifies the crystal properties is the air pressure. An estimate reported in ref. [7] shows that a pressure increase of 10 mm of Mercury induces a change on the optical indices by $-6 \cdot 10^{-6}$. Thus we can safely neglect the air pressure variations (see also our estimates in appendix 3.8 of chap. 3).

The surface roughness plays, a priori, an important role in High Accuracy Universal Polarimeters (HAUP[33]) where the light transmitted by the sample under study is analysed. Already in ref. [7] a section was devoted to ‘supposed surface effects’ in the determination of the quartz indices. Measurements of the optical indices (from the end of the 19th century) performed on the same quartz samples but before and after re-polishing are reported there and the effect of surface roughness is estimated to be of the order of $3 \cdot 10^{-4}$. I thus suspected roughness to be a dangerous systematic for our measurements but it turned out that it was not the case. As shown in section A.3 of appendix A, the bias introduced by roughness is at most of the order of σ/λ (i.e roughness dispersion over

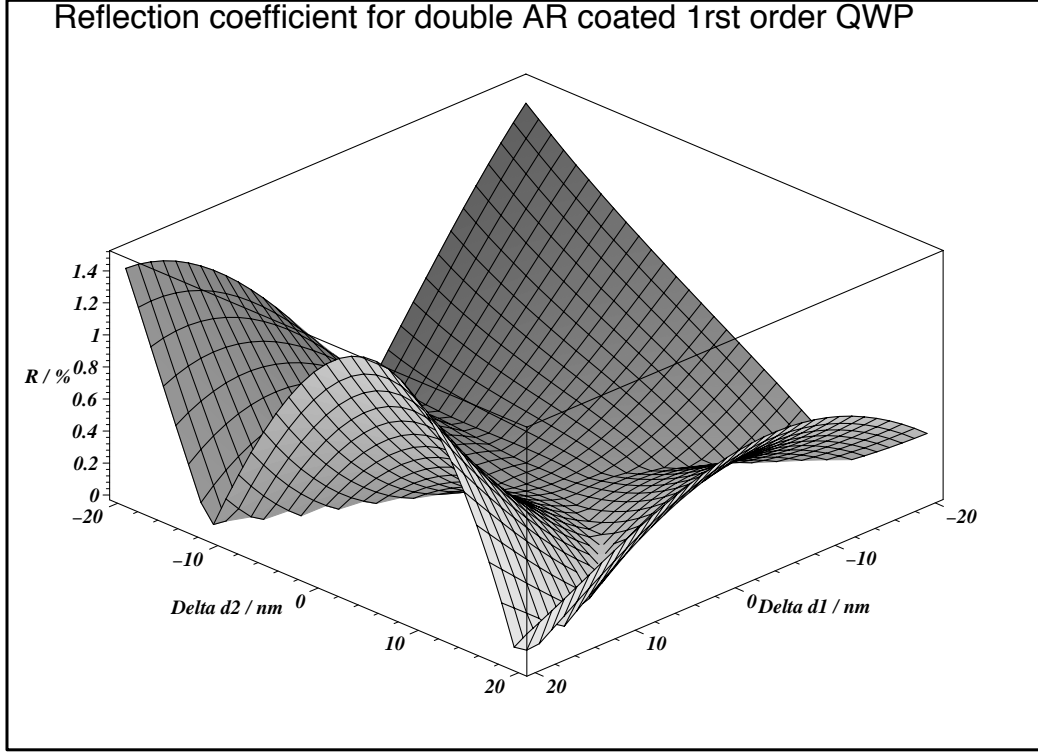


Figure 4.5: Numerical calculation of the reflection coefficient at normal incidence for a first order AR coated QWP of thickness $152.17 \mu\text{m}$ as a function of the two AR layers thicknesses. We used the optical indices and thicknesses of the double dielectric layer AR coating corresponding to $\lambda = 1064 \text{ nm}$ (these numbers were provided confidentially by the plate manufacturer). We use $n_o = 1.53419$ and $n_e = 1.54294$ for the ordinary and extraordinary quartz optical indices.

wavelength), that is, using the number given below, of the order of 10^{-4} .

The roughness of one of our quartz plates was measured with an Atomic Force Microscope [28] (AFM) ⁴. Fig. 4.6 and 4.7 represent 2D views of the same plate prior to cleaning (just received from the manufacturer) and after a microsonic bath in pure alcohol respectively. One sees that surface contamination appears like ‘stalagmites’ which are higher when the plate is not clean. The stalagmite density is of the order of a few peaks per μm^2 with a maximum height of ≈ 35 nm and ≈ 12 nm for the ‘dirty’ and clean surfaces respectively.

The height distributions corresponding to Fig. 4.6 and 4.7 are shown together in fig. 4.8. A sum of two Gaussians has been fitted to these two distributions, the first one describing the quartz roughness and the second one (restricted to positive heights) the contamination. A decrease of the surface contamination due to the pure alcohol ultrasonic bath is obvious and the roughness, defined by the one standard deviation of the pure surface height distribution is the same for both distribution: $\sigma = 3.3\text{\AA}$. This is a high quality plate roughness.

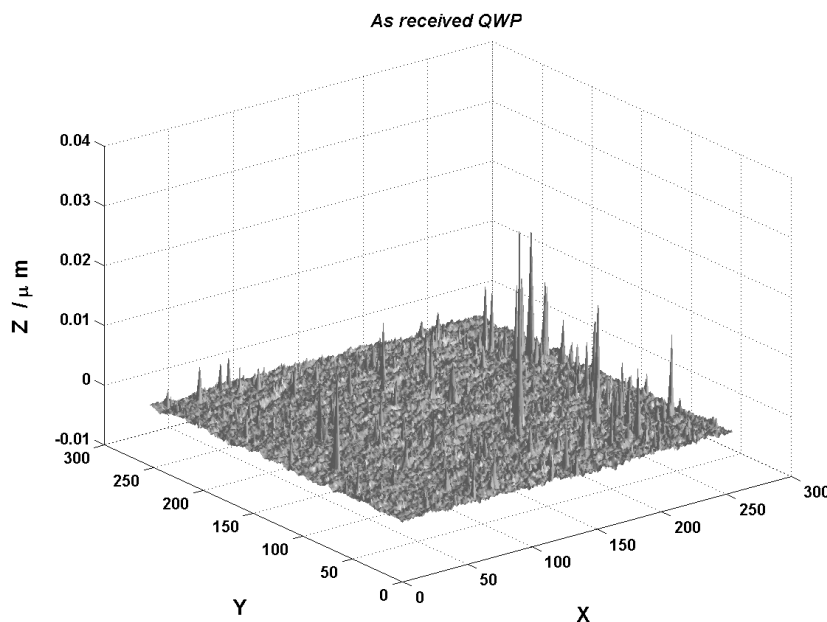


Figure 4.6: *Height measurement performed with an AFM. The total exploration length and the steps size (same x and y) are $30\mu\text{m}$ and $30/256\mu\text{m}$ respectively. The plate was as received from the manufacturer (the dust was blown away by a dry air flow).*

4.2 Principle of the ellipsometer

The ellipsometer used in our setup is shown in figs. 3.11 and 3.19 of chap. 3. The principle of the method used to determine the polarisation of the incident beam is simple: the QWP is rotated around its normal (i.e. the optical axis turns around the laser beam

⁴I thank A. Checco for having performed this measurement.

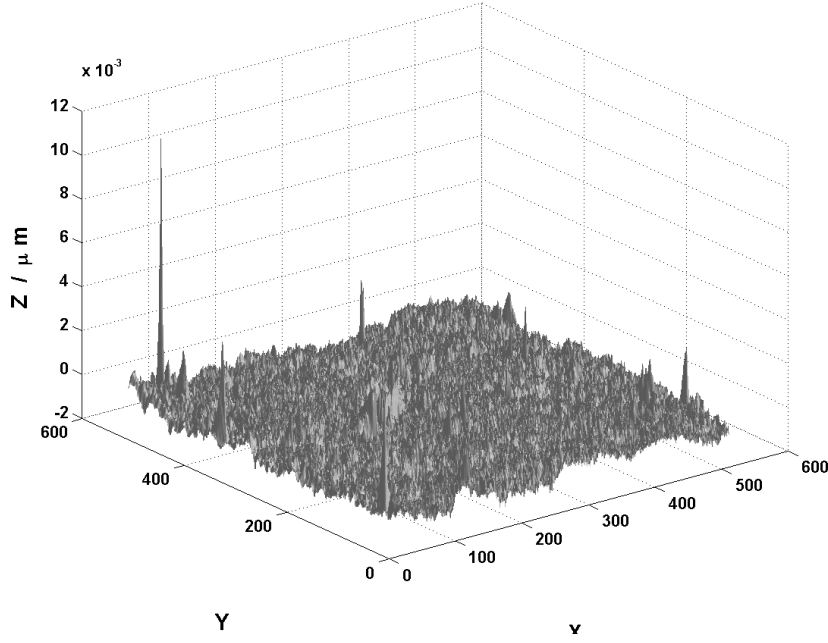


Figure 4.7: *Height measurement performed with an AFM. The total exploration length is $10\mu\text{m}$ in the x and y directions and the step size is $\approx 20\text{ nm}$. The plate was cleaned in a pure alcohol ultrasonic bath.*

axis) and the light intensity is measured after a linear polariser (a Wollaston prism) as a function of the rotation angle ϕ . A χ^2 fit to these measurements leads to the incident light polarisation.

To describe the determination of the light polarisation from this fit, we shall give here a textbook (or ideal) approach, i.e. we consider a perfectly anti-reflection coated QWP and a perfect Wollaston prism. In practice we use a complete model for our QWP and Wollaston prism (see next section). This textbook approach is very simple and we shall use it to estimate the precision required for our calibration procedure and for the intensity measurements.

The incident light polarisation can be described by the Stockes vector $(1, S_1, S_2, S_3)$ (see eq. 2.2 in chap. 2 for a definition) where the number 1 is the arbitrary light intensity. Using the textbook Mueller matrices we obtain the following expression [40]

$$I(\phi) = \frac{N}{2} \left(1 + S_1 [\cos^2 2(\phi + \phi_0) + \cos \varphi \sin^2 2(\phi + \phi_0)] \right. \\ \left. + S_2 \sin^2 \frac{\varphi}{2} \sin 4(\phi + \phi_0) - S_3 \sin \varphi \sin 2(\phi + \phi_0) \right), \quad (4.5)$$

for the light intensity of one of the two beams after the Wollaston prism (with our ideal optical components, the sum of the two intensities gives 1). In this expression, ϕ is the orientation of the optical axis of the QWP with respect to an arbitrary origin ϕ_0 , $\varphi = (2\pi/\lambda)e(n_e - n_o)$ is the phase shift and N is a global normalisation factor accounting for the laser beam power and the photodiode readout gains.

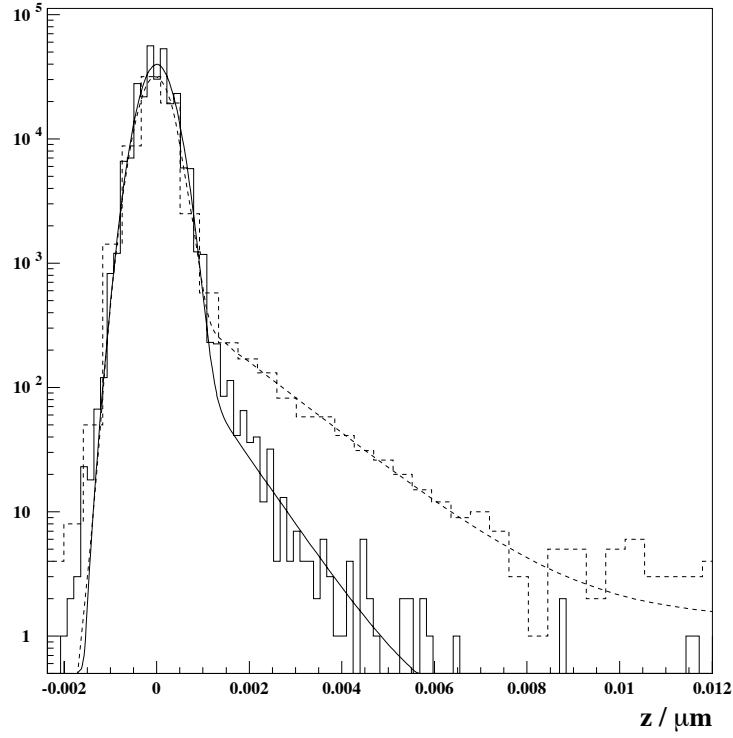


Figure 4.8: *Height distributions corresponding to fig. 4.7 (full curve and histogram) and 4.6 (dashed curve and histogram). The curves show the result of an empirical two Gaussian fit. The full histogram contains twice more entries than the dashed one.*

We next rewrite eq. (4.5) in the following form:

$$I(\phi) = a_0 + a_1 \cos 4\phi + a_2 \sin \phi + a_3 \sin 2\phi + a_4 \cos 2\phi \quad (4.6)$$

with

$$a_0 = N(1 + S_1 \cos^2 \frac{\varphi}{2}) \quad (4.7)$$

$$a_1 = N \sin^2 \frac{\varphi}{2} (+S_1 \cos 4\phi_0 + S_2 \sin 4\phi_0) \quad (4.8)$$

$$a_2 = N \sin^2 \frac{\varphi}{2} (-S_1 \sin 4\phi_0 + S_2 \cos 4\phi_0) \quad (4.9)$$

$$a_3 = N \sin \varphi \cos 2\phi_0 S_3 \quad (4.10)$$

$$a_4 = N \sin \varphi \sin 2\phi_0 S_3 \quad (4.11)$$

where we see that four independent harmonics appears with respect to eq. 4.5 so that ϕ_0 can also be determined together with S_1 , S_2 and S_3 .

Using eq. 4.6 for the fit function, with a_0, \dots, a_4 as four unknown parameters, a straightforward least square fit can be performed. The physical parameters can next be obtained by inverting the system defined by eq. (4.7-4.11):

$$S_1 = \frac{-2r_2 r_3 r_4 + r_1(r_3^2 - r_4^2)}{\sin^2 \frac{\varphi}{2}(r_3^2 + r_4^2) + \cos^2 \frac{\varphi}{2}(2r_2 r_3 r_4 - r_1(r_3^2 - r_4^2))} \quad (4.12)$$

$$S_2 = \frac{2r_1 r_3 r_4 + r_2(r_3^2 - r_4^2)}{\sin^2 \frac{\varphi}{2}(r_3^2 + r_4^2) + \cos^2 \frac{\varphi}{2}(2r_2 r_3 r_4 - r_1(r_3^2 - r_4^2))} \quad (4.13)$$

$$S_3 = \frac{(r_3^2 + r_4^2)^{3/2}}{\sin \varphi \left[r_3^2 + r_4^2 + \cot^2 \frac{\varphi}{2} (2r_2 r_3 r_4 - r_1(r_3^2 - r_4^2)) \right]} \quad (4.14)$$

$$\phi_0 = \frac{1}{4} \text{atan} \left(\frac{2r_3 r_4}{r_3^2 - r_4^2} \right) \quad (4.15)$$

with $r_i = a_i/a_0$.

From these expressions we can now estimate how precisely φ must be determined (i.e. the QWP plate thickness) and the required accuracy of the light intensity measurement (i.e. r_i). In our polarimeter setup, the incident light is circularly polarised so that $S_3 \approx \pm 1$ and $S_1, S_2 \approx 0$. This means that $r_1, r_2 \approx 0$ so that eq. (4.14) reads

$$S_3 \approx \sqrt{r_3^2 + r_4^2} / \sin \varphi$$

with $\sqrt{r_3^2 + r_4^2} \approx 1$ and $\varphi \approx \pi/2 + k\pi$. The plate thickness, and therefore φ , is determined by a calibration procedure (see section 4.3). A systematic error Δe on the calibration of the plate thickness leads to the following bias on S_3 :

$$\Delta S_3 \approx \frac{1}{2} \left(\frac{2\pi}{\lambda} (n_e - n_o) \Delta e \right)^2 \approx 10^{-3} \times (\Delta e)^2$$

with Δe in microns. Our QWP is about $90\mu\text{m}$ thick, therefore a determination of $(\Delta e)/e$ at the percent level (i.e. $\Delta e \approx 1\mu\text{m}$) leads to a determination of S_3 at the per mille level.

As mentioned above, a more sophisticated model for the QWP will be used in our analysis but, if we safely require a few per mille level on the plate thickness calibration we shall get a per mille level ellipsometer.

Taking $\phi_0 = 0$, one sees that $S_3 \approx r_4$ according the previous approximations. r_4 is determined from a fit and if enough data points enter this fit, this determination can be very accurate. However, if the intensity measurement is not stable enough during the time of measurements, inducing in a systematic drift of r_4 with time (and thus with ϕ), then a systematic shift is induced on S_3 . To measure S_3 at the per mille level, one must then also control the long term photodiode readout at the per mille level.

Let me mention again that the simple formulae given in this section will not be used in practice. They have been introduced here for the sake of simplicity.

4.3 Calibration of the quartz plate

During the studies described in the previous section, it appeared that we could simply calibrate a QWP by rotating and tilting it around a linearly, say vertically, polarised laser beam. A fit to the laser beam intensity measured after the QWP leads to an absolute calibration, i.e. the determination of the optical indices n_o and n_e and the plate thickness e . Theoretical expressions entering this fit are given in appendix A. The differences between this calibration procedure and the measurements described in section 4.1.4 are:

- to avoid a degeneracy in the determination of n_o , n_e and e , we must indeed measure separately the horizontal and vertical polarisation intensities after the QWP. We must also consider two identical quartz plates of different thicknesses.
- A high level of stability is required for the laser beam intensity measurements (the per mille level).

Since the tabulated quartz optical indices have high accuracy, one may wonder why we are including the determination of n_o and n_e in our calibration procedure. The answer is suggested by the comment of Sosman mentioned in section 4.1.2: if our fit disfavors the tabulated value it means that our procedure is not accurate. We shall therefore simply estimate the robustness of the precision of our calibration procedure with regard to the optical indices determination. In practice, because of our limited range for the incident angles, we did not have enough constraints to determine both n_o and n_e . We therefore fixed n_e and left n_o as a free parameter.

Let us mention that we realized *a posteriori* that our experimental calibration procedure is in fact a combination of the High Accuracy Universal Polariser of ref. [33] (rotating plate between a rotating polariser and an analyser) and the high accuracy plate thickness measurement of ref. [34] (tilting plate with its optical axis perpendicular or parallel to the plane of incidence).

4.3.1 Experimental set-up

The optical bench used at Orsay to estimate the robustness and precision of our QWP calibration procedure is different from the one used at DESY. The ellipsometer part is however the same and only the laser beam injection part differs.

The Orsay experimental set-up is shown in fig. 4.9. It consists of:

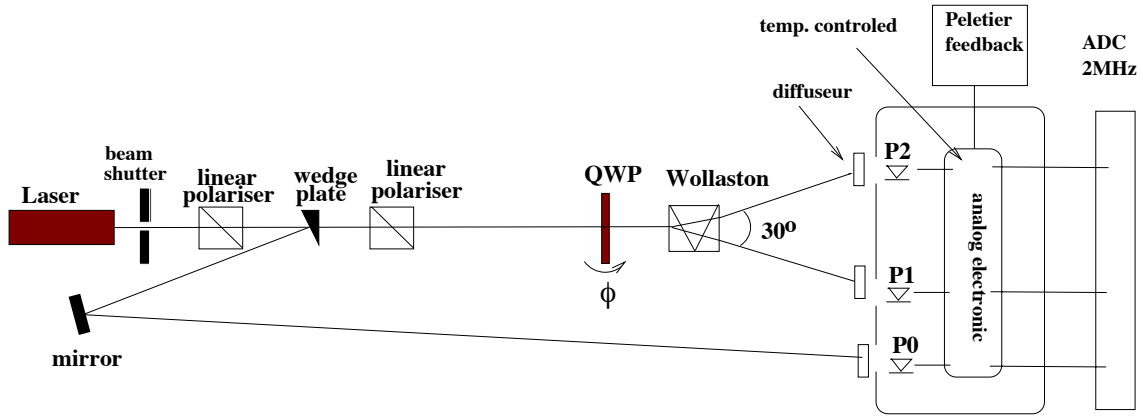


Figure 4.9: Schematic view of the optical scheme used to calibrate a QWP (see text).

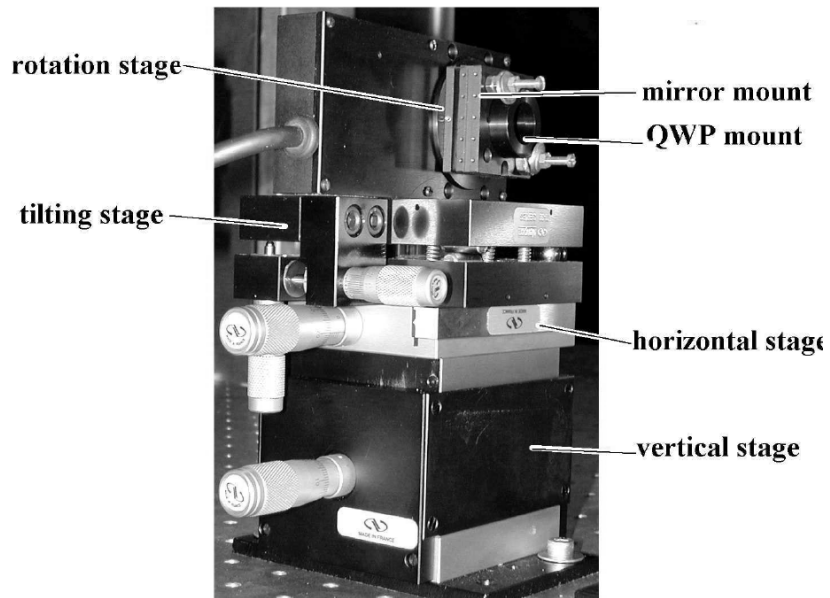


Figure 4.10: Picture of the QWP mount. Comments are on the picture.

Initial Power	100 mW
Noise amplitude (bandwidth 10 Hz to 50 MHz)	0.2% rms
Coherence length	>300 m
Polarisation	100:1, linear
Linewidth	<10 kHz
Beam pointing stability	<0.02 mrad
Frequency drift	≈ 100 MHz/hour
Waist size	0.45 mm
Beam divergence, full angle	3.6 mrad

Table 4.2: *Main characteristics of the CrystaLaser IRCL-100-1064S laser. Informations are provided by the manufacturer.*

- A high quality ND:YAG ($\lambda = 1064$ nm) laser (see table 4.2). The laser beam power stability is controlled by an InGaAs photodiode (denoted by P0) located in front of a 3° wedge plate (the second interface of the wedge is AR coated). The intensity recorded with P0 will be denoted by I_0 .
- A beam shutter remotely operated. It is used to determine the photodiode pedestals before each intensity measurement.
- A high quality Glan-Thomson prism (extinction around 10^{-5}) to provide a linear polarisation.
- A second Glan-Thomson prism to compensate for the polarisation modification induced by the wedge (anyway negligible).
- A quarter wave plate (QWP) is mounted on a light mirror mount (two screws allow to adjust the parallelism between the QWP and the rotating stage) fixed at the centre of a rotating stage. The rotating stage is mounted on two linear stages (vertical and horizontal) and on a two angle tilting stage. Linear and tilting stages are controlled manually with micro-metric screws. The azimuthal rotation is remotely operated. A picture of the QWP mounting is shown in fig. 4.10.
- A high quality Wollaston prism (extinction around 10^{-5}), preliminarily aligned along the axis defined by the first Glan-Thomson prism. The two beams emerging from this prism are linearly polarised along Ox and Oy . These axes define our absolute reference frame.
- Two InGaAs photodiodes P1 and P2 are used to record intensities (denoted by I_1 and I_2) transmitted by the Wollaston prism.

The photodiode electronics readout is standard (see ref. [35] for example). To avoid photodiode saturation, diffusers are located in front of the photodiodes [36]. These devices are not sensitive to incident power (unlike neutral filters) and they naturally reduce

the effect of beam position variation on the photodiode (typical photodiode homogeneity response is 2%, therefore one must reduce beam movements as much as possible...). Following ref. [36], special care has been taken for the photodiode and diffuser housing⁵.

As also shown in figure 4.9, the temperature of the photodiode electronics is controlled by a Peletier module and a related analogue feedback loop. The temperature stability is of the order of a few 0.01 K for external variations of the order of 0.2 K. The necessity for this stabilisation is explained in the next section.

All optical components are aligned using standard techniques. A particular method has been used to align the axis of rotation of the rotating stage with the laser beam axis. Since the interfaces of the quartz plate are not perfectly parallel, the signals $I1$ and $I2$ are modulated when these two axis are different. It can be shown (using the model described in appendix A) that, with the optical axis in the plane of interface, $I1$ and $I2$ have the same shape in the two azimuthal regions $[0, \pi]$ and $[\pi, 2\pi]$. Assuming that the interfaces are plane, the parallelism fault destroys this symmetry (see appendix 4.6) and restoring it provides an alignment method. A typical online measurement corresponding to four azimuthal turns of a misaligned plate is shown in fig. 4.11: to align the QWP, we must move it until the maxima equidistant by 180° have the same height. The residual misalignment depends on the stability of the photodiode readout. It is further determined by the fit.

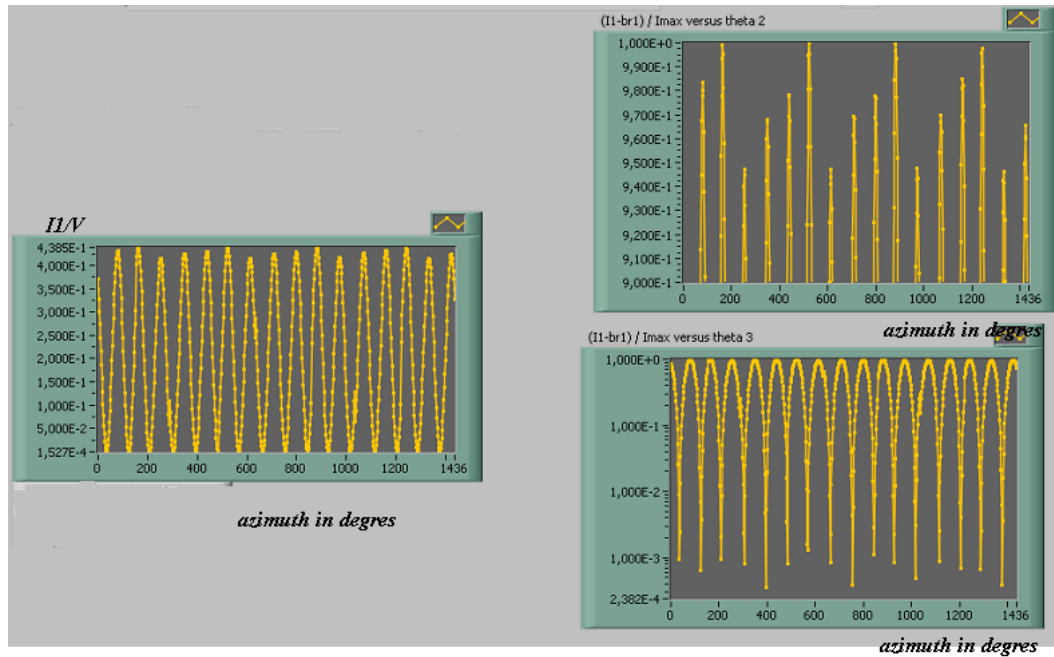


Figure 4.11: Online measurement of $I1$ as a function of the azimuthal angle. The left plot is the full scale measurement; the top right plot shows the upper part and the right bottom the lower part (in log scale).

⁵InGaAs are mainly used for fibre optics and then for $\lambda \approx 1.55 \mu\text{m}$. Our photodiode entrance windows are thus anti-reflection coated for this wavelength and not for $\lambda \approx 1.064 \mu\text{m}$.

4.3.2 Stability and precision of the photodiode readout

We need to provide both short term (a few Hertz) and long term (a day) stabilities for our laser beam intensity measurements. The main reasons are: first it takes typically a few hours to calibrate the quartz plate and during this procedure around 180 intensity measurements are performed; second, during HERA operations, we will need to stabilise our laser beam polarisation measurements during, at least, one electron fill ($\simeq 10$ h).

In fig. 4.12 we first show the pedestals of the three photodiodes (located in the dark to reduce the ambient light noise). The measurement dispersion is at the level of a few ADC bit (14 bit 2 MHz ADC and $[-1, 25, 1.25]$ V range), that is ≈ 0.1 mV. The pedestals are themselves of the order of a few millivolts. These non-vanishing values come mainly from the equilibrium of the differential amplifier which is used to send the signals to the ADCs. From this figure one also sees that we loose one ADC bit since our pedestal is close to zero. It is part of our improvement list to lower the pedestal by one volt in order not to loose this bit.

The stability of the pedestals as a function of time is shown in fig. 4.13. These typical measurements were performed over 12 h and the temperature variation was about ± 0.5 K. Using the ± 1.25 V ADC range, we conclude that pedestal variations are below the per mille level.

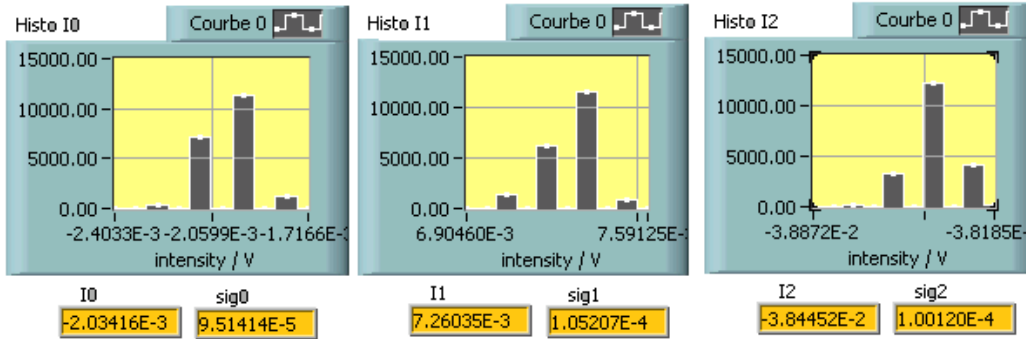


Figure 4.12: Typical online histograms of the photodiode P0 (I_0), P1 (I_1) and P2 (I_2) pedestals. The average and the root mean square (in Volt) are also indicated below each plot.

As we already mentioned, to compensate for laser beam power and cavity feedback variations, our analysis uses the ratios of the intensities after the Wollaston prism (photodiode P1 and P2) to the reference signal (photodiode P0). These ratios are measured at the ADC frequency (2 MHz) and then averaged over 20 K events. At this time scale the system is quasi stable and we checked that the distributions of the two ratios are almost Gaussian⁶. The short term stability of our measurements is thus very good.

⁶At this point it may be the moment to apologize for the bad quality of some of the online figures

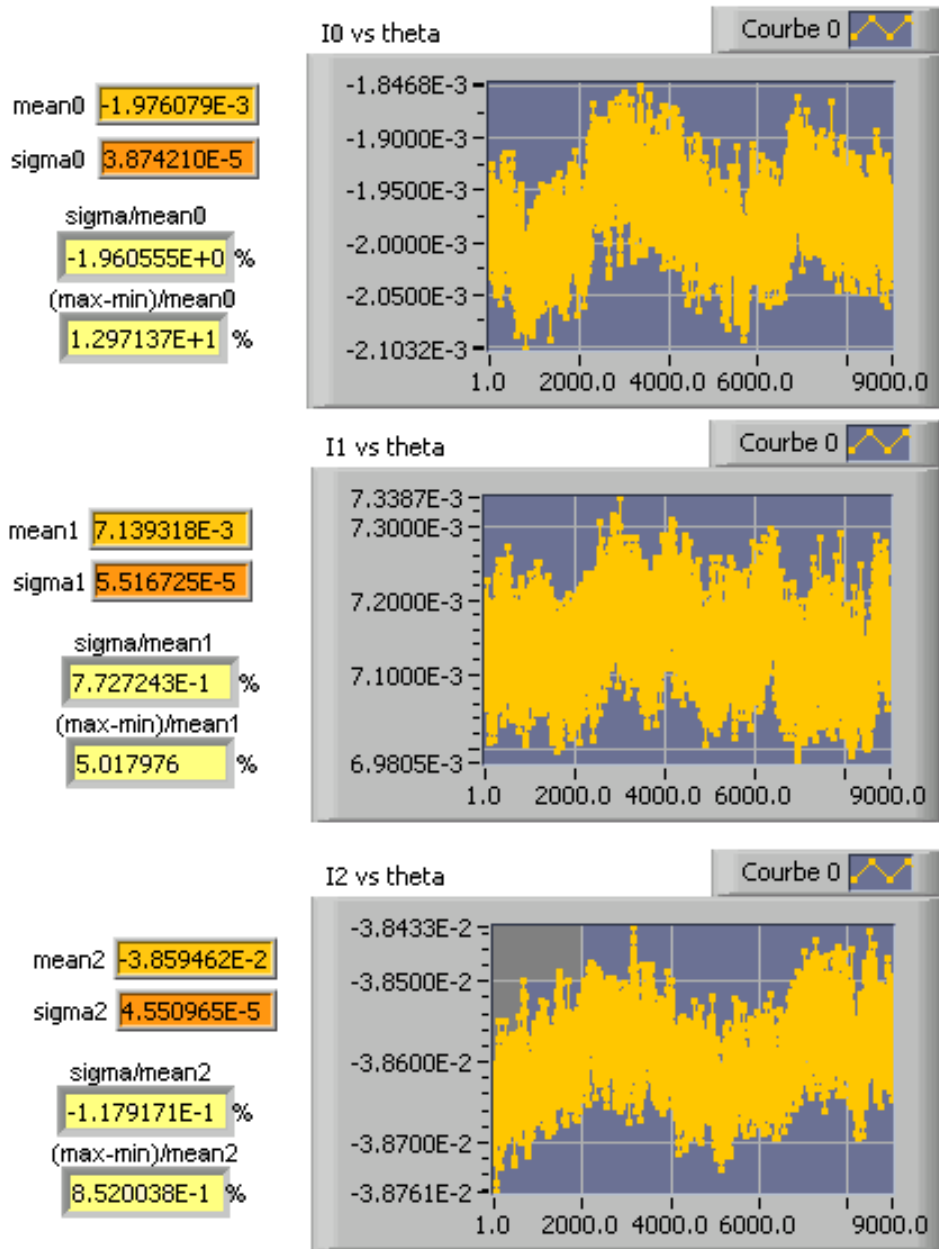


Figure 4.13: Typical variations of the pedestals (= averages of the histograms shown in fig. 4.12) as a function of time (arbitrary units, the measurement was performed over 12 h). Also indicated on the left side of the plots are the averages and the root mean squares (in Volt and relative).

This is not the case for the long term stability. To illustrate the influence of temperature, fig. 4.14 shows the two ratios $I1/I0$ and $I2/I0$ measured during ≈ 2 h when we increased the room temperature by ≈ 2 K. One can see that it leads to ratio variations of the order of 6%. Aiming for the per mille level of stability, we then operate a temperature control of the photodiode readout electronics. We effectively checked that the main effect comes from the electronics and not from the photodiodes themselves (quantum efficiencies of the Hamamatsu InGaAs photodiodes are almost not sensitive to temperature variations for our laser beam wavelength, see also ref. [37] where variations below the per mille level are reported for visible light and Si photodiodes⁷).

To achieve long term stability (still at the per mille level), we then supply a temperature control on the photodiode readout electronics using a Peletier module and related feedback electronics⁸. Fig. 4.15 shows the long term stability (≈ 12 h) of the intensity measurements and of the ratios. Temperature variations inside and outside the photodiode box are also shown. From these plots one sees that the level of stability is good enough for our applications. A 3 h zoom of this figure is shown in fig. 4.16. Small fluctuations at the level of a few 10^{-4} still remain in the ratio $I1/I0$ ($I2$ is particularly small for these plots). They are correlated with the outside temperature changes and are very probably due to photodiode efficiency variations with temperature [37] (also induced by the laser beam itself).

However, fig. 4.15 is one of our best results concerning the stability of the photodiode readout. This is because the room temperature was very stable (0.2 K variation within 12 h) for this particular measurement. At the time of writing this document we did not succeed to stabilise thermally the photodiode electronic box at a sufficient level for larger room temperature variations. A new system is under investigation and should be ready for the winter 2003 HERA shutdown.

4.3.3 Fit procedure

We perform a χ^2 fit to the ratios $I1/I0$ and $I2/I0$ for various azimuth orientations of the QWP optical axis and also for various angles of incidence. To determine the precision on our QWP calibration procedure, we shall combine the measurements done with two quartz plates from the same manufacturer but of different thicknesses:

- an order 1/2 QWP of thickness $\approx 91 \mu\text{m}$;
- an order 5 QWP of thickness $\approx 512 \mu\text{m}$.

Each plate is tilted and then turned azimuthally by steps of 1° . From a simulation study, it appeared that four angles of incidence ($2.45^\circ, 3.67^\circ, 4.59^\circ$ and 7.34°) for the thinnest

and for the absence of a figure describing the Gaussian like ratios. All the work presented here has been finalised in a very short time and during the start of the cavity installation at HERA. In the rush some information was lost.

⁷Concerning temperature effects, InGaAs and Si Hamamatsu photodiodes have approximately the same characteristics if near infrared light is considered in the first case and visible light in the second case.

⁸Instead of stabilising the temperature, we could have corrected the intensity measurements as a function of the temperature. Our temperature sensors are not stable enough (on the long term) for such a purpose and only Platinum sensors could have been used. It is worth mentioning that the readout of Pt sensors is very delicate [38] so that the temperature control appeared to be the simplest solution.

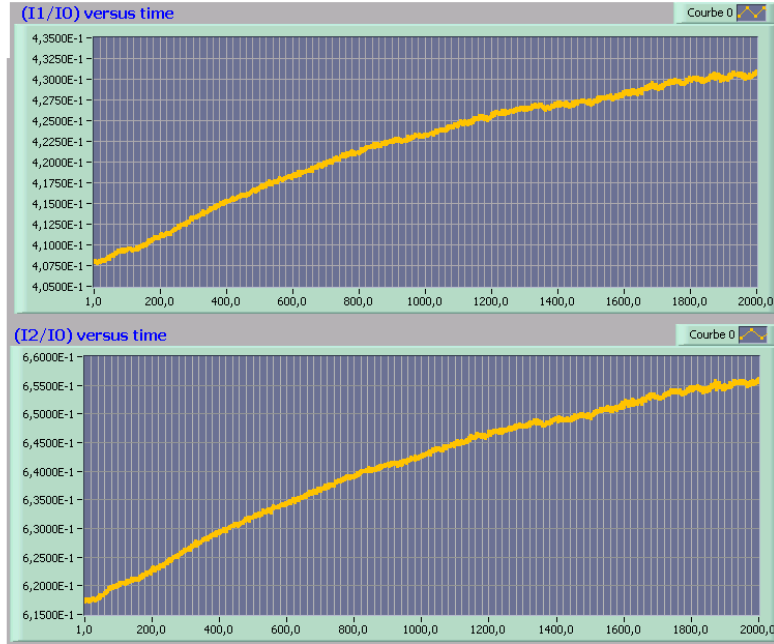


Figure 4.14: Variation of the ratios $I1/I0$ and $I2/I0$ (=averages of the histograms shown in fig. 4.12) as a function of time (arbitrary units, the measurement was performed during 2 h). The increasing slope is due to a 2 K air temperature variation.

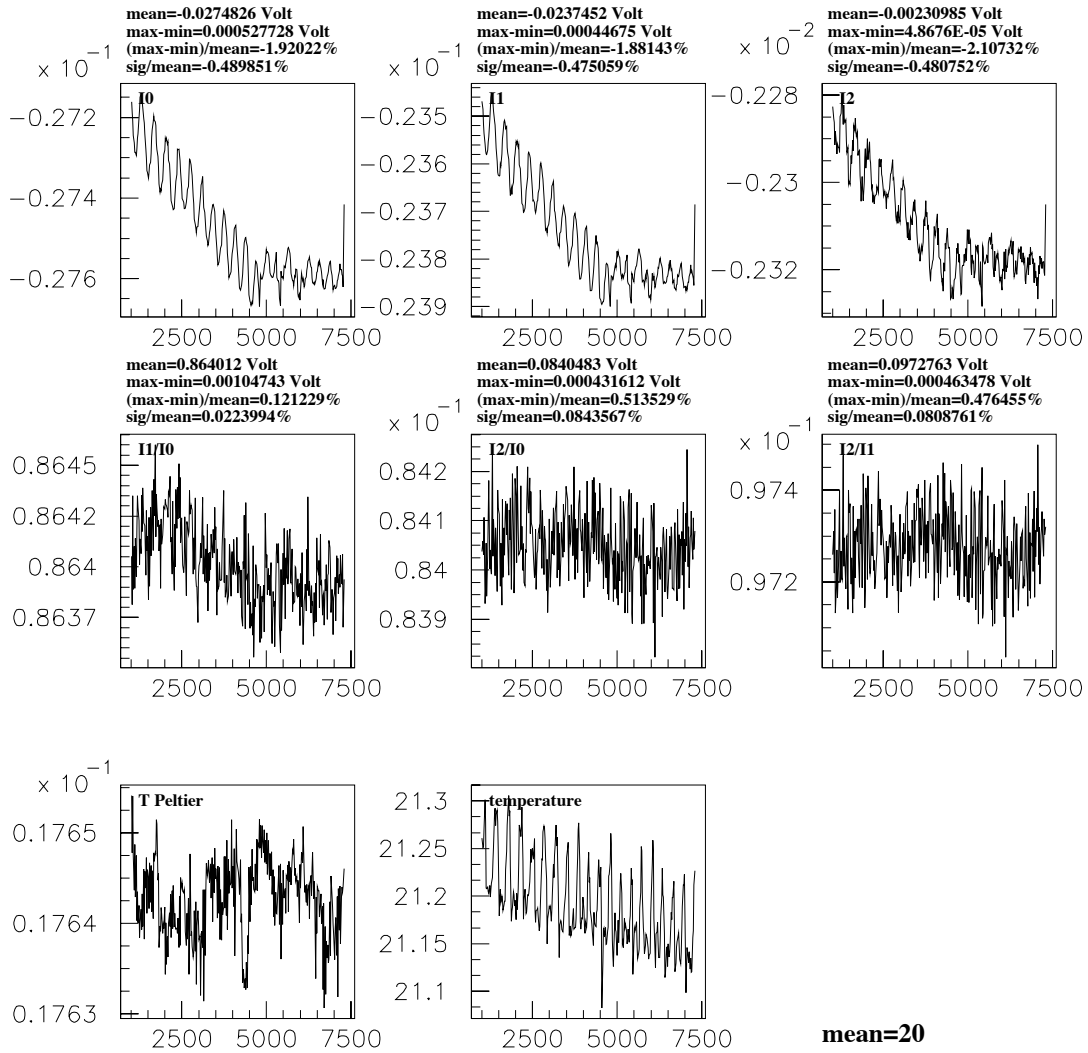


Figure 4.15: Variation of the intensities I_0 , I_1 , I_2 (in Volts, upper plots), ratios (middle plots) and temperature inside (in degree Celsius times 10^{-4} , bottom left) and outside (in degree Celsius, bottom right) the photodiode box as a function of time (in arbitrary units). The total duration for these measurements is 12 h. Absolute variations ('max-min'), and relative root mean squares ('sigma/mean') are also indicated for each plots. From [39].

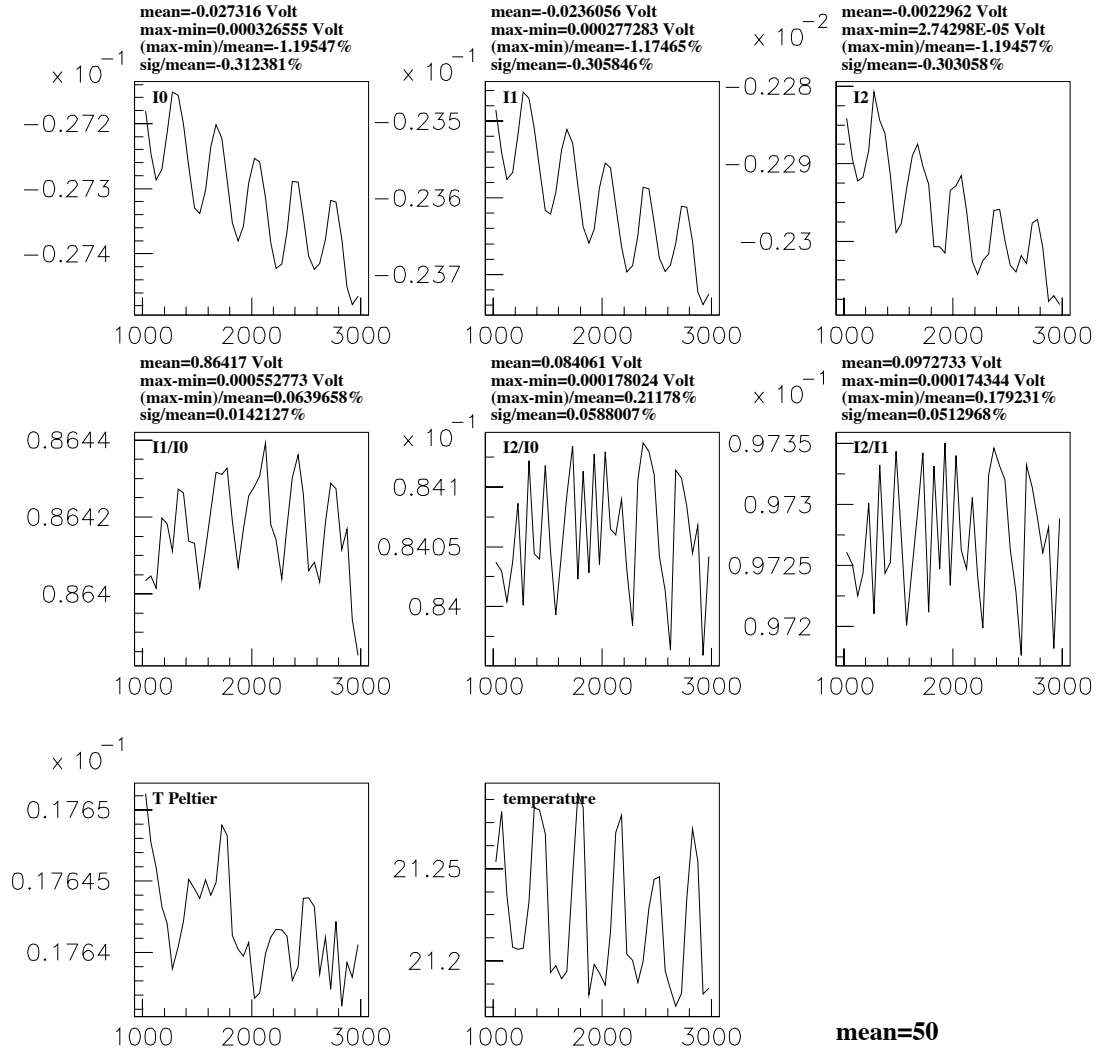


Figure 4.16: 3 h zoom of fig. 4.15. From [39]

plate and two for the other (2.45° and 3.67°) were required. For each angular position, the photodiode pedestals are first determined and next the signals are sampled simultaneously $4 \cdot 10^6$ times (for one angular position, the measurement takes around one minute). The χ^2 weights are defined by the statistical uncertainties on the $4 \cdot 10^6$ samplings. A 360° turn takes approximately six hours so that, according to our last comment in the previous section, our measurement accuracy is dominated by the long term variation of the signal readout.

The fit parameters are: the two plate thicknesses, one of the two quartz optical indices, the misalignment angles (see appendix 4.6), the overall normalisations (one parameter per data sample), the two ellipticities of the Wollaston prism (see below), two parameters to describe the incident light polarisation (see also below) and the angular step of the tilting stage used to vary the angle of incidence (only a rough value is provided by the manufacturer).

To compute the χ^2 , we have to model the light path through all optical elements: the Glan-Thomson prism, the QWP and the Wollaston prism for each of these angular configurations.

An elliptic polarisation state [40] is considered before the QWP. In doing so, we assume the most general state of a polarised light (neglecting depolarisation effects as justified below). Thus, the electric vector before the QWP reads:

$$\mathbf{E}_i = \begin{pmatrix} \cos \chi \\ \sin \chi \exp(i\varphi) \end{pmatrix},$$

where the parameters χ and φ can be related [40] to β and ϵ introduced in eq. 4.16. For good polarisers, one has $\chi \ll 1$ and φ is also expected to be small although it depends on the localisation of the crystal faults in the calcite Glan-Thomson prism and on the orientation of the optical axis (the polariser lengths are around 25 mm).

The general Jones matrix for an imperfect polariser, turned by an angle β with respect to the reference frame is given by [1]:

$$M_W = \frac{1}{2} \begin{pmatrix} (1 + \mathbb{P} \cos 2\beta \cos 2\epsilon) & \mathbb{P}(\sin 2\beta \cos 2\epsilon - i \sin 2\epsilon) \\ \mathbb{P}(\sin 2\beta \cos 2\epsilon + i \sin 2\epsilon) & (1 - \mathbb{P} \cos 2\beta \cos 2\epsilon) \end{pmatrix} \quad (4.16)$$

where \mathbb{P} is the degree of polarisation and ϵ is called the ellipticity. When $\mathbb{P} < 1$, the light is partially depolarised by the polariser. The main contribution to the beam depolarisation comes from scattering inside the polariser and on its interfaces [41] so that depolarisation is usually taken into account only for diffraction like polarisers (wire-grid polariser for ex. [19, 42] which are used for infrared light). Since calcite prisms are used in our setup we can safely assume $\mathbb{P} = 1$ in eq. 4.16.

Assuming an incident linear polarisation, it is easy to see that the extinction (the fraction of transmitted intensity when the polariser is orientated perpendicularly to the direction of the incident polarisation) is simply given by ϵ^2 . The two Glan-Thomson prisms used in our setup have an extinction of $1/2 \cdot 10^5$ and $1/5 \cdot 10^5$ and the Wollaston prism has the worse performance $1/10^5$. This leads to $\epsilon \approx 10^{-3}$.

After the Wollaston prism, the two electric vectors read

$$\mathbf{E}_X = \begin{pmatrix} 0 & -i\epsilon_x \\ i\epsilon_x & 1 \end{pmatrix} M_{QWP} \mathbf{E}_i, \mathbf{E}_Y = \begin{pmatrix} 1 & -i\epsilon_y \\ i\epsilon_y & 0 \end{pmatrix} M_{QWP} \mathbf{E}_i,$$

where X and Y refer to the two emerging beams and where we assumed that the ellipticities of the Wollaston prism are small, $\epsilon_x, \epsilon_y \ll 1$, but different for these two beams (because the optical paths inside the Wollaston prism are different). In this expression, M_{QWP} is the Jones matrix of the QWP (see appendix A) including the misalignment effects described in appendix 4.6. As for the model of laser beam propagation in the QWP, we checked that with our wavelength, plate thicknesses and angle of incidences, the plane wave approximation is precise enough to be used in the χ^2 .

For $\chi \ll 1$, the intensities recorded after the Wollaston prism read

$$I_x = |\mathbf{E}_X|^2 = |M_{21} + \chi M_{22} \exp i\varphi + i\epsilon_x M_{11}|^2 + |\epsilon_x M_{21}|^2 \quad (4.17)$$

$$I_y = |\mathbf{E}_Y|^2 = |M_{11} + \chi M_{12} \exp i\varphi - i\epsilon_y M_{21}|^2 + |\epsilon_y M_{11}|^2, \quad (4.18)$$

where M_{ij} are the elements of the complex matrix M_{QWP} . From these expressions one sees that ellipticity faults can contribute to the first order. The size of this contribution depends strongly on the orientation of the optical axis of the quartz plate (i.e on the components M_{ij}).

4.3.4 Results

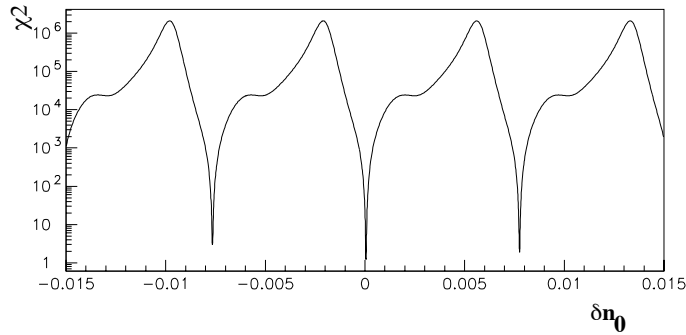


Figure 4.17: Variation of the χ^2 as a function of one of the fit parameters δn_0 (all the other parameters are fixed). From [43].

To get an idea of the difficulty to find the minimum χ^2 , the variation of the χ^2 as a function of one of the optical parameter – fixing all the other parameters – is shown in fig. 4.17. The narrow peak structure observed in this figure leads to two major difficulties:

- standard minimisers like MINUIT [44] cannot be used blindly because of the peak sharpness. The peak frequency is however quite independent of the other parameters so that our fitting procedure consists in searching for all minima in the parameter space and then identifying the deepest one. This is done by running the most precise minimiser of MINUIT in the neighbourhood of all peaks.
- a very high numerical precision on the sensitive parameters (i.e. thicknesses and optical indices) is required in order to identify the deeper minima.

Note that using two quartz plates, the plate thicknesses are uniquely determined, i.e. there is no degeneracy in the plate order.

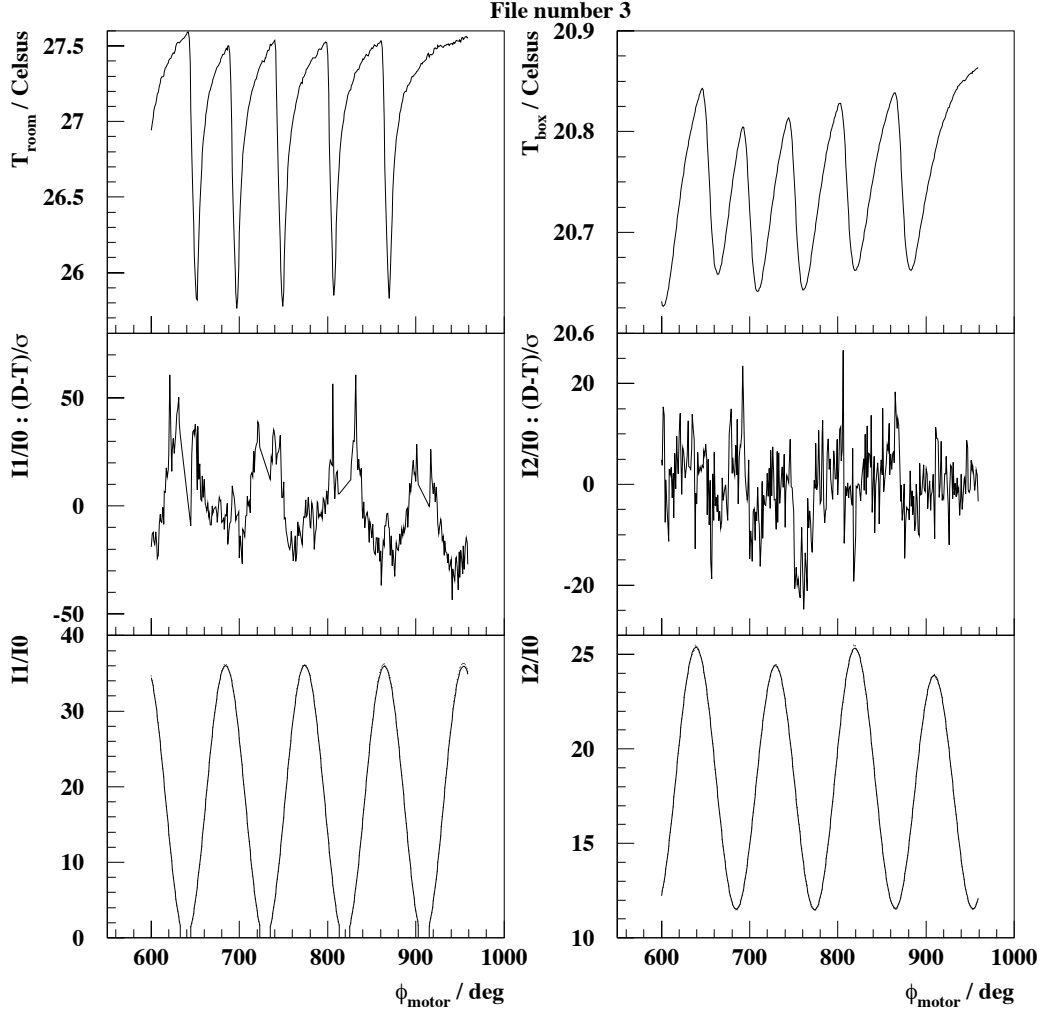


Figure 4.18: Variations as a function of the azimuthal angle of the QWP of: the room temperature, the temperature inside the photodiode box, the pools of $I1/I0$ and $I2/I0$, the data and the calculations of $I1/I0$ and $I2/I0$. The data file corresponds to the thinnest QWP and to the angle of incidence 3.67° . From [43].

δn_o	Δe_1 (μm)	Δe_2 (μm)	χ (mrad)	φ	ϵ_y	ϵ_x
$-2.6 \cdot 10^{-4}$ $\pm 2 \cdot 10^{-6}$	0.337 $\pm 10^{-3}$	0.265 $\pm 10^{-3}$	0.96 ± 0.04	34.6° $\pm 2^\circ$	$-2 \cdot 10^{-4}$ $\pm 10^{-5}$	0

Table 4.3: Values of the parameters determined by the fit (see text). The uncertainties are those given by the inverse of the Hessian matrix. We checked that they agree with the true uncertainty estimates.

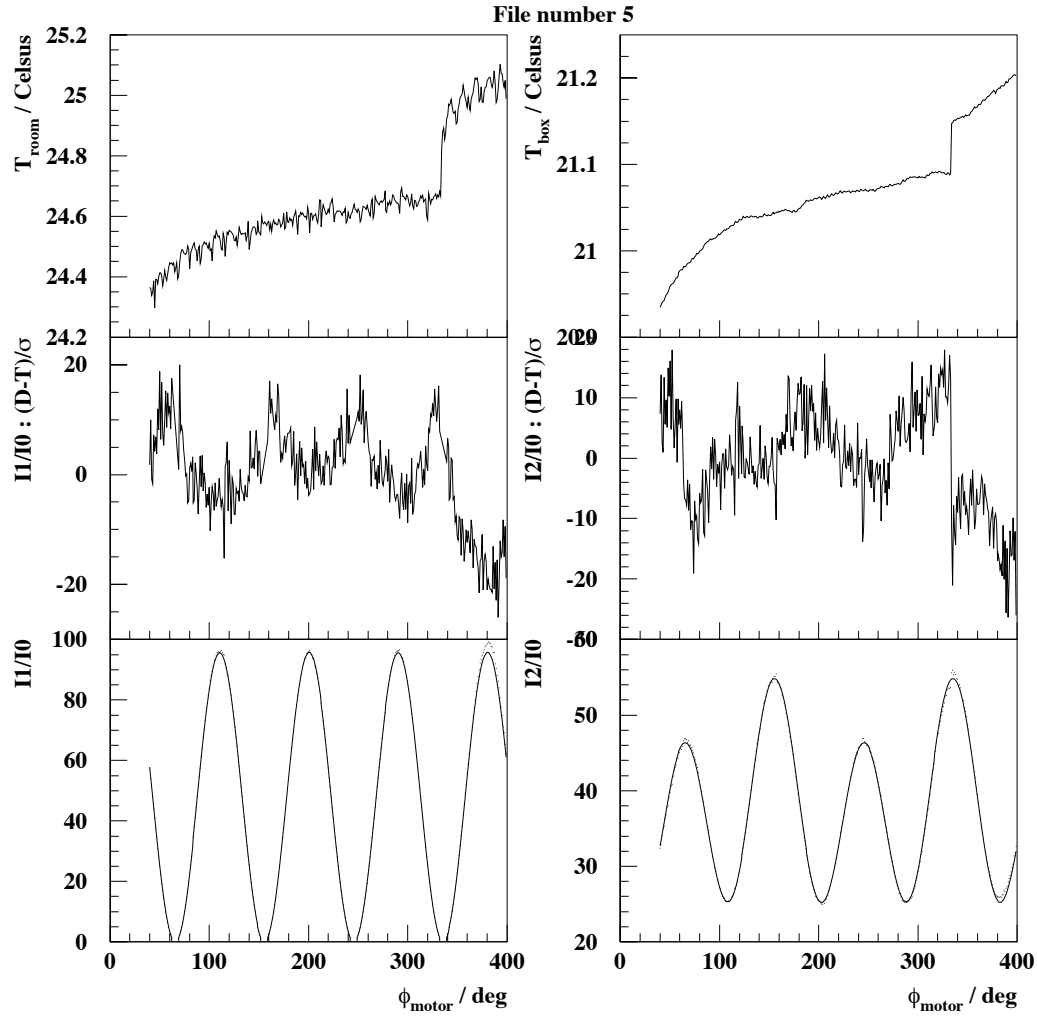


Figure 4.19: As in fig. 4.19 but for the thickest plate and the angle of incidence 3.67° . From [43].

The main fit parameters are given in table 4.3. In this table, δn_o is the relative shift with respect to value of table 4.1 which is determined by the fit (i.e. the ordinary index reads $n_o(1 + \delta n_o)$ in the fit). It agrees remarkably with the tabulated value and gives us confidence in the precision of our method. The thicknesses differences (Δe_1 and Δe_2) with respect to the value given by the manufacturer are also very small and are very precisely determined. According to section 4.2, the values of Δe_1 and Δe_2 are even below our requirement for a per mille ellipsometer. The parameters describing the incident polarisation state (φ and χ) are reasonable as well as the Wollaston prism defect (the fit was quite insensitive to ϵ_x). As for the parameters describing the misalignments, not reported in table 4.3 for sake of clarity, they are found to be also reasonable.

The fit results are presented in figs. 4.18 and 4.19 for two of the data files. Data and theory lie almost on the top of each other and the fit quality is better visualised by looking at the pool distributions⁹ of figs. 4.20 and 4.21. These histograms are reasonably Gaussian and Gaussian fits lead to standard deviations of the order of ten for $I2/I0$ and twenty for $I1/I0$. Since the experimental uncertainty entering the χ^2 expression is the statistical uncertainty, it is clear that systematics dominate.

We are confident in the accuracy of our model so that we don't expect that the main source of systematics comes from the theory. The main misalignment effect is related to the shift between the laser beam axis and the azimuthal rotation axis: because the plate interfaces being are not perfectly parallel, a variation of intensity is induced during one azimuthal turn. This shift is one of the fit parameters and it is weakly correlated to the other fit parameters (it describes the small asymmetry between data of the two azimuthal intervals $[0, \pi]$ and $[\pi, 2\pi]$). To model the parallelism fault we have assumed that the plate interfaces are plane and this assumption may not be justified. This is however unlikely since we checked that our misalignment formula describes correctly the data taken with well misaligned plates like the one of fig. 4.11. The other misalignment parameters have reasonable values and are rather uncorrelated with each other. We therefore suspect the stability of the photodiode readout.

The problem with the readout instability is its time dependence which, in our case, induces variations of the intensities as a function of the azimuthal angle. In figs. 4.18 and 4.19 we show the room temperature, the temperature inside the photodiode box, the variations of the pools as a function of ϕ_{motor} (the subscript motor indicates that the angle value is the one given by the rotation stage controller) for the intensity ratios and the intensities calculated and measured as a function of ϕ_{motor} . Fig. 4.18 describes the situation where the temperatures oscillate and Fig. 4.19 where the temperatures were well stabilised, though slowly drifting in time with a steep jump at the end of the measurements. The other data files are in between these two kinds of temperature behaviours: the temperature is oscillating for the measurements done with the thinnest QWP whereas the temperature is slowly drifting for the thickest QWP measurements (with a variation of 0.07 K at most)¹⁰.

⁹For each datum entering the χ^2 fit, the pool is defined by

$$pool = \frac{data - theory}{uncertainty}.$$

¹⁰The QWP alignment is a very long and painful procedure, it took more than a week to perform the measurements with the thinnest QWP. Because of hardware problems, the measurements of the thickest

We are not going to infer the pool variations from the box temperature variations since all the data points are mixed together in a non-trivial way during the χ^2 minimisation. Fig. 4.19 shows in any case that a steep variation of 0.05 K in the box leads to a significant discrepancy (visible on the bottom plots) between data and theory and fig. 4.18 indicates that a temperature oscillation acts as a periodic source of noise (five periods during the time of the measurements in this case).

Looking again to figs. 4.20 and 4.21, and assuming that temperature variations is the dominant source of noise, one can then give a qualitative explanation to the following features: the fact that the pools are ‘almost Gaussian’ but with a σ much greater than one and the multi-peak structure in some of the distributions. The former feature is due to an underestimation of the data uncertainty entering the χ^2 expression and is clearly due to a low frequency (much lower than the time between two successive measurements ≈ 1 mn) source of noise, i.e. temperature oscillations. The pool dispersion is of the order of ten for $I2/I0$ (the large dispersion of $I1/I0$ is discussed below) and the relative statistical uncertainties are around $5 \cdot 10^{-5}$. This means that temperature oscillation may be taken into account by including an additional uncertainty of five per mille approximately. As for the presence of peaks, they appear when the temperature is drifting in time (with a period of the same order or greater than the time of the measurements). Both phenomena can obviously be present in a given set of measurements (this is indeed the case) and there may be other sources of noise that we did not think about but, to identify them we first have to eliminate any temperature variations of the electronics box. Nevertheless, fig. 4.15 gives us confidence that the stabilisation of the box temperature is our main problem.

From the variations of the pools as a function of ϕ_{motor} (see figs. 4.18 and 4.19) one also sees that the largest contributions to the χ^2 come from the lowest values of $I1/I0$. This means that we have strongly underestimated the low intensity measurement uncertainties (measurements of $I1$ are below the microvolt for these points), so that the pools of $I1/I0$ have larger dispersions than those of $I2/I0$. It is not easy to provide a reliable estimate of these uncertainty because it implies to subtract, almost in real time, the pedestal from the signal (using a mode locking amplifier techniques for example). On the other hand these points have no particular weight in the χ^2 . One could then just rescale their uncertainties in order not to bias systematically the fit minimisation once good stability of the photodiode readout has been reached.

In summary, we are almost at the per mille level on the determination of the laser beam polarisation.

4.4 Shaping of the laser beam polarisation

In the optical scheme described in chap. 3, the laser beam is polarised circularly thanks to a Pockels cell. This optical element is a KD*P electro-optic uniaxial crystal (see appendix 4.7 for details). When a DC voltage is applied on this crystal, a linear birefringence is induced. Assuming that the crystal is perfectly anti-reflection coated, the Pockels cell acts like a retardation plate with a phase shift proportional to the DC voltage V (typically a few kV to reach the QWP regime).

QWP were done two weeks after and the different temperature behaviour reflect the outside temperature variations at Orsay during the spring ...

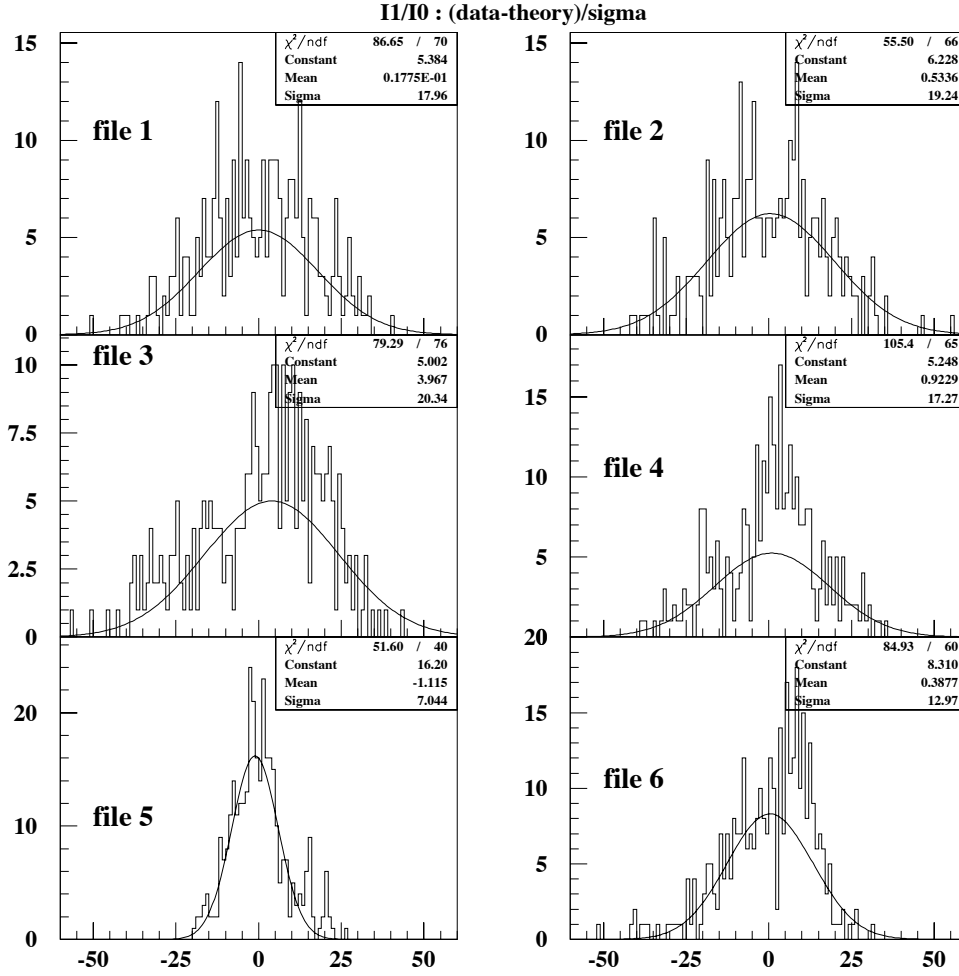


Figure 4.20: Pool distributions of $I1/I0$ for the six independent data files. Files 1, 2, 3 and 4 correspond to the angles of incidences 2.45° , 3.67° , 4.59° , 7.34° of the thinnest plate. Files 5 and 6 correspond to the angles of incidence 2.45° and 3.67° of the thickest plate. From [43].

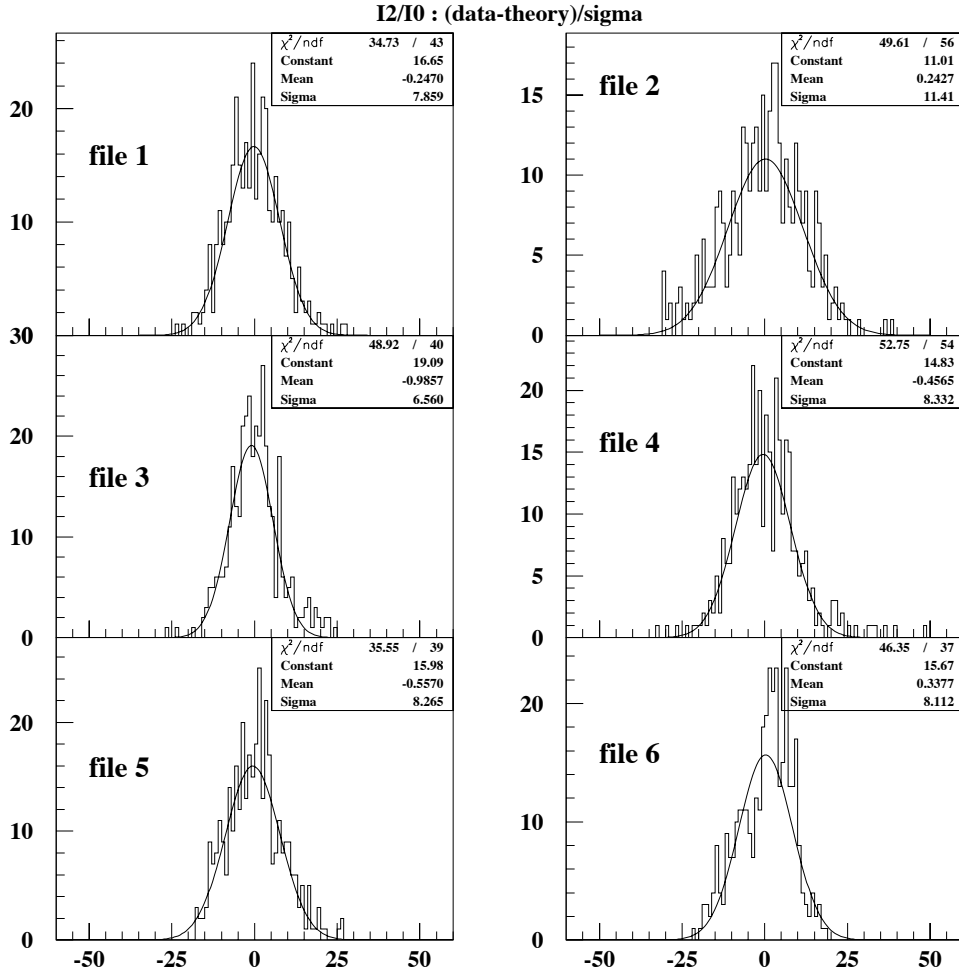


Figure 4.21: As in fig. 4.20 but for $I2/I0$. From [43].

Assuming that the crystal is perfectly anti-reflection coated, the Jones matrix is therefore given by eq. 4.2 but with $\varphi \propto V$. Denoting here by α the relative angle between the incident linear polarisation and the Pockels cell eigenvectors, the emerging polarisation state is given by eq. 4.3:

$$\mathbf{E}_{\text{out}} = R(-\alpha)MR(\alpha) \begin{pmatrix} 1 \\ 0 \end{pmatrix} = \begin{pmatrix} \cos^2 \alpha + \sin^2 \alpha \exp(i\varphi) \\ \cos \alpha \sin \alpha [1 - \exp(i\varphi)] \end{pmatrix}.$$

Since we do not measure absolute intensities, nor global phases, one can further write $\mathbf{E}_{\text{out}}^T = (1, \rho \exp(i\psi))$ where ρ and ψ are real numbers depending on α and φ : when $\rho = 1$ and $\psi = \pm\pi/2$ the emergent beam is circularly polarised, otherwise it is elliptically polarised or linearly polarised if $\psi = 0, \pi$ (see ref. [40]).

ρ and ψ are shown in figs. 4.22 and 4.23 as a function of α and φ . If we remember that our goal is to maximise the level of circular polarisation at the laser beam-electron beam interaction point (IP), and if we also remember that between the Pockels cell and the IP, four mirrors and the two wedges are expected to induce a noticeable ellipticity/birefringence, one sees that a circular polarisation at the IP does not imply a circular polarisation after the Pockels cell. But by varying both α (orientation of the Pockels cell) and φ (DC voltage) one can optimise the laser light polarisation by maximising the total Compton scattering rate (which is proportional to the level of circular polarisation at the IP). This is the online calibration procedure already described in section 3.3.4 of chap. 3. However, it is a very difficult task to rotate the Pockels cell (because of the HT wires and of the alignment), we therefore decided to rotate the incident polarisation using a half wave plate located in a remote controlled rotation mount.

Let me mention that the description of a Pockels cell given in this section may not be precise enough if a high precision is foreseen. On the other hand a more accurate model would be very hard to provide (we could get no technical information from the manufacturer...) and this is the reason why we have decided to provide a very precise measurement of the light polarisation.

4.5 Summary

As a concluding remark, it is fair to say that we spent much more effort on the light polarisation measurement than we thought could be needed at the beginning of the project. We also realised that the difficulty for going from the percent level to the per mille level does not increase linearly.

The calibration procedure of our ellipsometer, tested at Orsay, leads to ‘an almost per mille level’ accuracy. To safely claim that we do control our light polarisation at the per mille level, a modification of the photodiode readout scheme is necessary and we are currently working on this topic.

No results from HERA were presented in this chapter. A new photodiode box has been designed and installed at the very last moment of the HERA shutdown. Since we had very little time to test this new box, we did not succeed to operate the temperature regulation. This is another reason, if needed, to design a completely new system.

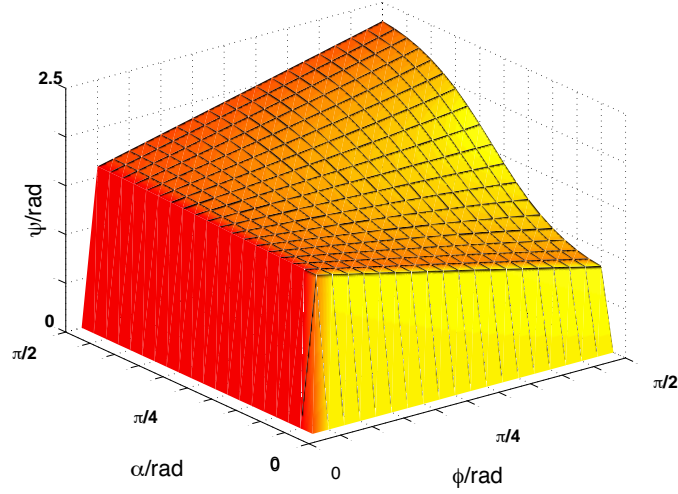


Figure 4.22: Variation of the relative phase shift between the two linear polarisation components of a plane wave after a Pockels cell as a function of the Pockels cell orientation (α) and phase retardation (here denoted ϕ instead of φ in the text.)

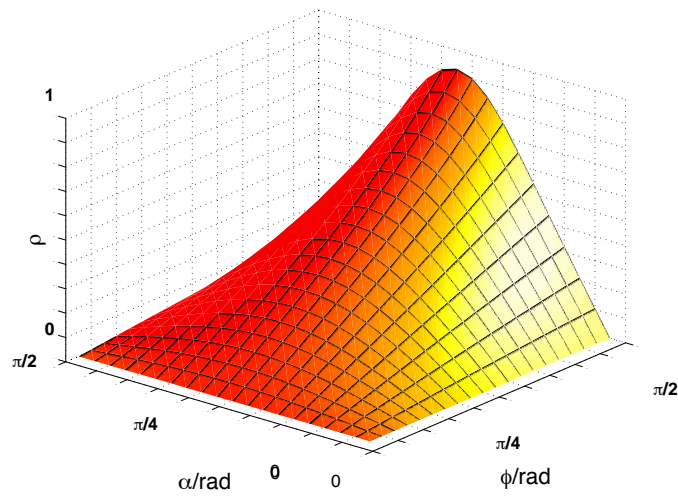


Figure 4.23: As in fig. 4.22 but for the ratio of the absolute amplitudes of the two linear polarisation components.

4.6 Appendix: Misalignments

A realistic description of an optical bench must take into account the experimental misalignments [1]. In our ellipsometer setup (see fig. 4.24), they are of prime importance.

Misalignment calculations must be done taking into account the dynamical mechanism of our optical mounts: the tilting stage is operated in the *mechanical horizontal plane* (rotation around the *mechanical vertical axes*) and the azimuthal rotation is operated by a remote controlled rotation mount which is fixed on the tilting stage (see fig. 4.10). It is important to distinguish the horizontal and vertical *mechanical axis* from the reference frame axes x and y attached to the two linear polarisation directions of the Wollaston prism. (see figs. 4.24). The difference between the two sets of axes is expected to be small but anyhow not negligible since the axes x and y are not explicitly ‘visible’.

Ideally, our quartz plate rotates around an axis perpendicular to its plane of interface and the laser beam enters the plate at the centre of this azimuthal rotation. In addition, the plate is tilted around the vertical y axis. With respect to the ideal situation, we shall then distinguish the following sources of misalignment:

1. the direction of the incoming polarisation (defined by the Glan-Thomson prism) may not exactly coincide with the vertical eigen-mode of the Wollaston prism which defines arbitrarily the reference axis y .
2. The plate is not tilted exactly around the vertical axis y but around the direction $\hat{\mathbf{u}}$ (see fig. 4.24).
3. The rotation mount may not be perfectly perpendicular to the tilting mount. Therefore the tilted direction $\hat{\mathbf{u}}$ and the azimuthal rotation direction $\hat{\mathbf{v}}$ may not be perpendicular as well (see fig. 4.24).
4. The laser beam does not enter the quartz plate exactly at the centre of the azimuthal rotation. The two faces of the plate being not perfectly parallel, the thickness thus varies during the rotation.
5. The direction of the azimuthal rotation $\hat{\mathbf{v}}$ does not coincide with the direction normal to the plate $\hat{\mathbf{n}}$. A precession of $\hat{\mathbf{n}}$ may thus occur.

The calculations are much simplified by using spherical coordinates and by reducing all misalignments to elementary rotations [45]. Starting from the fixed basis $\{\hat{\mathbf{x}}, \hat{\mathbf{y}}, \hat{\mathbf{z}}\}$, all vectors introduced in the following are obtained by applying two rotations on one of the three basis vectors: one rotation around the y axis (polar angle) followed by a rotation around the z axis (azimuthal angle).

In the following, we fix the laser beam propagation axis along $\hat{\mathbf{z}}$. The wave vector is thus $\mathbf{k} = k\hat{\mathbf{k}}$ with $\hat{\mathbf{k}} = \hat{\mathbf{z}}$.

The above sources of misalignments are investigated step by step in the following sections.

4.6.1 Glan-Thomson/Wollaston prisms misalignment

The Glan-Thomson prism and the Wollaston prism are aligned by putting them in front of each other and by minimising the ratio of intensities measured after the Wollaston prism.

As in section 4.3.3, we write the electric vector after the Glan-Thomson prism as

$$\mathbf{E}_i^T = (\cos \chi, \sin \chi \exp i\varphi)$$

where χ is small when the Glan-Thomson prism and the Wollaston prism are well aligned and where we introduced the phase φ to account for the Glan-Thomson prism defects.

Taking the Jones matrix of eq. 4.16 (with $\mathbb{P} = 1$) to describe the Wollaston prism, we obtain the expressions for the two intensities:

$$I_x = 1 - 2\chi\epsilon_x \sin \varphi - \epsilon_x^2, \quad I_y = \epsilon_y^2 + \chi^2 - 2\chi\epsilon_y \sin \varphi,$$

where we assumed that the Glan-Thomson and Wollaston prisms are almost aligned.

From these expressions one sees that $I_y/I_x \approx \epsilon_y^2 + \chi^2 - 2\chi\epsilon_y \sin \varphi$. We typically achieved an extinction stable at the level of $I_y/I_x \approx 10^{-5}$ so that the angle χ is known at the level of 3 mrad, i.e. at the same level as ϵ_y .

4.6.2 Misalignment of the tilt and azimuthal axes

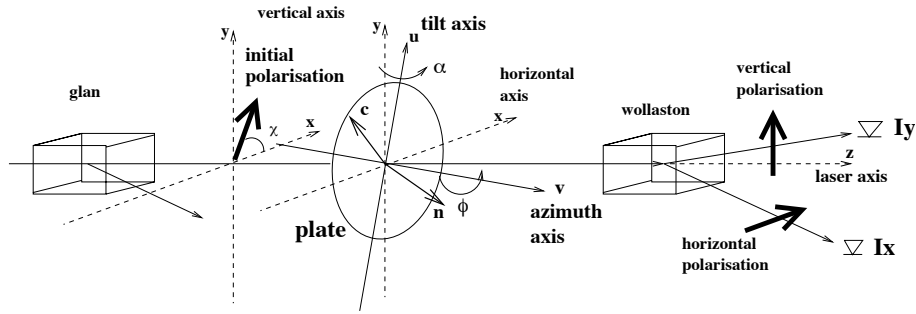


Figure 4.24: Schematic view of a quartz plate tilted around the direction $\hat{\mathbf{u}}$ by an angle α and rotated (azimuthal) by an angle ϕ around the direction $\hat{\mathbf{v}}$. The reference frame $\{x, y, z\}$ refers to the two linear polarisation directions as defined by the Wollaston prism. The angle β describe a misalignment of the incident polarisation. The normal to the plate $\hat{\mathbf{n}}$ and the orientation of the optical axis $\hat{\mathbf{c}}$ are also drawn.

The situation is schematically depicted in fig. 4.24. We denote by $\hat{\mathbf{u}}$ the unit vector along the tilt axis and by $\hat{\mathbf{v}}$ the unit vector along the azimuthal rotation axis. The azimuthal rotation is performed after the tilt so that $\hat{\mathbf{v}}$ changes with the tilt angle α . It is thus convenient to introduce the vector $\hat{\mathbf{v}}_0$ for $\hat{\mathbf{v}}$ when $\alpha = 0$.

Ideally one has $\hat{\mathbf{u}} = \hat{\mathbf{y}}$ and $\hat{\mathbf{u}} \cdot \hat{\mathbf{v}}_0 = 0$ but, because of misalignment, $\hat{\mathbf{u}}$ and $\hat{\mathbf{v}}_0$ are in fact described by two different pairs of angles (θ_u, ϕ_u) and (θ_v, ϕ_v) such that

$$\hat{\mathbf{u}} = R_z(\phi_u)R_y(\theta_u)\hat{\mathbf{y}} \quad \text{and} \quad \hat{\mathbf{v}}_0 = R_z(\phi_v)R_y(\theta_v)\hat{\mathbf{z}}$$

where R_z and R_y are the rotation matrices around $\hat{\mathbf{z}}$ and $\hat{\mathbf{y}}$

$$R_z(\phi) = \begin{pmatrix} \cos \phi & -\sin \phi & 0 \\ \sin \phi & \cos \phi & 0 \\ 0 & 0 & 1 \end{pmatrix}, \quad R_y(\theta) = \begin{pmatrix} \cos \theta & 0 & \sin \theta \\ 0 & 1 & 0 \\ -\sin \theta & 0 & \cos \theta \end{pmatrix}.$$

Let us first describe a rotation of angle α around $\hat{\mathbf{u}}$ in the fixed basis $\{\hat{\mathbf{x}}, \hat{\mathbf{y}}, \hat{\mathbf{z}}\}$. We define a direct orthogonal basis $\{\hat{\mathbf{u}}_1, \hat{\mathbf{u}}, \hat{\mathbf{u}}_3\}$ such $\hat{\mathbf{u}}_1 = R_z(\phi_u)R_y(\theta_u)\hat{\mathbf{x}}$ and $\hat{\mathbf{u}}_3 = R_z(\phi_u)R_y(\theta_u)\hat{\mathbf{z}}$. In this basis, the rotation α is made around the second axis. After this rotation, a vector $\hat{\mathbf{n}}_0$ is transformed into $\hat{\mathbf{n}}$ whose components are given by:

$$\begin{pmatrix} \hat{\mathbf{n}} \cdot \hat{\mathbf{u}}_1 \\ \hat{\mathbf{n}} \cdot \hat{\mathbf{u}} \\ \hat{\mathbf{n}} \cdot \hat{\mathbf{u}}_3 \end{pmatrix} = R_y(\alpha) \begin{pmatrix} \hat{\mathbf{n}}_0 \cdot \hat{\mathbf{u}}_1 \\ \hat{\mathbf{n}}_0 \cdot \hat{\mathbf{u}} \\ \hat{\mathbf{n}}_0 \cdot \hat{\mathbf{u}}_3 \end{pmatrix}.$$

Since

$$\begin{pmatrix} \hat{\mathbf{n}} \cdot \hat{\mathbf{u}}_1 \\ \hat{\mathbf{n}} \cdot \hat{\mathbf{u}} \\ \hat{\mathbf{n}} \cdot \hat{\mathbf{u}}_3 \end{pmatrix} = \begin{pmatrix} \hat{\mathbf{u}}_1 \cdot \hat{\mathbf{x}} & \hat{\mathbf{u}}_1 \cdot \hat{\mathbf{y}} & \hat{\mathbf{u}}_1 \cdot \hat{\mathbf{z}} \\ \hat{\mathbf{u}} \cdot \hat{\mathbf{x}} & \hat{\mathbf{u}} \cdot \hat{\mathbf{y}} & \hat{\mathbf{u}} \cdot \hat{\mathbf{z}} \\ \hat{\mathbf{u}}_3 \cdot \hat{\mathbf{x}} & \hat{\mathbf{u}}_3 \cdot \hat{\mathbf{y}} & \hat{\mathbf{u}}_3 \cdot \hat{\mathbf{z}} \end{pmatrix} \begin{pmatrix} \hat{\mathbf{n}} \cdot \hat{\mathbf{x}} \\ \hat{\mathbf{n}} \cdot \hat{\mathbf{y}} \\ \hat{\mathbf{n}} \cdot \hat{\mathbf{z}} \end{pmatrix} = \left[R_z(\phi_u)R_y(\theta_u) \right]^{-1} \begin{pmatrix} \hat{\mathbf{n}} \cdot \hat{\mathbf{x}} \\ \hat{\mathbf{n}} \cdot \hat{\mathbf{y}} \\ \hat{\mathbf{n}} \cdot \hat{\mathbf{z}} \end{pmatrix},$$

we obtain

$$\hat{\mathbf{n}} = T_u \hat{\mathbf{n}}_0 \text{ with } T_u = R_z(\phi_u)R_y(\theta_u)R_y(\alpha)R_y(-\theta_u)R_z(-\phi_u) \quad (4.19)$$

in the fixed basis $\{\hat{\mathbf{x}}, \hat{\mathbf{y}}, \hat{\mathbf{z}}\}$.

The expression for the azimuthal rotation of an angle ϕ around the direction $\hat{\mathbf{v}}$ is now straightforward. This rotation is performed after the tilt around $\hat{\mathbf{u}}$ so that $\hat{\mathbf{n}}_0$ is finally transformed into

$$\hat{\mathbf{n}} = T_v T_u \hat{\mathbf{n}}_0 \text{ with } T_v = T_u R_z(\phi_v)R_y(\theta_v)R_z(\phi)R_y(-\theta_v)R_z(-\phi_v)T_u^{-1}. \quad (4.20)$$

When the two rotation axes are perpendicular (i.e. $\hat{\mathbf{v}} = \hat{\mathbf{u}}_3$), one gets

$$\theta_u = \theta_v, \phi_u = \phi_v \Rightarrow T_v T_u = R_z(\phi_u)R_y(\theta_u)R_y(\alpha)R_z(\phi)R_y(-\theta_u)R_z(-\phi_u).$$

So far we have defined the transformation $T = T_v T_u$ corresponding to our manipulations of the quartz plate mounting system. We must now calculate the changes induced by this transformation on the vectors involved in the model describing the laser beam propagation in the quartz. That is:

- the orientation of the normal to the plate $\hat{\mathbf{n}}$ and thus on the angle of incidence $\theta_i = \arccos(\hat{\mathbf{z}} \cdot \hat{\mathbf{n}})$ (the incident wave vector is along $\hat{\mathbf{z}}$);
- the orientation of the plane of incidence (defined by $\{\hat{\mathbf{n}}, \hat{\mathbf{z}}\}$);
- the azimuthal ϕ_a orientation of the quartz optical axis with respect to the plane of incidence $\cos \phi_a = \hat{\mathbf{c}} \cdot \hat{\mathbf{t}}$ (with $\hat{\mathbf{c}}$ the orientation of the optical axis and $\hat{\mathbf{t}}$ the trace of the plane of incidence in the plane of interface).

It is convenient to introduce small angles. Since we expect that $\hat{\mathbf{n}} \approx \hat{\mathbf{v}}$ with $\hat{\mathbf{c}} \perp \hat{\mathbf{n}}$, we expand the initial vectors (i.e. before the first tilt) $\hat{\mathbf{n}}_0$ and $\hat{\mathbf{c}}_0$ in the basis attached to the direction $\hat{\mathbf{v}}_0$:

$$\begin{aligned} \hat{\mathbf{n}}_0 &= \cos \theta_{n0} \hat{\mathbf{v}}_0 + \sin \theta_{n0} \left(\cos \phi_{n0} \hat{\mathbf{v}}_2 + \sin \phi_{n0} \hat{\mathbf{v}}_1 \right), \\ \hat{\mathbf{c}}_0 &= \sin \theta_{c0} \hat{\mathbf{v}}_0 + \cos \theta_{c0} \left(\cos \phi_{c0} \hat{\mathbf{v}}_2 + \sin \phi_{c0} \hat{\mathbf{v}}_1 \right) \end{aligned}$$

with one of the four angles $(\theta_{n0}, \phi_{n0}, \theta_{c0}, \phi_{c0})$ determined by the condition

$$\hat{\mathbf{n}}_0 \cdot \hat{\mathbf{c}}_0 = 0 \Rightarrow \cos \theta_{n0} \sin \theta_{c0} + \cos \theta_{c0} \sin \theta_{n0} \cos(\phi_{n0} - \phi_{c0}) = 0$$

and where $\hat{\mathbf{v}}_1 = R_z(\phi_v)R_y(\theta_v)\hat{\mathbf{y}}$ and $\hat{\mathbf{v}}_2 = R_z(\phi_v)R_y(\theta_v)\hat{\mathbf{x}}$. Let us mention that the manufacturer gives $\hat{\mathbf{n}}_0 \cdot \hat{\mathbf{c}}_0 < 3 \cdot 10^{-3}$. This fault is taken into account as a systematic uncertainty in our analysis by fixing $\hat{\mathbf{n}}_0 \cdot \hat{\mathbf{c}}_0 = 3 \cdot 10^{-3}$ and repeating the fitting procedure.

Using eq. (4.20) we obtain

$$\cos \theta_i = \hat{\mathbf{z}} \cdot T\hat{\mathbf{n}}_0 ,$$

with $T = T_v T_u$.

The plane of incidence is described by the incident wave vector $\hat{\mathbf{k}}$ and by the normal to the plate $\hat{\mathbf{n}}$. The reference frame attached to this plane is denoted $\{\hat{\mathbf{s}}, \hat{\mathbf{p}}, \hat{\mathbf{k}}\}$ and it is the one used for the calculation of the plate Jones matrix (see appendix A for details). $\hat{\mathbf{s}}$ is perpendicular to the plane of incidence so that $\hat{\mathbf{s}} \cdot \hat{\mathbf{n}} = 0$ and $\hat{\mathbf{s}} \cdot \hat{\mathbf{k}} = 0$. With $\hat{\mathbf{k}} = \hat{\mathbf{z}}$ and $\hat{\mathbf{p}} = \hat{\mathbf{k}} \times \hat{\mathbf{s}}$, we obtain

$$\hat{\mathbf{s}} = (n_x^2 + n_y^2)^{-1/2} \begin{pmatrix} n_y \\ -n_x \\ 0 \end{pmatrix} , \quad \hat{\mathbf{p}} = (n_x^2 + n_y^2)^{-1/2} \begin{pmatrix} n_x \\ n_y \\ 0 \end{pmatrix}$$

with $\hat{\mathbf{n}}^T = (n_x, n_y, n_z)$ given by eq. 4.20.

Since the reference frame is attached to the Wollaston prism vertical and horizontal polarisation direction, the Jones matrix M is transformed into $\Omega M \Omega^T$ with

$$\Omega = \begin{pmatrix} \hat{\mathbf{x}} \cdot \hat{\mathbf{s}} & \hat{\mathbf{x}} \cdot \hat{\mathbf{p}} \\ \hat{\mathbf{y}} \cdot \hat{\mathbf{s}} & \hat{\mathbf{y}} \cdot \hat{\mathbf{p}} \end{pmatrix} = (n_x^2 + n_y^2)^{-1/2} \begin{pmatrix} n_y & n_x \\ -n_x & n_y \end{pmatrix} .$$

ϕ_a is the angle between the optical axis and the trace of the plane of incidence in the plane of interface. Writing $\hat{\mathbf{t}}$ for a unit vector aligned along this latter direction, one has

$$\cos \phi_a = \hat{\mathbf{c}} \cdot \hat{\mathbf{t}} = \hat{\mathbf{t}} \cdot T\hat{\mathbf{c}}_0$$

with $\hat{\mathbf{t}}$ defined by $\hat{\mathbf{t}} \cdot \hat{\mathbf{n}} = 0$ and $\hat{\mathbf{s}} \times \hat{\mathbf{t}} = 0$. Explicitly:

$$\hat{\mathbf{t}} = (n_x^2 + n_y^2)^{-1/2} \begin{pmatrix} n_x n_z \\ n_y n_z \\ -(n_x^2 + n_y^2) \end{pmatrix} .$$

To summarise, the angles α and ϕ correspond to the tilting and azimuthal angles of the rotation mounts respectively. The initial conditions are given by three of the four angles $(\theta_{n0}, \phi_{n0}, \theta_{c0}, \phi_{c0})$, by the orientations of the axes of rotation $(\theta_u, \phi_u, \theta_v, \phi_v)$ and by the angles χ and φ introduced in section 4.6.1. The initial optical alignments are performed experimentally ‘by eye’ with a typical accuracy of 1 mrad (i.e. a displacement of 1 mm at 1 m from the optical element. One should notice that a laser beam is divergent so that it is difficult to resolve small displacements within the laser spots). The misalignment angles must then be determined by the χ^2 fit of the model to the measurements. In doing so, correlations obviously appear between the seven angles defining the initial conditions. Since correlations are non-trivial, we proceed as follows to account for the misalignments:

we first assume that $\hat{\mathbf{u}} \perp \hat{\mathbf{v}}$ so that $\theta_u = \theta_v$ and $\phi_u = \phi_v$, we also assume that $\hat{\mathbf{c}} \perp \hat{\mathbf{v}}$ and $\hat{\mathbf{n}}_0 = \hat{\mathbf{z}}$ so that $\theta_{c0} = 0$ and $\theta_{n0} = \phi_{n0} = 0$. Next the correlations with the other angles are studied using the χ^2 Hessian matrix (i.e. the matrix of second derivatives of χ^2). By requiring a definite positive Hessian matrix we end-up with three angles to be determined by the χ^2 fit: θ_u , ϕ_u and ϕ_{c0} .

To account for the 1 mrad misalignments, the angles θ_v and ϕ_v are fixed to +1 mrad and -1 mrad successively and the χ^2 minimisation is performed. This leads to a systematic uncertainty. Nevertheless, because the experimental results presented in section 4.3.4 are not precise enough, we didn't perform any systematic studies yet.

4.6.3 Rotation axis misalignment

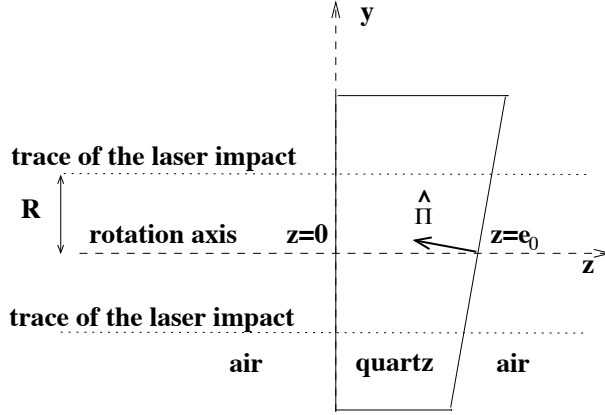


Figure 4.25: Schematic view of an imperfect quartz plate rotating around the z axis. The path of a laser beam entering the plate off the rotation axis is shown as dotted lines. To simplify the drawing, the normal incidence is presented.

This fault appears when the axis of rotation of the QWP mount does not coincide with the laser beam impact on the plate [46]. Since the plate interfaces are not perfectly parallel, the optical path inside the plate depends on the angular position of the rotation mount ϕ , on the relative orientation of the two interfaces and on the distance between the laser beam impact point and the plate mount rotation axis R (see fig. 4.25). We assume here that the two interfaces are plane, i.e. we neglect a possible curvature effect.

For the calculations, we introduce the basis $\{\hat{\mathbf{x}}', \hat{\mathbf{y}}', \hat{\mathbf{z}}'\}$ attached to the first interface. $\hat{\mathbf{z}}'$ is normal to this interface and this basis coincide with the reference basis $\{\hat{\mathbf{x}}, \hat{\mathbf{y}}, \hat{\mathbf{z}}\}$ when the plate is not tilted. Next we define the normal to the second interface in $\{\hat{\mathbf{x}}', \hat{\mathbf{y}}', \hat{\mathbf{z}}'\}$: $\hat{\Pi} = \sin \theta_{\Pi} \cos \phi_{\Pi} \hat{\mathbf{x}}' + \sin \theta_{\Pi} \sin \phi_{\Pi} \hat{\mathbf{y}}' + \cos \theta_{\Pi} \hat{\mathbf{z}}'$. The reason for this choice is the following: for a laser beam impact point on the first interface $(x', y', z' = 0)$, the plate thickness is simply the value z' corresponding to the position (x', y', z') on the second interface. In addition x' and y' are directly related to the azimuthal position of the rotation mount ϕ : $x' = \rho \cos \phi$ and $y' = \rho \sin \phi$ where ρ depends on incident direction of the laser beam and on the laser impact point on the first interface. ρ is easily determined by assuming that the plate is fixed and that the laser beam describes a circle in the fixed

basis $\{\hat{\mathbf{x}}, \hat{\mathbf{y}}, \hat{\mathbf{z}}\}$. In doing so we obtain

$$\begin{cases} x = T_{11}x' + T_{12}y' \\ y = T_{21}x' + T_{22}y' \\ x^2 + y^2 = R^2 \end{cases}$$

where we fixed the impact point on the first interface by imposing $z' = 0$ and where T_{ij} are the elements of the transformation matrix given in the previous section. The solution of this system gives

$$\rho = R \left([T_{11} \cos \phi + T_{12} \sin \phi]^2 + [T_{21} \cos \phi + T_{22} \sin \phi]^2 \right)^{-1/2}$$

By construction, the centre of the circle is on the axis of the azimuthal rotation. Denoting by e_0 the plate thickness at this point, one gets

$$x' \hat{\Pi} \cdot \hat{\mathbf{x}}' + y' \hat{\Pi} \cdot \hat{\mathbf{y}}' + z' \hat{\Pi} \cdot \hat{\mathbf{z}}' = e_0 \hat{\Pi} \cdot \hat{\mathbf{z}}'$$

so that the thickness finally reads as

$$e = z' = e_0 \left(1 + \frac{R \tan \theta_{\Pi}}{e_0} \frac{\cos(\phi - \phi_{\Pi})}{\sqrt{(T_{11} \cos \phi + T_{12} \sin \phi)^2 + (T_{21} \cos \phi + T_{22} \sin \phi)^2}} \right).$$

For an oblique incidence θ_i , assuming that the plate is tilted around the axis y , we obtain:

$$e(\phi) = e_0 \left(1 + \frac{R \tan \theta_{\Pi}}{e_0} \frac{\cos(\phi - \phi_{\Pi})}{\sqrt{1 - \cos^2 \phi \sin^2 \theta_i}} \right). \quad (4.21)$$

We know that $\theta_{\Pi} < 10^{-5}$ rad. So for each set of measurements (= one angle of incidence and one turn in ϕ) we must adjust an effective parameter $R \tan \theta_{\Pi} / e_0$ to account for a remaining small alignment error. The parameter ϕ_{Π} must also be adjusted but its value is the same for all tilt angles since we start all azimuthal rotations at the same initial value.

4.7 Appendix: Electro-optic crystal

Electro-optic crystals are uniaxially anisotropic media which become biaxially anisotropic when an external static electric field is applied (i.e. coupling between a static and dynamic fields, i.e. non-linear optics [47]). In the case of the Pockels effect, the birefringence variation is linearly proportional to the applied electric field. In order to derive an expression for the Jones matrix of a Pockels cell, we shall not consider, as usual, the *index of ellipsoid* [48], but rather the dielectric tensor and the Maxwell equations. In this way, formulae derived in appendix A are directly usable. Our Pockels cell is a Potassium Dideuterium Phosphate (KD*P or DKDP) uniaxial crystal plate with its optical axis along the normal of the interface. It is natural to choose the crystallographic basis $\{\hat{\mathbf{x}}, \hat{\mathbf{y}}, \hat{\mathbf{z}}\}$ such that $\hat{\mathbf{x}}$ is along the optical axis and $\hat{\mathbf{x}}, \hat{\mathbf{y}}$ are in the planes of interface.

KD*P crystals belong to the crystallographic class $\bar{4}2m$. It has been shown that [49] if the external static field is supplied along the optical axis and if the laser beam propagates along this axis, then the optical activity (see section 4.1.1) does not contribute to the induced birefringence. We shall therefore only consider the dipolar response of KD*P to the electromagnetic field excitation in the Maxwell equations.

To simplify the calculations without losing generality, one can also assume that the plane of incidence is in the y, z plane. In this basis and in absence of an external electric field, the dielectric tensor reads:

$$\bar{\epsilon}_0 = \begin{pmatrix} \epsilon_o & 0 & 0 \\ 0 & \epsilon_o & 0 \\ 0 & 0 & \epsilon_e \end{pmatrix}$$

with $\epsilon_o = n_o^2$ and $\epsilon_e = n_e^2$ (and taking $\epsilon_0 = 1$). When a static field $\mathcal{E} = \mathcal{E}_x \hat{\mathbf{x}} + \mathcal{E}_y \hat{\mathbf{y}} + \mathcal{E}_z \hat{\mathbf{z}}$ is applied, what we can determine using the optical tensor is the modification of the inverse of the dielectric tensor [6]:

$$\bar{\epsilon}_0^{-1} \Rightarrow \bar{\epsilon}^{-1} = \bar{\epsilon}_0^{-1} + \Delta \bar{\epsilon}^{-1}.$$

In the linear approximation, one has (taking into account the KD*P crystal symmetry):

$$\begin{pmatrix} \Delta \bar{\epsilon}_{xx}^{-1} \\ \Delta \bar{\epsilon}_{yy}^{-1} \\ \Delta \bar{\epsilon}_{zz}^{-1} \\ \Delta \bar{\epsilon}_{yz}^{-1} \\ \Delta \bar{\epsilon}_{xz}^{-1} \\ \Delta \bar{\epsilon}_{xy}^{-1} \end{pmatrix} = \begin{pmatrix} 0 & 0 & 0 \\ 0 & 0 & 0 \\ 0 & 0 & 0 \\ r_{41} & 0 & 0 \\ 0 & r_{41} & 0 \\ 0 & 0 & r_{63} \end{pmatrix} \begin{pmatrix} \mathcal{E}_x \\ \mathcal{E}_y \\ \mathcal{E}_z \\ 0 \\ 0 \\ 0 \end{pmatrix}$$

with the electrooptic parameters for KD*P $r_{41} = 8.8 \cdot 10^{-12} \text{m/V}$ and $r_{61} = 25 \cdot 10^{-12} \text{m/V}$ (details can be find in refs. [6, 40, 47]). Executing the inverse of $\bar{\epsilon}^{-1}$ one obtains:

$$\bar{\epsilon} = \frac{1}{F} \begin{pmatrix} \epsilon_o(1 - r_{41}^2 \mathcal{E}_x^2 \epsilon_o \epsilon_e) & \epsilon_o^2(\epsilon_e r_{41}^2 \mathcal{E}_x \mathcal{E}_y - r_{63} \mathcal{E}_z) & \epsilon_o \epsilon_e r_{41}(\epsilon_o r_{63} \mathcal{E}_z \mathcal{E}_x - \mathcal{E}_y) \\ \epsilon_o^2(\epsilon_e r_{41}^2 \mathcal{E}_x \mathcal{E}_y - r_{63} \mathcal{E}_z) & \epsilon_o^2(1 - r_{41}^2 \mathcal{E}_y^2 \epsilon_o \epsilon_e) & \epsilon_e r_{41}(\epsilon_o r_{63} \mathcal{E}_z \mathcal{E}_y - \mathcal{E}_x) \\ \epsilon_o \epsilon_e r_{41}(\epsilon_o r_{63} \mathcal{E}_z \mathcal{E}_x - \mathcal{E}_y) & \epsilon_e r_{41}(\epsilon_o r_{63} \mathcal{E}_z \mathcal{E}_y - \mathcal{E}_x) & \epsilon_e(1 - \epsilon_o^2 r_{63}^2 \mathcal{E}_z^2) \end{pmatrix} \quad (4.22)$$

with

$$F = 1 - \epsilon_o \epsilon_e r_{41}^2 (\mathcal{E}_x^2 + \mathcal{E}_y^2) - \epsilon_o^2 r_{63}^2 \mathcal{E}_z^2 + 2 \epsilon_o^2 \epsilon_e r_{63} r_{41}^2 \mathcal{E}_x \mathcal{E}_y \mathcal{E}_z.$$

From Maxwell's equations one gets the wave equation in lossless anisotropic media. In the \mathbf{k} space one obtains [50]

$$\mathbf{k} \times (\mathbf{k} \times \mathbf{E}) + \bar{\epsilon} \mathbf{E} = 0 \quad (4.23)$$

where we have set $\mu = 1$ (the magnetic permeability) and $\omega = 1$ (the angular frequency) and where \mathbf{E} is the electric field of the electromagnetic wave propagating inside the anisotropic media. By definition of the basis vectors $\{\hat{\mathbf{x}}, \hat{\mathbf{y}}, \hat{\mathbf{z}}\}$, the wave vector \mathbf{k} is given by

$$\mathbf{k} = \beta \hat{\mathbf{y}} + k_z \hat{\mathbf{z}},$$

with β given by the boundary condition at the air-crystal interface: if θ_i is the incident angle, $\beta = \sin \theta_i$. Eq. 4.23 can be expressed in a matrix form $M\mathbf{E} = 0$ with

$$M = \begin{pmatrix} \epsilon_{xx} - \beta^2 - k_z^2 & \epsilon_{xy} & \epsilon_{xz} \\ \epsilon_{xy} & \epsilon_{yy} - k_z^2 & \epsilon_{yz} + \beta k_z \\ \epsilon_{xz} & \epsilon_{yz} + \beta k_z & \epsilon_{zz} - \beta^2 \end{pmatrix}$$

with an obvious notation for the matrix elements of $\bar{\epsilon}$: ϵ_{xx} , ϵ_{yy} , ϵ_{zz} , ϵ_{xy} , ϵ_{xz} and ϵ_{yz} .

Non-trivial solutions of the wave equation exist if $\det(M)=0$. This gives a quartic equation in k_z (the only unknown) corresponding to: two forward and two backward propagating waves. To determine the electric vector \mathbf{E} for the four solutions, a theorem of linear algebra has been utilised in ref. [50]: solutions of an inhomogeneous system of n linear equations of rank $n - 1$ are given by the cofactors of one of the lines of the matrix M *provided not all the cofactors vanish*. The solution is then given by¹¹

$$\mathbf{E} \propto \begin{pmatrix} (\epsilon_{yy} - k_z^2)(\epsilon_{zz} - \beta^2) - (\epsilon_{yz} + \beta k_z)^2 \\ \epsilon_{xz}(\epsilon_{yz} + \beta k_z) - \epsilon_{xy}(\epsilon_{zz} - \beta^2) \\ \epsilon_{xy}(\epsilon_{yz} + \beta k_z) - \epsilon_{xz}(\epsilon_{yy} - k_z^2) \end{pmatrix} \quad (4.24)$$

$$\text{or: } \begin{pmatrix} \epsilon_{xz}(\epsilon_{yz} + \beta k_z) - \epsilon_{xy}(\epsilon_{zz} - \beta^2) \\ (\epsilon_{xx} - \beta^2 - k_z^2)(\epsilon_{zz} - \beta^2) - \epsilon_{xz}^2 \\ \epsilon_{xy}\epsilon_{xz} - (\epsilon_{yz} + \beta k_z)(\epsilon_{xx} - \beta^2 - k_z^2) \end{pmatrix} \quad (4.25)$$

$$\text{or: } \begin{pmatrix} \epsilon_{xy}(\epsilon_{yz} + \beta k_z) - \epsilon_{xz}(\epsilon_{yy} - k_z^2) \\ \epsilon_{xy}\epsilon_{xz} - (\epsilon_{xx} - \beta^2 - k_z^2)(\epsilon_{yz} + \beta k_z) \\ (\epsilon_{xx} - \beta^2 - k_z^2)(\epsilon_{yy} - k_z^2) - \epsilon_{xy}^2 \end{pmatrix} \quad (4.26)$$

up to a normalisation factor and for the four values of k_z such $\det(M)=0$.

Once \mathbf{E} and the wave vectors are known, results of appendix A are usable and a Jones matrix for the Pockels cell is obtained. In general one has to solve this equation numerically but, under normal incidence (i.e. $\beta = 0$) or for particular static field configurations, solutions of $\det(M)=0$ are analytical. Since our Pockels cell is longitudinal ($\mathcal{E}_x = \mathcal{E}_y = 0$) and the incidence angle is small, analytical expressions can be derived. They are given in the following sections. As the alignment of such a device is also very important, expressions for $\mathcal{E} = 0$ are also given.

¹¹Only the first form was published, and this was the reason of a long standing 'bug' in my numerical programmes. We therefore give the full solution in this document.

4.7.1 Null static field

When $\mathcal{E}_x = \mathcal{E}_y = \mathcal{E}_z = 0$, $\bar{\epsilon}$ is diagonal (see eq. 4.22) and the solutions of $\det(M)=0$ read

$$k_{oz,\pm} = \pm\sqrt{\epsilon_o - \beta^2}, \quad k_{ez,\pm} = \pm\sqrt{\epsilon_o\left(1 - \frac{\beta^2}{\epsilon_e}\right)}$$

where the \pm sign corresponds to the direction of the wave propagation along the z axis.

To determine the directions of the electric vectors, one cannot use the first solution of eq. 4.24 since it vanishes for the extraordinary wave. Using the second solution of eq. 4.25 one gets $\mathbf{E}_{o,\pm}^T = (1, 0, 0)$ and $\mathbf{E}_{e,\pm}^T \propto (0, \beta(k_{ez,\pm}^2 + \beta^2 - \epsilon_e), k_{ez,\pm}(\beta^2 + k_{ez,\pm}^2 - \epsilon_o))$.

For the particular case $\beta = 0$, the crystal is equivalent to an isotropic medium of optical index n_o .

4.7.2 Longitudinal static field

When $\mathcal{E}_x = \mathcal{E}_y = 0$, the solutions for $\det(M)=0$ read

$$k_{1z\pm} = \frac{\pm 1}{4\epsilon_e\sqrt{\epsilon_o}} \left(4\epsilon_o\epsilon_e - \beta^2(\epsilon_o + \epsilon_e) - \sqrt{4\epsilon_o^4\epsilon_e^2r_{63}^2\mathcal{E}_z^2 + \beta^4(\epsilon_o - \epsilon_e)^2} \right) \quad (4.27)$$

$$k_{2z\pm} = \frac{\pm 1}{4\epsilon_e\sqrt{\epsilon_o}} \left(4\epsilon_o\epsilon_e - \beta^2(\epsilon_o + \epsilon_e) + \sqrt{4\epsilon_o^4\epsilon_e^2r_{63}^2\mathcal{E}_z^2 + \beta^4(\epsilon_o - \epsilon_e)^2} \right) \quad (4.28)$$

to second order in β and first order in r_{63} . Expressions for the electric vectors are too long to be reported here.

When $\beta = 0$ and restoring the dimension factor $2\pi/\lambda$, one obtains the following phase shift between the two refracted rays

$$\varphi = e(k_{2z+} - k_{1z+}) = \frac{2\pi}{\lambda} en_o^3 r_{63} \mathcal{E}_z = \frac{2\pi}{\lambda} n_o^3 r_{63} V$$

where e is the KD*P thickness and V is the high-voltage applied on the crystal along the z axis. The two neutral axis are given by eq. 4.24, $\mathbf{E}_{o,\pm}^T = (1, 1, 0)$ and $\mathbf{E}_{e,\pm}^T \propto (-1, 1, 0)$. The usual results [40] are thus recovered.

Bibliography

- [1] R.M.A. Azzam and N.M. Bashara, *Ellipsometry and polarized light* (Amsterdam, North-Holland, 1977).
- [2] G. Bardin et al., “Conceptual design report of a Compton polarimeter for Cebaf Hall A” (1996). Document available on www.cebaf.gov/Compton.
- [3] R.C. Jones, ‘A new calculus for the treatment of optical systems. VII. Properties of the N-Matrices’, J. Opt. Soc. Am. (1948) 671. See table I in particular.
- [4] D.G. Drummond, ‘The infra-red absorption spectra of quartz and fused silica from 1 to $7.5\mu\text{m}$. II-experimental results’, Proc. R. Soc. Lond. 153 (1936) 328.
- [5] M. Kremers and H. Meekes, “The interpretation of HAUP measurements: a study of the systematic errors”, J. Phys. D: Appl. Phys 28 (1995) 1195; C.L. Folcia, J. Ortega and J. Etxebarria, “Study of the systematic errors in HAUP measurements”, J. Phys. D: Appl. Phys 32 (1999) 2266.
- [6] J.F. Nye, *Physical properties of crystals*, Oxford Science Publications 1985.
- [7] R.B. Sosman, *The properties of Silica* (Chem. Catalog Co., New-York 1927).
- [8] H.A. Lorentz, “Double refraction by regular crystals”, Proc. R. Ac. Amst., 24 (1921) 22.
- [9] J. Pastrnak and K. Vedam, “Optical anisotropy of silicon single crystals”, Phys. Rev. B3 (1971) 2567.
- [10] M.J. Gunning and E.R. Raab, “Electric-field-induced optical activity in nonmagnetic crystals”, J. Opt. Soc. Am. B 14 (1997) 1692.; E.B. Graham and R.E. Raab, “Light propagation in cubic and other anisotropic crystals”, Proc. R. Soc. Lond. A430 (1990) 593; E.B. Graham, J. Pierrus and R.E. Raab, “Multipole moments and Maxwell’s equations”, J. Phys. B25 (1992) 4673.
- [11] M. Born and E. Wolf, *Principles of Optics* (Pergamon Press, third edt. 1965).
- [12] E.R. Raab and J.H. Cloete, “An eigenvalue theory of circular birefringence and dichroism in a non-magnetic chiral medium”, J. Electr. Waves Appl., 8 (1994) 1073.
- [13] C. Chou, Y.C. Huang and M. Chang, “Effect of elliptical birefringence on the measurement of the phase retardation of a quartz wave plate by an heterodyne polarimeter”, J. Opt. Soc. Am. A, 14 (1997) 1367.

- [14] A.A. Maradudin and D.L. Mills, ‘Scattering and absorption of electromagnetic radiation by a semi-infinite medium in the presence of surface roughness’, Phys. Rev. B 11, 1392-1415 (1975). Usefull formula are given in the appendix of this article.
- [15] M. O’Donoghue, *Quartz* (Butterworths Gem Books, London 1987).
- [16] A. Carvallo, “Recherche sur la dispersion infra-rouge du quartz”, *Compte Rendus* 126 (1896) 728.
- [17] F. Paschen, “Über die dispersion des quartz im ultrarot”, *Ann. Physik* 35 (1911) 1005.
- [18] J.H. Shields and J.W. Ellis, “Dispersion of birefringence of Quartz in the near infrared”, *J. Opt. Soc. Am.* 46 (1956) 263.
- [19] *Hanbook of optics* (Mc Graw-Hill, New-York, 1978).
- [20] *American institute of physics hanbook* (Mc Graw-Hill, New-York, third etd. 1982).
- [21] T. Toyoda and M. Yabe, “The temperature dependence of the refractive indices of fused silica and crystal quartz”, *J. Phys. D16* (1983) L97.
- [22] S.M. Etzel, A.H. Rose and C.M. Wang, “Dispersion of the temperature dependence of the retardance in SiO₂ and MgF₂”, *Appl. Opt.* 39 (2000) 5796.
- [23] *Handbook of optics, Vol. II* (Mc Graw-Hill, New-York, 1995).
- [24] J. Fichou Optique de precision, www.optiquefichou.fr.
- [25] P.D. Hale and G.W. Day, “Stability of birefringent linear retarders (waveplates)”, *Appl. Opt.* 27 (1998) 5146.
- [26] J.M. Bennett and L. Mattson, *Introduction to surface roughness and scattering*, (Opt. Soc. Am., Washington D.C., second edition 1999).
- [27] D.A. Bolon and C.O. Kunz, “Ultraviolet Depolymerization of photoresist polymers”, *Polym. Eng. Sci.* 12 (1972) 109.; R.R. Sowell et al., “Surface cleaning by ultraviolet radiation”, *J. Vac. Sci. Technol.* 11 (1974) 474.
- [28] J.M. Bennett et al., “Scanning force microscope as a tool for studying optical surfaces”, *Appl. Opt.* 34 (1995) 213.
- [29] *Surface contamination, genesis, detection and control*, Vol. I and II, K.L. Mittal Editor (Plenum Press, New-York 1979).
- [30] J. R. Vig and J. W. Le Bus, “UV/Ozone cleaning of surfaces”, *IEE Trans. Parts, Hyb. and Pack.* 12 (1976) 365.
- [31] See for ex.: A. Alvarez-Herrero et al., “Absorption of water on porous vycor glass studied by ellipsometry”, *Appl. Opt.* 40 (2001) 527.

- [32] See for ex.: T.A. Germer, “Angular dependence and polarization of out-of-plane optical scattering from particulate contamination, subsurface defects, and surface microroughness”, Appl. Opt. 36 (1997) 8798.
- [33] J. Kobayashi and Y. Uesu, “A new optical method and apparatus “HAUP” for measuring simultaneously optical activity and birefringence of crystals. I. Principle and construction ”, J. Appl. Cryst. 16, 204-211 (1983). For an historical review see: J.R.L. Moxon and R. Renshaw, “The simultaneous measurement of optical activity and circular dichroism in birefringent linearly dichroic crystal sections: I. Introduction and description of the method”, J. Phys.: Condens. Matter 2, 6807-6836 (1990).
- [34] J. Poirson et al., “Jones matrix of a quarter-wave plate for Gaussian beams”, Appl. Opt. 34, 6806-6818 (1995).
- [35] G. Eppeldauer and J.E. Hardis, “Fourteen-decade photocurrent measurements with large-area silicon photodiodes at room temperature”, Appl. Opt. 30 (1991) 1.
- [36] G. Eppeldauer, “ Near infrared radiometer standards”, SPIE Proceedings, 2815 (1996) 42.
- [37] G. Eppeldauer, ‘Temperature monitored/controlled Silicon photodiodes for standardization’, SPIE Proceedings, 1479 (1991) 11.
- [38] P. Puzo, private communication.
- [39] M. Jacquet, private communication.
- [40] S. Huard, *Polarisation de la lumière* (Masson, Paris, 1993).
- [41] S-M. Nee, “Error analysis of null ellipsometry with depolarization”, Appl. Opt. 38, 5388-5398 (1999).
- [42] S-M. Nee et al., “Characterization for imperfect polarizers under imperfect conditions”, Appl. opt. 37,54-64 (1998).
- [43] From Marie Jacquet-Lemire.
- [44] CERN library program, Long Writup.
- [45] See Annexe B of, D. Chauvat, *Innovation et optimisation de polarimétrie pompe-sonde avec des faiceaux impulsionnels en vue de la mesure précise de violation de parité dans l’atome de césium*, Ph.D. Thesis (Université Paris-11, 1998).
- [46] J.R. Zeidler et al., “Beam deviation errors in ellipsometric measurements; an analysis”, Appl. Opt. 13 (1974) 1938.
- [47] A. Yariv, *Quantum Electronics*, (J. Wiley and sons, Inc., New-York, 2nd edt. 1998).
- [48] T.A. Maldonado and T.K. Gaylord, “Electrooptic effect calculations: simplified procedure for arbtrary cases”, Appl. Opt. 27 (1988) 5051.
- [49] E. M. Meintjes and R. Raab, “A new theory of Pockels birefringence in non-magnetic crystals”, J. Opt. A: Pure Appl. Opt. 1 (1999) 146

- [50] P. Yeh, “Electromagnetic propagation in birefringent media”, J. Opt. Soc. Am. 69, 742-756 (1979); P. Yeh, “Optics of anisotropic layered media: a new 4×4 matrix algebra”, Surf. Sci. 96, 41-53 (1980).

Chapter 5

Results of the operation of a test cavity and of the final cavity

A test cavity, together with a simplified optical scheme was successfully operated for one year starting in September 2001. The final cavity was tested and operated at Orsay from December 2002 to February 2003 and finally installed in the HERA beam pipe during Spring 2003.

Our main experimental results concerning the laser/cavity coupling and of the cavity locking operation are described in this chapter.

5.1 Setup of the test cavity

To test the principle of a 2 m long confocal monolithic cavity with mirrors mounted on the optical table, a test cavity has been designed and constructed in the L.A.L workshop. It consists in a stainless steel cylindrical vessel mounted on two legs such that the cylinder axis lies at 32 cm above the table, just like the final cavity. It is shown in fig. 5.1. Unlike the final cavity, the optical and geometrical axes are horizontal and the vessel only contains the two cavity mirrors (i.e. no piece of beam pipe). In addition, the vessel is rigidly fixed to the optical table which is itself not isolated from the ground.

The vacuum is obtained in three stages via a primary pump, a turbo pump and for permanent operations, one ionic pump. We obtained a residual pressure of 10^{-9} Torr and thus fit the HERA requirements. Vacuum windows are similar to those used for the final cavity.

This test cavity also allowed us to study the geometrical alignment of the two cavity mirrors. This was done using a red HeNe laser (see fig.5.2) together with a set of diaphragms. We used an autocollimation method. First, two collimators were located at the entrance and at the output of the cavity to define the cavity *geometrical axis*. The HeNe laser beam was next aligned along this axis and additional collimators were located inside the cavity to replace the cavity mirrors. Once the cavity mirror mounts were aligned onto the *geometrical axis*, now defined by the the HeNe laser beam, the diaphragms were removed and the cavity mirrors were installed (under a class 10 air flow). To align the cavity mirrors onto the *geometrical axis* the reflections of the red laser light on the cavity mirrors were matched to the incident laser beam (by moving the cavity mirrors). We typically achieved a 1 mrad, 1 mm precision after this procedure. For the alignment of

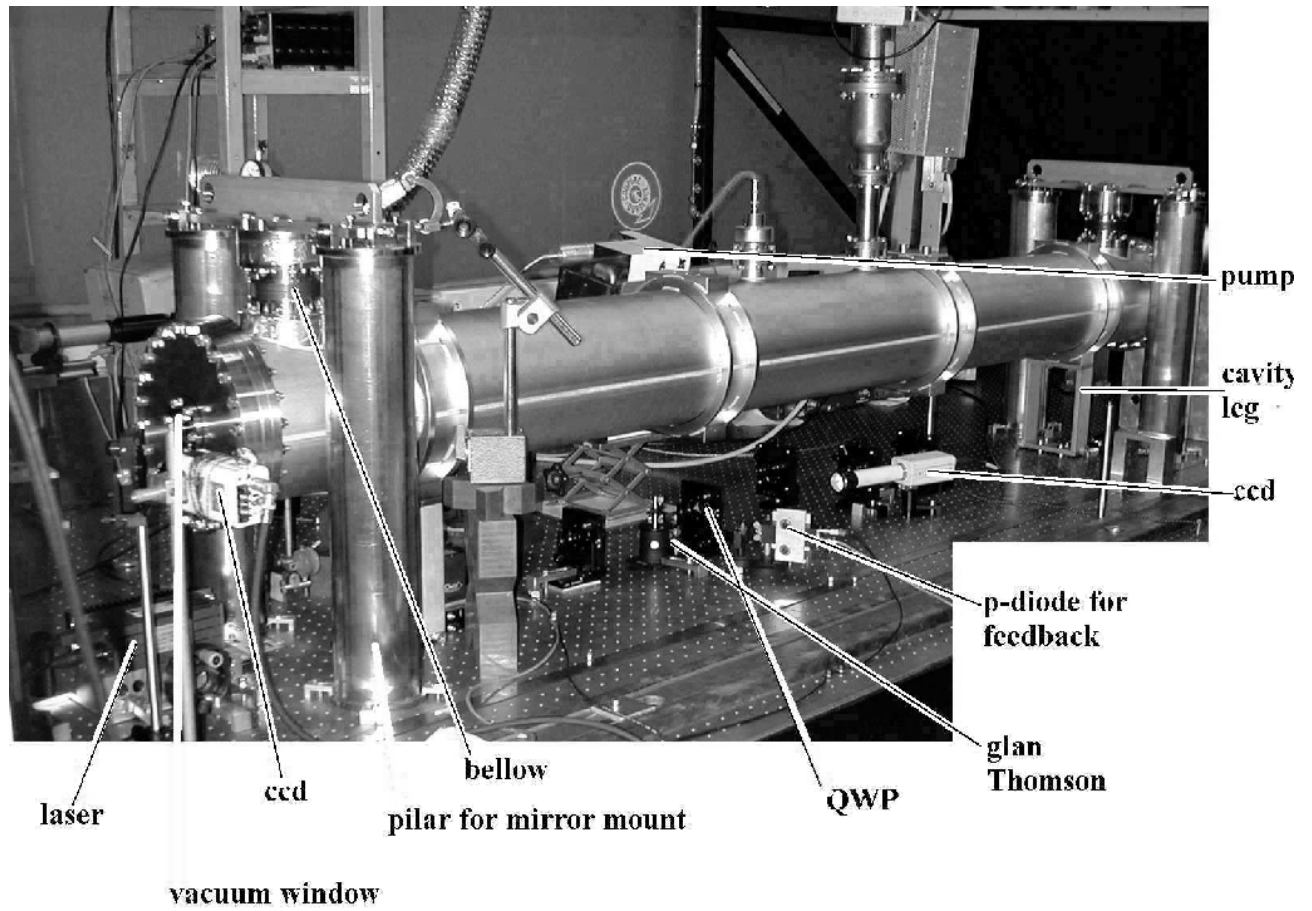


Figure 5.1: Picture of the test-cavity setup at Orsay. Also indicated are some of the optical elements.

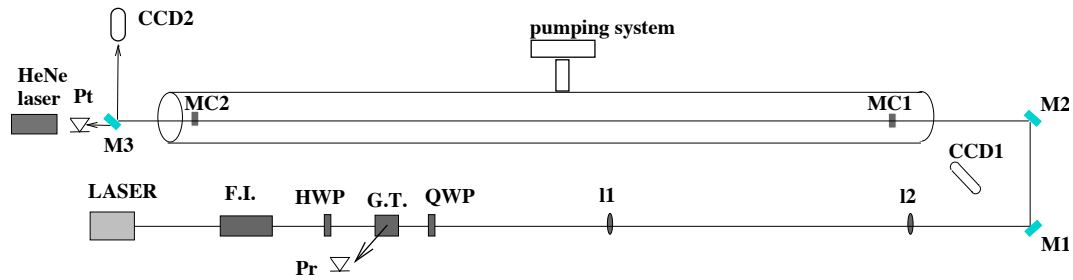


Figure 5.2: Optical scheme of the test cavity set-up. The HeNe red laser is used to align the two cavity mirrors MC1 and MC2 with respect to each other. The mirror M3 and the photodiode Pt are removed during this geometrical alignment.

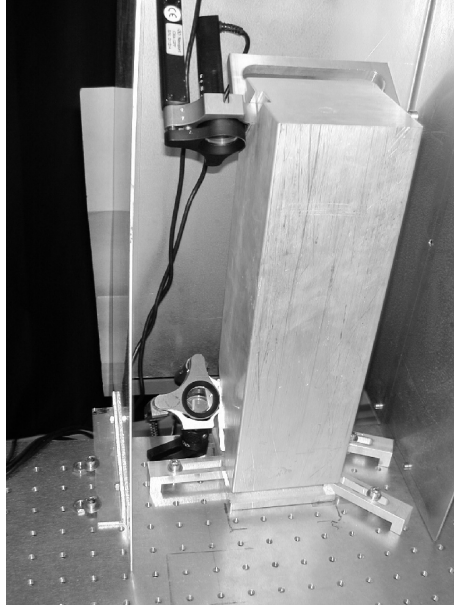


Figure 5.3: *Aluminium pillar and the two motorised mirrors M1 and M2 of the test cavity setup.*

the final cavity, this procedure has been simplified (see chap. 3).

The main problem with the cavity test was that the cavity mirrors couldn't be moved around the vertical axis from outside. We had to open the cavity and carefully move the mirror mounts by hand under a class 10 air flow. This was a painful and a time consuming operation and this pushed us to find another mechanical solution for the final cavity (see chap. 3).

The optical scheme of the test cavity is shown in fig. 5.2. The differences between the final scheme described in chap. 3 are: a QWP instead of a Pockels cell is used to circularly polarise the laser light; two lenses, instead of three and two motorised mirrors (M1 and M2) are used instead of the four mirror scheme (we were not interested to the light polarisation transport for this test setup).

The Cebaf scheme is used to pick-up the beam reflected by the cavity (i.e. for the feedback): a Glan-Thomson prism followed by a QWP (the principle is illustrated in fig. 5.4). Although this scheme also acts as a first stage isolation for the laser (the second stage being the Faraday isolator), it has the disadvantage of providing a reflected signal level dependent on the laser light polarisation. As a result, replacing the QWP by a Pockels cell and next changing its polarity (or reducing its power supply towards zero) we couldn't keep the cavity locked. This is the reason why we finally used another scheme – described in chap. 3 – to extract the reflected signal independently of its polarisation.

5.2 Laser beam/cavity coupling

The main goal of the cavity test operations was the study of the laser beam/cavity couplings. That is:

- the spatial mode matching.

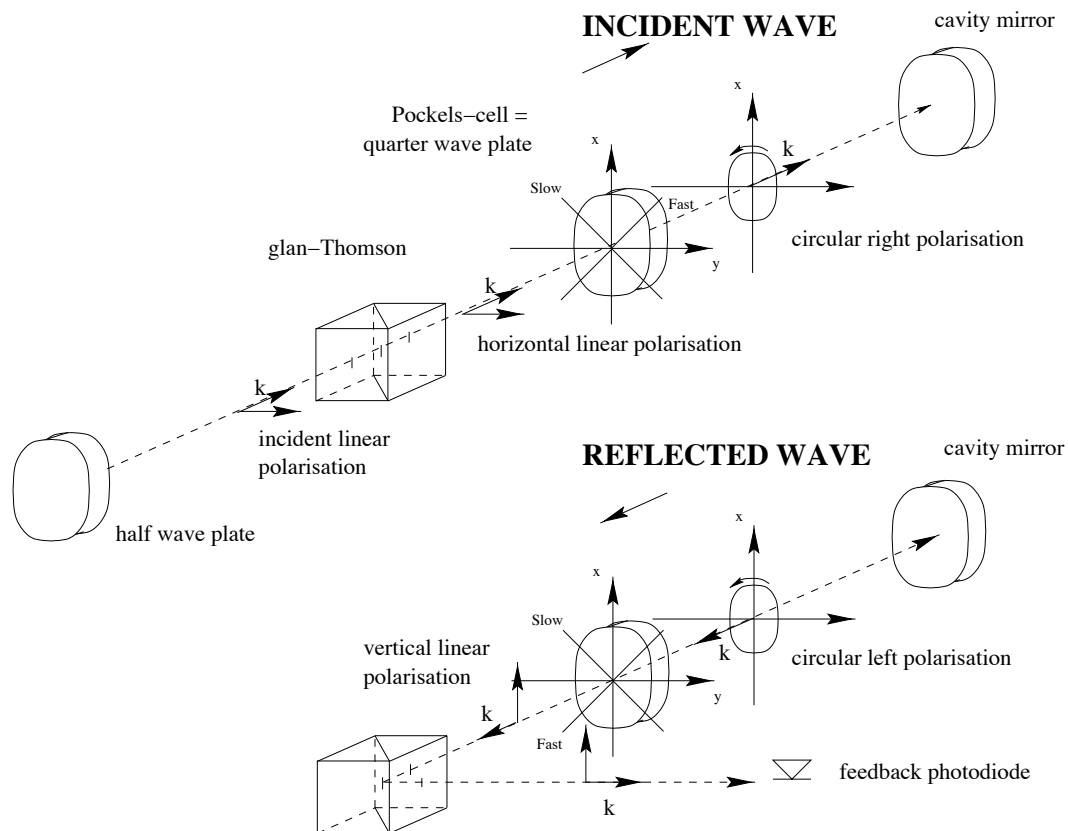


Figure 5.4: Comparison of the incident and reflected light passes in the optical scheme. This figure illustrates how the reflected beam is extracted to perform the laser beam frequency feedback corrections. From [1].

- the phase matching, that is the operation of the locking feedback system;

The latter topic is reported in the next section, we shall concentrate here on the former topic.

Once the cavity mirrors are geometrically aligned (see section 5.1), the laser beam axis and the cavity optical axis (see Appendix 3.7.3) must be aligned in order to provide the laser/cavity mode matching. There exist automatic procedures [2, 3] to perform such an alignment. The principle is to reduce the couplings to the higher transverse mode, which are the signatures of misalignments, by making use of the Guoy phase differences between the fundamental and these higher order modes. However, these procedures already assume that the cavity is “almost” well aligned so that only couplings to the first two higher order modes are considered. In practice, one has to start from a completely misaligned system and, in our case, a small residual misalignment leads just to a small decrease of the power inside the cavity. Clearly, we can live with a small loss of a few percent in our experiment so that the automatic procedures cited above are too sophisticated. We shall therefore use a much simpler method, as described below.

When the cavity mirrors are geometrically aligned, misalignments between the optical and geometrical axes of the cavity are given by the mechanical tolerances (1 mrad and 1 mm, see section 5.1). At this stage, the incident laser beam is also aligned using the HeNe laser beam so that the laser/cavity optical alignment is of the same order.

In contrast to what is done in section 3.7.3 of chap. 3, we must compute here (numerically) the exact couplings of the laser Gaussian mode to the cavity Hermite-Gauss modes¹ in order to model our misaligned cavity. For an angular shift $\Delta\alpha_x = 1$ mrad and an axial shift $\Delta x = 1$ mm ($\Delta\alpha_y = 0$ and $\Delta y = 1$) which correspond to the mechanical tolerances, we obtain the result shown in fig. 5.6. In this example, a large number of modes are excited and the distribution is centred on the 5th order mode. The coupling to the fundamental mode is very small so that only excited modes are visible. A typical excited mode, measured after the cavity with a CCD camera is shown in fig. 5.5.

In figs. 5.1 and 5.7 numerical calculations of the average excited mode, the dispersion and the maximum coupling are shown as a function of the angular misalignment. From these figures, one can see that: the more the cavity is misaligned, the larger the number of excited modes and the smaller the coupling to each of these modes.

To perform the laser/cavity optical alignment, the two mirrors M1 and M2 of fig. 5.2 are motorised (two stepper motors per mirror, see fig. 5.3). To move the mirror M1 and M2, a Labview procedure has been written [4]. The principle is the following: once the position of the mirrors and the laser beam impact on M1 are determined (with a typical accuracy of ≈ 0.1 mm and 1 mrad) the four mirror displacements are transformed into the four degrees of freedom of the laser beam axis displacements in a given plane along the laser beam propagation axis. These degrees of freedom are: the spatial x , y intersection coordinates of the laser beam axis with the reference plane and the corresponding angular inclinations α_x and α_y (the z axis being defined by the cavity geometrical axis).

In practice we therefore proceed as follows:

- we choose the plane of reference on the entrance cavity mirror MC1 (see fig. 5.2).

¹Here we forget about the diffractive nature of our laser beam. As mentioned latter in this chapter, we shall take diffraction into account in the near future.

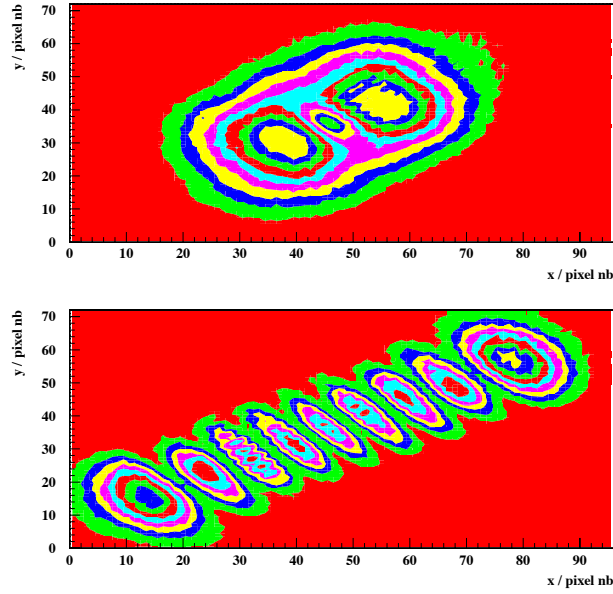


Figure 5.5: Two examples of excited modes measured after the cavity using a CCD camera: most likely TEM01 (upper plot) and TEM08 (lower plot) modes.

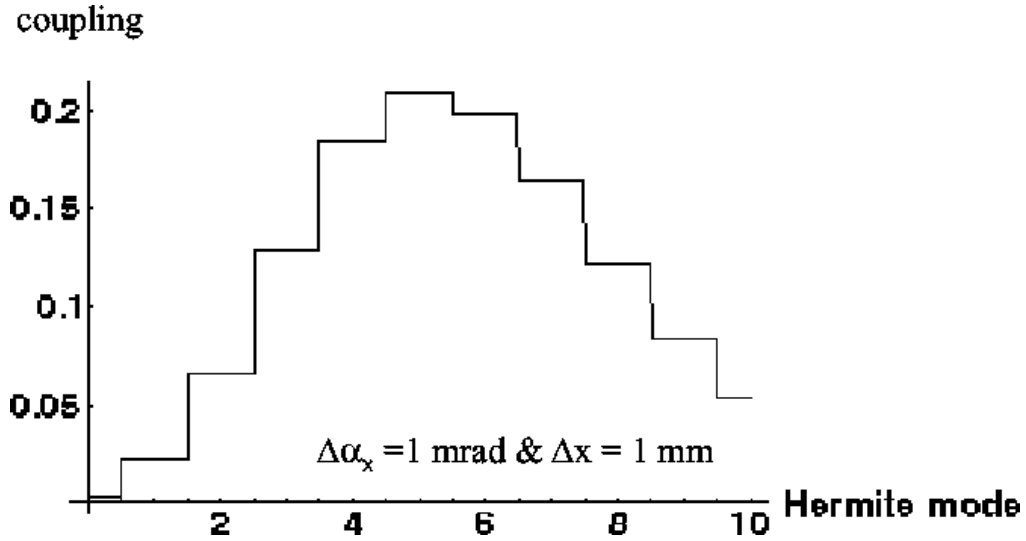


Figure 5.6: Numerical calculation of the coupling of the Gaussian laser beam to the cavity Hermite-Gauss eigen-modes as a function of the mode order for the faults indicated in the plot. The cavity and laser beam waists are assumed to be perfectly matched.

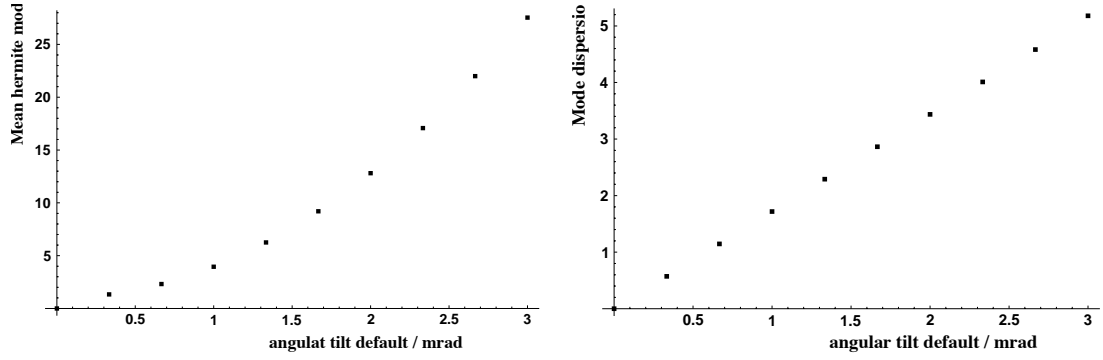


Table 5.1: *Left plot: numerical calculation of the mean value of the distribution of the excited Hermite-Gauss modes as a function of a single angular misalignment. Right plot: numerical calculation of the root mean square of the distribution of the excited Hermite-Gauss modes as a function of a single angular misalignment.*

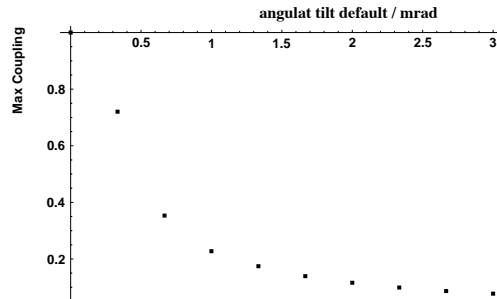


Figure 5.7: *Numerical calculation of the maximum coupling to the excited Hermite-Gauss modes as a function of a single angular misalignment.*

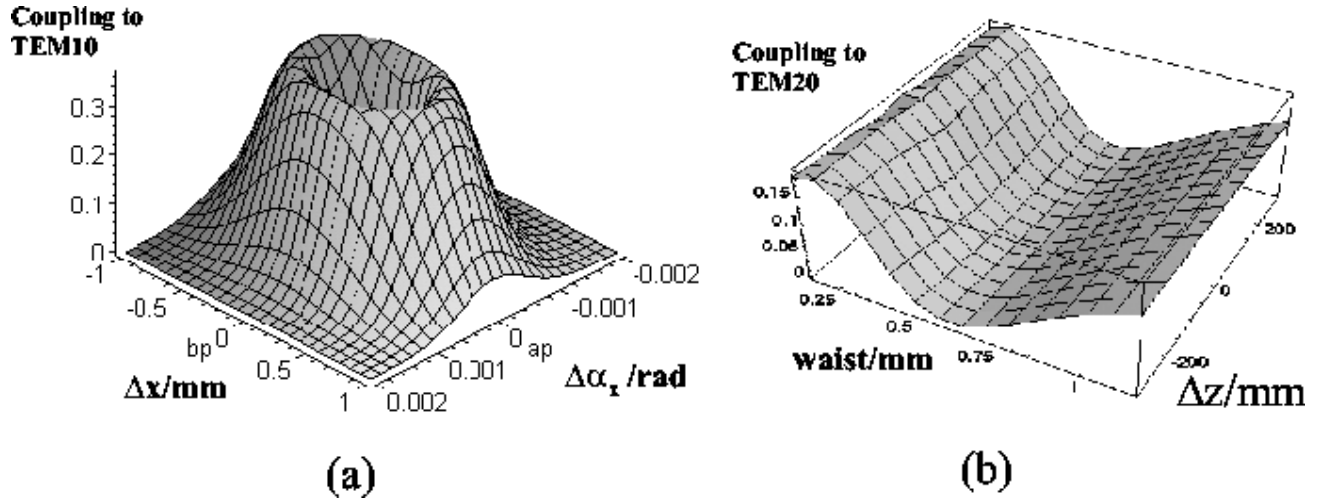


Figure 5.8: Numerical calculation of: (a) the coupling to the TEM01 mode as a function of the angular and axial shift faults; (b) the coupling to the TEM02 mode as a function of the laser beam waist value and location. $z = 0$ is taken at the centre of the cavity.

- Using the camera CCD1 (see fig. 5.2) we match spatially the incident and reflected beams by looking at the light diffusion on the mirror M1. To do so, with our choice for the reference plane, we just have to vary α_x and α_y . This matching is nothing but the normal incidence alignment of the laser beam on MC1 which is anyway mandatory because of the mirror sphericity. The matching accuracy is given by the laser beam spot sizes on M1 (≈ 1 mm) and by the distance of M1 from MC1 (≈ 1 m), that is ≈ 0.5 mrad. This is enough at this step of the alignment procedure. CCD pictures of a slightly misaligned beam are shown in fig. 5.5.
- a 10 V peak-peak ramp is applied piezo transducer acting on the laser crystal (laser fast channel). The number and the level of the cavity modes are controlled by the photodiode Pt and by the camera CCD2 (see fig. 5.2). A typical oscilloscope view is reported in fig. 5.9 and a TEM01 mode measured by CCD2 is shown in fig. 5.5.
- We change x and y (and then α_x and α_y to keep the normal incidence) to minimise the number of modes observed with Pt. Our criterion is to minimise the number of maxima seen in CCD2 while maximising the highest intensity peak as measured with Pt.

When the alignment is nearly good, one must carefully check with CCD2 that one effectively maximises the fundamental mode and not the TEM10 (there is a position for which the TEM10 coupling is maximum, see fig. 5.8(a)).

Once an “almost good alignment” is reached, the cavity is locked on the fundamental mode and a fine adjustment is performed to maximise the signal measured by Pt².

²The cavity stays locked even when the necessary backlash correction is applied to the stepper motor movement control (this effect is due to the finite step size of the stepper motor screw. The correction simply consists of adding a finite $+5\mu\text{m}$ step to each movement so that the motor stops always on the same side of the screw steps).

The whole procedure takes about an hour and leads to a stable alignment in a thermally controlled room.

The two lenses $l1$ and $l2$ (see fig. 5.2) are used to adjust the laser beam waist to the cavity waist at the centre of the cavity. Because of the cavity geometry, the power loss through the coupling to the TEM₂₀ mode is low as shown in fig.5.8(b) (see also Appendix 3.7.3). A fine tuning of the lens positions is then not required.

Finally, we mentioned in section 3.3.1 that our laser beam exhibits a diffraction pattern (see fig. 3.17). This is obviously not the case after the cavity since only the fundamental mode is transmitted. We measured the beam intensity after the cavity and observed a beautiful Gaussian (see fig. 5.10). By verifying the propagation of this Gaussian beam we deduce that there is no noticeable diffraction inside the cavity.

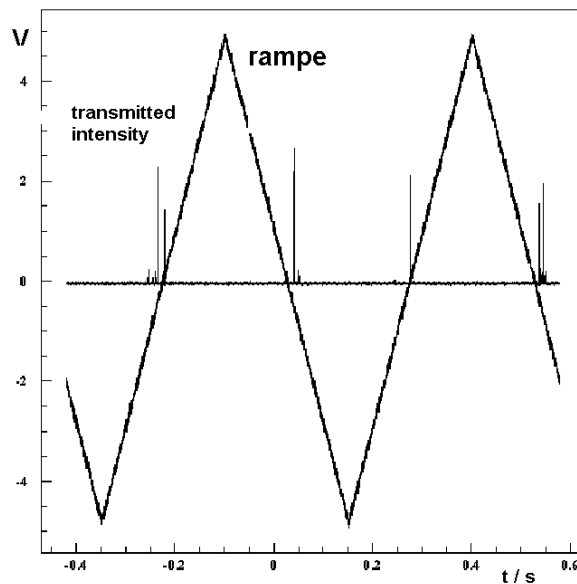


Figure 5.9: 10 V peak-peak ramp together with the transmitted signal measured by the photodiodes Pt . The later signal has been scaled by an arbitrary factor for this plot. The peaks correspond to cavity resonances. Away from the cavity resonance frequencies, the transmitted signal vanishes (this is a DC oscilloscope view).

5.3 Feedback operations and cavity gain performance

The feedback electronics has been successfully operated for both the test and final cavities. The locking is quite stable when the “room” temperature is stable. For example, we once kept the cavity locked for 12 hours at HERA and during that time we lost the locking only once. With the automatic procedure the locking was recovered after a few minutes. Note that the HERA tunnel is noisy because of water cooling of the beam pipe and electron cavities (we measured an acoustic noise of frequency ≈ 3 kHz around the cavity, both with an accelerometer and a microphone).

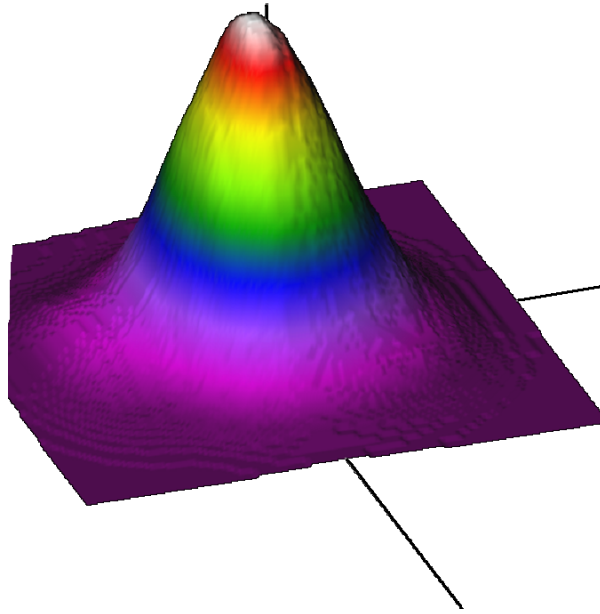


Figure 5.10: *Measurement of the beam intensity after the cavity.*

However, when operating the Pockels cell with zero voltage and with only one Faraday isolator we hardly succeeded in locking the final cavity (it was only possible after a fine tuning of the Faraday isolator alignment). Then once locked we observed a noisy transmitted signal and finally the loss of the locking after ≈ 2 h. Since temperature was also varied during this operation (by $+1.5$ K) we attributed this instability to the variation of the Verdet constant with temperature [5]³ and therefore to a decrease of the laser isolation (see chap. 3). We introduced a second isolation stage (Isowave 40 db Faraday isolator) to avoid this problem.

One important feature of resonators is the spectral response. We checked that spectral characteristics of our cavity and the Cebaf's one are similar (for a complete study, see again ref. [1]). Here we only report on the spectral transfer function measurement. When the cavity is locked, a periodic perturbation is sent to the fast channel of the laser by a spectrum analyser. Spectral densities of the reflected and transmitted signals are then computed⁴ by the same device as a function of the perturbation's frequency. The ratio of the transmitted to reflected power densities is the cavity transfer function. It is shown in fig. 5.12 and it has the characteristic behaviour of a low pass filter, as expected. At Orsay, the table was not isolated from the ground and the locking was lost once or twice per hour. This is consistent with the role of low pass filter played by the cavity (ground vibrations were, most likely, more important at Orsay).

³The change of the light polarisation is proportional to the length of the TGG crystal, the magnetic field surrounding the crystal and the Verdet constant which describes the rotation power of the crystal.

⁴The spectral density of a signal is just the squared modulus of its Fourier transform. It gives access to the distribution of the various harmonics constituting this signal.

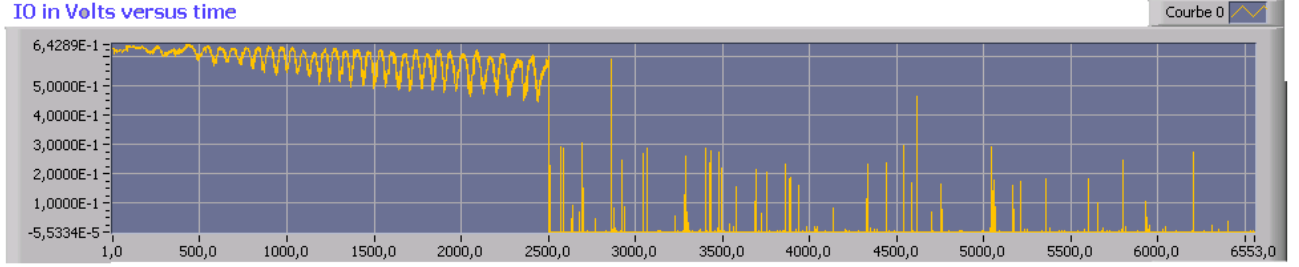


Figure 5.11: Measurement of the intensity transmitted by the cavity as a function of time (arbitrary units, the full measurement time is around six hours). At the origin of the abscissa the cavity is locked and one can see the signal becoming noisier as time increases. The locking break appears at $t = 2500$ a.u (approximately 2 h) and the peaks observed afterwards correspond to cavity resonances (the feedback was in open-loop mode).

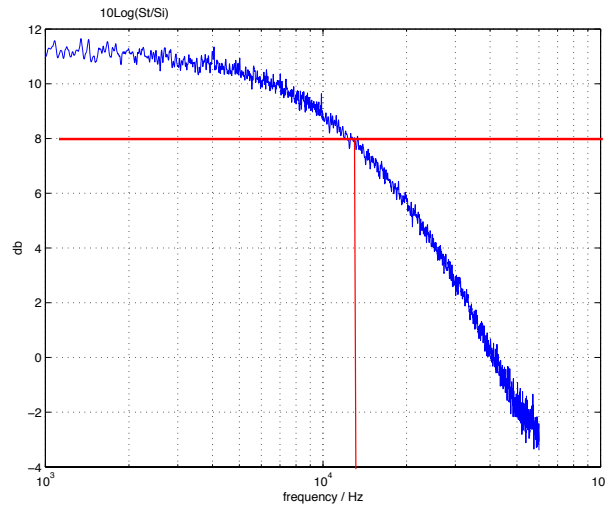


Figure 5.12: Transfer function of the cavity. This measurement was performed on the low finesse test cavity at Orsay.

5.3.1 Estimate of the cavity gain

To estimate the gain of a Fabry-Perot cavity one measures the cavity finesse. There are various ways to perform this measurement (see ref. [1] for an overview) to perform this measurement. They all rely on “external” information (it is obviously impossible to measure the power inside the cavity). The simplest method is the measurement of the cavity decay time: we first lock the cavity, next we switch off the laser pumping diode and record the transmitted power. This power decreases exponentially towards zero and the time constant is proportional to the finesse: the larger the finesse, the higher the time constant. It can be shown [1] that, for high finesse,

$$F \approx \frac{\pi c \tau}{L}$$

where τ is the time constant, L is the cavity length and the c is the velocity of light.

Fig. 5.13 shows a decay time measurement performed on the cavity installed at HERA. From an exponential fit, we find

$$\tau \approx 62 \mu s \Rightarrow F \approx 29000, FWHM \approx 3 \text{ kHz}, G_{max} \approx \frac{F^2}{\pi^2 \tau} \approx 9000,$$

with G_{max} the maximum gain of the cavity.

This high finesse was measured at the first step in the installation at HERA in April 2003. We repeated this measurement after connecting the cavity with the HERA beam pipe vacuum and at the end of the shutdown in July 2003 and measured the same finesse.

We also performed this measurement on the test cavity at Orsay. At that time we tried to understand why the finesse was lower than expected. Since the decay time was smaller, we had to determine the decay time of the input laser (when we switch off the pumping diode, the laser beam power is not switched off instantaneously) by simply measuring the laser beam power on one side of the Glan-Thomson prism (see fig. 5.13). The convolution of two exponentials led to $\tau \approx 30 \mu s$, $F \approx 15000$ and $FWHM \approx 6 \text{ kHz}$ ⁵. Note that various estimates of the cavity finesse agreed for our low finesse cavities.

To check the decay time method, we also performed an analysis of the shape of the reflected and transmitted signals. Following [1], we calculate the variations of these signals as a function of time when the 10 V peak-peak ramp is supplied on the laser fast channel. Because of this ramp, the laser beam frequency changes continuously. Therefore, when a cavity resonance frequency is crossed, the plane waves stored inside the cavity have various wavelengths and a time interference pattern is observed (see fig. 5.14).

To model the signals of fig. 5.14, it is actually possible to compute numerically such a plane wave superposition [1]. But for a high finesse cavity (i.e. high mirror reflectivities) this superposition consumes too much computer time for it to be useful for a fitting procedure. A simplified formulation of the problem was fortunately derived in ref. [6] leading to reasonably fast numerical computations. In this calculation, the main parameters are the ramp’s slope and frequency (a few Hertz), the piezo conversion factor (around 4 MHz/V) and the cavity finesse. This fit describes accurately the signals emitted

⁵The FWHM number can also be obtained from fig. 5.12: the frequency cut of a low pass filter corresponds to a decrease of 3 db from the plateau. It can be shown that [1] the frequency cut is at half of the FWHM. In our example, we obtain $FWHM \approx 24 \text{ kHz}$, i.e. $F \approx 4000$. This was our first bad finesse cavity (cavity mirrors and mirror alignment were changed a few times during our test period).

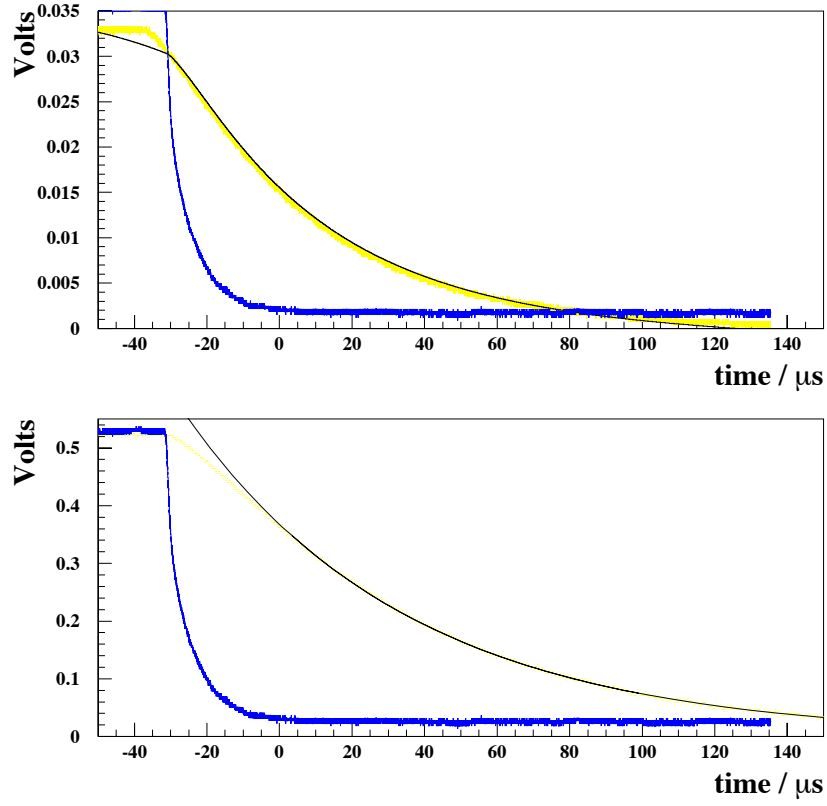


Figure 5.13: Decay time of the cavity (yellow) and of the laser (blue). Top plot: low finesse cavity, the black curve shows a convolution of two exponentials (one for the laser decay time and one for the cavity). Bottom plot: same signals but for the high finesse cavity.

by the low finesse test cavity (fig. 5.14) but not by the high finesse cavity (fig. 5.15). In the latter case, the best fit gives $F \approx 20000$ and that is a result significantly different of the one obtain from the cavity decay time.

By playing with the model, i.e adding a non-linear variation of the laser beam frequency or going back to the plane wave superposition calculation, didn't increase significantly the fit quality. The only phenomenon which has a noticeable impact is the laser beam linewidth [7, 8]: assuming that the laser beam frequency spectrum is a Lorentzian of a few kHz width we obtain the fit result shown in fig. 5.16. As a result, the finesse determined from this fit is in agreement with the cavity decay time. Note that a better fit could be obtained by considering a random phase emission instead of a Lorentzian spectrum [9] which is in fact a kind of average description.

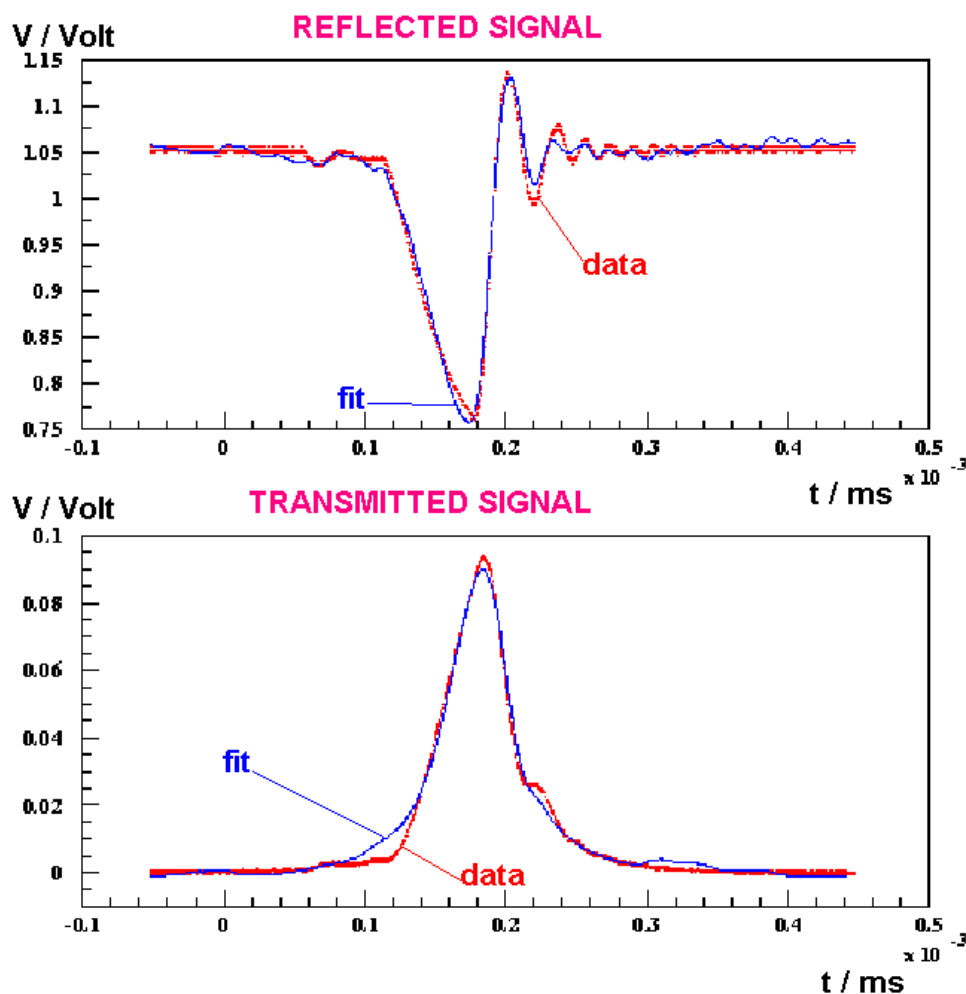


Figure 5.14: *Reflected and transmitted signals in the vicinity of a cavity resonance when the 10 V peak-peak ramp is supplied on the laser fast channel. The data were taken on the low finesse test cavity. Also shown is the fit result described in the text. The model used for the fit does not include the laser beam linewidth. From [9].*

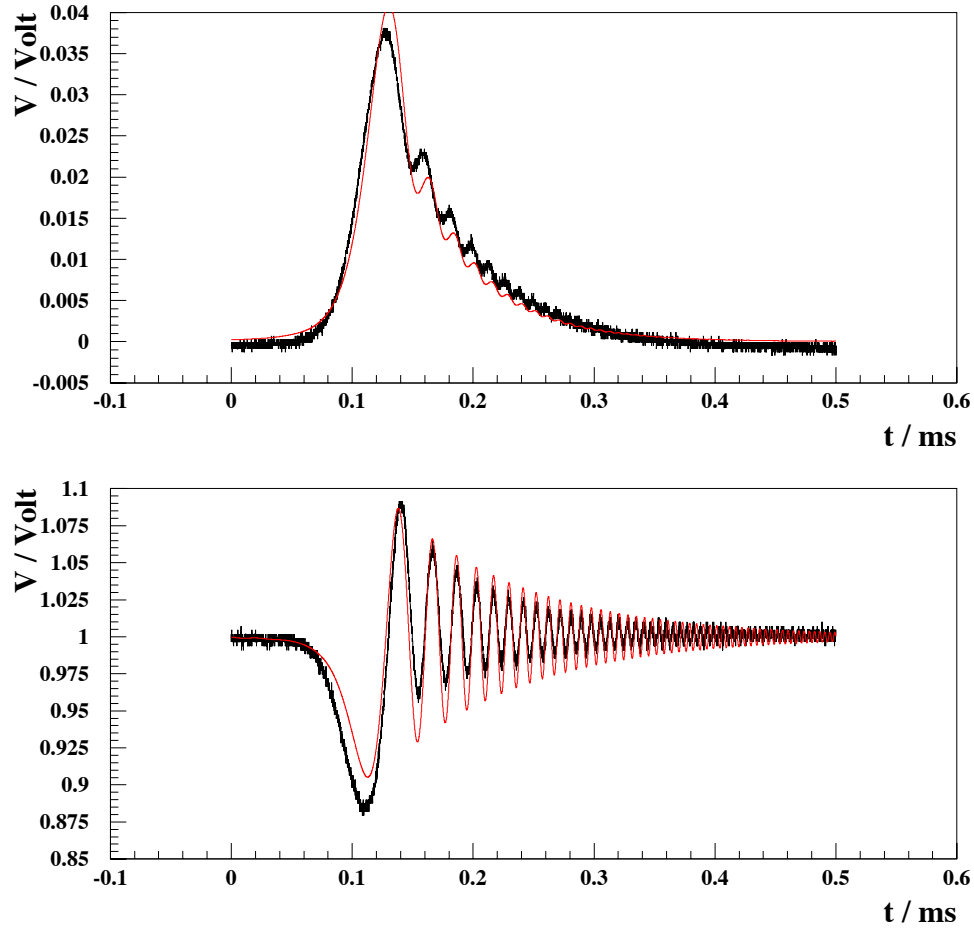


Figure 5.15: *Transmitted (top) and reflected (bottom) signals in the vicinity of a cavity resonance when the 10 V peak-peak ramp is supplied on the laser fast channel. The data were taken on the high finesse cavity. Also shown is the fit result described in the text. The model used for the fit does not include the laser beam linewidth. From [9].*

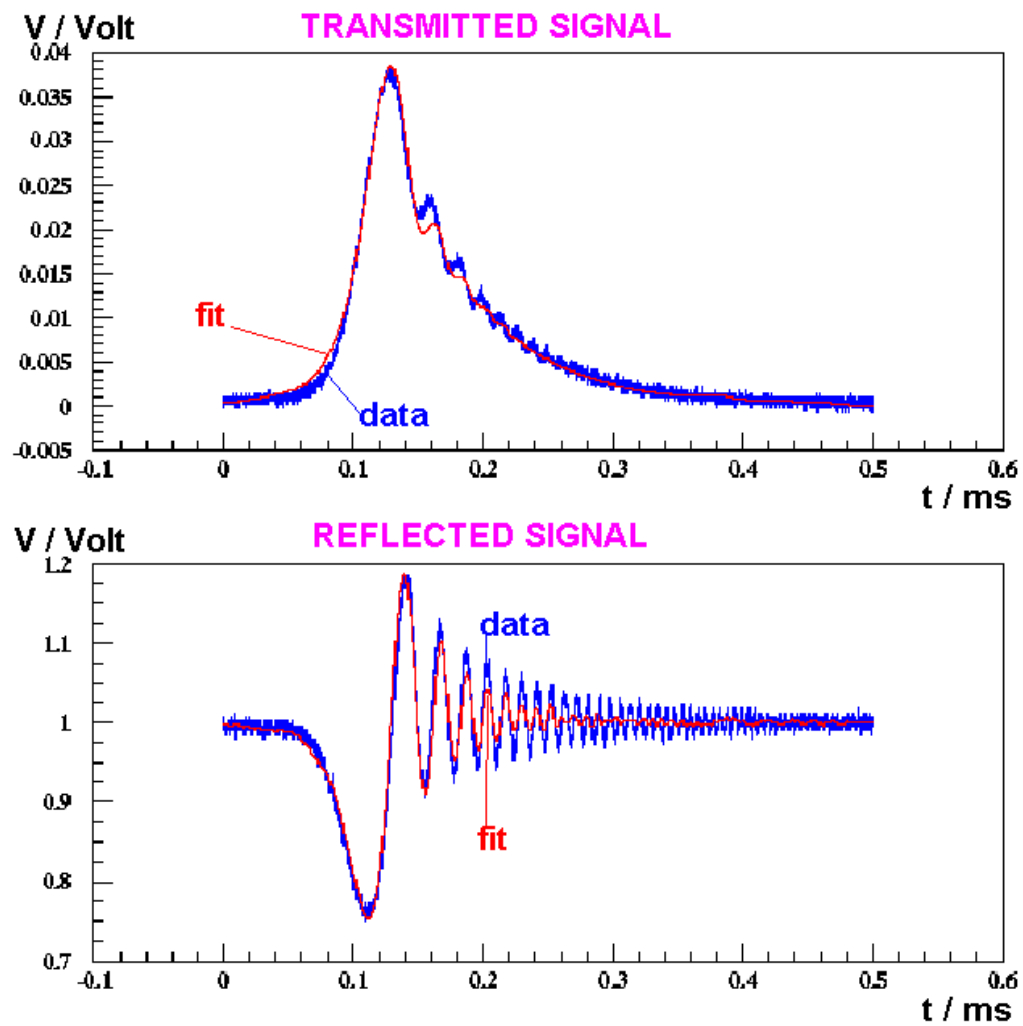


Figure 5.16: Same as fig. 5.15 but taking into account the laser beam linewidth. From [9].

This observation gives a hint to another problem: even after a quasi-perfect laser/cavity alignment⁶, it has never been possible to couple all the incident laser beam power to the final cavity: our best observation was $\approx 70\%$. It can be shown that when the cavity is locked, the reflected intensity is reduced ideally by a factor $F^2(D + A)^2/\pi^2$ with D and A the mirror coating's diffusion and absorption coefficients. With the numbers given in appendix 3.7 of chap. 3, one expects $F^2(D + A)^2/\pi^2 \approx 0$ whereas we never measured something less than 0.3.

As we mentioned in chap. 3, the laser beam is not perfectly Gaussian. Hence, a perfect laser/cavity coupling is not expected but this cannot explain why we can only couple $\approx 70\%$ of the incident laser beam power⁷. The reasons are the following: first, the cavity position seems to correspond to small values of the Fresnel number [12] (i.e. we observe that the beam gets more and more Gaussian on the way from the laser box to the cavity entrance); second, if the beam would be not Gaussian at the 30% level, then we would see resonances of a large number of higher order modes when varying the laser beam frequency⁸.

A simple explanation is suggested by the results of the fits performed to the reflected signal: since the laser beam linewidth is of the order of the final cavity *FWHM*, only part of the laser beam power is coupled to the cavity. When the finesse is low, the laser beam linewidth is not needed to describe the reflected signal because the cavity *FWHM* is of the order of 20 kHz (see fig. 5.14). On the contrary, if the finesse is high (*FWHM* ≈ 3 kHz), a laser beam linewidth of the order of 5 kHz is required. This is a reasonable assumption, given the manufacturer information (see table 3.1 of chap. 3).

To confirm this hypothesis, one should measure the laser beam linewidth, but this is a very complicated task. On the other hand, there is no other phenomenon one can think of and the fit described above has indeed been used, at least in two publications [7, 8] to my knowledge, to determine the laser beam linewidth.

Note that this fit procedure is independent of the cavity feedback system. Therefore, the power loss cannot be attributed to bad behaviour of the system.

Finally, the power circulating inside the cavity can be estimated:

$$P_{in} \approx 0.7 \times G_{max} \times P_0 \approx 4 \text{ kW}$$

where $P_0 \approx 0.7$ W. From fig. 2.19 of chap. 2, we conclude that this is certainly enough to reach a high precision on the measurement of the electron beam polarisation.

⁶We know that the cavity is well aligned when the level of the higher order modes, located at frequency separation $FSR/2$ are quasi-invisible.

⁷One may question here the validity of the paraxial approximation of the Maxwell equations from which the Gaussian beam solution is obtained. It can be shown that the first order correction to this approximation is proportional to $\lambda/(2\pi\omega_0)$ [10, 11], i.e. of the order of 10^{-4} in the field and therefore negligible for the intensity.

⁸To confirm these statements, we plan to model the diffractive nature of our beam using the Fresnel-Huygens integral [13] in the near future.

Bibliography

- [1] N. Falletto, *Etude, conception et réalisation d'une cavité Fabry-Perot pour le polarimètre Compton de TJNAF*, Université Joseph Fourier-Grenoble 1, 1999. DAPNIA/SPhN-99-03T.
- [2] D.Z. Anderson, "Alignment of resonant cavities", Appl. Opt. 23 (1984) 2944.
- [3] E. Morrison, B.J. Meers, D.I. Robertson and H. Ward, "Automatic alignment of optical interferometers", Appl. Opt. 33 (1994) 5041.
- [4] C. Dobrzynski, "Mise au point d'une procédure d'alignement d'un laser dans une cavité Fabry-Perot", available on www.lal.recherche/h1/hardware/poll.html.
- [5] N. P. Barnes and L.B. Petway, 'Variation of the Verdet constant with temperature of terbium gallium garnet', J. Opt. Soc. Am. B 9, 1912-1915 (1992)
- [6] M.J. Lawrence et al., 'Dynamic response of a Fabry-Perot interferometer', J. Opt. Soc. Am. B 16, 523-532 (1999).
- [7] J. W. Hahn et al., 'Cavity ringdown spectroscopy with a continuous-wave laser: calculation of couplings efficiency and a new spectrometer design', Appl. Opt. 38, 1859-1866 (1999).
- [8] J. Morville et al., 'Effects of laser phase noise on the injection of a high-finesse cavity', Appl. Opt. 41, 6980-6990 (2002)
- [9] C. Pascaud, internal note available on www.lal.recherche/h1/hardware/poll.html.
- [10] M. Lax, W.H. Louisell and W.B. McKnight, 'From Maxwell to paraxial wave optics', Phys. Rev. A 11, 1365-1370 (1975).
- [11] P. Varga and P. Torok, 'Exact and approximate solutions of Maxwell's equations for a confocal cavity', Opt. Lett. 21, 1523-1525 (1996).
- [12] A.E. Siegman, *Lasers* (University Science books, 1986).
- [13] H.G. Kraus, 'Huygens-Fresnel-Kirchhoff wave-front diffraction formulation: paraxial and exact Gaussian laser beams', J. Opt. Soc. Am. A 7, 47-65 (1990).

Conclusion

Thanks to the contributions of the persons whose names are given in the introduction, it has been possible to design, build and finally install successfully at HERA the polarimeter described in this document.

At the time of writing this conclusion, no beam is yet running inside the cavity and the polarimeter is ready for commissioning. The laser power available for Compton scattering matches the requirements of the high luminosity polarised electron-proton physics. The cavity locking stability is excellent in spite of the very noisy acoustic environment of the HERA tunnel.

A careful experimental study of the light polarisation measurement has been done at Orsay. Using a detailed model for light propagation in quartz, we have reached the per mille accuracy on the ellipsometric measurements. However, the thermal control of the photodiode electronics, used in our ellipsometer, did not work properly once installed at HERA. Therefore, instead of the per mille level obtained with the Orsay ellipsometer prototype, we are limited at the percent level at HERA.

With regards to our goal of measuring the electron beam polarisation at the per mille level, we therefore have to change our photodiode readout system. High quality commercial products do exist but they are prohibitively expensive. We have therefore started a new experimental design in order to reach a temperature stability of 0.01 K, independently of the outside temperature. We are now confident of succeeding in this objective, thanks to the experience accumulated during the past months.

The final precision on the electron polarisation measurement obviously does not depend only the laser polarisation measurement accuracy but also on the calorimeter performance. From the studies presented in chapter 2, we see that Compton scattering in the few photons mode offers two advantages: a huge number of scattered photons within a few seconds of DAQ and discernable kinematic reference points. With an adequate calorimeter, we are therefore confident in reaching a few per mille level of accuracy on the electron polarisation measurement.

As I mentioned in the introduction, this rather long document brings together disparate technical information useful for the design and construction of an optical resonator in a collider environment. It is worth mentioning again that part of the technical information given in chapter 3 comes from the cavity installed on the CEBAF accelerator, which was a great benefit to us. I therefore hope that this account will be useful to future similar projects.

Appendix A

Model for the propagation of Gaussian beams in anisotropic plates

To model the effects of anisotropic plates on the polarisation state of an electromagnetic plane wave, the text book Jones or Mueller formalisms are generally used [1, 2]. In doing so, important effects like multiple reflections inside the plate, oblique incidence and Gaussian distribution of the light intensity are neglected.

It has been known for a long time [5] that even under normal incidence, multiple internal reflections must be taken into account when high precision polarimetry is foreseen. This effect is fully taken into account for plane wave using the very general 4×4 matrix method of Ref. [6]. However, to our knowledge, no explicit and simple expressions for the corresponding Jones matrices are available.

In previous works concerning uniaxial crystals, particular geometries were generally assumed [5, 7, 8, 4], prohibiting a precise description of a simultaneously tilted and rotating plate. Thus we present here a 2×2 matrix method describing plane wave propagation inside anisotropic media. The powerful 4×4 matrix formalism of Ref. [6] is used as a starting point, thereby avoiding the heavy algebraic manipulations of former approaches [9, 10]. To benefit by the results obtained with the 4×4 matrix formalism, but applied to single interfaces [11, 12], we use the intuitive method introduced in Ref. [13]. It will be shown that the 4×4 matrix formalism can then be reduced to a 2×2 matrix algebra without loss of generality.

This 2×2 matrix method provides compact and general expressions for the so called *generalised Jones matrices* but one of its advantages is that it is also suitable for Gaussian beams.

In this appendix, we begin by describing the 2×2 matrix algebra. The complete model, describing the transmission of Gaussian beams by anisotropic platelets is described in section A.2. In section A.3, the effects of the surface roughness on the transmitted beam are estimated.

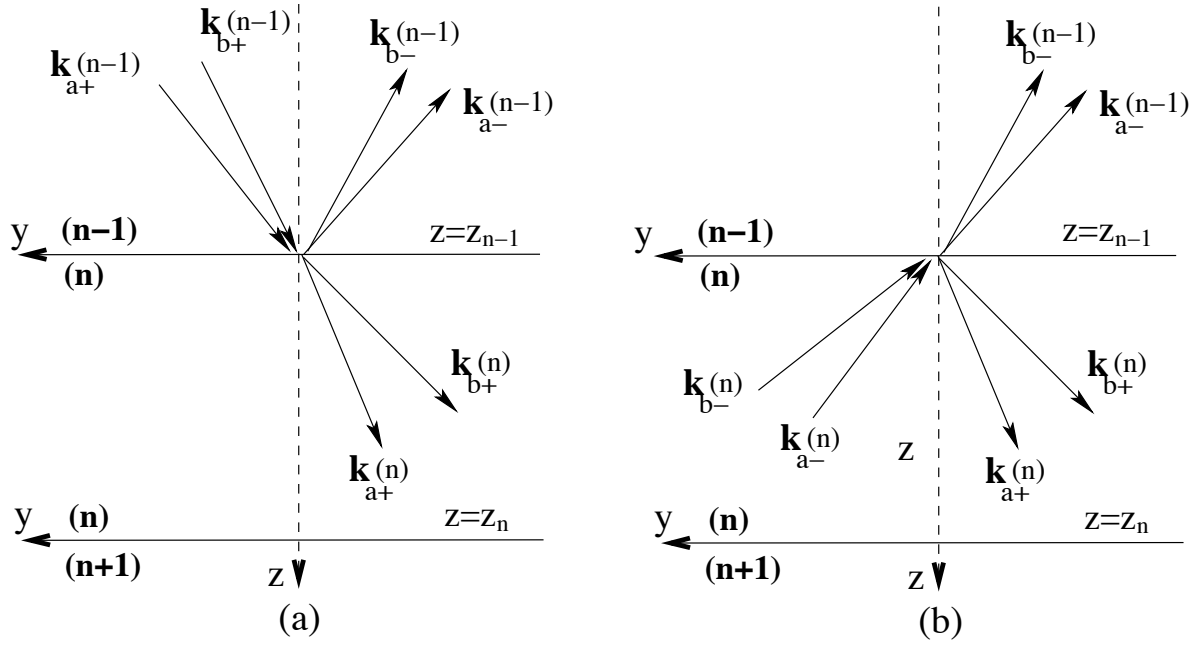


Figure A.1: Schematic view of the interface between two anisotropic media: (a) incident wave is propagating in the forward ($z > 0$) direction, (b) incident wave is propagating in the backward ($z < 0$) direction.

A.1 A 2×2 matrix method for anisotropic parallel plates. I: plane waves

A.1.1 Multi-layer anisotropic parallel plates

In this section, general formula are derived for multi-anisotropic layers. Arbitrary orientations of the optic axis and arbitrary incidence angles are considered. The following assumptions will hold: the anisotropic medium is lossless and homogeneous; interfaces between layers are plane and parallel to each other; the light is coherent and monochromatic; electromagnetic fields are described by plane waves.

A coordinate system attached to the layers is used: unit vectors $\hat{\mathbf{x}}$ and $\hat{\mathbf{y}}$ are in the plane of interface and the unit vector $\hat{\mathbf{z}}$ is perpendicular to the interface.

Following Ref. [11] we write the electric field in the n^{th} layer

$$\begin{aligned} \mathbf{E}_+ &= A_{a+}(n) \hat{\mathbf{p}}_{a+}(n) \exp(-i\mathbf{k}_{a+}(n) \cdot \mathbf{r}) + A_{b+}(n) \hat{\mathbf{p}}_{b+}(n) \exp(-i\mathbf{k}_{b+}(n) \cdot \mathbf{r}), \\ \mathbf{E}_- &= A_{a-}(n) \hat{\mathbf{p}}_{a-}(n) \exp(-i\mathbf{k}_{a-}(n) \cdot \mathbf{r}) + A_{b-}(n) \hat{\mathbf{p}}_{b-}(n) \exp(-i\mathbf{k}_{b-}(n) \cdot \mathbf{r}) \end{aligned}$$

and the corresponding magnetic fields as

$$\begin{aligned} \mathbf{H}_+ &= A_{a+}(n) \mathbf{q}_{a+}(n) \exp(-i\mathbf{k}_{a+}(n) \cdot \mathbf{r}) + A_{b+}(n) \mathbf{q}_{b+}(n) \exp(-i\mathbf{k}_{b+}(n) \cdot \mathbf{r}), \\ \mathbf{H}_- &= A_{a-}(n) \mathbf{q}_{a-}(n) \exp(-i\mathbf{k}_{a-}(n) \cdot \mathbf{r}) + A_{b-}(n) \mathbf{q}_{b-}(n) \exp(-i\mathbf{k}_{b-}(n) \cdot \mathbf{r}). \end{aligned}$$

In these expressions:

- the time dependence $\exp(i\omega t)$, with ω the optical angular frequency, has been omitted;
- the spatial coordinate vector reads as

$$\{ \mathbf{r} = x\hat{\mathbf{x}} + y\hat{\mathbf{y}} + (z - z_n)\hat{\mathbf{z}} \mid z_{n-1} \leq z \leq z_n \};$$

- the subscripts a_{\pm} and b_{\pm} correspond to the four wave propagations inside the medium n (two directions $z > 0$ and $z < 0$ for each solution labelled a and b);
- $\mathbf{k}_{a_{\pm}}(n)$ and $\mathbf{k}_{b_{\pm}}(n)$ are the four propagation wave vectors. Projections of these vectors in the transverse plane (x, y) are given by the boundary conditions at the interface and the projection along the z axis is given by the solutions of the wave equation (see Ref. [6]).
- $\hat{\mathbf{p}}_{a_{\pm}}(n)$ and $\hat{\mathbf{p}}_{b_{\pm}}(n)$ are the four polarisation directions of the electric fields (see also Ref. [6]) ;
- $\mathbf{q}_{a_{\pm}}(n) = c/(\mu\omega)[\mathbf{k}_{a_{\pm}}(n) \times \hat{\mathbf{p}}_{a_{\pm}}(n)]$ and $\mathbf{q}_{b_{\pm}}(n) = c/(\mu\omega)[\mathbf{k}_{b_{\pm}}(n) \times \hat{\mathbf{p}}_{b_{\pm}}(n)]$ with μ the magnetic permittivity and c the light velocity;
- $A_{a_{\pm}}(n)$ and $A_{b_{\pm}}(n)$ are the four wave amplitudes.

As in Ref. [6], we write the field amplitude transformation using a matrix formulation

$$\begin{pmatrix} A_{a_+}(n-1) \\ A_{b_+}(n-1) \\ A_{a_-}(n-1) \\ A_{b_-}(n-1) \end{pmatrix} = T \begin{pmatrix} A_{a_+}(n) \\ A_{b_+}(n) \\ A_{a_-}(n) \\ A_{b_-}(n) \end{pmatrix}. \quad (\text{A.1})$$

but here the ordering of the amplitudes is different: with respect to Ref. [6], positions of $A_{b_+}(n-1)$ and $A_{a_-}(n-1)$ are exchanged. The 4×4 matrix T will be determined by the method developed in Ref. [13] for dielectric multi-layer media.

Let us first consider a forward wave plane propagating across the interface between media $n-1$ and n (Fig. A.1a). Relations between incident, refracted and reflected amplitudes are obtained by applying the continuity conditions of the electric and magnetic field at the interface $z = z_{n-1}$:

$$D(n-1) \begin{pmatrix} A_{a_+}(n-1) \\ A_{b_+}(n-1) \\ A_{a_-}(n-1) \\ A_{b_-}(n-1) \end{pmatrix} = D(n) \begin{pmatrix} A_{a_+}(n) \exp(-i\delta_{a_+}(n)) \\ A_{b_+}(n) \exp(-i\delta_{b_+}(n)) \\ 0 \\ 0 \end{pmatrix}, \quad (\text{A.2})$$

where

$$\delta_{a_{\pm}}(n) = (\mathbf{k}_{a_{\pm}}(n) \cdot \hat{\mathbf{z}})d_n, \quad \delta_{b_{\pm}}(n) = (\mathbf{k}_{b_{\pm}}(n) \cdot \hat{\mathbf{z}})d_n,$$

with $d_n = z_n - z_{n-1}$ and

$$D(n) = \begin{pmatrix} \hat{\mathbf{p}}_{a_+}(n) \cdot \hat{\mathbf{x}} & \hat{\mathbf{p}}_{b_+}(n) \cdot \hat{\mathbf{x}} & \hat{\mathbf{p}}_{a_-}(n) \cdot \hat{\mathbf{x}} & \hat{\mathbf{p}}_{b_-}(n) \cdot \hat{\mathbf{x}} \\ \hat{\mathbf{p}}_{a_+}(n) \cdot \hat{\mathbf{y}} & \hat{\mathbf{p}}_{b_+}(n) \cdot \hat{\mathbf{y}} & \hat{\mathbf{p}}_{a_-}(n) \cdot \hat{\mathbf{y}} & \hat{\mathbf{p}}_{b_-}(n) \cdot \hat{\mathbf{y}} \\ \mathbf{q}_{a_+}(n) \cdot \hat{\mathbf{x}} & \mathbf{q}_{b_+}(n) \cdot \hat{\mathbf{x}} & \mathbf{q}_{a_-}(n) \cdot \hat{\mathbf{x}} & \mathbf{q}_{b_-}(n) \cdot \hat{\mathbf{x}} \\ \mathbf{q}_{a_+}(n) \cdot \hat{\mathbf{y}} & \mathbf{q}_{b_+}(n) \cdot \hat{\mathbf{y}} & \mathbf{q}_{a_-}(n) \cdot \hat{\mathbf{y}} & \mathbf{q}_{b_-}(n) \cdot \hat{\mathbf{y}} \end{pmatrix}$$

where the four unknowns are $A_{a-}(n-1)$, $A_{b-}(n-1)$, $A_{a+}(n)$ and $A_{b+}(n)$. The solution of this system can be formally written as [11]

$$\begin{pmatrix} A_{a-}(n-1) \\ A_{b-}(n-1) \end{pmatrix} = \mathcal{R}_{n-1,n} \begin{pmatrix} A_{a+}(n-1) \\ A_{b+}(n-1) \end{pmatrix} \quad (\text{A.3})$$

and

$$\begin{pmatrix} A_{a+}(n) \\ A_{b+}(n) \end{pmatrix} = \mathcal{P}_+^{-1}(n) \mathcal{T}_{n-1,n} \begin{pmatrix} A_{a+}(n-1) \\ A_{b+}(n-1) \end{pmatrix} \quad (\text{A.4})$$

with

$$\mathcal{P}_\pm(n) = \begin{pmatrix} e^{-i\delta_{a\pm}(n)} & 0 \\ 0 & e^{-i\delta_{b\pm}(n)} \end{pmatrix}$$

where $\mathcal{R}_{n-1,n}$ and $\mathcal{T}_{n-1,n}$ are the 2×2 matrices describing the reflection and transmission at the interface between medium $n-1$ and n .

Since eq. (A.1) is a general expression, the relations obtained for the particular case of a single interface (Eqs.(A.3) and (A.4)) must be recovered by setting $A_{a-}(n) = 0$ and $A_{a+}(n) = 0$. We then have to identify the matrix elements of T with the solution of Eq. (A.2), i.e. Eqs. (A.3) and (A.4). This leads to the following expressions:

$$\begin{pmatrix} T_{11} & T_{12} \\ T_{21} & T_{22} \end{pmatrix} = \mathcal{T}_{n-1,n}^{-1} \mathcal{P}_+(n), \quad (\text{A.5})$$

$$\begin{pmatrix} T_{31} & T_{32} \\ T_{41} & T_{42} \end{pmatrix} = \mathcal{R}_{n-1,n} \mathcal{T}_{n-1,n}^{-1} \mathcal{P}_+(n). \quad (\text{A.6})$$

To determine the remaining elements of T the same method is applied to a backward wave plane crossing the interface between media n and $n-1$ (Fig. A.1b). The continuity conditions at the interface lead to the following system:

$$D(n-1) \begin{pmatrix} 0 \\ 0 \\ A_{a-}(n-1) \\ A_{b-}(n-1) \end{pmatrix} = D(n) \begin{pmatrix} A_{a+}(n)e^{-i\delta_{a+}(n)} \\ A_{b+}(n)e^{-i\delta_{b+}(n)} \\ A_{a-}(n)e^{-i\delta_{a-}(n)} \\ A_{b-}(n)e^{-i\delta_{b-}(n)} \end{pmatrix}, \quad (\text{A.7})$$

where the unknowns are $A_{a-}(n-1)$, $A_{b-}(n-1)$, $A_{a+}(n)$ and $A_{b+}(n)$. The relations between amplitudes are:

$$\begin{pmatrix} A_{a+}(n) \\ A_{b+}(n) \end{pmatrix} = \mathcal{P}_+^{-1}(n) \mathcal{R}_{n,n-1} \mathcal{P}_-(n) \begin{pmatrix} A_{a-}(n) \\ A_{b-}(n) \end{pmatrix} \quad (\text{A.8})$$

$$\begin{pmatrix} A_{a-}(n-1) \\ A_{b-}(n-1) \end{pmatrix} = \mathcal{T}_{n,n-1} \mathcal{P}_-(n) \begin{pmatrix} A_{a-}(n) \\ A_{b-}(n) \end{pmatrix}. \quad (\text{A.9})$$

Using Eq. (A.6) together with Eqs. (A.8) and (A.9), one gets

$$\begin{pmatrix} T_{13} & T_{14} \\ T_{23} & T_{24} \end{pmatrix} = -\mathcal{T}_{n-1,n}^{-1} \mathcal{R}_{n,n-1} \mathcal{P}_-(n), \quad (\text{A.10})$$

$$\begin{pmatrix} T_{33} & T_{34} \\ T_{43} & T_{44} \end{pmatrix} = \left[\mathcal{T}_{n,n-1} - \mathcal{R}_{n-1,n} \mathcal{T}_{n-1,n}^{-1} \mathcal{R}_{n,n-1} \right] \mathcal{P}_-(n). \quad (\text{A.11})$$

Eqs. (A.5), (A.6), (A.10) and (A.11) suggest the following compact notation:

$$\mathcal{A}_{\pm}(n) = \begin{pmatrix} A_{a_{\pm}}(n) \\ A_{b_{\pm}}(n) \end{pmatrix},$$

so that Eq. (A.1) becomes

$$\begin{pmatrix} \mathcal{A}_+(n-1) \\ \mathcal{A}_-(n-1) \end{pmatrix} = I_{n-1,n} P(n) \begin{pmatrix} \mathcal{A}_+(n) \\ \mathcal{A}_-(n) \end{pmatrix}, \quad (\text{A.12})$$

with

$$P(n) = \begin{pmatrix} \mathcal{P}_+(n) & 0 \\ 0 & \mathcal{P}_-(n) \end{pmatrix}, I_{n-1,n} = \begin{pmatrix} \mathcal{I}_{(n-1)+,n+} & \mathcal{I}_{(n-1)+,n-} \\ \mathcal{I}_{(n-1)-,n+} & \mathcal{I}_{(n-1)-,n-} \end{pmatrix} \quad (\text{A.13})$$

and

$$\mathcal{I}_{(n-1)+,n+} = \mathcal{T}_{n-1,n}^{-1} \quad (\text{A.14})$$

$$\mathcal{I}_{(n-1)+,n-} = -\mathcal{T}_{n-1,n}^{-1} \mathcal{R}_{n,n-1} \quad (\text{A.15})$$

$$\mathcal{I}_{(n-1)-,n+} = \mathcal{R}_{n-1,n} \mathcal{T}_{n-1,n}^{-1} \quad (\text{A.16})$$

$$\mathcal{I}_{(n-1)-,n-} = \mathcal{T}_{n,n-1} - \mathcal{R}_{n-1,n} \mathcal{T}_{n-1,n}^{-1} \mathcal{R}_{n,n-1}. \quad (\text{A.17})$$

These expressions show that it is possible to perform all the calculations using a 2×2 matrix algebra only. In this algebra, two phase matrices and eight interface matrices per layer are involved.

Eqs. (A.14-A.17) can now be compared to the corresponding expressions obtained for a dielectric layer (see Ref. [13]). It appears that a simple matrix transformation of the Fresnel coefficients

$$\begin{aligned} r_{n-1,n} &\rightarrow \mathcal{R}_{n-1,n} \\ t_{n-1,n} &\rightarrow \mathcal{P}_+^{-1}(n) \mathcal{T}_{n-1,n} \\ r_{n,n-1} &\rightarrow \mathcal{P}_+^{-1}(n) \mathcal{R}_{n,n-1} \mathcal{P}_-(n) \\ t_{n,n-1} &\rightarrow \mathcal{T}_{n,n-1} \mathcal{P}_-(n) \end{aligned}$$

leads to Eqs. (A.14-A.17).

We can also easily prove that our transfer matrix $I_{n-1,n} P(n)$ is equivalent to the general expression of Ref. [6]. For this one must show that

$$I_{n-1,n} = D^{-1}(n-1)D(n).$$

Rewriting Eq. (A.2)

$$\begin{pmatrix} \mathcal{A}_+(n-1) \\ \mathcal{A}_-(n-1) \end{pmatrix} = D^{-1}(n-1)D(n)P(n) \begin{pmatrix} \mathcal{A}_+(n) \\ 0 \end{pmatrix},$$

we see that the two 2×2 matrices of Eq. (A.6) are equivalent to the corresponding 2×2 blocks of the 4×4 matrix $D^{-1}(n-1)D(n)$. Since one can rewrite Eq. (A.7) in the same way and since the expressions of Eq. (A.6) are used in the derivation of Eq. (A.11) we conclude that the transfer matrix of Eq. (A.12) is an equivalent form of the 4×4 transfer matrix of Ref. [6] but with a different ordering of the wave amplitudes.

Therefore, the transfer matrix for N anisotropic layers located between two infinite media 0 and $N + 1$ is given by Eq. (21) of Ref. [6]:

$$\begin{pmatrix} \mathcal{A}_+(0) \\ \mathcal{A}_-(0) \end{pmatrix} = S \begin{pmatrix} \mathcal{A}_+(N+1) \\ \mathcal{A}_-(N+1) \end{pmatrix}, \quad S = T_{0,1} T_{1,2} \cdots T_{N,N+1}$$

with $d_{N+1} = 0$ and $T_{n,n-1} = I_{n-1,n} P(n)$. But here the calculation of S only involves the 2×2 matrices of Eqs. (A.14-A.17) and the diagonal 2×2 phase matrices $\mathcal{P}_\pm(n)$. The Jones matrices for transmission and reflection are finally defined by:

$$\mathcal{A}_+(N+1) = \mathcal{M}_t \mathcal{A}_+(0), \quad \mathcal{A}_-(0) = \mathcal{M}_r \mathcal{A}_+(0)$$

with $\mathcal{A}_-(N+1) = 0$. They are then given by

$$\mathcal{M}_t = \mathcal{S}_{1,1}^{-1}, \quad \mathcal{M}_r = \mathcal{S}_{2,1} \mathcal{S}_{1,1}^{-1} \quad (\text{A.18})$$

where

$$\begin{pmatrix} \mathcal{S}_{1,1} & \mathcal{S}_{1,2} \\ \mathcal{S}_{2,1} & \mathcal{S}_{2,2} \end{pmatrix} \equiv S.$$

A.1.2 Anisotropic parallel plate

To illustrate the simplicity of the 2×2 matrix method described above, we shall give here general formulae to model the transmission and reflection of plane waves through an anisotropic parallel plate. Since this optical component is extensively used in ellipsometry, we shall also consider the effect of an anti-reflection coating.

Uncoated parallel plate

The transfer matrix of an anisotropic parallel plate within two semi-infinite media is given by

$$S_a = I_{1,a} P(a) I_{a,2} \quad (\text{A.19})$$

where subscripts 1, 2 and a refer to the two dielectric and the anisotropic media respectively.

In a dielectric medium, the polarisation directions coincide with the directions perpendicular and parallel to the plane of incidence, $\hat{\mathbf{s}}_\pm$ and $\hat{\mathbf{p}}_\pm$ respectively. They are defined by

$$\hat{\mathbf{p}}_\pm = \mathbf{k}_\pm \times \hat{\mathbf{s}}_\pm / |\mathbf{k}|, \quad \hat{\mathbf{s}}_+ = \hat{\mathbf{s}}_-$$

and

$$\mathbf{k}_- = \mathbf{k}_+ - 2(\mathbf{k}_+ \cdot \hat{\mathbf{z}}) \hat{\mathbf{z}}$$

where \mathbf{k}_+ is the forward wave vector. One therefore writes the incident and transmitted field component as

$$\mathcal{A}_\pm(n) = \begin{pmatrix} A_{s_\pm}(n) \\ A_{p_\pm}(n) \end{pmatrix}, \quad (\text{A.20})$$

with $n = 1, 2$.

For extended Jones matrices defined in Eq. (A.18), we obtain:

$$\begin{aligned}\mathcal{M}_t &= \left[\mathcal{I}_{1+,a+} \mathcal{P}_+(a) \mathcal{I}_{a+,2+} + \mathcal{I}_{1+,a-} \mathcal{P}_-(a) \mathcal{I}_{a-,2+} \right]^{-1}, \\ \mathcal{M}_r &= \left[\mathcal{I}_{1-,a+} \mathcal{P}_+(a) \mathcal{I}_{a+,2+} + \mathcal{I}_{1-,a-} \mathcal{P}_-(a) \mathcal{I}_{a-,2+} \right]^{-1} \mathcal{M}_t\end{aligned}$$

which gives, using Eqs. (A.14-A.17):

$$\mathcal{M}_t = \mathcal{T}_{a2} \left[1 - \mathcal{P}_+^{-1}(a) \mathcal{R}_{a1} \mathcal{P}_-(a) \mathcal{R}_{a2} \right]^{-1} \mathcal{P}_+^{-1}(a) \mathcal{T}_{1a}, \quad (\text{A.21})$$

$$\mathcal{M}_r = \mathcal{R}_{1a} + \mathcal{T}_{a1} \mathcal{P}_-^{-1}(a) \mathcal{R}_{a2} \left[1 - \mathcal{P}_+^{-1}(a) \mathcal{R}_{a1} \mathcal{P}_-(a) \mathcal{R}_{a2} \right]^{-1} \mathcal{P}_+^{-1}(a) \mathcal{T}_{1a} \quad (\text{A.22})$$

where 1 stands for the 2×2 identity matrix. For normal incidence but taking into account circular anisotropy, Eq. (A.21) is equivalent to the expression derived in Ref. [14].

These expressions can also be derived by taking into account explicitly the multi-reflections of the wave planes inside the plate. Using Eqs. (A.3), (A.4), (A.8) and (A.9) for the reflection and transmission interface matrices one gets:

$$\begin{aligned}\mathcal{A}_+(2) &= \left[\mathcal{T}_{a2} \mathcal{P}_+^{-1}(a) \mathcal{T}_{1a} + \mathcal{T}_{a2} \mathcal{P}_+^{-1}(a) \mathcal{R}_{a1} \mathcal{P}_-(a) \mathcal{R}_{a2} \mathcal{P}_+^{-1}(a) \mathcal{T}_{1a} + \dots \right] \mathcal{A}_+(1) \\ &= \left[\mathcal{T}_{a2} \left(\sum_{j=0}^{\infty} \left[\mathcal{P}_+^{-1}(a) \mathcal{R}_{a1} \mathcal{P}_-(a) \mathcal{R}_{a2} \right]^j \right) \mathcal{P}_+^{-1}(a) \mathcal{T}_{1a} \right] \mathcal{A}_+(1), \\ \mathcal{A}_-(1) &= \left[\mathcal{R}_{1a} + \mathcal{T}_{a1} \mathcal{P}_-(a) \mathcal{R}_{a2} \mathcal{P}_+^{-1}(a) \mathcal{T}_{1a} + \right. \\ &\quad \left. \mathcal{T}_{a1} \mathcal{P}_-(a) \mathcal{R}_{a2} \mathcal{P}_+^{-1}(a) \mathcal{R}_{a1} \mathcal{P}_-(a) \mathcal{R}_{a2} \mathcal{P}_+^{-1}(a) \mathcal{T}_{1a} + \dots \right] \mathcal{A}_+(1) \\ &= \left[\mathcal{R}_{1a} + \mathcal{T}_{a1} \mathcal{P}_-(a) \mathcal{R}_{a2} \left(\sum_{j=0}^{\infty} \left[\mathcal{P}_+^{-1}(a) \mathcal{R}_{a1} \mathcal{P}_-(a) \mathcal{R}_{a2} \right]^j \right) \mathcal{P}_+^{-1}(a) \mathcal{T}_{1a} \right] \mathcal{A}_+(1)\end{aligned}$$

which lead to Eqs. (A.21) and (A.22) with $\sum_{j=0}^{\infty} X^j = (1 - X)^{-1}$ and $\mathcal{A}_+(2) = \mathcal{M}_t \mathcal{A}_+(1)$, $\mathcal{A}_-(1) = \mathcal{M}_r \mathcal{A}_+(1)$.

Eqs. (A.21) and (A.22) are again simple matrix versions of the formulae obtained for dielectric layers. However, the ordering of the reflection and transmission interface matrices is important here since none of them commute with the others a priori.

In practice, some of the interface matrices can be found in published articles [11, 15, 12] for uniaxial-dielectric and dielectric-uniaxial interfaces. For the general case of a biaxial-biaxial interface, the polarisation directions and solutions of the wave equation can be found in Ref. [16]. Once all this information is gathered all matrix interfaces can be determined by solving the linear Eqs. (A.2) and (A.7).

Anti-reflection coated parallel plates

Anti-reflection coated parallel plates are frequently utilized in ellipsometry. Let us then consider a double layer anti-reflection coated parallel plate [17]. Two layers of optical

index N_2 and N_3 and thickness d_2 and d_3 are deposited on each side of the plate. The coated plate is then located in an infinite ambient dielectric medium of index N_1 . In order to simplify the calculation, we introduce a zero thickness layer of index N_1 between the anisotropic plate and the dielectric coating on each sides. Then the sequence of layers is 1|2|3|1|a|1|3|2|1. Using this trick [11], the expression derived in section A.1.2 can be used without any modifications.

The wave amplitudes are given by A.20 and the transfer matrix between the two dielectric layers is determined using Eqs. (A.13) and (A.14-A.17):

$$P(n) = \begin{pmatrix} \begin{pmatrix} e^{i\delta(n)} & 0 \\ 0 & e^{i\delta(n)} \end{pmatrix} & 0 \\ 0 & \begin{pmatrix} e^{-i\delta(n)} & 0 \\ 0 & e^{-i\delta(n)} \end{pmatrix} \end{pmatrix}, \quad (\text{A.23})$$

$$I_{n-1,n} = \begin{pmatrix} \begin{pmatrix} \frac{1}{t_s(n-1)} & 0 \\ 0 & \frac{1}{t_p(n-1)} \end{pmatrix} & \begin{pmatrix} \frac{r_s(n-1)}{t_s(n-1)} & 0 \\ 0 & \frac{r_p(n-1)}{t_p(n-1)} \end{pmatrix} \\ \begin{pmatrix} \frac{r_s(n-1)}{t_s(n-1)} & 0 \\ 0 & \frac{r_p(n-1)}{t_p(n-1)} \end{pmatrix} & \begin{pmatrix} \frac{1}{t_s(n-1)} & 0 \\ 0 & \frac{1}{t_p(n-1)} \end{pmatrix} \end{pmatrix} \quad (\text{A.24})$$

where $t_{s,p}(n-1)$ and $r_{s,p}(n-1)$ are the Fresnel coefficients (see Ref. [13]) and $\delta(n) = 2\pi N_n d_n / \lambda$ with λ the wavelength. In the case of a dielectric interface, all the 2×2 block matrices constituting the transfer matrix are then diagonal.

The transfer matrix of the double dielectric layers, plus the zero thickness layer, can be written as

$$S_{in} = \begin{pmatrix} \mathcal{U}_{in} & \mathcal{V}_{in}^* \\ \mathcal{V}_{in} & \mathcal{U}_{in}^* \end{pmatrix}$$

with

$$\mathcal{U}_{in} = \begin{pmatrix} \frac{e^{i\Sigma} + r_s(3)[r_s(1)e^{i\Delta} + r_s(2)e^{-i\Delta}] + r_s(1)r_s(3)e^{-i\Sigma}}{t_s(1)t_s(2)t_s(3)} & 0 \\ 0 & \frac{e^{i\Sigma} + r_p(3)[r_p(1)e^{i\Delta} + r_p(2)e^{-i\Delta}] + r_p(1)r_p(3)e^{-i\Sigma}}{t_p(1)t_p(2)t_p(3)} \end{pmatrix}, \quad (\text{A.25})$$

$$\mathcal{V}_{in} = \begin{pmatrix} \frac{r_s(1)e^{i\Sigma} + r_s(3)e^{-i\Sigma} + r_s(3)[e^{i\Delta} + r_s(1)r_s(2)e^{-i\Delta}]}{t_s(1)t_s(2)t_s(3)} & 0 \\ 0 & \frac{r_p(1)e^{i\Sigma} + r_p(3)e^{-i\Sigma} + r_p(3)[e^{i\Delta} + r_p(1)r_p(2)e^{-i\Delta}]}{t_p(1)t_p(2)t_p(3)} \end{pmatrix} \quad (\text{A.26})$$

where $\Sigma = \delta(2) + \delta(3)$, $\Delta = \delta(3) - \delta(2)$ and \mathcal{U}_{in}^* (\mathcal{V}_{in}^*) is the complex conjugate of \mathcal{U}_{in} (\mathcal{V}_{in}). Eqs. (A.25) and (A.26) are equivalent to the corresponding standard expression (see Eq. (4.183) in Ref. [13]) and one can remark that, even though S_{in} is a 4×4 matrix, the calculations only involve 2×2 diagonal matrices.

Using Eq. (A.19), the transfer matrix of the coated anisotropic plate is finally given by

$$S_{in} \left[I_{1,a} P(a) I(a, 1) \right] S_{out},$$

where the elements of S_{out} are obtained by permuting 2 by 3 in Eqs. (A.25) and (A.26).

A.2 A 2×2 matrix method for anisotropic parallel plates. II: Gaussian beam

In this section, a version of an article published in Journal of the Optical Society of America [18] is reproduced ¹.

A.2.1 Introduction

Anisotropic parallel plates are extensively used in ellipsometry [1]. To precisely describe such experiments, it is necessary to take into account internal multiple reflections inside these plates [1] and the Gaussian nature of laser beams [4]. However, to the author's knowledge, no general expression of a corresponding Mueller matrix can be found in the literature.

In Ref. [4], the problem is solved for Gaussian beams but in a particular case: a uniaxial parallel plate tilted around the optical axis (itself located in the plane of incidence). Although very important results are provided, the formalism introduced by the authors cannot be generalised to an arbitrary geometrical configuration, i.e. to a rotating tilted birefringent plate with an optical axis not necessarily in the plate interface. Moreover, in this work, the calculations were carried out in the direct (x, y, z) space. This feature has two major implications: 1) effects related to the beam divergence cannot be studied and more importantly, 2) the fact that a Jones matrix is only defined under a particular approximation cannot be pointed out.

An adequate formalism to carry out the full calculations is Fourier optics. The theoretical ground for the scalar and vector Fourier optics has been set up some time ago in a series of articles [19, 20]. Thanks to this formalism and to the 4×4 matrix method of Ref. [6], general and compact expressions describing the transmission and reflection of a Gaussian beam by anisotropic parallel plates are provided. This is the topic of the present article.

This paper is organised as follows. In the first section, useful features of the vector Fourier formalism are summarised. This formalism is then used in section A.2.3 to derive a general expression for anisotropic parallel plates. Only the paraxial approximation is used at this stage. A useful approximation, named here 'scalar Fourier approximation', is then introduced in section A.2.4. This approximation, implicitly introduced in Ref. [4], provides simpler formulae and the possibility to define an extended Mueller matrix for birefringent parallel plates. Numerical examples are finally given in section A.2.5.

A.2.2 Vector Fourier optics in the paraxial approximation

All through this article we shall only be concerned with lossless homogeneous anisotropic media and monochromatic Gaussian beams. In this section, we start by considering the propagation of a Gaussian beams in isotropic media. The main results obtained in Ref. [21] are recalled together with additional information required for following the present paper.

¹This is the input version sent to the Journal including some modifications suggested by one of the referee of this document.

To describe the beam propagation, the direct system axis (x, y, z) is chosen in such way that $\hat{\mathbf{z}} = \mathbf{k}/k$ where \mathbf{k} is the Gaussian beam centre's wave vector and $k = |\mathbf{k}|$ (see Fig. A.2). The origin $z = 0$ is taken at the position where the beam size is minimum, i.e. at the beam waist position. The position vector will be written as $\mathbf{r} = \mathbf{r}_\perp + z\hat{\mathbf{z}}$ with $\mathbf{r}_\perp = x\hat{\mathbf{x}} + y\hat{\mathbf{y}}$ and where $\hat{\mathbf{x}}$, $\hat{\mathbf{y}}$ and $\hat{\mathbf{z}}$ are unit vectors along the ox , oy and oz axis respectively.

In the paraxial approximation, an electromagnetic scalar field amplitude $\psi(\mathbf{r}_\perp, z = 0)$ can be expanded according to

$$\psi(\mathbf{r}_\perp, 0) = \mathcal{F}[\bar{\psi}(\mathbf{k}_\perp)] = \frac{1}{2\pi} \iint \bar{\psi}(\mathbf{k}_\perp) \exp(-i\mathbf{k}_\perp \cdot \mathbf{r}) d^2\mathbf{k}_\perp \quad (\text{A.27})$$

where the time dependence has been omitted and where $\mathbf{k}_\perp = k_x\hat{\mathbf{x}} + k_y\hat{\mathbf{y}}$ and $|\mathbf{k}_\perp| \ll k$ so that $k_z \approx k(1 - |\mathbf{k}_\perp|^2/(2k^2))$. In Eq. (A.27), $\bar{\psi}(\mathbf{k}_\perp)$ is the scalar field amplitude in the \mathbf{k}_\perp space. To satisfy the paraxial approximation, $\bar{\psi}(\mathbf{k}_\perp)$ must be such that the integral has appreciable values only for $|\mathbf{k}_\perp| \ll k$.

At a given plane $z \neq 0$, the field is given by [22]

$$\psi(\mathbf{r}_\perp, z) = \exp\left(\frac{-iz}{2k}(P_x^2 + P_y^2)\right) \psi(\mathbf{r}_\perp, 0) \quad (\text{A.28})$$

where, as all through this article, the term $\exp(ikz)$ has been omitted and where

$$P_x = -i\frac{\partial}{\partial x}, \quad P_y = -i\frac{\partial}{\partial y}.$$

Eq. (A.27) can then be written as

$$\psi(\mathbf{r}_\perp, z) = \mathcal{F}[\bar{\psi}(\mathbf{k}_\perp, z)],$$

where we define for convenience

$$\bar{\psi}(\mathbf{k}_\perp, z) = \bar{\psi}(\mathbf{k}_\perp) \exp\left(\frac{iz}{2k}\mathbf{k}_\perp^2\right).$$

For a paraxial Gaussian beam, it is easy to show that

$$\psi(\mathbf{r}_\perp, 0) = \sqrt{\frac{2}{\pi w_0^2}} \exp\left(\frac{-\mathbf{r}_\perp^2}{w_0^2}\right) \Rightarrow \begin{cases} \psi(\mathbf{r}_\perp, z) = \sqrt{\frac{2}{\pi w_0^2}} \frac{-iz_R}{q(z)} \exp\left(\frac{-ik\mathbf{r}_\perp^2}{2q(z)}\right) \\ \bar{\psi}(\mathbf{k}_\perp, z) = \frac{w_0}{\sqrt{2\pi}} \exp\left(\frac{iq(z)\mathbf{k}_\perp^2}{2k}\right) \end{cases}$$

where w_0 is the beam waist, $q(z) = z + iz_R$ is the complex radius of curvature and $z_R = kw_0^2$ is the Rayleigh range.

Eq. (A.27) is the plane wave expansion of the scalar Gaussian beam. Wave vectors of these plane waves are defined by

$$\mathbf{k}_{\text{pw}} = \mathbf{k}_\perp + k_z\hat{\mathbf{z}} \approx \mathbf{k}_\perp + k(1 - \frac{|\mathbf{k}_\perp|^2}{2k^2})\hat{\mathbf{z}} \quad (\text{A.29})$$

in the paraxial approximation. However, Eq. (A.27) does not take into account the vectorial nature of the electromagnetic field. To keep the orthogonality between the

electric field, magnetic field and wave vector of each plane wave, one must introduce the six component vector [21]

$$F(\mathbf{r}_\perp, 0) = \begin{pmatrix} E_x(\mathbf{r}_\perp, 0) \\ E_y(\mathbf{r}_\perp, 0) \\ E_z(\mathbf{r}_\perp, 0) \\ B_x(\mathbf{r}_\perp, 0) \\ B_y(\mathbf{r}_\perp, 0) \\ B_z(\mathbf{r}_\perp, 0) \end{pmatrix}$$

and use the following Fourier transformation [21]

$$F(\mathbf{r}_\perp, 0) = \frac{1}{2\pi} \iint \bar{\psi}(\mathbf{k}_\perp) \exp(-i\mathbf{k}_\perp \cdot \mathbf{r}_\perp) \exp\left(i\frac{k_x}{k}G_x + i\frac{k_y}{k}G_y\right) \begin{pmatrix} a_1 \\ a_2 \\ 0 \\ -a_2 \\ a_1 \\ 0 \end{pmatrix} d^2\mathbf{k}_\perp \quad (\text{A.30})$$

where G_x and G_y are 6×6 matrices which are derived from the Poincaré group algebra [20]. Expressions for these matrices can be found in Ref. [21]. It should be noticed that the orthogonality between the electric field, the magnetic field and the wave vector of the plane wave only holds in the paraxial approximation, i.e. up to the order $|\mathbf{k}_\perp|^2/k^2$.

Expression for $F(\mathbf{r}_\perp, z)$ is obtained similarly to Eq. (A.28)

$$F(\mathbf{r}_\perp, z) = \frac{1}{2\pi} \iint \bar{\psi}(\mathbf{k}_\perp, z) \exp(-i\mathbf{k}_\perp \cdot \mathbf{r}_\perp) M_{6 \times 6} \begin{pmatrix} a_1 \\ a_2 \\ 0 \\ -a_2 \\ a_1 \\ 0 \end{pmatrix} d^2\mathbf{k}_\perp, \quad (\text{A.31})$$

with

$$M_{6 \times 6} = \begin{pmatrix} 1 + \frac{k_y^2 - k_x^2}{8k^2} & \frac{-k_y k_x}{4k^2} & \frac{k_x}{2k} & \frac{k_y k_x}{4k^2} & \frac{k_y^2 - k_x^2}{8k^2} & \frac{-k_y}{2k} \\ \frac{-k_y k_x}{4k^2} & 1 - \frac{k_y^2 - k_x^2}{8k^2} & \frac{k_y}{2k} & \frac{k_y^2 - k_x^2}{8k^2} & \frac{-k_y k_x}{4k^2} & \frac{k_x}{2k} \\ \frac{-k_x}{2k} & \frac{-k_y}{2k} & 1 & \frac{k_y}{2k} & \frac{-k_x}{2k} & 0 \\ \frac{-k_y k_x}{4k^2} & \frac{-k_y^2 + k_x^2}{8k^2} & \frac{k_y}{2k} & 1 + \frac{k_y^2 - k_x^2}{8k^2} & \frac{-k_y k_x}{4k^2} & \frac{k_x}{2k} \\ \frac{-k_y^2 + k_x^2}{8k^2} & \frac{k_y k_x}{4k^2} & \frac{-k_x}{2k} & \frac{-k_y k_x}{4k^2} & 1 - \frac{k_y^2 - k_x^2}{8k^2} & \frac{k_y}{2k} \\ \frac{-k_y}{2k} & \frac{k_x}{2k} & 0 & \frac{-k_x}{2k} & \frac{-k_y}{2k} & 1 \end{pmatrix}.$$

Focusing on the electric field, Eq. (A.31) can be reduced to a 3×3 matrix equation

$$\begin{aligned} \begin{pmatrix} E_x(\mathbf{r}) \\ E_y(\mathbf{r}) \\ E_z(\mathbf{r}) \end{pmatrix} &= \mathcal{F}[\bar{\psi}(\mathbf{k}_\perp, z) M_{3 \times 3} \mathbf{E}_0] \\ &= \frac{1}{2\pi} \iint \bar{\psi}(\mathbf{k}_\perp, z) \exp(-i\mathbf{k}_\perp \cdot \mathbf{r}_\perp) M_{3 \times 3} \mathbf{E}_0 d^2\mathbf{k}_\perp \end{aligned} \quad (\text{A.32})$$

with $\mathbf{E}_0^T = (a_1, a_2, 0)$ and

$$M_{3 \times 3} = \begin{pmatrix} 1 + \frac{k_y^2 - k_x^2}{4k^2} & \frac{-k_y k_x}{2k^2} & 0 \\ \frac{-k_y k_x}{2k^2} & 1 - \frac{k_y^2 - k_x^2}{4k^2} & 0 \\ \frac{-k_x}{k} & \frac{-k_y}{k} & 0 \end{pmatrix}. \quad (\text{A.33})$$

Note that the same expression holds for the magnetic field.

One can verify that, for an electric vector polarised along $\hat{\mathbf{x}}$ (i.e. $\mathbf{E}_0^T = (1, 0, 0)$), the integration of Eq. (A.32) over \mathbf{k}_\perp leads to the results of Ref. [21]. The angular divergence of a Gaussian beam therefore generates crossed polarisation effects.

A.2.3 Application to anisotropic layer

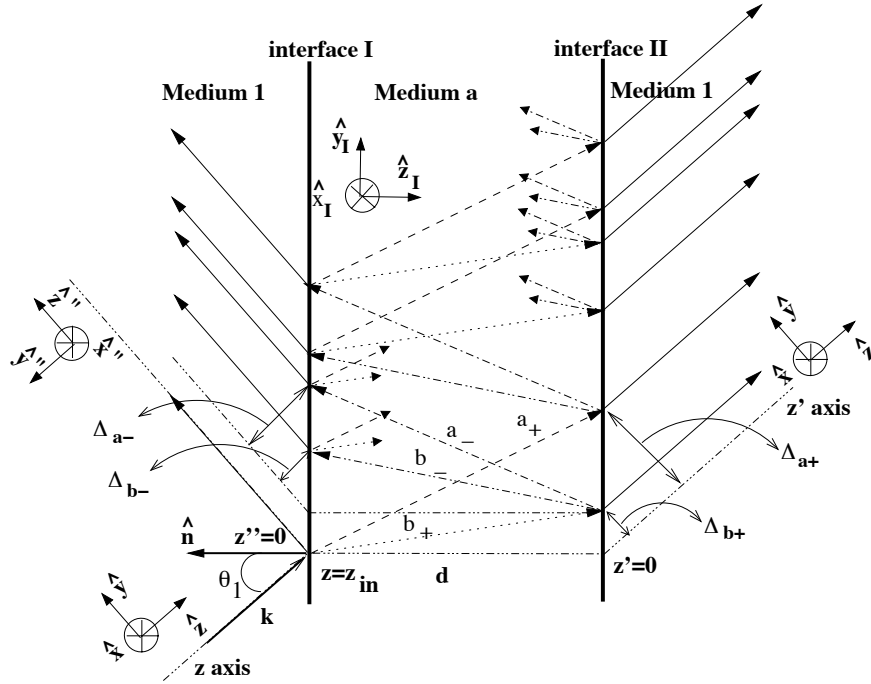


Figure A.2: Schematic view of the plane wave propagation in the anisotropic slab. For the sake of clarity, some of the inner reflected rays are represented by small arrows. The plane of incidence coincides with the plane yz . Symbols a_\pm and b_\pm correspond to the four possible propagation directions for the incident angle θ_1 . The four elementary transverse walk-offs, $\Delta_{a\pm}$ and $\Delta_{b\pm}$, are indicated. The various vector basis used throughout this article are also shown: $\{\hat{\mathbf{x}}, \hat{\mathbf{y}}, \hat{\mathbf{z}}\}$ for the incident and transmitted beams, $\{\hat{\mathbf{x}}'', \hat{\mathbf{y}}'', \hat{\mathbf{z}}''\}$ for the reflected beam, $\{\hat{\mathbf{x}}_I, \hat{\mathbf{y}}_I, \hat{\mathbf{z}}_I\}$ to perform calculations of the birefringence effects. Attached to the two former bases are the axis of propagation: z axis for the incident beam, z' axes for the transmitted beam and z'' axis for the reflected beam.

We shall now consider a Gaussian beam crossing a single anisotropic parallel plate of thickness d surrounded by a dielectric medium of optical index N_1 . The plate is located at $z = z_{in}$ and tilted with respect to \mathbf{k} (see Fig. A.2). The optical axis has an *a priori* arbitrary orientation. To compute the transmitted beam, the vector Fourier optics and

the 4×4 matrix formalism of Ref. [6] will be combined. In doing so, multiple reflections inside the parallel plate will be taken into account.

As indicated in Ref. [23], polarisation effects induced by the anisotropic plate can be computed by defining an operator acting on every plane wave constituting the Gaussian beam. This is further justified since we only consider here homogeneous anisotropic media. Hence, writing $\mathbf{E}_t(\mathbf{r})$ for the transmitted beam, one obtains [23, 24]

$$\mathbf{E}_t(\mathbf{r}') = \exp\left(\frac{-iz'}{2k}(P_x^2 + P_y^2)\right) \mathcal{F}\left[\overline{M}_t \exp\left(\frac{-iz_{in}}{2k}(P_x^2 + P_y^2)\right) \overline{\psi}(\mathbf{k}_\perp, 0) M_{3 \times 3} \mathbf{E}_0\right]. \quad (\text{A.34})$$

In Eq. (A.34), \overline{M}_t is a 3×3 matrix acting on the polarisation state of each plane wave and z' is an axis parallel to the z axis with $z' = 0$ at the exit of the plate (see Fig. A.2). This axis is used to describe the beam propagation after the plate. Inside the plate, the propagation of the plane waves is described by the matrix \overline{M}_t . Let us mention that the position of the z' axis along the exit face of the plate can be arbitrarily chosen since it only introduces a global phase shift.

However, in Eq. (A.34) \overline{M}_t is determined in the basis $\{\hat{\mathbf{x}}, \hat{\mathbf{y}}, \hat{\mathbf{z}}\}$. For consistency with the general 4×4 matrix method [6], \overline{M}_t must be determined in the plane wave polarisation basis. The polarisation vector basis is denoted by $\{\hat{\mathbf{s}}_{\text{pw}}, \hat{\mathbf{p}}_{\text{pw}}, \hat{\mathbf{k}}_{\text{pw}}\}$ where

$$\hat{\mathbf{s}}_{\text{pw}} = \frac{\hat{\mathbf{k}}_{\text{pw}} \times \hat{\mathbf{n}}}{|\hat{\mathbf{k}}_{\text{pw}} \times \hat{\mathbf{n}}|}, \quad \hat{\mathbf{p}}_{\text{pw}} = \hat{\mathbf{k}}_{\text{pw}} \times \hat{\mathbf{s}}_{\text{pw}}$$

correspond to the TE and TM waves respectively and where $\hat{\mathbf{n}}$ is the unit vector normal to the interface. The direction of the wave vector reads $\hat{\mathbf{k}}_{\text{pw}} = \mathbf{k}_{\text{pw}}/k$ with \mathbf{k}_{pw} given by Eq. (A.29) and by convention, $\{\hat{\mathbf{s}}_{\text{pw}}, \hat{\mathbf{p}}_{\text{pw}}, \hat{\mathbf{k}}_{\text{pw}}\} = \{\hat{\mathbf{x}}, \hat{\mathbf{y}}, \hat{\mathbf{z}}\}$ when $\mathbf{k}_\perp = 0$.

Since the plane of incidence is related to the plane wave vector one gets

$$\overline{M}_t = \Omega M_t \Omega^T \quad (\text{A.35})$$

with

$$\Omega = \begin{pmatrix} \hat{\mathbf{x}} \cdot \hat{\mathbf{s}}_{\text{pw}} & \hat{\mathbf{x}} \cdot \hat{\mathbf{p}}_{\text{pw}} & \hat{\mathbf{x}} \cdot \hat{\mathbf{k}}_{\text{pw}} \\ \hat{\mathbf{y}} \cdot \hat{\mathbf{s}}_{\text{pw}} & \hat{\mathbf{y}} \cdot \hat{\mathbf{p}}_{\text{pw}} & \hat{\mathbf{y}} \cdot \hat{\mathbf{k}}_{\text{pw}} \\ \hat{\mathbf{z}} \cdot \hat{\mathbf{s}}_{\text{pw}} & \hat{\mathbf{z}} \cdot \hat{\mathbf{p}}_{\text{pw}} & \hat{\mathbf{z}} \cdot \hat{\mathbf{k}}_{\text{pw}} \end{pmatrix}, \quad (\text{A.36})$$

$$M_t = \begin{pmatrix} \mathcal{M}_t & 0 \\ 0 & 0 \end{pmatrix} \quad (\text{A.37})$$

and where \mathcal{M}_t is the 2×2 matrix describing the transmission of the plane waves in the $\{\hat{\mathbf{s}}_{\text{pw}}, \hat{\mathbf{p}}_{\text{pw}}\}$ basis. The matrix \mathcal{M}_t is obtained by reducing the 4×4 matrix method of Ref. [6] to a 2×2 matrix algebra as described in section A.1.

Transmitted beam Intensity

Returning back to the transmission of Gaussian beams, Eq. (A.34) can be further simplified when one is interested in intensity measurements. For example, if an optical

polarisation component is located up stream of the anisotropic medium, the out-coming electric field reads as

$$\mathbf{E}_{out}(\mathbf{r}) = \frac{w_0}{\sqrt{2\pi}} \mathcal{F} \left[\exp \left(i \frac{(z_{in} + z') \mathbf{k}_\perp^2}{k} \right) \exp \left(\frac{-w_0^2 \mathbf{k}_\perp^2}{4} \right) J \overline{\mathcal{M}}_t M_{3 \times 3} \mathbf{E}_0 \right]$$

where

$$J = \begin{pmatrix} & & \\ \mathcal{J} & & 0 \\ 0 & 0 & 0 \end{pmatrix}$$

and \mathcal{J} is the 2×2 Jones matrix corresponding to this component [24]. The total intensity measured for this component is given by

$$\begin{aligned} I_{out} &= \iint |\mathbf{E}_{out}|^2 d^2 \mathbf{r}_\perp \\ &= \frac{w_0^2}{(2\pi)^3} \int \cdots \int \exp \left(\frac{-w_0^2 (\mathbf{k}_\perp^2 + \mathbf{k}'_\perp^2)}{4} \right) \exp \left(i \frac{(z_{in} + z') (\mathbf{k}_\perp^2 + \mathbf{k}'_\perp^2)}{k} \right) \\ &\quad \left[O_{3 \times 3} \mathbf{E}_0 \right] \cdot \left[O_{3 \times 3}^* (\mathbf{k}'_\perp) \mathbf{E}_0^* \right] \exp(i(\mathbf{k}_\perp - \mathbf{k}'_\perp) \cdot \mathbf{r}_\perp) d^2 \mathbf{k}_\perp d^2 \mathbf{k}'_\perp d^2 \mathbf{r}_\perp \quad (\text{A.38}) \end{aligned}$$

with $O_{3 \times 3} = J \overline{\mathcal{M}}_t M_{3 \times 3}$ and where the symbol $*$ stands for the complex conjugate.

If the matrix J does not depend on the transverse spatial coordinates, the previous equation is simplified to

$$I_{out} = \frac{w_0^2}{2\pi} \iint \exp \left(\frac{-w_0^2 \mathbf{k}_\perp^2}{2} \right) \left| O_{3 \times 3} \mathbf{E}_0 \right|^2 d^2 \mathbf{k}_\perp \quad (\text{A.39})$$

after integration over \mathbf{r}_\perp and \mathbf{k}'_\perp and using

$$\delta^2(\mathbf{k}_\perp - \mathbf{k}'_\perp) = (2\pi)^2 \iint \exp(i(\mathbf{k}_\perp - \mathbf{k}'_\perp) \cdot \mathbf{r}_\perp) d^2 \mathbf{r}_\perp$$

where $\delta^2(\mathbf{k}_\perp - \mathbf{k}'_\perp)$ is the Dirac distribution.

Eq. (A.39) shows explicitly that the total intensity depends only on the waist size and not on the beam size inside the anisotropic system. This observation has been already made and experimentally tested in Ref. [4].

Up to now only the transmission has been considered. Equivalent expressions can be obtained for the reflection by simply replacing \mathcal{M}_t by the extended Jones matrix describing the reflection.

Eq. (A.39) was obtained under the paraxial approximation. This equation can be used as it is but, depending on the required accuracy, one can perform further simplifications: the plane wave approximation and the Scalar Fourier approximation. The latter is the topic of the following section.

A.2.4 Scalar Fourier Approximation

Although vector Fourier optics is a useful formalism for describing the Gaussian beam, the cross polarisation effects are indeed very small [21] (though being observable but

essentially only in extinction experiments[23]). In addition, the birefringence induced by the beam angular divergence is also expected to be small, at least for realistic ellipsometry experiments.

To a good approximation, one can then assume that all plane waves constituting the Gaussian beam have the same wave vector \mathbf{k} (i.e. $\mathbf{k}_\perp = 0$). The polarisation effects induced by a birefringent plate will then be only related to the direction of the Gaussian beam's centre.

This approximation thus amounts to accounting for the Gaussian nature of the beam only in the calculation of the interference pattern of the beam after the plate, as in Ref. [4]. After the anisotropic plate, the beam is made of a sum of Gaussian beams transversally shifted by a distance (the transverse walk-off), induced by successive internal reflections (see Fig. A.2). Using Eqs. (A.14-A.17), the first transmitted beam can be written as

$$\mathbf{E}_{1t}(\mathbf{r}') = \left(\frac{2}{\pi\omega_0^2} \right)^{1/2} \frac{-iz_R}{q(z' + z_{in})} \exp\left(\frac{-ikx'^2}{2q(z' + z_{in})} \right) \left[\begin{array}{c} \exp\left(\frac{-ik(y' - \Delta_{a+})^2}{2q(z' + z_{in})} \right) \\ 0 \\ 0 \end{array} \exp\left(\frac{-ik(y' - \Delta_{b+})^2}{2q(z' + z_{in})} \right) \right] \mathcal{P}_+^{-1} \mathcal{T}_{1a+} \mathbf{e}_0 \quad (\text{A.40})$$

with $\mathbf{e}_0^T = (a_1, a_2)$ and where Δ_{a+} and Δ_{b+} are the transverse walk-offs. In biaxial media there are four different elementary transverse walk-offs

$$\Delta_{a\pm} = \frac{c}{\omega} \frac{N_1 d \sin \theta_1 \cos \theta_1}{|\bar{\mathbf{k}}_{a\pm} \cdot \hat{\mathbf{n}}|}, \quad \Delta_{b\pm} = \frac{c}{\omega} \frac{N_1 d \sin \theta_1 \cos \theta_1}{|\bar{\mathbf{k}}_{b\pm} \cdot \hat{\mathbf{n}}|},$$

where $\bar{\mathbf{k}}_{a\pm}$ and $\bar{\mathbf{k}}_{b\pm}$ are the wave vectors inside the anisotropic plate corresponding to the incident wave vector \mathbf{k} , i.e. the centre of the Gaussian beam. We should recall that all the matrices of Eqs. (A.17-A.17) are also determined with respect to the direction of the centre of the Gaussian beam.

When the transmission and reflection interface matrices are not diagonal it becomes difficult, if not impossible, to write a general formula for the n^{th} transmitted beam. However, using the following property of the Fourier transform

$$\psi(\mathbf{r}_\perp, z) = \mathcal{F}[\bar{\psi}(\mathbf{k}_\perp, z)] \Rightarrow \psi(\mathbf{r}_\perp - \Delta \hat{\mathbf{y}}, z) = \mathcal{F}[\bar{\psi}(\mathbf{k}_\perp, z) \exp(i\Delta k_y)], \quad (\text{A.41})$$

and taking the inverse Fourier transform of Eq. (A.40), one obtains

$$\mathcal{F}^{-1}[\mathbf{E}_{1t}(\mathbf{r}')] = \left(\frac{w_0^2}{2\pi} \right)^{1/2} \exp\left(i \frac{(z_{in} + z') \mathbf{k}_\perp^2}{k} \right) \exp\left(\frac{-w_0^2 \mathbf{k}_\perp^2}{4} \right) \left[\begin{array}{c} \exp(ik_y \Delta_{a+}) \\ 0 \end{array} \exp(ik_y \Delta_{b+}) \right] \mathcal{P}_+^{-1} \mathcal{T}_{1a+} \mathbf{e}_0.$$

It is therefore possible to sum up all the transmitted beams in the \mathbf{k}_\perp space by introducing a new set of 2×2 matrices:

$$\mathcal{W}_\pm = \begin{pmatrix} \exp(i\Delta_{a\pm} k_y) & 0 \\ 0 & \exp(i\Delta_{b\pm} k_y) \end{pmatrix} \quad (\text{A.42})$$

describing the transverse walk-off of the Gaussian beam's centre (see Fig. A.2). Following the method introduced in the previous section, one then obtains

$$\begin{aligned}\mathbf{E}_t(\mathbf{r}') &= \left(\frac{w_0^2}{2\pi}\right)^{1/2} \mathcal{F} \left[\exp\left(i\frac{(z_{in} + z')\mathbf{k}_\perp^2}{k}\right) \exp\left(\frac{-w_0^2\mathbf{k}_\perp^2}{4}\right) \left(\mathcal{T}_{a_{1+}} \tilde{\mathcal{P}}_+^{-1} \mathcal{T}_{1a_+} + \right. \right. \\ &\quad \left. \left. \mathcal{T}_{a_+} \tilde{\mathcal{P}}_+^{-1} \mathcal{R}_{a_{1-}} \tilde{\mathcal{P}}_- \mathcal{R}_{a_{1+}} \tilde{\mathcal{P}}_+^{-1} \mathcal{T}_{1a_+} + \dots \right) \mathbf{e}_0 \right] \\ &= \left(\frac{w_0^2}{2\pi}\right)^{1/2} \mathcal{F} \left[\exp\left(i\frac{(z_{in} + z')k_y^2}{k}\right) \exp\left(\frac{-w_0^2 k_y^2}{4}\right) \widetilde{\mathcal{M}}_t \mathbf{e}_0 \right],\end{aligned}\quad (\text{A.43})$$

with

$$\tilde{\mathcal{P}}_+^{-1} = \mathcal{W}_+ \mathcal{P}_+^{-1} \quad (\text{A.44})$$

$$\tilde{\mathcal{P}}_- = \mathcal{W}_- \mathcal{P}_- \quad (\text{A.45})$$

$$\widetilde{\mathcal{M}}_t = \mathcal{T}_{a_{1+}} \left[1 - \tilde{\mathcal{P}}_+^{-1} \mathcal{R}_{a_{1-}} \tilde{\mathcal{P}}_- \mathcal{R}_{a_{1+}} \right]^{-1} \tilde{\mathcal{P}}_+^{-1} \mathcal{T}_{1a_+}. \quad (\text{A.46})$$

In the scalar Fourier approximation the usual Stokes vectors [2] can be defined

$$S_{in} = \begin{pmatrix} |a_1|^2 + |a_2|^2 \\ |a_1|^2 - |a_2|^2 \\ a_1 a_2^* + a_1^* a_2 \\ i(a_1 a_2^* - a_1^* a_2) \end{pmatrix}, \quad S_{out} = \begin{pmatrix} \iint (|E_{tx}|^2 + |E_{ty}|^2) d^2 \mathbf{r}_\perp \\ \iint (|E_{tx}|^2 - |E_{ty}|^2) d^2 \mathbf{r}_\perp \\ \iint (E_{tx} E_{ty}^* + E_{tx}^* E_{ty}) d^2 \mathbf{r}_\perp \\ i \iint (E_{tx} E_{ty}^* - E_{tx}^* E_{ty}) d^2 \mathbf{r}_\perp \end{pmatrix},$$

where S_{in} and S_{out} are related to the incident beam and transmitted beam respectively. From Eq. (A.43) and following the calculation steps of section A.2.3 one can then determine the extended Mueller matrix of the plate M_S such that $S_{out} = M_S S_{in}$:

$$M_S = \begin{pmatrix} (\rho_{11}^2 + \rho_{12}^2)/2 + & (\rho_{11}^2 + \rho_{21}^2)/2 - & \rho_{11,12} \cos \phi_{11,12} + & \rho_{11,12} \sin \phi_{11,12} + \\ (\rho_{21}^2 + \rho_{22}^2)/2 & (\rho_{12}^2 + \rho_{22}^2)/2 & \rho_{21,22} \cos \phi_{21,22} & \rho_{21,22} \sin \phi_{21,22} \\ \\ (\rho_{11}^2 + \rho_{12}^2)/2 - & (\rho_{11}^2 + \rho_{22}^2)/2 - & \rho_{11,12} \cos \phi_{11,12} - & \rho_{11,12} \sin \phi_{11,12} - \\ (\rho_{21}^2 + \rho_{22}^2)/2 & (\rho_{21}^2 + \rho_{12}^2)/2 & \rho_{21,22} \cos \phi_{21,22} & \rho_{21,22} \sin \phi_{21,22} \\ \\ \rho_{11,21} \cos \phi_{11,21} + & \rho_{11,21} \cos \phi_{11,21} - & \rho_{11,22} \cos \phi_{11,22} + & \rho_{11,22} \sin \phi_{11,22} - \\ \rho_{12,22} \cos \phi_{12,22} & \rho_{12,22} \cos \phi_{12,22} & \rho_{12,21} \cos \phi_{12,21} & \rho_{12,21} \sin \phi_{12,21} \\ \\ -\rho_{11,21} \sin \phi_{11,21} - & -\rho_{11,21} \sin \phi_{11,21} + & -\rho_{11,22} \sin \phi_{11,22} - & \rho_{11,22} \cos \phi_{11,22} - \\ \rho_{12,22} \sin \phi_{12,22} & \rho_{12,22} \sin \phi_{12,22} & \rho_{12,21} \sin \phi_{12,21} & \rho_{12,21} \cos \phi_{12,21} \end{pmatrix} \quad (\text{A.47})$$

with

$$\rho_{ij}^2 = \frac{w_0}{\sqrt{2\pi}} \int \exp\left(\frac{-w_0^2 k_y^2}{2}\right) |m_{ij}|^2 dk_y, \quad (\text{A.48})$$

$$\begin{aligned}\rho_{ij,kl} &= \frac{w_0}{\sqrt{2\pi}} \left| \int \exp\left(\frac{-w_0^2 k_y^2}{2}\right) m_{ij} m_{kl}^* dk_y \right| \\ \cos \phi_{ij,kl} &= \frac{1}{2\rho_{ij,kl}} \int \exp\left(\frac{-w_0^2 k_y^2}{2}\right) [m_{ij} m_{kl}^* + m_{ij}^* m_{kl}] dk_y \\ \sin \phi_{ij,kl} &= \frac{1}{2i\rho_{ij,kl}} \int \exp\left(\frac{-w_0^2 k_y^2}{2}\right) [m_{ij} m_{kl}^* - m_{ij}^* m_{kl}] dk_y\end{aligned}\quad (\text{A.49})$$

and $i, j, k, l = 1, 2$. The matrix elements m_{ij} are defined by

$$\mathcal{J}\widetilde{\mathcal{M}}_t = \begin{pmatrix} m_{11} & m_{12} \\ m_{21} & m_{22} \end{pmatrix}.$$

One feature related to the integral form of Eqs. (A.48-A.49) is that $\rho_{ij,kl} \neq \rho_{ij}\rho_{kl}$. This means that one cannot define a Jones matrix (integrated over \mathbf{k}_\perp).

A.2.5 Example: uniaxial parallel plate

To illustrate our model we shall now consider the very important example of a quarter wave quartz plate (QWP) [3]. The equivalence between our approach and the results of Ref. [4] is formally proved in annex I and details concerning the evaluation of Eq. (A.39) are given in annex II.

To study the accuracy of the plane wave and scalar Fourier approximations we shall adopt one of the examples of Ref. [4]: a Gaussian laser beam of wavelength $\lambda = 0.6328 \mu\text{m}$ and waist $w_0 = 100 \mu\text{m}$. For this wavelength, the quartz ordinary and extraordinary optical indices are $n_o = 1.542637$ and $n_e = 1.551646$.

Since interference effects are sensitive to the plate thickness, we choose to compare two realistic components: a first order QWP ($d = 87.6010 \mu\text{m}$) and a tenth order QWP ($d = 719.9686 \mu\text{m}$). Finally, two different polar orientations of the optical axis (see annex II) are chosen: $\theta_c = \pi/2$ (= optical axis in the plane of interface) and $\theta_c = \pi/4$. The remaining geometric degrees of freedom are the optical axis azimuth ϕ_c and the incidence angle of the centre of the Gaussian beam θ_1 .

The incident beam is assumed to be polarised along ox so that $\mathbf{E}_0 = \hat{\mathbf{x}}$ (or $S_{in} = (1, 1, 0, 0)$). As in Fig. A.2, the beam crosses a quartz plate and we shall first consider that an intensity measurement is performed after a perfect linear polariser aligned along ox . We shall denote by $I_{||,Gauss}$ and $I_{||,pw}$ the corresponding intensities computed according to Eq. (A.47) (scalar Fourier approximation) and in the plane wave approximation. We checked numerically that the results obtained in the scalar Fourier approximation agree with the general expression of A.39 (to observe noticeable differences one must consider beam waist as small as $10 \mu\text{m}$ which are outside the scope of this article).

The relative numerical precision of the results presented below has been estimated to be of the order of 10^{-6} . This number was determined by checking the energy conservation and by looking at the difference between the plane wave and the scalar Fourier approximation at normal incidence (they are similar by construction).

$I_{||,Gauss}$ is shown as a function of ϕ_c and θ_1 in Fig. A.3(a-b) and A.4(a-b) for two plate thicknesses and two orientations of the optical axis. As expected [4], the interference pattern is denser for the tenth order plate (Fig. A.4(a) and (b)) and the intensity is not π symmetric in ϕ_c when $\theta_c < \pi/2$ and $\theta_1 \neq 0$ (Fig. A.3(b) and A.4(a)).

Fixing ($\theta_c = \pi/2, \phi_c = 0$) and ($\theta_c = \pi/4, \phi_c = \phi/4$), $I_{||,Gauss}$ and $I_{||,pw}$ are plotted as a function of θ_1 in Fig. A.5 (a), (b) respectively for the tenth order QWP. In these figures, $I_{||,Gauss}$ is also computed for two beam waists $w_0 = 100 \mu\text{m}$ and $200 \mu\text{m}$. Sizable differences appear which increase with the incident angle but decrease when the beam waist increases.

To quantify the differences the following ratio is computed

$$\delta(I_{||}) = \frac{I_{||,Gauss} - I_{||,pw}}{I_{||,Gauss}}$$

and plotted as a function of ϕ_c and θ_1 in Fig. A.6(a-b) and A.7(a-b) for the two plate thicknesses and the two orientations of the optical axis. One can see that $\delta(I_{||})$ increases with the plate thickness and the angle of incidence. At $\theta_1 \approx 0.2$ rad and $\theta_c = \pi/2$, large differences of the order of 10% appear for the tenth QWP. Variations of $\delta(I_{||})$ with ϕ_c are also sizable, especially for $\theta_c < \pi/4$ where interference amplitudes are badly reproduced by the plane wave approximation for small values of $I_{||}$.

Another interesting quantity is the degree of circular polarisation when the beam passes through a perfect circular polariser, instead of the linear polariser of the above example. If the polariser is circular left, using Eq. (A.47) and the standard Mueller matrices for perfect polarisers [2] the beam intensity reads as

$$I_L = \frac{\rho_{11}^2 + \rho_{21}^2}{2} - \rho_{11,21} \sin \phi_{11,21}$$

for $S_{in} = (1, 1, 0, 0)$ and $\theta_c = \pi/2$. When $\phi_c \approx \pi/4$, I_L is small and can be minimised in the (θ_1, ϕ_c) space [4]. We present here I_L^{-1} as a function of θ_1 and ϕ_c for the tenth order QWP in Fig. A.8(a). The results of Ref. [4] are recovered, although rotating the plate and rotating the polarisation, as done in this reference, are not strictly equivalent [25, 11, 12]. In Fig. A.8(b) the relative difference between the plane wave and the Gaussian beam intensities

$$\delta(I_L) = \frac{I_{L,Gauss} - I_{L,pw}}{I_{L,Gauss}}$$

is shown. Large differences corresponding to small values of I_L are observed. This demonstrates the necessity of accounting for the Gaussian nature of the beam in such particular, but important, cases. Note that the scalar Fourier approximation and the general paraxial calculations are also in perfect agreement here.

Finally the ratio $\rho_{11}\rho_{21}/\rho_{11,21}$ is computed. It increases with θ_1 and the plate thickness but, even for the tenth order QWP, it does not exceed 0.2 % for any values of ϕ_c and $\theta_1 = 0.2$ rad. Assuming $\rho_{11}\rho_{21} \approx \rho_{11,21}$, a Jones matrix can thus be defined with an accuracy of the order of a few per mille.

From this study one may conclude that:

- the scalar Fourier approximation is very closed to the paraxial approximation when the beam waist is not too small;
- the plane wave approximation mainly holds for thin quartz plates, small incident angles, large beam waists and optical axes nearly in the interface plane. If these conditions are not fulfilled, the Gaussian nature of the beam must be taken into account.
- It is crucial to account for the Gaussian nature of the beam when high performances of QWP are foreseen.

More generally, accuracies of the various approximations depend strongly on the medium birefringence and geometrical configurations.

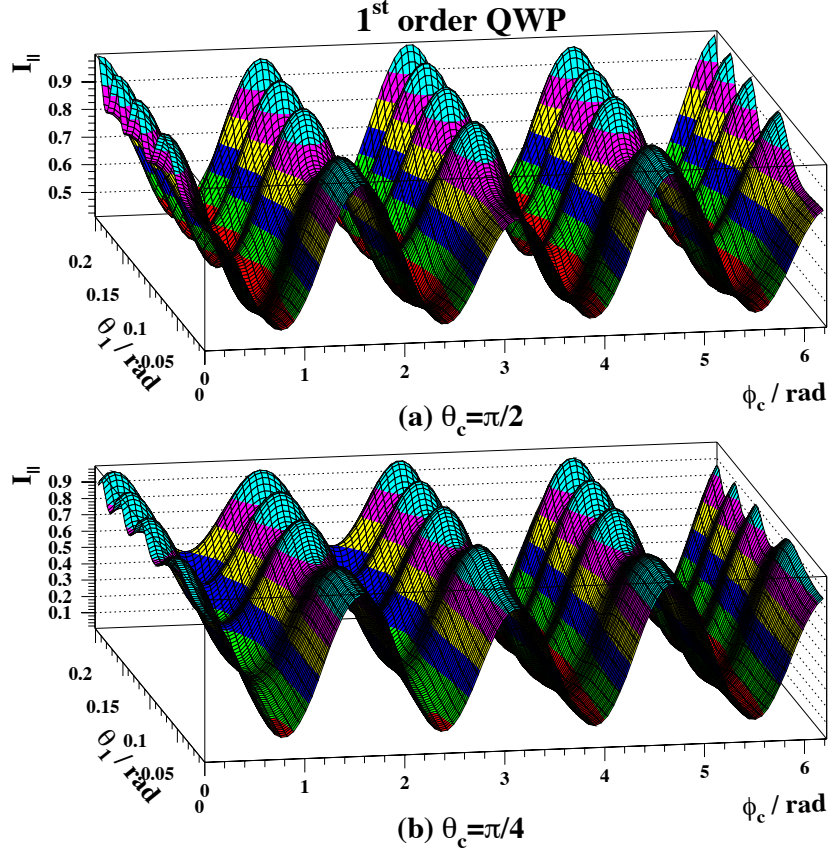


Figure A.3: The intensity of a Gaussian beam measured after a first order QWP and a perfect linear polariser: (a) for an optical axis in the plane of interface, (b) for an optical axis inclined by $\pi/4$ with respect to the plane of interface. The calculations are performed using the scalar Fourier approximation and are shown as a function of the angle of incidence θ_1 and the azimuthal angle of the optical axis ϕ_c .

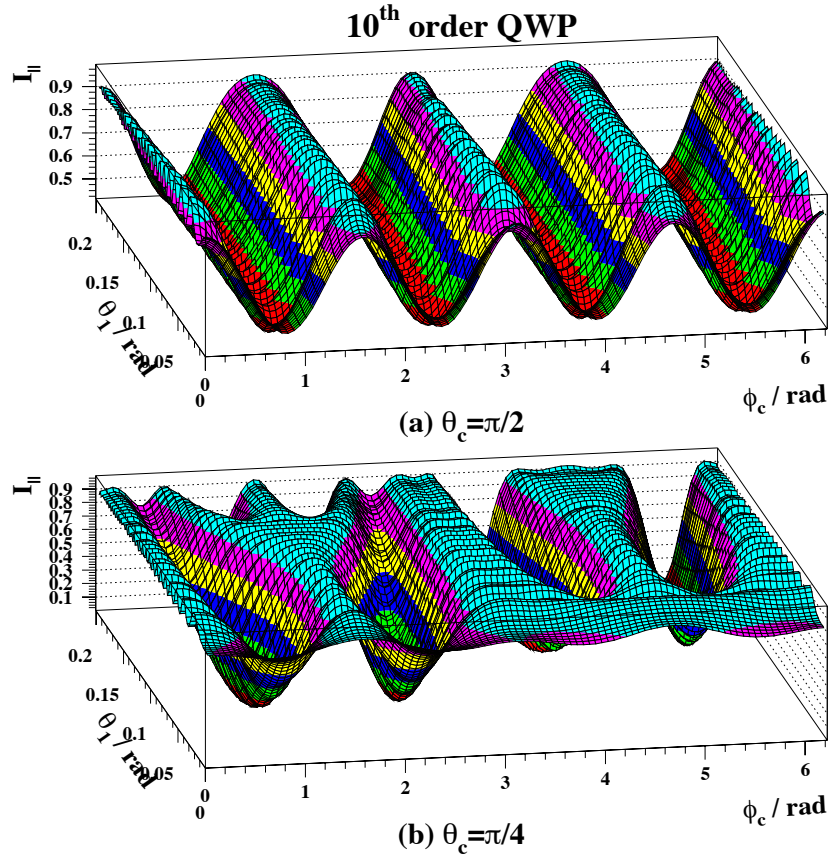


Figure A.4: As in Fig. A.3 but for a tenth order QWP.

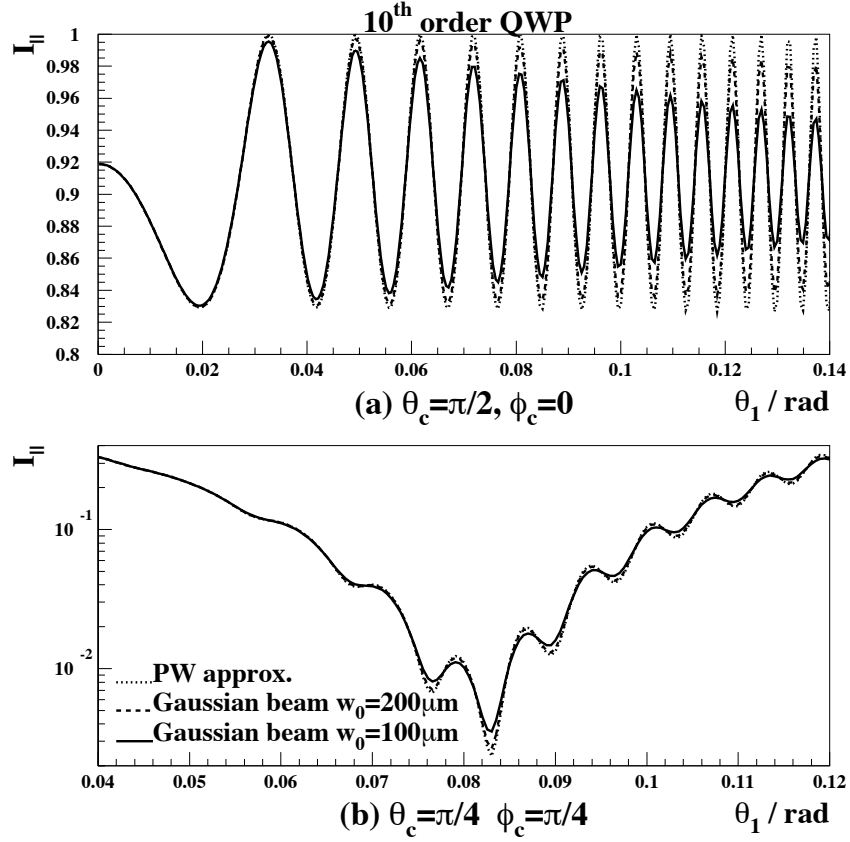


Figure A.5: The intensity of a Gaussian beam measured after a tenth order QWP and a perfect linear polariser as a function of the angle of incidence θ_1 . The orientations of the QWP optical axis are fixed to: (a) $\theta_c = \pi/2$ and $\phi_c = 0$, (b) $\theta_c = \pi/4$ and $\phi_c = \pi/4$. The full lines and dashed lines represent the calculations performed using the scalar Fourier approximations for $w_0 = 100 \text{ m}\mu$ and $w_0 = 200 \text{ m}\mu$ respectively. The dotted lines show the calculations performed using the plane wave approximation.

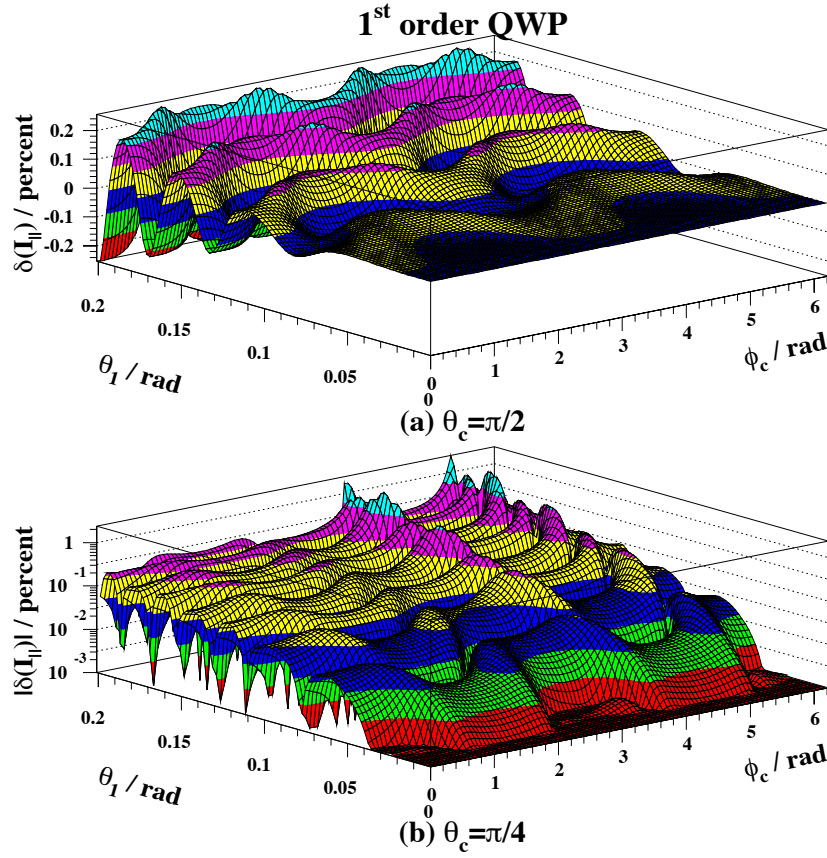


Figure A.6: *Relative differences between the quantities of Fig. A.3 using the plane wave approximation and the scalar Fourier approximation.*

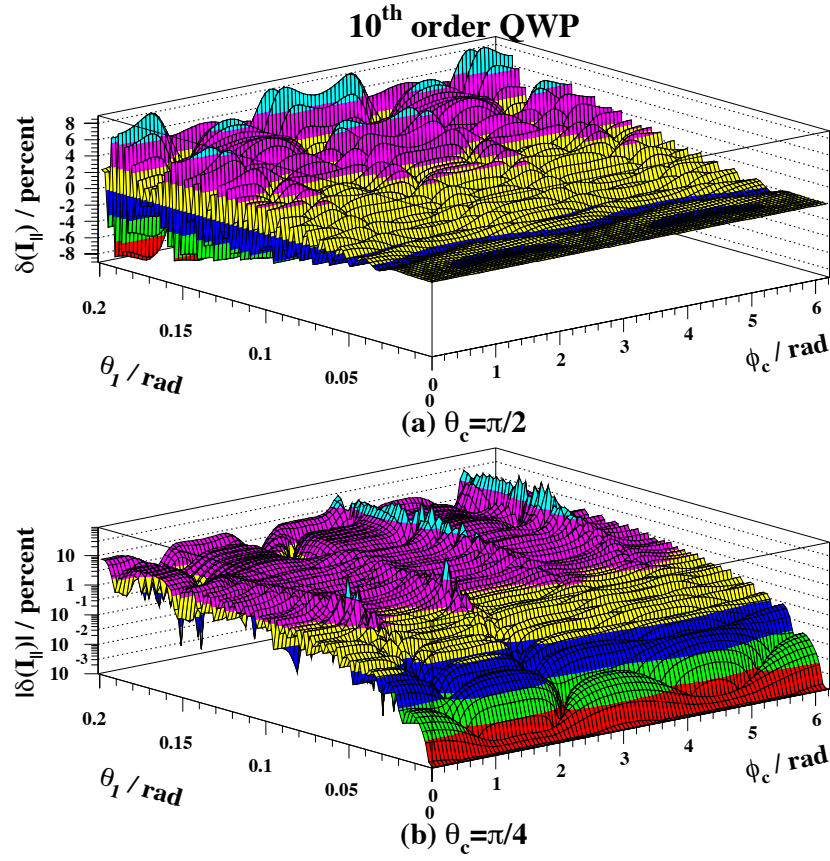


Figure A.7: As in a Fig. A.6 but for the quantities of Fig. A.4.

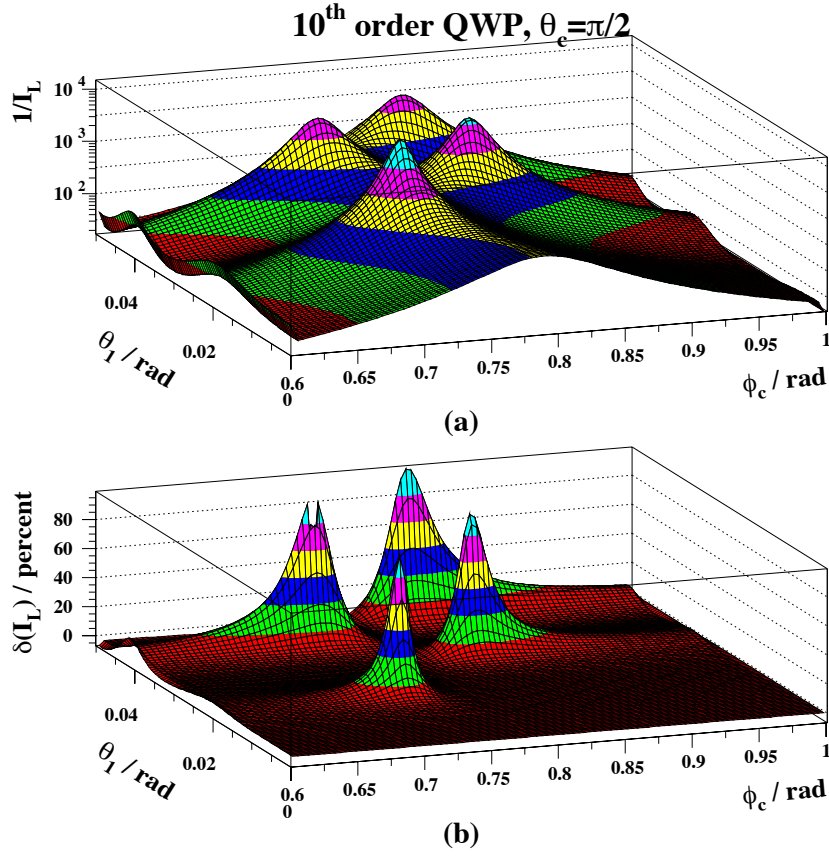


Figure A.8: (a) The inverse of the intensity measured after a tenth order QWP and a perfect left circular polariser. The calculations are performed using the scalar Fourier approximation and are shown as a function of the incident angle θ_1 and the azimuthal angle of the optical axis ϕ_c . (b) Relative difference between the quantity shown in the top plot calculated using the scalar Fourier approximation and the plane wave approximation. For these figures, the optical axis is taken to be in the plane of interface ($\theta_c = \pi/2$).

A.2.6 Conclusion

General expressions describing the transmission and reflection of a Gaussian beam by anisotropic parallel plates have been obtained. The vector Fourier optics formalism of Refs. [20, 21] has been used as general framework. Multiple reflections inside the anisotropic medium are taken into account using a 2×2 matrix algebra derived from the general 4×4 matrix formalism of Ref.[6]. The only assumption supplied for these calculations is the paraxial approximation.

To simplify the calculations, a useful approximation introduced in Ref. [4] is then considered. This approximation consists of taking into account the Gaussian nature of the beam only in the interference pattern of the transmitted (or reflected) beam. Birefringence effects induced by the angular divergence of the beam are then neglected. The accuracy of this approximation was checked for the particular case of uniaxial quartz parallel plates. For beam waists that are not too small, no noticeable differences were observed compared to the general expression.

The precision of the plane wave approximation has also been checked using the example of quartz plates. Noticeable differences were observed here. These discrepancies do not depend trivially on the geometrical parameters. Roughly, we concluded that they increase with the plate thickness and the angle of incidence. In the case of ellipsometry where high purity circular polarisation is foreseen, it was shown that an account of the Gaussian nature of the beam is necessary.

As a general remark, the accuracies of the various approximations presented in this article depend decisively on the birefringence of the medium, laser wavelength, geometrical configuration and type of energy measurement. They must then be checked case by case.

Interference effects, observed in the variations of the transmitted beam intensity as a function of the angle of incidence and optical axis azimuth, suggest that a very precise calibration of a birefringent plate can be performed without any other optical components.

A.2.7 Annex I

In Ref. [4], the transmission of a Gaussian beam through a tilted quartz plate has been determined. The configuration is restricted to a tilt axis perpendicular or parallel to the optical axis which is itself located in the interface. In this section we show the equivalence between the results of Ref. [4] and the formalism of section A.2.4.

The elements of the transmission matrix are written as

$$\begin{aligned} m_{oo} &= \frac{t_{1o}t_{o1} \exp(-i(k_y\Delta_o + \delta_o))}{1 - r_o^2 \exp(-2i(k_y\Delta_o + \delta_o))} \\ m_{ee} &= \frac{t_{1e}t_{e1} \exp(-i(k_y\Delta_e + \delta_e))}{1 - r_e^2 \exp(-2i(k_y\Delta_e + \delta_e))} \\ m_{oe} &= m_{eo} = 0 \end{aligned}$$

where e and o refer to the extraordinary and ordinary waves respectively. The non zero

extended Mueller matrix elements are given by:

$$|\rho_{oo}|^2 = \sqrt{\frac{w_0^2 k^2}{2\pi}} \int |m_{oo}|^2 \exp\left(\frac{-w_0^2 k_y^2}{2}\right) dk_y \quad (\text{A.50})$$

$$|\rho_{ee}|^2 = \sqrt{\frac{w_0^2 k^2}{2\pi}} \int |m_{ee}|^2 \exp\left(\frac{-w_0^2 k_y^2}{2}\right) dk_y \quad (\text{A.51})$$

$$\begin{aligned} \rho_{oo;ee} \sin \phi_{oo;ee} &= \frac{1}{2i} \int [m_{oo} m_{ee}^* - m_{oo}^* m_{ee}] \exp\left(\frac{-w_0^2 k_y^2}{2}\right) dk_y \\ &= \sqrt{\frac{w_0^2 k^2}{2\pi}} \int [\Re(m_{ee}) \Im(m_{oo}) - \Re(m_{oo}) \Im(m_{ee})] \exp\left(\frac{-w_0^2 k_y^2}{2}\right) dk_y \end{aligned} \quad (\text{A.52})$$

$$\begin{aligned} \rho_{oo;ee} \cos \phi_{oo;ee} &= \frac{1}{2} \int [m_{oo} m_{ee}^* + m_{oo}^* m_{ee}] \exp\left(\frac{-w_0^2 k_y^2}{2}\right) dk_y \\ &= \sqrt{\frac{w_0^2 k^2}{2\pi}} \int [\Re(m_{ee}) \Re(m_{oo}) + \Im(m_{oo}) \Im(m_{ee})] \exp\left(\frac{-w_0^2 k_y^2}{2}\right) dk_y \end{aligned}$$

with $m_{ij} = \Re(m_{ij}) + i\Im(m_{ij})$ and where $r_e, r_o, t_{e1}, t_{o1}, t_{1e}, t_{1o}$ are the Fresnel coefficients for the particular geometrical configuration studied here (expressions can be found in Ref. [8]).

In Ref. [4] a Jones matrix

$$\begin{pmatrix} \sqrt{2a_1} & 0 \\ 0 & \sqrt{2a_2} \exp\left(-i \arcsin \frac{a_3}{\sqrt{a_1 a_2}}\right) \end{pmatrix} \quad (\text{A.53})$$

is defined and expressions for a_1, a_2 and a_3 are provided (Eqs. (A16a), (A16b) and (A16c) in Appendix I of Ref. [4]).

To demonstrate the equivalence between our approach and the one of Ref. [4] we must show that Eqs. (A.50), (A.51) and (A.52) are equivalent forms of $2a_1, 2a_2$ and $2a_3$ respectively. In order to prove this one just has to expand the integral kernels and then perform the integration over k_y . Since the scalar Fourier approximation was implicitly assumed in Ref. [4], one finds:

$$\begin{aligned} \frac{|\rho_{oo}|^2}{2} &= \frac{t_x^2}{2} \left(1 + r_x^2 \left[1 + 2 \cos(4\varphi_x) \exp\left(\frac{-2\Delta^2}{w_0^2}\right) \right] + \right. \\ &\quad \left. 2r_x^3 \left[\cos(2\varphi_x) \exp\left(\frac{-\Delta^2}{2w_0^2}\right) + \cos(6\varphi_x) \exp\left(\frac{-9\Delta^2}{2w_0^2}\right) \right] \right. \\ &\quad \left. + r_x^4 \left[1 + 2 \cos(4\varphi_x) \exp\left(\frac{-2\Delta^2}{w_0^2}\right) + 2 \cos(8\varphi_x) \exp\left(\frac{-8\Delta^2}{w_0^2}\right) \right] + \dots \right) \end{aligned} \quad (\text{A.54})$$

where the notations of Ref. [4] $r_x = r_o^2, t_x = t_{1o} t_{o1}, \varphi_x = \delta_e, \varphi_x = \delta_o$ and $\Delta \approx 2\Delta_o \approx 2\Delta_e$ have been adopted. Eq. (A.54) can be further written as a series, and this leads to Eq. (A16a) of Ref. [4].

The series expansion of $|\rho_{ee}|^2/2$ is obviously obtained by replacing r_x and t_x by $r_y = r_e^2$ and $t_y = t_{1e} t_{e1}$ respectively in Eq. (A.54). This leads to Eq. (A16b) of Ref. [4].

In the same way one finally obtains

$$\begin{aligned} \frac{\rho_{oo;ee}}{2} \sin \phi_{oo;ee} = & \frac{t_x t_y}{2} \left\{ -\sin(\varphi_x - \varphi_y) + \exp\left(\frac{-\Delta^2}{2w_0^2}\right) \left(r_x \sin(3\varphi_x - \varphi_y) - r_y \sin(3\varphi_y - \varphi_x) \right) + \right. \\ & r_x r_y \left[-\sin(3[\varphi_x - \varphi_y]) + \exp\left(\frac{-\Delta^2}{2w_0^2}\right) \left(r_y \sin(5\varphi_y - 3\varphi_x) - r_x \sin(5\varphi_x - 3\varphi_y) \right) + \right. \\ & \exp\left(\frac{-2\Delta^2}{w_0^2}\right) \left(\frac{r_y}{r_x} \sin(5\varphi_y - \varphi_x) - \frac{r_x}{r_y} \sin(5\varphi_x - \varphi_y) \right) + \\ & \left. \left. \exp\left(\frac{-9\Delta^2}{2w_0^2}\right) \left(\frac{r_y^2}{r_x} \sin(7\varphi_y - \varphi_x) - \frac{r_x^2}{r_y} \sin(7\varphi_x - \varphi_y) \right) \right] + \dots \right\} \end{aligned}$$

which leads to Eq. (A16c) of Ref. [4].

Let us mention that, as stated in section A.2.4, Eq. (A.53) represents the Jones matrix of a quarter wave plate only under the approximation $\rho_{oo,ee} \approx \rho_{oo}\rho_{ee}$.

A.2.8 Annex II

In this section, ingredients for the calculation of the double integral of Eq. (A.39) are given.

Following Ref. [12] we write

$$\hat{\mathbf{c}} = \sin \theta_c \cos \phi_c \hat{\mathbf{x}}_{\mathbf{I}} + \sin \theta_c \sin \phi_c \hat{\mathbf{y}}_{\mathbf{I}} + \cos \theta_c \hat{\mathbf{z}}_{\mathbf{I}}$$

for the direction of the optical axis inside the quartz plate. $\{\hat{\mathbf{x}}_{\mathbf{I}}, \hat{\mathbf{y}}_{\mathbf{I}}, \hat{\mathbf{z}}_{\mathbf{I}}\}$ is the basis attached to the quartz plate (see Fig. A.2). In this basis, the wave vectors of the plane wave (see Eq. (A.29)) and Gaussian beam centre are given by:

$$\begin{aligned} \mathbf{k}_{\mathbf{pw}} &= k_x \hat{\mathbf{x}}_{\mathbf{I}} + (k_y \cos \theta_1 + k_z \sin \theta_1) \hat{\mathbf{y}}_{\mathbf{I}} + (k_z \cos \theta_1 - k_y \sin \theta_1) \hat{\mathbf{z}}_{\mathbf{I}} \\ \mathbf{k} &= k \sin \theta_1 \hat{\mathbf{y}}_{\mathbf{I}} + k \cos \theta_1 \hat{\mathbf{z}}_{\mathbf{I}} \end{aligned}$$

with $k_z \approx k(1 - \mathbf{k}_{\perp}^2/(2k^2))$. The plane wave incident and azimuthal angles read as

$$\cos \theta_{1pw} = \frac{k_z}{k} \cos \theta_1 - \frac{k_y}{k} \sin \theta_1, \quad \tan \phi_{pw} = \frac{k_z \sin \theta_1 + k_y \cos \theta_1}{k_x}.$$

The ordinary and extraordinary wave vectors corresponding to $\mathbf{k}_{\mathbf{pw}}$ and $\hat{\mathbf{c}}$ are determined using the compact expression of Ref. [12]. The electric polarisation vectors inside the plate are determined using the general formula of Ref. [6].

Expressions for the interface matrices of Eqs. (A.14-A.17) are formally determined using the Maple software package [26]. These expressions are much too long to be reproduced here.

The rotation matrix Ω (see Eq. (A.36)) is obtained from

$$\begin{aligned} \hat{\mathbf{s}}_{\mathbf{pw}} &= N_s [(k_y \cos \theta_1 + k_z \sin \theta_1) \hat{\mathbf{x}} - k_x \cos \theta_1 \hat{\mathbf{y}} - k_x \sin \theta_1 \hat{\mathbf{z}}] \\ \hat{\mathbf{p}}_{\mathbf{pw}} &= N_p [(k_x k_z \cos \theta_1 - k_x k_y \sin \theta_1) \hat{\mathbf{x}} + (k_y k_z \cos \theta_1 + k_z^2 \sin \theta_1 + k_x^2 \sin \theta_1) \hat{\mathbf{y}} \\ &\quad + (-\mathbf{k}_{\perp}^2 \cos \theta_1 - k_y k_z \sin \theta_1) \hat{\mathbf{z}}] \\ \hat{\mathbf{k}}_{\mathbf{pw}} &= N_k [k_x \hat{\mathbf{x}} + k_y \hat{\mathbf{y}} + k_z \hat{\mathbf{z}}] \end{aligned}$$

where N_s , N_p and N_k are normalisation factors.

A.3 Effects of surfaces roughness on the transmission of Gaussian beams by anisotropic parallel plates

In this section, an article published in Journal of Physics D [27] is reproduced.

A.3.1 Introduction

The high-accuracy universal polarimeter (HAUP) [28] has proved to be a very useful instrument to measure crystal optical properties (see for instance [29, 30, 31] and references therein). The principle is simple and was introduced a long time ago (see [32] for an historical introduction): the light intensity measured after a rotating high quality polariser, a crystal plate (the sample) and a high quality rotating analyser, is fitted to a theoretical formula with several coefficients as free parameters where the delay due to birefringence and optical activity can be determined.

The accuracy of this instrument has now reached the few 10^{-5} level and systematic errors contributing at this order of magnitude have been investigated [33, 34, 35]. The conclusion is that roughness is very probably one of the main source of systematic uncertainties.

However, despite an extensive literature on surface roughness [36, 37], no theoretical expression for the transmission of a Gaussian beam by an anisotropic rough platelet is available. It is the purpose of this article to provide this expression. We consistently take into account the Gaussian nature of the laser beam, the multiple reflection inside the plate and the roughness of both plate faces. To simplify the calculations we further restrict ourselves to uniaxial homogeneous crystals. As a result, we find that unlike plane waves, specular Gaussian beams are affected by the surface roughness, even in first order perturbation theory.

The physical origin of this phenomenon is the angular distribution, or plane wave expansion, of Gaussian beams [38]. Since the plane waves constituting a Gaussian beam have different wave vectors, a given plane wave can then be scattered in the specular direction of the other ones. The resulting interference pattern leads to an *a priori* non-vanishing contribution of the scattered field in the specular region. To some extent, this phenomenon is thus related to the near-specular scattering by rough surfaces introduced in [39].

Another aspect of realistic platelet surfaces is the interface parallelism fault. Depending on the wedge angle, this fault can compete with roughness in the modifications of the transmitted beam polarisation. The nature of these effects is however different. Given the relative orientation of the two plate interfaces, the wedge effect is univocal whereas roughness, as will be shown in this paper, is of random nature. It is then most likely that these two effects cannot compensate each other. In principle, the perturbative calculations reported in the present article hold for both effects. Nevertheless, the wedge effect can be described by the boundary matching method applied a long time ago to isotropic wedges [40]. We shall report this calculation in a future publication and restrict ourselves here to platelet roughness.

This article is organised as follows. In section A.3.2 we derive the theoretical expressions and numerical simulations of quartz plates are presented in section A.3.3.

A.3.2 Formalism

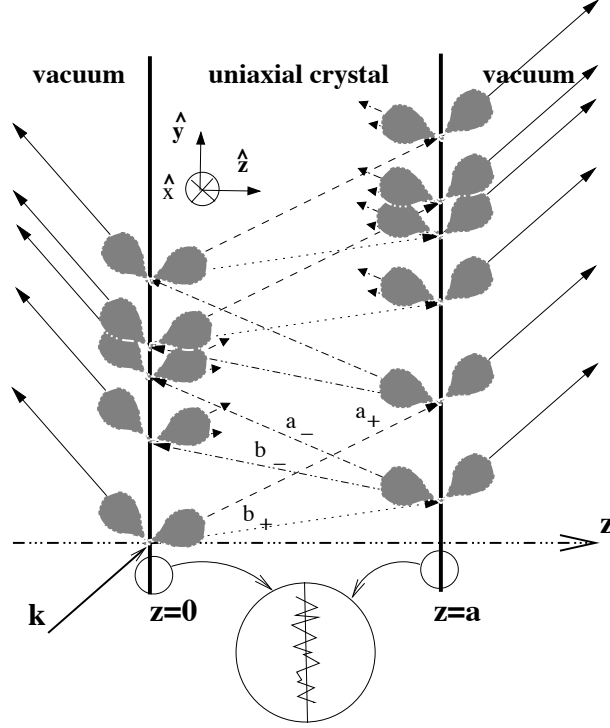


Figure A.9: *Schematic view of the plane wave propagation in the anisotropic slab. For the sake of clarity, some of the inner reflected rays are represented by small arrows. The plane of incidence coincides with the plane yz . Symbols a_{\pm} and b_{\pm} correspond to the four possible propagation directions inside the medium. The vector basis $\{\hat{x}, \hat{y}, \hat{z}\}$ used throughout this article is also shown. The grey areas symbolise the scattered light due to surface roughness.*

The choice of the theoretical formalism is driven by the properties of the crystal plate surfaces under study. Fortunately, an exhaustive experimental study on crystal surfaces has recently been published [41]. Most of the high quality polished crystal surfaces used in optics have a profile surface correlation length of the order of the optical wavelength and a root mean square roughness of the order of a few angströms. This means that one can safely use a first order perturbation theory neglecting the local field effects[42, 43]. The formalism more suitable for our problem is the one introduced in [44] and generalised to anisotropic over-layers in [44, 45]. However, in the latter reference, the anisotropy is treated perturbatively and only the reflection of plane waves is considered. We shall then extend this formalism to platelet transmission taking fully into account the plate anisotropy and treating perturbatively the plate roughness.

In the following we try to be concise, referring to [44, 45] for further details. The wave equation corresponding to the system represented in figure A.9 is:

$$\nabla \times \nabla \times \mathbf{E}(\mathbf{r}) = \omega^2 \mu_0 \mathbf{D}(\mathbf{r}) \quad (\text{A.55})$$

with $\mathbf{D}(\mathbf{r}) = \mathcal{E}(\mathbf{z})\mathbf{E}(\mathbf{r})$ and

$$\begin{aligned} \mathcal{E}(z) = \Theta\left(-z + h_0(x, y)\right)\epsilon_0\mathbf{1} + \left[\Theta\left(z - h_0(x, y)\right) - \Theta\left(z - a - h_a(x, y)\right)\right]\underline{\epsilon} \\ + \Theta\left(z - a - h_a(x, y)\right)\epsilon_0\mathbf{1} \quad (\text{A.56}) \end{aligned}$$

where $\mathbf{1}$ is the 3×3 identity matrix and Θ is the Heaviside function. For uniaxial media, it is useful to write [46]

$$\underline{\epsilon} = \epsilon_\perp\mathbf{1} + (\epsilon_\parallel - \epsilon_\perp)\hat{\mathbf{c}}\hat{\mathbf{c}}$$

with $\hat{\mathbf{c}}^T = \{c_x, c_y, c_z\}$ the unit vector along the optical axis, $\hat{\mathbf{c}}\hat{\mathbf{c}}$ a dyad and $\epsilon_\perp = n_o^2\epsilon_0$, $\epsilon_\parallel = n_e^2\epsilon_0$ the ordinary and extraordinary components of the dielectric tensor. In equation (A.56), the two functions $h_0(x, y)$ and $h_a(x, y)$ are the profiles of the two surfaces located at $z = 0$ and $z = a$ respectively. As usual [47], we assume that the two planes $z = 0$ and $z = a$ are defined such that the mean profiles vanish, i.e. $\langle h_0 \rangle = \langle h_a \rangle = 0$.

The solution of equation (A.55) can be written $\mathbf{E}(\mathbf{r}) = \mathbf{E}_0(\mathbf{r}) + \mathbf{E}'(\mathbf{r})$ with $\mathbf{E}_0(\mathbf{r})$ given by the zero order wave equation

$$\nabla \times \nabla \times \mathbf{E}_0(\mathbf{r}) = \omega^2 \mu_0 \mathbf{D}_0(\mathbf{r}) \quad (\text{A.57})$$

where $\mathbf{D}_0(\mathbf{r}) = \mathcal{E}_0(z)\mathbf{E}_0(\mathbf{r})$ and

$$\mathcal{E}_0(z) = \Theta(-z)\epsilon_0\mathbf{1} + \left(\Theta(z) - \Theta(z - a)\right)\underline{\epsilon} + \Theta(z - a)\epsilon_0\mathbf{1}. \quad (\text{A.58})$$

To first order in $\omega h/c$ [45], one has $\mathcal{E}(z) = \mathcal{E}_0(z) + \delta\mathcal{E}(z)$ with

$$\delta\mathcal{E}(z) \approx \left(h_a(x, y)\delta(z - a) - h_o(x, y)\delta(z)\right) \left[(\epsilon_\perp - \epsilon_0)\mathbf{1} + (\epsilon_\parallel - \epsilon_\perp)\hat{\mathbf{c}}\hat{\mathbf{c}}\right] \quad (\text{A.59})$$

with $\delta(z)$ the Dirac distribution.

To derive the differential equation for the first order scattered field $\mathbf{E}'(\mathbf{r})$, we introduce the Fourier transform

$$\mathbf{E}(\mathbf{K}; z) = \mathcal{F}[\mathbf{E}(\mathbf{r})] = \frac{1}{2\pi} \int \mathbf{E}(\mathbf{r}) \exp(i\mathbf{K} \cdot \mathbf{R}) d^2\mathbf{R}$$

where $\mathbf{R} = (\mathbf{r} \cdot \hat{\mathbf{x}})\hat{\mathbf{x}} + (\mathbf{r} \cdot \hat{\mathbf{y}})\hat{\mathbf{y}}$ and $\mathbf{K} = (\mathbf{k} \cdot \hat{\mathbf{x}})\hat{\mathbf{x}} + (\mathbf{k} \cdot \hat{\mathbf{y}})\hat{\mathbf{y}}$ with \mathbf{k} the wave vector. Here, since we are considering Gaussian beams, no spatial length is introduced in the Fourier transformation.

Taking the Fourier transforms of equations (A.55) and (A.57) and then subtracting them, one obtains[45]

$$\left(-i\mathbf{K} + \hat{\mathbf{z}} \frac{\partial}{\partial z}\right) \left(-i\mathbf{K} \cdot \mathbf{E}'(\mathbf{K}; z) + \frac{\partial E'_z(\mathbf{K}; z)}{\partial z}\right) - \left(-K^2 + \frac{\partial^2}{\partial z^2}\right) \mathbf{E}'(\mathbf{K}; z) = \omega^2 \mu_0 \mathbf{D}'(\mathbf{K}; z), \quad (\text{A.60})$$

with $\mathbf{D}'(\mathbf{K}; z) = \mathbf{D}(\mathbf{K}; z) - \mathbf{D}_0(\mathbf{K}; z)$. For perturbative stability, the wave equation must be written as a function of the continuous electric field components [44], that is E'_x , E'_y

and D'_z . We shall do this separately for the s and p scattered waves as in [44]. However, before providing the solutions we introduce[45] the following useful vector function:

$$\mathbf{F}(\mathbf{r}) = \mathbf{D}(\mathbf{r}) - \mathcal{E}_0(z)\mathbf{E}(\mathbf{r}) = \delta\mathcal{E}(z)\mathbf{E}(\mathbf{r}) \Leftrightarrow \mathbf{F}(\mathbf{r}) = \mathbf{D}'(\mathbf{r}) - \mathcal{E}_0(z)\mathbf{E}'(\mathbf{r}), \quad (\text{A.61})$$

which gathers the infinitesimal contributions to the perturbed wave equation. To first order, one gets:

$$F_x(\mathbf{r}) \approx \frac{1}{\mathcal{E}_{zz}(z)} \left(\delta\mathcal{E}_{xz}(z)D_z(\mathbf{r}) + \left[\mathcal{E}_{zz}(z)\delta\mathcal{E}_{xx}(z) - \mathcal{E}_{xz}(z)\delta\mathcal{E}_{xz}(z) \right] E_x(\mathbf{r}) + \left[\mathcal{E}_{zz}(z)\delta\mathcal{E}_{xy}(z) - \mathcal{E}_{yz}(z)\delta\mathcal{E}_{xz}(z) \right] E_y(\mathbf{r}) \right), \quad (\text{A.62})$$

$$F_y(\mathbf{r}) \approx \frac{1}{\mathcal{E}_{zz}(z)} \left(\delta\mathcal{E}_{yz}(z)D_z(\mathbf{r}) + \left[\mathcal{E}_{zz}(z)\delta\mathcal{E}_{xy}(z) - \mathcal{E}_{xz}(z)\delta\mathcal{E}_{yz}(z) \right] E_x(\mathbf{r}) + \left[\mathcal{E}_{zz}(z)\delta\mathcal{E}_{yy}(z) - \mathcal{E}_{yz}(z)\delta\mathcal{E}_{yz}(z) \right] E_y(\mathbf{r}) \right), \quad (\text{A.63})$$

$$F_z(\mathbf{r}) \approx \frac{1}{\mathcal{E}_{zz}(z)} \left(\delta\mathcal{E}_{zz}(z)D_z(\mathbf{r}) + \left[\mathcal{E}_{zz}(z)\delta\mathcal{E}_{xz}(z) - \mathcal{E}_{xz}(z)\delta\mathcal{E}_{zz}(z) \right] E_x(\mathbf{r}) + \left[\mathcal{E}_{zz}(z)\delta\mathcal{E}_{yz}(z) - \mathcal{E}_{yz}(z)\delta\mathcal{E}_{zz}(z) \right] E_y(\mathbf{r}) \right). \quad (\text{A.64})$$

where $\mathcal{E}_{ij}(z)$ and $\delta\mathcal{E}_{ij}(z)$ are the components of the symmetric dielectric tensors of equations (A.56) and (A.59). In leading order perturbation theory, one further sets [44] $E_x(\mathbf{r}) \approx E_{0x}(\mathbf{r})$, $E_y(\mathbf{r}) \approx E_{0y}(\mathbf{r})$ and $D_z(\mathbf{r}) \approx D_{0z}(\mathbf{r})$ in equations (A.62-A.64).

p scattered wave

Projecting equation (A.60) onto $\hat{\mathbf{z}}$ and utilising the relation $\nabla \cdot \mathbf{D} = 0$ and equation (A.61), we obtain the p wave equation:

$$\begin{aligned} & -\frac{\partial}{\partial z} \frac{1}{\epsilon_0(z)} \frac{\partial D'_z(\mathbf{K}; z)}{\partial z} - \omega^2 \mu_0 D'_z(\mathbf{K}; z) + \\ & i(\mathbf{K} \cdot \hat{\mathbf{c}}) \frac{\partial}{\partial z} \left[\frac{\Delta(z)}{\epsilon_0(z)\mathcal{E}_{zz}(z)} \left(c_z D'_z(\mathbf{K}; z) + \epsilon_0(z) \left[c_x E'_x(\mathbf{K}; z) + c_y E'_y(\mathbf{K}; z) \right] \right) \right] + \\ & \frac{K^2}{\mathcal{E}_{zz}(z)} \left(D'_z(\mathbf{K}; z) - \mathcal{E}_{xz}(z) E'_x(\mathbf{K}; z) - \mathcal{E}_{yz}(z) E'_y(\mathbf{K}; z) \right) \\ & = \frac{\partial}{\partial z} \frac{1}{\epsilon_0(z)} \left(-i\mathbf{K} \cdot \mathbf{F}(\mathbf{K}; z) + i \frac{\Delta(z)}{\mathcal{E}_{zz}(z)} (\mathbf{K} \cdot \hat{\mathbf{c}}) c_z F_z(\mathbf{K}; z) \right) \\ & + \frac{K^2}{\mathcal{E}_{zz}(z)} F_z(\mathbf{K}; z) \end{aligned} \quad (\text{A.65})$$

where we introduced $\epsilon_0(z) = \left[\Theta(-z) + \Theta(z-a) \right] \epsilon_0 + \left[\Theta(z) - \Theta(z-a) \right] \epsilon_\perp$ and $\Delta(z) = \left[\Theta(z) - \Theta(z-a) \right] (\epsilon_\parallel - \epsilon_\perp)$ such that equation (A.58) reads as $\mathcal{E}_0(z) = \epsilon_0(z)\mathbf{1} + \Delta(z)\hat{\mathbf{c}}\hat{\mathbf{c}}$.

The solutions of equation (A.65) are obtained using Green functions[44, 45]. There exist, *a priori*, nine Green functions and thanks to the Dirac distributions appearing in

equation (A.59), they must only be determined for $z' = 0$ and for $z' \geq a$ (we recall that we are interested in the solution in the region $z \gg a$). Furthermore, for $z \gg a$ and $z < 0$, all terms of equation (A.65) in front of the field components $E'_x(\mathbf{K}; z)$ and $E'_y(\mathbf{K}; z)$ vanish. Hence, since the wave equation is expressed as a function of the continuous field components, only one non-zero Green function $G_p(\mathbf{K}; z, z')$ exists[44, 45] in the two relevant regions $z > a'$, $z' \leq 0$ and $z > z'$, $z' \geq a$. For $z > a$, the solution of equation (A.65) therefore reads as:

$$D'_z(\mathbf{K}; z) = \int_{-\infty}^{\infty} G_p(\mathbf{K}; z, z') \left(\frac{\partial}{\partial z'} \frac{1}{\epsilon_0(z')} \left[-i\mathbf{K} \cdot \mathbf{F}(\mathbf{K}; z') + i \frac{\Delta(z')}{\mathcal{E}_{zz}(z')} (\mathbf{K} \cdot \hat{\mathbf{c}}) c_z F_z(\mathbf{K}; z') \right] + \frac{K^2}{\mathcal{E}_{zz}(z')} F_z(\mathbf{K}; z') \right) dz', \quad (\text{A.66})$$

where the Green function, as given by [48], is

$$G_p(\mathbf{K}; z, z') = \frac{1}{W} \left(E_p^<(\mathbf{K}; z) E_p^>(\mathbf{K}; z') \Theta(z' - z) + E_p^>(\mathbf{K}; z) E_p^<(\mathbf{K}; z') \Theta(z - z') \right) \quad (\text{A.67})$$

with

$$W = E_p^<(\mathbf{K}; z) \frac{\partial E_p^>(\mathbf{K}; z)}{\partial z} - E_p^>(\mathbf{K}; z) \frac{\partial E_p^<(\mathbf{K}; z)}{\partial z}$$

according to a theorem that can be found in [49]. Here $E_p^<(\mathbf{K}; z)$ and $E_p^>(\mathbf{K}; z)$ are the two independent plane-wave solutions of the unperturbed equation (A.57): $E_p^>(\mathbf{K}; z)$ corresponds to a wave going from $z \rightarrow -\infty$ and $E_p^<(\mathbf{K}; z)$ to a wave going from $z \rightarrow +\infty$. They are thus defined by the following boundary conditions:

$$\begin{aligned} \lim_{z \rightarrow +\infty} E_p^>(\mathbf{K}; z) &\propto \exp(-ik_z z) \\ \lim_{z \rightarrow -\infty} E_p^<(\mathbf{K}; z) &\propto \exp(ik_z z). \end{aligned}$$

with $k_z = +(k^2 - K^2)^{1/2}$.

Integrating the first term in the integral of equation (A.66) by part and using equations (A.62-A.64), one gets for $z > a$

$$\begin{aligned} E'_p(\mathbf{K}; z) = & \pi \left\{ -i\hat{\mathbf{K}} \cdot \hat{\mathbf{c}} \Delta_n \left(1 + \frac{1}{n_o^2(n_o^2 + \Delta_n c_z^2)^2} \right) c_z \widetilde{D}_z^{p'}(\mathbf{K}) \right. \\ & - i \frac{n_o^4 - 1}{n_o^2} \left(\hat{\mathbf{K}} \cdot \hat{\mathbf{x}} \widetilde{E}_x^{p'}(\mathbf{K}; z) + \hat{\mathbf{K}} \cdot \hat{\mathbf{y}} \widetilde{E}_y^{p'}(\mathbf{K}; z) \right) \\ & - i \frac{\Delta_n \hat{\mathbf{K}} \cdot \hat{\mathbf{c}}}{n_o^2 + \Delta_n c_z^2} \left[1 + n_o^2 + \Delta_n c_z^2 \left(1 - \frac{1}{n_o^2(n_o^2 + \Delta_n c_z^2)} \right) \right] \\ & \times \left(\widetilde{E}_x^{p'}(\mathbf{K}) c_x + \widetilde{E}_y^{p'}(\mathbf{K}) c_y \right) \\ & + K \left[1 + \frac{1}{(n_o^2 + \Delta_n c_z^2)^2} \right] \left(\left[n_o^2 - 1 + \Delta_n c_z^2 \right] \widetilde{D}_z(\mathbf{K}; z) \right. \\ & \left. \left. + c_z \Delta_n \left[c_x \widetilde{E}_x^p(\mathbf{K}; z) + c_y \widetilde{E}_y^p(\mathbf{K}; z) \right] \right) \right\} \quad (\text{A.68}) \end{aligned}$$

with $\Delta_n = n_e^2 - n_o^2$ and $\hat{\mathbf{K}} = (K_x \hat{\mathbf{x}} + K_y \hat{\mathbf{y}})/K$. To obtain this expression, we used the definition $\mathbf{E}'_p(\mathbf{K}; z) = k/K \mathbf{E}'_z(\mathbf{K}; z)$ with $\hat{\mathbf{K}} = \hat{\mathbf{y}}$ when $K = 0$ [45] (see figure A.9 for the definition of the reference axes). To shorten equation (A.68) we also introduced

$$\begin{aligned} \widetilde{D}_z^p(\mathbf{K}; z) = & G_p(\mathbf{K}; z, a) \mathcal{F} \left[D_{0z}(\mathbf{R}; a) \frac{h_a(\mathbf{R})}{\lambda} \right] - \\ & G_p(\mathbf{K}; z, 0) \mathcal{F} \left[D_{0z}(\mathbf{R}; 0) \frac{h_0(\mathbf{R})}{\lambda} \right] \end{aligned} \quad (\text{A.69})$$

$$\begin{aligned} \widetilde{D}_z^{p'}(\mathbf{K}; z) = & \frac{dG_p(\mathbf{K}; z, z')}{dz'} \bigg|_{z'=a} \mathcal{F} \left[D_{0z}(\mathbf{R}; a) \frac{h_a(\mathbf{R})}{\lambda} \right] - \\ & \frac{dG_p(\mathbf{K}; z, z')}{dz'} \bigg|_{z'=0} \mathcal{F} \left[D_{0z}(\mathbf{R}; 0) \frac{h_0(\mathbf{R})}{\lambda} \right] \end{aligned} \quad (\text{A.70})$$

where λ is the laser beam wavelength. Identical expressions hold for $\widetilde{E}_x^p(\mathbf{K})$, $\widetilde{E}_y^p(\mathbf{K})$, $\widetilde{E}_x^{p'}(\mathbf{K})$ and $\widetilde{E}_y^{p'}(\mathbf{K})$.

To derive equation (A.68) we assumed that [50]

$$\int_{-\infty}^{\infty} f(z) \delta(z) dz = \frac{1}{2} \left[\lim_{z \rightarrow 0^+} f(z) + \lim_{z \rightarrow 0^-} f(z) \right] \quad (\text{A.71})$$

where $f(z)$ is a discontinuous function, but with a finite jump. Although this expression is not mathematically justified as stated in [50], it can however be used by considering that the Heaviside functions of equations (A.56, A.58) are given by the limit

$$\Theta(z) = \lim_{\zeta \rightarrow 0} [1 + \tanh(z/\zeta)]/2.$$

This choice is justified by the freedom existing in the determination of the dielectric tensor at $z = 0$ [51]. It is to mention that equation (A.71) leads to a disagreement with the boundary matching method for isotropic-isotropic interfaces in the case of oblique incidence. Another prescription was proposed in [52] to avoid this discrepancy. But, as mentioned in [53], no general proof was provided in [52]. There is then no reason for this particular prescription to work also for isotropic-anisotropic interfaces. In addition, since we are going to restrict ourselves to normal incidence, we choose to use the more intuitive and symmetric prescription of equation (A.71) for our calculations.

s scattered wave

Following the lines of the previous section, we get the s wave equation:

$$\begin{aligned} & \left(K^2 - \omega^2 \mu_0 \epsilon_0(z) - \frac{\partial^2}{\partial z^2} \right) E'_s(\mathbf{K}; z) - \\ & \omega^2 \mu_0 \frac{\Delta(z)}{\mathcal{E}_{zz}(z)} \hat{\mathbf{s}} \cdot \hat{\mathbf{c}} \left(\epsilon_0(z) \left[c_x E'_x(\mathbf{K}; z) + c_y E'_y(\mathbf{K}; z) \right] + c_z D'_z(\mathbf{K}; z) \right) \\ & = \omega^2 \mu_0 \left(\mathbf{F}(\mathbf{K}; z) \cdot \hat{\mathbf{s}} - \frac{\Delta(z)}{\mathcal{E}_{zz}(z)} \hat{\mathbf{c}} \cdot \hat{\mathbf{s}} c_z F_z(\mathbf{K}; z) \right) \end{aligned} \quad (\text{A.72})$$

with $E'_s(\mathbf{K}; z) = \hat{\mathbf{s}} \cdot \mathbf{E}'(\mathbf{K}; z)$ and $\hat{\mathbf{s}} = (-K_y \hat{\mathbf{x}} + K_x \hat{\mathbf{y}})/K$. The solution is given by

$$E'_s(\mathbf{K}; z) = \omega^2 \mu_0 \int_{-\infty}^{\infty} G_s(\mathbf{K}; z, z') \left(\mathbf{F}(\mathbf{K}; z') \cdot \hat{\mathbf{s}} - \frac{\Delta(z')}{\mathcal{E}_{zz}(z')} \hat{\mathbf{c}} \cdot \hat{\mathbf{s}} c_z F_z(\mathbf{K}; z') \right) dz',$$

with $G_s(\mathbf{K}; z, z')$ the s wave Green function for which an expression similar to equation (A.67) holds. After integration, one finds

$$\begin{aligned} E'_s(\mathbf{K}; z) = & \frac{2\pi^2}{\lambda} \left\{ (n_o^2 - 1) \left[s_x \tilde{E}_x(\mathbf{K}; z) + s_y \tilde{E}_y(\mathbf{K}; z) \right] \right. \\ & + \frac{\Delta_n}{n_o^2 + \Delta_n c_z^2} \hat{\mathbf{s}} \cdot \hat{\mathbf{c}} \left(n_o^2 - \frac{\Delta_n^2 c_z^2}{n_o^2 + \Delta_n c_z^2} \right) \left[c_x \tilde{E}_x(\mathbf{K}; z) + c_y \tilde{E}_y(\mathbf{K}; z) \right] \\ & \left. + \Delta_n \hat{\mathbf{s}} \cdot \hat{\mathbf{c}} \left(1 + \frac{1}{(n_o^2 + \Delta_n c_z^2)^2} \right) c_z \tilde{D}_z(\mathbf{K}; z) \right\} \end{aligned} \quad (\text{A.73})$$

where $\tilde{E}_x^s(\mathbf{K}; z)$, $\tilde{E}_y^s(\mathbf{K}; z)$ and $\tilde{D}_z^s(\mathbf{K}; z)$ are obtained by substituting $G_p(\mathbf{K}; z, z')$ by $G_s(\mathbf{K}; z, z')$ in equations (A.69-A.70).

Transmitted intensity

Anticipating the numerical studies of section A.3.3, we shall now consider a Gaussian beam at normal incidence coming from the region $z < 0$. Expressions for the electric field at $z = 0$ and $z = a$ read:

$$\begin{aligned} \mathbf{E}_0(\mathbf{K}; 0) &= \mathbf{E}_i(\mathbf{K}; 0) + \mathbf{E}_r(\mathbf{K}; 0) \\ \mathbf{E}_0(\mathbf{K}; a) &= \mathbf{E}_t(\mathbf{K}; a) \end{aligned}$$

with[18]

$$\mathbf{E}_i(\mathbf{K}; 0) = \frac{w_0}{\sqrt{2\pi}} \exp\left(-\frac{w_0^2 K^2}{4}\right) M_{3 \times 3} \mathbf{E}_0 \quad (\text{A.74})$$

$$\mathbf{E}_r(\mathbf{K}; 0) = \frac{w_0}{\sqrt{2\pi}} \exp\left(-\frac{w_0^2 K^2}{4}\right) \Omega M_r^> \Omega^T M_{3 \times 3} \mathbf{E}_0 \quad (\text{A.75})$$

$$\mathbf{E}_t(\mathbf{K}; a) = \frac{w_0}{\sqrt{2\pi}} \exp\left(-\frac{w_0^2 K^2}{4}\right) \Omega M_t^> \Omega^T M_{3 \times 3} \mathbf{E}_0 \quad (\text{A.76})$$

where we chose the beam waist position at $z = 0$ and where[18]: \mathbf{E}_0 is the electric vector describing the polarisation of the Gaussian beam centre (i.e. $\mathbf{K} = 0$), $M_{3 \times 3}$ is a 3×3 matrix describing the polarisation of the plane waves constituting the Gaussian beam[20], $M_r^>$ and $M_t^>$ are the Jones matrices describing the reflection and transmission by the uniaxial parallel plate (the upper script $>$ indicates that these matrices correspond to an incident wave coming from $z < 0$). These Jones matrices take into account the multiple reflections inside the platelet. They are determined [6] in the basis $\{\hat{\mathbf{s}}, \hat{\mathbf{p}}, \hat{\mathbf{k}}\}$ and then transformed to the basis $\{\hat{\mathbf{x}}, \hat{\mathbf{y}}, \hat{\mathbf{z}}\}$ using the transfer matrix Ω .

The Green functions are given by

$$G_m(\mathbf{K}; z, z') = \begin{cases} (2ik_z)^{-1} \left(\exp(ik_z[z - z']) + M_{r_{mm}}^< \exp(ik_z[z + z']) \right); & z' \geq a \\ (2ik_z)^{-1} M_{t_{mm}}^< \exp(ik_z[z - z']); & z' \leq 0 \end{cases}$$

with $m = 1, 2$ for s and p waves respectively. It is to mention that $M_r^< = M_r^>$ and $M_t^< = M_t^>$ when the optical axis is in the plane of interface, i.e. when $c_z = 0$.

From the above expressions, one can evaluate equations (A.69-A.70) and then the s and p scattered fields. In doing so, the following kind of Fourier transform is to be evaluated:

$$\mathcal{F}\left[E_{0x}(\mathbf{R}; a)h_a(\mathbf{R})\right] = \int \int E_{0x}(\mathbf{K}'; a)h_a(\mathbf{K} - \mathbf{K}')d^2\mathbf{K}', \quad (\text{A.77})$$

where, because $\langle h_a \rangle = 0$, the Fourier transform of the surface profile $h_a(\mathbf{K} - \mathbf{K}')$ vanishes when $\mathbf{K} = \mathbf{K}'$. However, and this is one of the major points of this article, since $E_{0x}(\mathbf{K}; a) \propto \exp(-w_0^2 K^2/4)$ at normal incidence, then $\mathcal{F}[E_{0x}(\mathbf{R}; a)h_a(\mathbf{R})]$ does not necessarily vanish when $K = 0$, in contrast to the case for a single plane wave. Consequently, the specularly transmitted beam receives a non-vanishing contribution from the scattered field, even in first order perturbation theory. If the Gaussian beam is viewed as a superposition of plane waves [38], then this phenomenon is due to the angular distribution of the plane waves. However, since this contribution depends on $h_a(\mathbf{K} - \mathbf{K}')$, a realistic description of the surface roughness is needed to evaluate the integral of equation (A.77). This is the subject of the next section.

To exhibit this contribution, let us assume that a Wollaston prism is located after the anisotropic plate and that its axes corresponds to the $\hat{\mathbf{x}}$ and $\hat{\mathbf{y}}$ directions. Writing the scattered electric field in the basis $\{\hat{\mathbf{x}}, \hat{\mathbf{y}}, \hat{\mathbf{z}}\}$,

$$\begin{aligned} E'_x(\mathbf{K}; z) &= \Omega_{11}E'_s(\mathbf{K}; z) + \Omega_{12}E'_p(\mathbf{K}; z) \\ E'_y(\mathbf{K}; z) &= \Omega_{21}E'_s(\mathbf{K}; z) + \Omega_{22}E'_p(\mathbf{K}; z) \end{aligned}$$

one obtains

$$\begin{aligned} I_x &= \int \int |\hat{\mathbf{x}} \cdot \mathbf{E}_t(\mathbf{K}; z)|^2 d^2\mathbf{K} + \int \int |E'_x(\mathbf{K}; z)|^2 d^2\mathbf{K} + \\ &\quad \int \int \left[\hat{\mathbf{x}} \cdot \mathbf{E}_t(\mathbf{K}; z) \left(E'_x(\mathbf{K}; z) \right)^* + \left(\hat{\mathbf{x}} \cdot \mathbf{E}_t(\mathbf{K}; z) \right)^* E'_x(\mathbf{K}; z) \right] d^2\mathbf{K} \\ I_y &= \int \int |\hat{\mathbf{y}} \cdot \mathbf{E}_t(\mathbf{K}; z)|^2 d^2\mathbf{K} + \int \int |E'_y(\mathbf{K}; z)|^2 d^2\mathbf{K} + \\ &\quad \int \int \left[\hat{\mathbf{y}} \cdot \mathbf{E}_t(\mathbf{K}; z) \left(E'_y(\mathbf{K}; z) \right)^* + \left(\hat{\mathbf{y}} \cdot \mathbf{E}_t(\mathbf{K}; z) \right)^* E'_y(\mathbf{K}; z) \right] d^2\mathbf{K} \end{aligned}$$

for the two intensities I_x and I_y measured after the Wollaston. Writing $I_x = I_x^{[0]} + I_x^{[1]} + I_x^{[2]}$, and I_y in the same way, with

$$I_x^{[0]} = \int \int |\hat{\mathbf{x}} \cdot \mathbf{E}_t(\mathbf{K}; z)|^2 d^2\mathbf{K} \quad (\text{A.78})$$

$$I_x^{[1]} = \int \int \left[\hat{\mathbf{x}} \cdot \mathbf{E}_t(\mathbf{K}; z) \left(E'_x(\mathbf{K}; z) \right)^* + \left(\hat{\mathbf{x}} \cdot \mathbf{E}_t(\mathbf{K}; z) \right)^* E'_x(\mathbf{K}; z) \right] d^2\mathbf{K} \quad (\text{A.79})$$

$$I_x^{[2]} = \int \int |E'_x(\mathbf{K}; z)|^2 d^2\mathbf{K} \quad (\text{A.80})$$

one sees that the specular beam-scattered beam interference term $I_x^{[1]}$ is of first order in $\sqrt{\langle h^2 \rangle}/\lambda$. As $w_0 \rightarrow \infty$, the Fourier transforms of the electric field components lead to

Dirac distributions and the usual plane wave result is recovered. This interference term is therefore expected to depend on the laser beam waist size.

Let us finally note that equation (A.80) does not completely describe the second order contribution $I_x^{[2]}$ in the specular region, the interference between the specular and the second order scattered field being omitted in our calculation.

A.3.3 Numerical simulations

To estimate the specular beam-scattered beam interference term, we now consider a laser beam crossing of a quartz platelet at normal incidence. The incident electric vector is fixed to $\mathbf{E}_0 = \hat{\mathbf{x}}$, i.e. perpendicular to the plane of incidence of the Gaussian beam's centre, and the intensities recorded after a Wollaston prism are calculated as in the previous section.

Numerical ingredients and input parameters

As described in the previous section, the specular beam-scattered beam interference term can only be evaluated if a simulation of the surface roughness is provided. Thus profiles of the quartz surfaces h_0 and h_a have been generated. Then the scattered fields are computed for various orientations of the optical axis and the two intensities of equations (A.78-A.80) are determined. The procedure is then repeated for a set of random series in order to obtain a statistical distribution of the intensities. The numerical integrations of equations (A.78-A.80) are performed in the domain $\arctan(K/k) < 1^\circ$, which roughly corresponds to the angular acceptance of a 1 inch diameter optical lens located at 1 m from the plate. In practice this limit does not affect the value of the interference term but only the second order contribution.

Random profile generations are performed as follows. First, the height distributions are determined according to a Gaussian distribution of mean value zero and root mean square $\sigma = 6 \text{ \AA}$. This is a typical value for a high quality polished quartz plate [54]. The heights are stored in a grid $\{x, y\}$ of length $L \times L$ containing $2^n \times 2^n$ nodes. The value of n is limited by the computer memory capacity, $n = 11$ in our case. Next, the Fourier transform is computed and then weighted by the square root of a two dimensional spectral density function [47] (PSD2). Although we are going to consider an isotropic roughness distribution, we shall not use the reduced one dimensional radial PSD1 [47, 55]. Nevertheless we fully account for the random nature of the surface roughness in the evaluation of the specular beam-scattered beam interference term (the use of a PSD1 would lead to a smaller dispersion of our numerical results).

The result of [54] for the PSD2 is used:

$$PSD2(K) = \begin{cases} 2\pi\sigma^2 l^2 (1 + K^2 l^2)^{-3/2} ; K \geq K_{min} \\ 0 ; K < K_{min} \end{cases} \quad (\text{A.81})$$

where the cut-off spatial frequency K_{min} has been introduced to account for the surface profile property $\langle h \rangle = 0 \Rightarrow PSD2(0) = 0$ [56]. The correlation length l is of the order of [54] $1\mu\text{m}$ and K_{min} is smaller than $10^{-3}\mu\text{m}^{-1}$ [41]. The parameter $1/K_{min}$ acts as a spatial frequency threshold for the laser beam radius: roughly speaking, for $w_0 > \sqrt{2}/K_{min}$ the Gaussian beam behaves as a plane wave and the specular beam-scattered

beam interference term vanishes. Nevertheless, the present values of K_{min} are limited by the acceptance of the surface profile measurements: values as small as $10^{-4}\mu\text{m}^{-1}$ for Si substrates [56] and $10^{-5}\mu\text{m}^{-1}$ for K_{min} for Si wafers [57] have been reported (notice that these numbers lead to a laser beam radius threshold greater than 15 mm). Finally, the inverse Fourier transform is computed leading to a ‘coloured’ random surface.

The grid parameters are determined by the correlation length l and the laser beam waist w_0 . The distance between two points of the grid $\{x, y\}$ must be at least twice smaller than l and the distance between two points of the grid $\{K_x, K_y\}$ approximately ten times smaller than $\sqrt{2}/w_0$. This leads to the following “experimental” parameters: $w_0 = 100\mu\text{m}$, $l = 1.6\mu\text{m}$ and $L = 8w_0$. For the laser beam wavelength we choose $\lambda = 0.6328\mu\text{m}$ and we choose $n_0 = 1.542637$ and $n_e = 1.551646$ for the quartz indices. The ratio σ/λ is therefore of the order of 10^{-3} in our numerical examples.

Using the numbers given above, we have written a computer program to estimate the specular beam-scattered beam interference term. Calculations of the unperturbed electric fields and of the Green functions are performed according to [18]. A fast Fourier transform (FFT) algorithm is used to compute the various Fourier transforms. The numerical precision for the unperturbed intensities is of the order of 10^{-6} [18]. The specular beam-scattered beam interference term is thus known to an accuracy better than $\sigma/\lambda \times 10^{-6} \approx 10^{-9}$ (with our grid size, the FFTs do not reduce this accuracy). However, the CPU-time is quite sizable: with a SPECfp2000 1288 computer, the random generation of the surfaces takes 22 s and then the computation of the intensities for one given orientation of the optical axis takes 183 s.

Numerical results

We first consider a quartz plate thickness $a = 0.720\text{ mm}$ with the optical axis located in the plane of interface ($\theta_c = \arccos(c_z) = \pi/2$), i.e. a tenth order quarter-wave plate. $I_x^{[0]}$ and $I_y^{[0]}$ are shown in figure A.10 as a function of the optical axis azimuth $\phi_c = \arctan(c_y/c_x)$. The results for the first order contributions $I_x^{[1]}$ and $I_y^{[1]}$ are shown in figures A.11, A.12. Each curve of these plots corresponds to different surface profiles. Considering one given profile, one sees that: the size of the specular beam-scattered beam interference strongly depends on the surface profile and can reach the per mille level of the zero order contribution, its sign changes with ϕ_c and its shape is not regular with ϕ_c . The change of sign is expected since the intensity averaged over a large number of profiles obviously vanishes. The erratic shape is also expected since the fields change with ϕ_c and so do the Fourier transforms as in equation (A.77).

The second order contribution (calculated from equation (A.80)) is six orders of magnitude smaller than the zero order contribution. However, we do not show any results since our second order calculation is not complete with respect the specular angular range.

Large differences are indeed observed when the plate thickness is changed. The specular beam-scattered beam interference contributions are computed for $a = 0.562\text{ mm}$ as in [35] (i.e. $(8 + 10^{-3}) \times 2\pi$ retardation plate with our choice for the optical indices) and $a = 5\text{ mm}$ as in [34] (i.e. $(71 + 0.18) \times 2\pi$ retardation plate), and still with $\theta_c = \pi/2$. They are then compared to the values obtained with the tenth order quarter wave plate and the same surface profiles. The results are presented in figures A.13, A.14. $I_x^{[1]}$ and $I_y^{[1]}$ are proportional to $I_x^{[0]}$ and $I_y^{[0]}$ (see figure A.10). In particular, the oscillations of $I_x^{[1]}$ are damped when $I_x^{[0]}$ gets flat (i.e. for the almost zero retardation plate $a = 0.562\text{ mm}$).

To investigate the dependence in equations (A.73,A.68) on the optical axis polar angle θ_c , the calculations were performed fixing $\theta_c = \pi/4$ for the plate thickness $a = 0.720$ mm. Here again the variations are noticeable (see figures A.13 and A.14).

From the figures A.12 and A.14, one can see that $I_y^{[1]}$ tends to be of opposite sign in the regions $0 < \phi_c < \pi/2$ and $\pi/2 < \phi_c < \pi$. But this is not a general rule as it seems to come out from experiments [35, 34]. One can also observe two fix points at $\phi_c = 0$ and $\pi/2$ on figures A.12 and A.14. Since $I_y^{[1]}$ is the interference between the scattered field and the zero order field, these fixed points correspond to the zeros of the zero order field (see $I_y^{[0]}$ on figure A.10). This is not the case for the second order term of equation (A.80) which is of the order of 10^{-6} and therefore dominates around $\phi_c = 0, \pi/2$ (here the missing term of equation (A.80) is not relevant since it describes the interference between the specular and the second order scattered fields). However, the dispersion of $I_y^{[1]}$ around zero for $\phi_c = 0, \pi/2$ (not visible on these figures) differ very slightly from zero, it is of the order of 10^{-10} for $w_0 = 100 \mu\text{m}$ and $\approx 10^{-8}$ for $w_0 = 25 \mu\text{m}$. This is a cross-polarisation effect, i.e. this is due to the matrix $M_{3 \times 3}$ in equations (A.74-A.76).

The numerical results presented here are rather independent of the choice for the PSD2 provided a quartz plate of optical grade is considered. It is indeed experimentally demonstrated [41, 47, 55, 56, 57] that the PSDs of optical element surfaces have an inverse-power-law (or Fractal-like) behaviour. Therefore, as justified in [55], various smooth mathematical representations of the PSD (see [58, 59] for examples) are reducible to equation (A.81).

As a concluding remark, we point out that three important dimensionless parameters ω_0/l , σ/λ and l/λ have been encountered in our calculations. ω_0/λ describes the cross-polarisation effects discussed above and is therefore not relevant here.

As mentioned in section A.3.2, the validity of the perturbation treatment depends on σ/λ and l/λ . For the first order perturbation theory to be valid, the severe conditions $\sigma/\lambda \ll 1$ and $l/\lambda \simeq 1$ must hold[42]. They are fortunately fulfilled by optical grade quartz plates. To study the influence of the correlation length l , we changed the value of l to $0.7 \mu\text{m}$ and $2 \mu\text{m}$ and we observed no significant qualitative differences with respect to the results described above.

As for the last dimensionless parameter ω_0/l , we have already mentioned that when $\omega_0/l \rightarrow \infty$ the usual result for plane waves is recovered (i.e. the specular beam-scattered beam interference term vanishes) although, with regard to the cut-off parameter K_{min} , this limit seems to be idealistic for a finite size quartz plate. To get an idea of the influence of w_0 , we increased it to $200 \mu\text{m}$ and here again, no significant differences were observed. Much larger values for w_0 could not be tried while keeping a reasonable correlation length, because of the computer memory limitation. Finally, let us mention that the other limit $\omega_0 \ll l$ corresponds to the scattering by gratings [60]. In this limit the specular beam-scattered beam interference term vanishes since the diffusion occurs at large angles with respect to the specular beam direction.

A.3.4 Conclusion

We have computed, in the leading orders of perturbation theory, the effect of surface roughness on uniaxial platelet transmittance. Taking into account the Gaussian nature of laser beams we showed that the interference between the specular and scattered fields contributes to the intensity observed in the specular region.

This contribution is of first order in the ratio of the root mean square roughness to the laser beam wavelength σ/λ . It depends strongly on the plate surface profiles and on the crystal optical properties, the orientation of the optical axis, the thickness and optical indices (i.e. temperature). It is therefore not sensible to implement the roughness calculation in a HAUP type of fitting procedure. In addition, the numerical calculations consume too much computer time.

In view of our numerical results, it is most likely that simple over-layer models [35] cannot describe accurately the properties of our main formulae in equations (A.68,A.73). Nevertheless, we point out that, because of the random nature of the specular beam-scattered beam interference term, a simple way to avoid it is to perform a series of measurements at various locations on the plate and then to average the results. Although this procedure would increase the uncertainty on the determination of the crystal optical parameters, it should however decrease the systematic bias. The determination of the plate thickness *in situ* could be done by varying the laser beam incident angle (i.e. by tilting the plate) [4].

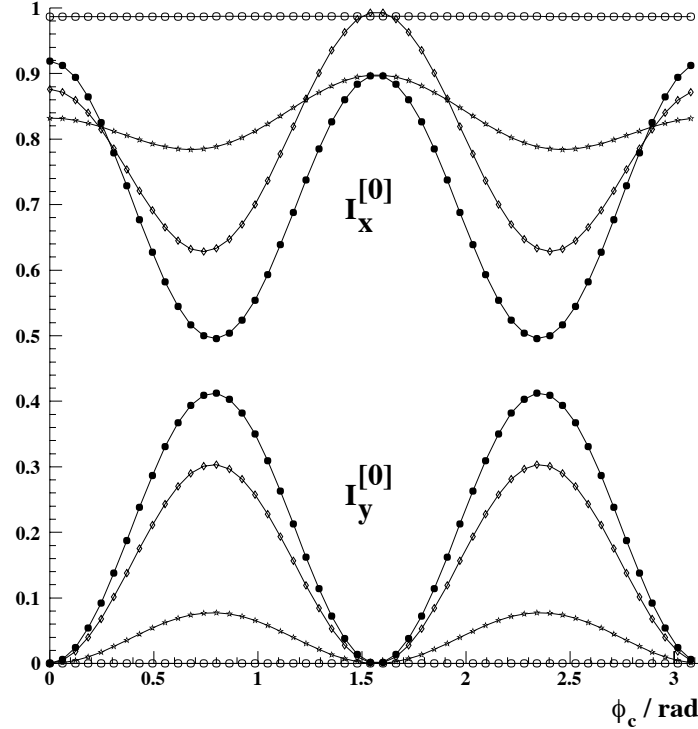


Figure A.10: The intensity of the specular beams as a function of the optical axis azimuth for various quartz plates: a tenth order quarter wave plate (full dots), 0.562 mm thickness (open dots), 5 mm thickness (diamonds) and a tenth order plate thickness but with the optical axis polar angle fixed to $\theta_c = \pi/4$ (stars). The upper set of curves represents the intensities $I_x^{[0]}$ and the lower set of curves $I_y^{[0]}$.

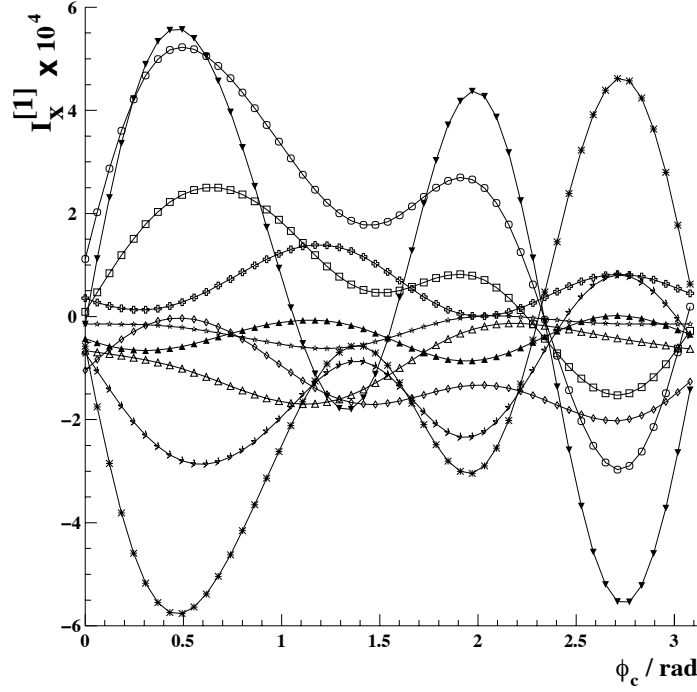


Figure A.11: The interference between the specular and scattered transmitted fields $I_x^{[1]}$ as a function of the optical axis azimuth. The plate is a tenth order quarter wave plate and the beam waist is $w_0 = 100 \mu\text{m}$. Different symbols correspond to different randomly generated surface profiles.

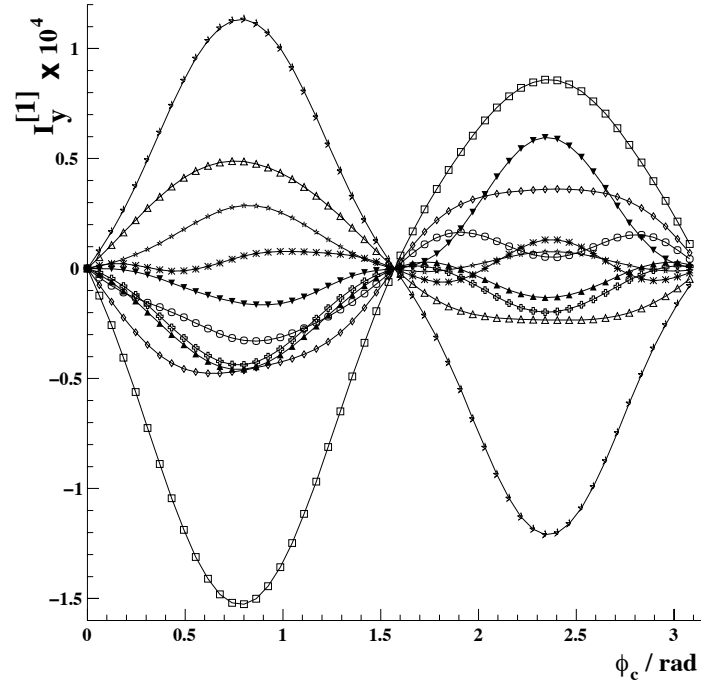


Figure A.12: The interference between the specular and scattered transmitted fields $I_y^{[1]}$ as a function of the optical axis azimuth. The plate is a tenth order quarter wave plate and the beam waist is $w_0 = 100 \mu\text{m}$. Different symbols correspond to different randomly generated surface profiles.

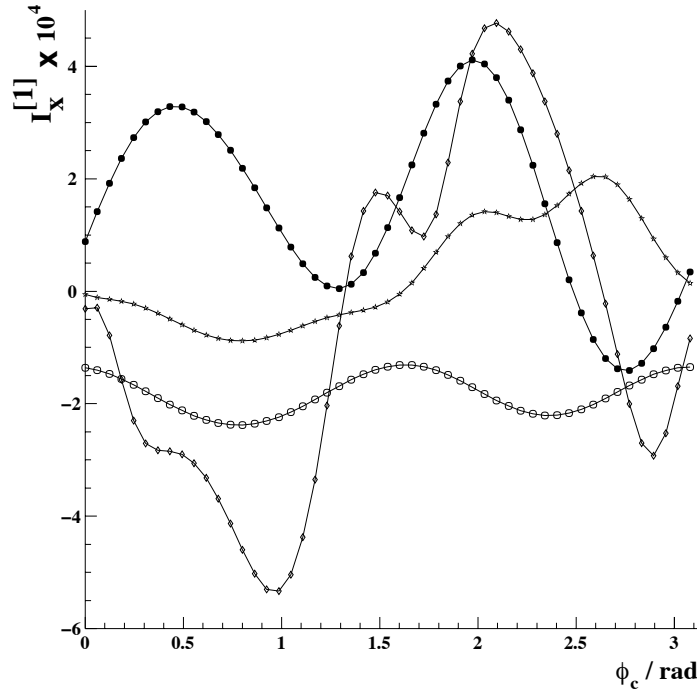


Figure A.13: The interference between the specular and scattered transmitted fields $I_x^{[1]}$ as a function of the optical axis azimuth for: a tenth order quarter wave plate (full dots), 0.562 mm thickness (open dots), 5 mm thickness plate (diamonds) and a tenth order plate thickness but with the optical axis polar angle fixed to $\theta_c = \pi/4$ (stars). The surface profiles are the same for the four curves.

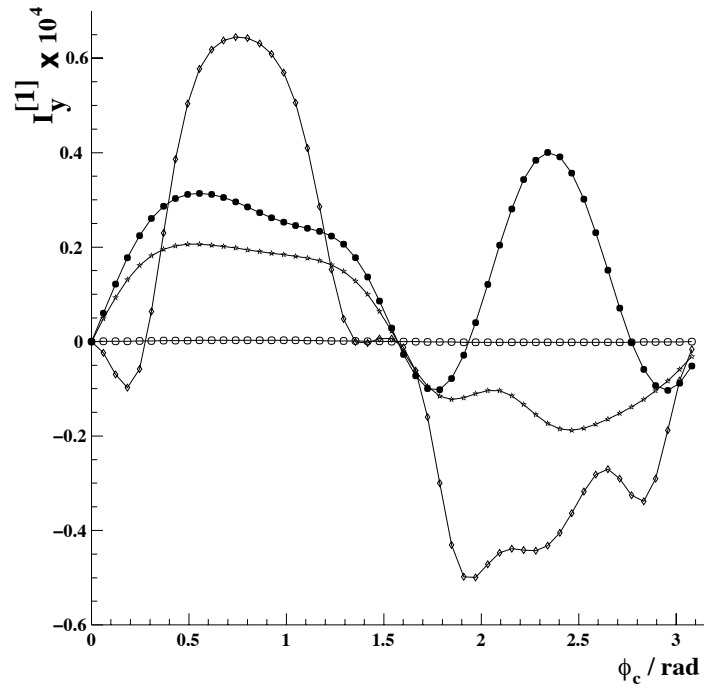


Figure A.14: As in figure A.13 but for $I_y^{[1]}$.

Bibliography

- [1] R.M.A. Azzam and N.M. Bashara, *Ellipsometry and polarized light* (Amsterdam, North-Holland, 1977).
- [2] S. Huard, *Polarisation de la lumière* (Masson, Paris, 1993).
- [3] *Hanbook of optics* (Mc Graw-Hill, New-York, 1978).
- [4] J. Poirson et al., “Jones matrix of a quarter-wave plate for Gaussian beams”, Appl. Opt. 34, 6806-6818 (1995).
- [5] See D.A. Holmes, “Exact theory of retardation plates”, J. Opt. Soc. Am. 54, 1115-1120 (1964), and references therein.
- [6] P. Yeh, “Electromagnetic propagation in birefringent media”, J. Opt. Soc. Am. 69, 742-756 (1979); P. Yeh, “Optics of anisotropic layered media: a new 4×4 matrix algebra”, Surf. Sci. 96, 41-53 (1980).
- [7] D. Den Engelsen, “Ellipsometry of anisotropic films”, J. Opt. Soc. Am. 61, 1460-1466 (1971).
- [8] K. Zander, J. Moser and H. Melle, “Change of polarization of linearly polarized, coherent light transmitted through plane-parallel anisotropic plates”, Optik 70, 6-13 (1985).
- [9] See paragraph 4.6 in Ref. [1] and references therein.
- [10] J. Lekner, “Reflection and refraction by uniaxial crystals”, J. Phys. Condens. Matter 3, 6121-6133 (1991).
- [11] P. Yeh, “Extended Jones matrix method”, J. Opt. Soc. Am. 72, 507-513 (1982).
- [12] C. Gu and P. Yeh, “Extended Jones matrix method. II”, J. Opt. Soc. Am. A10, 966-973 (1993).
- [13] P.C.S. Hayfield and G.W.T. White, “An assessment of the suitability of the Drude Tronstad polarised light method for the study of film growth on polycrystalline metals”, in *Ellipsometry in the measurement of surfaces and thin film*, Natl. Bur. Std. Misc. Publ. 256 (U.S. Govn’t Printing Office, Washington, 1964). See also paragraph 4.7 in Ref. [1].
- [14] K. Pietraszkiewicz et al., “Effect of multiple reflections in retardation plates with elliptical birefringence”, J. Opt. Soc. Am. A12, 420-424 (1995).

- [15] P. Yeh, *Optical waves in layered media* (Wiley, New-York, 1988).
- [16] G.D. Landry and T.A. Maldonado, "Complete method to determine transmission and reflection characteristics at a planar interface between arbitrarily oriented biaxial media", J. Opt. Soc. Am. A12, 2048-2063 (1995).
- [17] Sh.A. Furman and A.V. Tikhonravov, *Optics of multilayer systems* (Frontieres, Gif-sur-Yvette, 1992).
- [18] F. Zomer, "Transmission and reflexion of Gaussian beams by anisotropic parallel plates", J. Opt. Soc. Am. A. 20, 172-182 (2003).
- [19] E.C.G. Sudarshan, R. Simon and N. Mukunda, "Paraxial-wave optics and relativistic front description. I. The scalar theory" Phys. Rev. A 28, 2921-2932 (1983).
- [20] N. Mukunda, R. Simon and E.C.G. Sudarshan, "Paraxial-wave optics and relativistic front description. I. The vector theory", Phys. Rev. A 28, 2933-2942 (1983).
- [21] R. Simon, E.C.G. Sudarshan and N. Mukunda, "Cross polarization in laser beams", Appl. Opt. 26, 1589-1593 (1987).
- [22] H. Bacry and M. Cadihac, "Metaplectic group and Fourier optics", Phys. Rev. A 23, 2533-2536 (1981).
- [23] Y. Fainman and J. Shamir, "Polarization of nonplanar wave fronts", Appl. Opt. 23, 3188-3195 (1984).
- [24] N. Mukunda, R. Simon and E.C.G. Sudarshan, "Paraxial Maxwell beams: transformation by general linear optical systems", J. Opt. Soc. Am. A 2, 1291-1296 (1985).
- [25] X. Zhu, "Explicit Jones transformation matrix for a tilted birefringent plate with its optic axis parallel to the plate interface", Appl. opt. 33, 3502-3506 (1994).
- [26] Maple V software program (Waterloo Maple Inc., Ontario, Canada).
- [27] F. Zomer, "Surfaces roughness effects on the transmission of Gaussian beams by anisotropic parallel plates ", J. Phys. D: Appl. Phys. 36, 2697-2704 (2003).
- [28] J. Kobayashi and Y. Uesu, "A new optical method and apparatus "HAUP" for measuring simultaneously optical activity and birefringence of crystals. I. Principle and construction ", J. Appl. Cryst. 16, 204-211 (1983).
- [29] J.R.L. Moxon, A.R. Renshaw and I.J. Tebbutt, "The simultaneous measurement of optical activity and circular dichroism in birefringent linearly dichroic crystal sections: II. Description of apparatus and results for quartz, nickel sulphate hexahydrate and benzil", J. Phys. D: Appl. Phys. 24, 1187-1192 (1991).
- [30] J. Ortega, J. Etxebarria, J. Zubillaga, T. Brezczewski and M.J. Tello, "Lack of optical activity in the incommensurate phases of Rb_2ZnBr_4 and $[\text{N}(\text{CH}_3)_4]_2\text{CuCl}_4$ ", Phys. Rev. B 45, 5155-5162 (1992).

- [31] C. Hernández-Rodríguez and P. Gómez-Garrido, “Optical anisotropy of quartz in the presence of temperature-dependent multiple reflections using a high-accuracy universal polarimeter”, J. Phys. D: Appl. Phys. 33, 2985-2994 (2000).
- [32] J.R.L. Moxon and R. Renshaw, “The simultaneous measurement of optical activity and circular dichroism in birefringent linearly dichroic crystal sections: I. Introduction and description of the method”, J. Phys.: Condens. Matter 2, 6807-6836 (1990).
- [33] M. Kremers and H. Meekes, “Interpretation of HAUP measurements: a study of the systematic errors”, J. Phys. D: Appl. Phys. 28, 1195-1211 (1995).
- [34] J. Simon, J. Weber and H-G Unruh, “Some new aspects about the elimination of systematical errors in HAUP measurements”, J. Phys. D: Appl. Phys. 30, 676-682 (1997).
- [35] C.L. Folcia, J. Ortega and J. Etxebarria, “Study of the systematic errors in HAUP measurements”, J. Phys. D: Appl. Phys. 32, 2266-2277 (1999).
- [36] F.G. Bass and I.M. Fuks, *Wave scattering from statistically rough surfaces* (Pergamon, Oxford, 1979).
- [37] J.A. Ogilvy, *Theory of wave scattering from random rough surfaces* (IOP Publishing Ltd, London, 1991).
- [38] Siegman A E 1986 *Lasers* (Sausalito, California: University Science Books)
- [39] S. F. Nee, “Polarisation of specular reflection and near-specular scattering by rough surface”, Appl. Opt. 35, 3570-3582 (1996).
- [40] J. Brossel, “Multiple-beam localized fringes: Part I.- Intensity distribution and localization”, Proc. Phys. Soc. 59, 224-242 (1947)
- [41] A. Dupparé, J. Ferre-Borrull, S. Gleich, G. Notni, J. Steinert, and J.M. Bennett, “Surface characterization techniques for determining the root-mean-square roughness and power spectral densities of optical components”, Appl. Opt. 41, 154-171 (2002).
- [42] E.I. Thorsos and D.R. Jackson, “The validity of the perturbation approximation for rough surface scattering using a Gaussian roughness spectrum”, J. Acoust. Soc. Am. 86, 261-277 (1989).
- [43] W.L. Mochàn and R.G. Barrera, “Electromagnetic response of systems with spatial fluctuations. II Applications” Phys. Rev. B 32, 4989-5001 (1985).
- [44] N.R. Hill, “Integral-equation perturbative approach to optical scattering from rough surfaces”, Phys. Rev. B 24, 7112-7120 (1981).
- [45] V. Celli, T.T. Ong and P. Tran, “Light scattering from a random orientated anisotropic layer on a rough surface”, J. Opt. Soc. Am. A 11, 716-722 (1994).
- [46] R.A. Depine and M.E. Inchaussandague, “Corrugated diffraction gratings in uniaxial crystals”, J. Opt. Soc. Am. A 11, 173-180 (1994).

- [47] J.M. Bennett and L. Mattson, *Introduction to surface roughness and scattering*, (Opt. Soc. Am., Washington D.C., second edition 1999).
- [48] D.L. Mills and A.A. Maradudin, "Surface roughness and the optical properties of a semi-infinite material; the effect of a dielectric overlayer", Phys. rev. B 12, 2943-2958 (1975).
- [49] B. Friedman, *Principles and techniques of applied mathematics* (Wiley, New-York, 1960). See Chap. 3.
- [50] A.A. Maradudin and D.L. Mills, "Scattering and absorption of electromagnetic radiation by semi-infinite medium in the presence of surface roughness", Phys. Rev. B 11, 1392-1415 (1975).
- [51] P. Bousquet, F. Flory and P. Roche, "Scattering from multilayer thin films: theory and experiment", J. Opt. Soc. Am. 71, 1115-1123 (1981).
- [52] D.L. Mills, "Attenuation of surface polaritons by surface roughness", Phys. Rev. B 10, 4036-4046 (1975).
- [53] A.A. Maradudin and W. Zierau, "Effect of surface roughness on the surface-polariton dispersion relation", Phys. Rev. B 14, 484-499 (1976).
- [54] V.V. Azarova et al., "Measuring the roughness of high-precision quartz substrates and laser mirrors by angle resolved scattering", J. Opt. Technol. 69, 125-128 (2002).
- [55] E.L. Church and P.Z. Takacs, "The optimal estimation of finish parameters", in Optical Scatter: Applications, Measurements and Theory, J.C. Stover, ed., Proc. Soc. Photo-Opt. Instrum. Eng. 1530, 71-78 (1991).
- [56] E.L. Church, "Fractal surface finish", Appl. Opt. 27, 1518-1526 (1988).
- [57] E. Marx, I.J. Malik, Y.E. Strausser, T. Bristow, N. Poduje and J.C. Stover, "Power spectral densities: a multiple technique study of different Si wafer surfaces", J. Vac. Sci. Technol. B 20, 31-41 (2002).
- [58] J.M. Elson and J.M. Bennett, "Relation between the angular dependence of scattering and the statistical properties of optical surfaces", J. Opt. Soc. Am. 69, 31-47 (1979).
- [59] G. Rasigni, F. Varnier, M. Rasigni, J.P. Palmari and A. Liebaria, "Spectral-density function of the surface roughness for polished optical surfaces", J. Opt. Soc. Am. 73, 1235-1239 (1983).
- [60] G. Tayeb, "Sur l'étude numérique de réseaux de diffraction constitués de matériaux anisotropes", C. R. Acad. Sci. Paris 307, 1501-1504 (1988).

Remerciements

Pour commencer, je tiens à remercier les membres de mon jury d'habilitation.

Durant les années qui se sont écoulées depuis ma soutenance de thèse, j'ai travaillé, tout d'abord sous la direction de Christian Pascaud, puis en sa collaboration. J'aimerais le remercier pour le savoir qu'il m'a communiqué, la liberté dont il m'a toujours laissé faire usage et l'ambiance amicale dans laquelle s'est déroulé notre travail. Travailler ensemble a toujours été, et est toujours, une joie.

Je souhaite aussi remercier les "anciens" et "actuels" membres du groupe H1 : Sylvestre Baudrand, Jean-Claude Bizot, Violette Brisson, André Courau, Benoit Delcourt, Laurent Favard, Marie Jacquet-Lemire, Agnieszka Jacholkowska, Michel Jaffré, Smain Kermiche, Elise Lebailly, Georges Lobo, Roman Poeschl et Benjamin Porthault pour l'ambiance amicale qui a toujours régné au sein du groupe.

A plus de dix années d'intervalle, j'ai pu compter à nouveau sur l'aide précieuse d'Anne Marie Lutz et de Marie-Hélène Schune pour un travail de relecture fastidieux. Je les en remercie ainsi que Violette Brisson et Desmond Barber qui ont contribué à rendre mon document d'habilitation plus clair, plus précis et mieux écrit.

Sur le projet du polarimètre, j'ai travaillé étroitement avec Ties Behnke, Roger Bernier, Violette Brisson, Thierry Caceres, Ronic Chiche, Pascale Deck, Eckhard Elsen, Marie Jacquet-Lemire, Norbert Meyners, Daniel Pitzl, Yannick Queinec, André Reboux, Stefan Schmitt, Viktor Sousskov, Claude Vallée et Zhiqing Zhang. Je voudrais les remercier pour l'ambiance agréable et stimulante dans laquelle nous avons travaillé.

Je remercie mes collègues du CEA/Saclay, Martial Autier, Christian Cavata, Georges Cozzika, Nathalie Colombel, Alain Delbart, Nicolas Faletto et Damien Neyret pour leur collaboration et pour nous avoir prêté du matériel.

Je dois beaucoup à Michel Lintz concernant la mesure et le contrôle de la polarisation d'un faisceau laser. Je le remercie vivement du temps qu'il a consacré à répondre à mes questions, des conseils pratiques qu'il m'a donnés, du matériel qu'il m'a prêté et des mesures de biréfringence qu'il a effectuées pour le montage du polarimètre.

Françoise Maréchal m'a toujours aidé à me procurer des articles, parfois "trop vieux" ou même "introuvables". Je l'en remercie sincèrement.

L'idée d'installer une cavité Fabry-Perot autour d'un faisceau d'électrons m'a été suggérée par Patrice Hello au cours d'une surveillance d'examen de Mécanique-Quantique. Je l'en remercie amicalement.

Enfin, remercier nommément les membres des services administratif et technique du Laboratoire reviendrait à transformer cette page en un annuaire... Je voudrais souligner ici leurs qualités et leur indispensable soutien.